공학박사학위논문

A study on the Advanced Thermo-Mechanical Analysis of Laminated Composite and Sandwich Plates using Enhanced Shear Deformable Theories

개선된 전단변형 이론을 이용한 복합재료 및 샌드위치 적층 구조물에 대한 효율적 열-기계 연성 해석 기법에 대한 연구

2016 년 2 월

서울대학교 대학원

기계항공공학부

한 장 우

Abstract

In this dissertation, efficient and accurate models based on enhanced theories (enhanced first-order theories, enhanced higher-order theories and enhanced zig-zag theory) are proposed for the thermo-mechanical analysis of laminated composite and sandwich plates. In addition, co-rotational formulation with enhanced first-order theory is developed to investigate the geometrically nonlinear behaviors. In enhanced models, a couple of displacement fields are independently assumed to provide a reasonable compromise between solution accuracy and efficiency. The main objective of this dissertation is to systematically establish the relationships between two independent fields through the mixed variational theorem (MVT) as well as the strain energy transformation. According to the relationships, enhanced models have the same computational advantage of the simple models (conventional FSDT, HSDT, LCW, etc.) while improving upon its performance by utilizing the post-process procedure. Additionally, the convolution theorem of Laplace transformation is applied to circumvent the complexity of dealing with linear viscoelastic materials.

The enhanced theories proposed in this dissertation have the following advantages.

- Transverse shear stress continuity conditions at the interfaces between layers are satisfied.
- Transverse shear free conditions at the top and bottom surfaces of the composite and sandwich plates are satisfied.
- The number of primary variables is independent of the number of layers.
- C^0 interpolation function is only required in the finite element implementation, so computational efficiency can be further improved.

The robustness, accuracy and computational efficiency of the enhanced models are demonstrated by comparing numerical results obtained herein to those of the 3-D exact solution, 3-D FEM solution as well as other theories available in the open literature.

Keywords: Laminated Composite and Sandwich Plates, Enhanced theories, Mixed variational Theorem, Strain Energy Transformation, Thermo-

Mechanical Analysis, Viscoelastic Analysis, Geometrically Nonlinear Analysis.

Student Number: 2009-20740.

Contents

Abstract
i

Chapter 1. Introduction
1

1.1. Motivations & Objective ····· 1

1.2. Basic Concept of the Strain Energy Matching Scheme ····· 6

1.3. Thesis outline ····· 9

Chapter 2. Enhanced First-order Shear Deformation Theory
12

2.1. Enhanced First-order Shear Deformation Theory including Transverse Normal Effect via the MVT ····· 12

2.1.1. Literature Review ····· 12

2.1.2. Mixed Formulation ····· 14

2.1.3. Enhanced First-order Shear Deformation Theory including Transverse Normal Effect via the MVT ····· 23

2.1.4. Numerical examples and discussion ····· 29

2.2. Enhanced First-order Shear Deformation Theory in Laplace domain ····· 50

2.2.1. Literature Review ····· 50

2.2.2. Constitutive equation for linear viscoelastic materials ····· 53

2.2.3. Enhanced first-order shear deformation theory for the linear viscoelastic model ····· 54

2.2.4. Numerical examples and discussion ····· 65

Chapter 3. Enhanced Higher-order Shear Deformation Theory 83

3.1. Enhanced Higher-order Shear Deformation Theory based on the MVT ·· 83

3.1.1. Literature Review ····· 83

3.1.2. Mixed Formulation ····· 86

3.1.3. Enhanced higher-order shear deformation theory based on the MVT ····· 91

3.1.4. Numerical examples and discussion ····· 96

3.2. Enhanced Lo-Christensen-Wu Theory via the MVT ····· 119

3.2.1. Literature Review ····· 119

3.2.2. Mixed formulation ····· 122

3.2.3. Enhanced Lo-Christensen-Wu Theory via the MVT ····· 128

3.2.4. Numerical investigation and discussion ····· 132

Chapter 4. Enhanced Zig-zag Shear Deformation Theory 160

4.1. Enhanced C^0-type Efficient Higher-order Zig-zag Theory based on the MVT ····· 160

4.1.1. Literature Review ····· 160

4.1.2. Mixed Formulation ····· 162

4.1.3. Enhanced C^0-type efficient higher-order zig-zag theory based on the MVT ····· 170

4.1.4. Numerical examples and discussion ····· 173

Chapter 5. Geometrically Nonlinear Analysis Based on Enhanced FSDT 191

5.1. Co-rotational Geometrically Nonlinear Formulation based on EFSDT · 191

5.1.1. Literature Review ····· 191

5.1.2. Co-rotational Formulation ····· 194

5.1.3. Enhanced first-order shear deformation theory ····· 202

5.1.4. Numerical results and discussion ····· 209

Chapter 6. Concluding remarks
230

Bibliography **235**

Appendix **246**

List of Figures

Fig. 1.1. Geometry and coordinates of laminated plate ····· 11

Fig. 2.1.1. Flowchart of the EFSDTM_TN ····· 37

Fig. 2.1.2. Transverse shear stress of a single layer composite plate ($T_0 \neq 0$) ···· 38

Fig. 2.1.3. Transverse normal stress of a single layer composite plate ($T_0 \neq 0$) · 38

Fig. 2.1.4. In-plane stress of a [0/90/0] composite plates ($T_0 \neq 0$) ····· 39

Fig. 2.1.5. Transverse shear stress of a [0/90/0] composite plates ($T_0 \neq 0$) ····· 39

Fig. 2.1.6. Transverse normal stress of a [0/90/0] composite plates ($T_0 \neq 0$) ····· 40

Fig. 2.1.7. In-plane displacement of a [0/90/0/90] composite plates ($T_0 \neq 0$) ···· 40

Fig. 2.1.8. Transverse shear stress of a [0/90/0/90] composite plates ($T_0 \neq 0$) ··· 41

Fig. 2.1.9. Transverse shear stress of a $[0/90/0/90/0]_s$ composite plates ($T_0 \neq 0$) ·

····· 41

Fig. 2.1.10. Transverse normal stress of a $[0/90/0/90/0]_s$ composite plates ($T_0 \neq 0$) 42

Fig. 2.1.11. In-plane stress of a [0/Core/0] sandwich plates ($T_0 \neq 0$) 42

Fig. 2.1.12. Transverse shear stress of a [0/Core/0] sandwich plates ($T_0 \neq 0$) 43

Fig. 2.1.13. Transverse normal stress of a [0/Core/0] sandwich plates ($T_0 \neq 0$) 43

Fig. 2.1.14. Transverse shear stress of a single layer composite plate ($T_1 \neq 0$) 44

Fig. 2.1.15. Transverse normal stress of a single layer composite plate ($T_1 \neq 0$) 44

Fig. 2.1.16. In-plane stress of a [0/90/0] composite plates ($T_1 \neq 0$) 45

Fig. 2.1.17. Transverse normal stress of a [0/90/0] composite plates ($T_1 \neq 0$) 45

Fig. 2.1.18. Transverse shear stress of a [0/90/0/90] composite plates ($T_1 \neq 0$) 46

Fig. 2.1.19. Transverse normal stress of a [0/90/0/90] composite plates ($T_1 \neq 0$) 46

Fig. 2.1.20. Transverse shear stress of a $[0/90/0/90/0]_s$ composite plates ($T_1 \neq 0$) 47

Fig. 2.1.21. Transverse normal stress of a $[0/90/0/90/0]_s$ composite plates ($T_1 \neq 0$) 47

Fig. 2.1.22. In-plane stress of a [0/Core/0] sandwich plates ($T_1 \neq 0$) 48

Fig. 2.1.23. Transverse shear stress of a [0/Core/0] sandwich plates ($T_1 \neq 0$)..... 48

Fig. 2.1.24. Transverse normal stress of a [0/Core/0] sandwich plates ($T_1 \neq 0$) . 49

Fig. 2.2.1. [0/90/0]: time-dependent in-plane displacements for the creep process 78

Fig. 2.2.2. [90/0/90/0]: time-dependent in-plane displacements for the creep process 78

Fig. 2.2.3. [0/Core/0]: time-dependent in-plane displacements for the creep process 79

Fig. 2.2.4. [0/90/0]: time-dependent transverse shear stresses for the creep process 79

Fig. 2.2.5. [0/Core/0]: time-dependent transverse shear stresses for the creep process 80

Fig. 2.2.6. [0/90/0]: time-dependent in-plane stresses for the relaxation process 80

Fig. 2.2.7. [0/Core/0]: time-dependent in-plane stresses for the relaxation process 81

Fig. 2.2.8. [90/0/90/0]: time-dependent transverse shear stresses for the relaxation process 81

Fig. 2.2.9. $[90/0/90/0]_2$: time-dependent transverse shear stresses for the relaxation process ····· 82

Fig. 2.2.10. [90/Core/0]: time-dependent transverse shear stresses for the relaxation process ····· 82

Fig. 3.1.1. Loading and boundary conditions of semi-infinite plates ····· 107

Fig. 3.1.2. Displacement and stress of a simply-supported plate, S=4 ····· 108

Fig. 3.1.3. Transverse normal stresses of a simply-supported plate, Case 2 and 4 ····· 109

Fig. 3.1.4. Normalized tip deflections of the clamped-free sandwich plate ····110

Fig. 3.1.5. In-plane normal stresses of the clamped-free plate for the anti-symmetric angle-ply (Case 3), S=4 ·····111

Fig. 3.1.6. Transverse shear stresses of the clamped-free plate for the nearly symmetric cross-ply (Case 1), S=4·····112

Fig. 3.1.7. Transverse normal stresses of the clamped-free plate for the sandwich (Case 4), S=4 ·····113

Fig. 3.1.8. Schematic of a semi-infinite clamped-free plate for the boundary layer and interior zone·····114

Fig. 3.1.9. The change in the maximum value of the stresses along the axial coordinate (S=40)·····115

Fig. 3.1.10. Variations of the through-the-thickness stress distributions of the clamped-free isotropic plate (S=40) ·····116

Fig. 3.1.11. Variations of the through-the-thickness stress distributions of the symmetric cross-ply composite plates (S=40) ·····117

Fig. 3.1.12. Variations of the through-the-thickness stress distributions of the sandwich plates (S=40) ····· 118

Fig. 3.2.1. Flowchart of the ELCWM ····· 144

Fig. 3.2.2. In-plane displacements for [$0^o / 90^o / 0^o$] laminated plates under mechanical loading ····· 145

Fig. 3.2.3. In-plane stresses for [$0^o / 90^o / 0^o$] laminated plates under mechanical loading ····· 145

Fig. 3.2.4. Transverse shear stresses computed from constitutive equations for [$0^o / 90^o / 0^o$] laminated plates under mechanical loading ····· 146

Fig. 3.2.5. Transverse shear stresses computed from equilibrium equations for [$0^o / 90^o / 0^o$] laminated plates under mechanical loading ····· 146

Fig. 3.2.6. In-plane displacements for [$0^o / 90^o / 0^o / 90^o$] laminated plates under mechanical loading ····· 147

Fig. 3.2.7. In-plane stresses for [$0^o / 90^o / 0^o / 90^o$] laminated plates under mechanical loading ····· 147

Fig. 3.2.8. Transverse shear stresses computed from constitutive equations for [$0^o / 90^o / 0^o / 90^o$] laminated plates under mechanical loading····· 148

Fig. 3.2.9. Transverse shear stresses computed from equilibrium equations for [$0^o / 90^o / 0^o / 90^o$] laminated plates under mechanical loading····· 148

Fig. 3.2.10. In-plane displacements for [$0^o / core / 0^o$] sandwich plates under mechanical loading ····· 149

Fig. 3.2.11. In-plane stresses for [$0^o / core / 0^o$] sandwich plates under mechanical loading ····· 149

Fig. 3.2.12. Transverse shear stresses computed from constitutive equations for [$0^o / core / 0^o$] sandwich plates under mechanical loading ····· 150

Fig. 3.2.13. Transverse shear stresses computed from equilibrium equations for $[0^o / core / 0^o]$ sandwich plates under mechanical loading ····· 150

Fig. 3.2.14. In-plane stresses for a single layer plate under uniform temperature ····· 151

Fig. 3.2.15. Transverse shear stresses for a single layer plate under uniform temperature ····· 151

Fig. 3.2.16. In-plane displacements for $[0^o / 90^o / 0^o / 90^o]$ laminated plates under uniform temperature ····· 152

Fig. 3.2.17. Transverse shear stresses for $[0^o / 90^o / 0^o / 90^o]$ laminated plates under uniform temperature ····· 152

Fig. 3.2.18. In-plane stresses for $[0^o / core / 0^o]$ sandwich plates under uniform temperature ····· 153

Fig. 3.2.19. Transverse shear stresses for $[0^o / core / 0^o]$ sandwich plates under uniform temperature ····· 153

Fig. 3.2.20. In-plane stresses for $[0^o / 90^o / 0^o]$ laminated plates under temperature gradient ····· 154

Fig. 3.2.21. Transverse shear stresses for $[0^o / 90^o / 0^o]$ laminated plates under temperature gradient ····· 154

Fig. 3.2.22. In-plane stresses for $[0^o / 90^o / 0^o / 90^o]$ laminated plates under temperature gradient ····· 155

Fig. 3.2.23. Transverse shear stresses for $[0^o / 90^o / 0^o / 90^o]$ laminated plates under temperature gradient ····· 155

Fig. 3.2.24. In-plane stresses for $[0^o / 90^o / 0^o]$ laminated plates under uniform temperature-mechanical coupled load ····· 156

Fig. 3.2.25. Transverse shear stresses for [$0^o/90^o/0^o$] laminated plates under uniform temperature-mechanical coupled load ····· 156

Fig. 3.2.26. In-plane stresses for [$0^o/90^o/0^o/90^o$] laminated plates under uniform temperature-mechanical coupled load ····· 157

Fig. 3.2.27. Transverse shear stresses for [$0^o/90^o/0^o/90^o$] laminated plates under uniform temperature-mechanical coupled load ····· 157

Fig. 3.2.28. In-plane stresses for [$0^o/90^o/0^o$] laminated plates under temperature gradient-mechanical coupled load ····· 158

Fig. 3.2.29. In-plane stresses for [$0^o/90^o/0^o$] laminated plates under temperature gradient-mechanical coupled load ····· 158

Fig. 3.2.30. In-plane stresses for [$0^o/90^o/0^o/90^o$] laminated plates under temperature gradient-mechanical coupled load ····· 159

Fig. 3.2.31. In-plane stresses for [$0^o/90^o/0^o/90^o$] laminated plates under temperature gradient-mechanical coupled load ····· 159

Fig. 4.1.1. In-plane displacements for [$0^o/90^o/0^o$] laminated plates under uniform temperature ····· 180

Fig. 4.1.2. In-plane stresses for [$0^o/90^o/0^o$] laminated plates under uniform temperature ····· 180

Fig. 4.1.3. In-plane stresses for [$0^o/90^o/0^o$] laminated plates under uniform temperature ····· 181

Fig. 4.1.4. Transverse shear stresses for [$0^o/90^o/0^o$] laminated plates under uniform temperature ····· 181

Fig. 4.1.5. In-plane displacements for [$0^o / 90^o / 0^o$] laminated plates under temperature gradient ····· 182

Fig. 4.1.6. In-plane stresses for [$0^o / 90^o / 0^o$] laminated plates under temperature gradient····· 182

Fig. 4.1.7. Transverse shear stresses for [$0^o / 90^o / 0^o$] laminated plates under temperature gradient ····· 183

Fig. 4.1.8. In-plane displacements for [$0^o / 90^o / 0^o$] laminated plates under mechanical loading ····· 183

Fig. 4.1.9. In-plane stresses for [$0^o / 90^o / 0^o$] laminated plates under mechanical loading ····· 184

Fig. 4.1.10. Transverse shear stresses for [$0^o / 90^o / 0^o$] laminated plates under mechanical loading ····· 184

Fig. 4.1.11. Transverse shear stresses for [$0^o / 90^o / 0^o$] laminated plates under mechanical loading ····· 185

Fig. 4.1.12. In-plane displacements for [$0^o / 90^o / 0^o / 90^o$] laminated plates under uniform temperature····· 185

Fig. 4.1.13. In-plane stresses for [$0^o / 90^o / 0^o / 90^o$] laminated plates under uniform temperature····· 186

Fig. 4.1.14. In-plane stresses for [$0^o / 90^o / 0^o / 90^o$] laminated plates under uniform temperature····· 186

Fig. 4.1.15. Transverse shear stresses for [$0^o / 90^o / 0^o / 90^o$] laminated plates under uniform temperature····· 187

Fig. 4.1.16. In-plane displacements for [$0^o / 90^o / 0^o / 90^o$] laminated plates under temperature gradient ····· 187

Fig. 4.1.17. In-plane stresses for [$0^o / 90^o / 0^o / 90^o$] laminated plates under temperature gradient ····· 188

Fig. 4.1.18. Transverse shear stresses for [$0^o / 90^o / 0^o / 90^o$] laminated plates under temperature gradient ····· 188

Fig. 4.1.19. In-plane displacements for [$0^o / 90^o / 0^o / 90^o$] laminated plates under mechanical loading ····· 189

Fig. 4.1.20. In-plane stresses for [$0^o / 90^o / 0^o / 90^o$] laminated plates under mechanical loading ····· 189

Fig. 4.1.21. Transverse shear stresses for [$0^o / 90^o / 0^o / 90^o$] laminated plates under mechanical loading ····· 190

Fig. 5.1.1. Kinematics of EICR ····· 217

Fig. 5.1.2. Three-node plate element with 18 DOF ····· 217

Fig. 5.1.3. Cantilever plate subjected to end shear force ····· 218

Fig. 5.1.4. Load-deflection curves for isotropic cantilever subjected to end shear force ····· 218

Fig. 5.1.5. Middle axis deformation for isotropic cantilever subjected to end shear force ····· 219

Fig. 5.1.6. Cantilever plate subjected to end bending moment ····· 220

Fig. 5.1.7. Load-deflection curves for isotropic cantilever subjected to end bending moment ····· 220

Fig. 5.1.8. Middle axis deformation for isotropic cantilever subjected to end bending moment ····· 221

Fig. 5.1.9. Load-deflection curves for $[0^o/90^o/90^o/0^o]$ composite cantilever subjected to end shear force ····· 222

Fig. 5.1.10. Load-deflection curves for $[90^o/0^o/90^o/0^o]$ composite cantilever subjected to end shear force ····· 222

Fig. 5.1.11. Geometry of the sandwich plates ····· 223

Fig. 5.1.12. Variation of deflection against the magnitude of pressure ····· 223

Fig. 5.1.13. In-plane displacement under sinusoidal pressure ····· 224

Fig. 5.1.14. In-plane stress under sinusoidal pressure ····· 224

Fig. 5.1.15. In-plane stress under sinusoidal pressure ····· 225

Fig. 5.1.16. Transverse shear stress (c) under sinusoidal pressure ····· 225

Fig. 5.1.17. Transverse shear stress (e) under sinusoidal pressure ····· 226

Fig. 5.1.18. Variation of deflection against the magnitude of pressure ····· 226

Fig. 5.1.19. In-plane displacement under uniform pressure ····· 227

Fig. 5.1.20. In-plane stress under uniform pressure ····· 227

Fig. 5.1.21. In-plane stress under uniform pressure ····· 228

Fig. 5.1.22. Transverse shear stress (c) under uniform pressure ····· 228

Fig. 5.1.23. Transverse shear stress (e) under uniform pressure ····· 229

List of Tables

Table 2.2.1. The time-dependent function of relaxation modulus of GY70/399 composite material ····· 74

Table 2.2.2. The time-dependent function of relaxation modulus of the core of sandwich plate ····· 75

Table 2.2.3. The value of time-dependent creep deflection W for the laminated composite plates ····· 76

Table 2.2.4. The value of time-dependent creep deflection W for the sandwich plates ····· 77

Table 3.1.2. A list of lamination sequence for laminated and sandwich plates 104

Table 3.1.2. Comparison of center deflections of simply-supported semi-infinite plates under a sinusoidal load ····· 105

Table 3.1.3. Comparison of boundary layer and interior zones of the clamped-free edge plates ····· 106

Chapter 1

Introduction

1.1. Motivations & Objectives

In the recent past, aerospace structure, vehicle and many other high-performance industrial facilities demand light weight and high specific strength structures. Because advanced structures made of laminated composite panels are characterized by the high stiffness-to-weight ratio as well as excellent fatigue strength, they have been extensively used in various fields of engineering.

With the increased use of laminated composite structures, appropriate computational models are therefore required to accurately predict their static and dynamic responses. Because laminated composite structures are vulnerable to the transverse stresses, accurate prediction of the transverse stresses at the layer interfaces in an important issue in investigation of the failure analysis (i.e., debonding the interfaces). Thus numerous theoretical research activities which can be found in the open literature have been performed in order to accurately analyze the through-the-thickness distributions of transverse stresses.

In the early stage of the development of models, the classical laminate plate

theory (CLPT) is used to analyze the laminated composite plates, its results are inaccurate even for the global behavior. It is not adequate for the prediction of transverse stresses, because it neglects the shear deformation effect that is of great importance in the laminated composite plates. Thus, CLPT is applicable for only thin structures (length to thickness ratio > 30). To overcome this, various plate theories have been developed. A first-order shear deformation theory (FSDT) proposed by Reissner (1945) and Mindlin (1951) introduces the shear deformation into the theory [1-3], but the FSDT cannot precisely predict the through-thelayer transverse stress distributions. In addition to this, it requires a shear correction factor which calls the additional sophisticate work (Whitney, 1973; Noor and Burton, 1984) [4, 5]. On the other hands, there have been many efforts to improve the FSDT by introducing a higher-order shear deformation effect.

There are tremendous work in this topic, and interesting readers are referred to the review article [21, 22] and the book (Reddy, 2004). Historical Research works relevant to the present thesis are therefore briefly reviewed.

A higher order shear deformation theory (HSDT) with smeared displacement fields can provide more accurate results than the FSDT [6-9]. However, it is not able to capture so called ‘zigzag effect’ due to the material discontinuity through the thickness of laminated composite plates. Layer-wise plate theories are able to predict the stress distributions in detail and are matched well with the elasticity solutions [10]. However the number of primary variables is proportional to the number of layers, which results in many computational resources. Therefore, they are not suitable for the composite plates with many layers.

In the accurate and efficient modeling of laminated composite structures, it is

important to satisfy transverse shear continuity conditions across the layer interfaces. Thus, various zig-zag analysis models have also developed to provide a reasonable compromise between solution accuracy and efficiency [11-14]. A zigzag theory becomes popular after the work of Di Sciuva (1986). Among others, the efficient higher order plate theory (EHOPT) proposed by Cho and Parmerter [12,13] is known to be one of the most efficient model to analyze the through-the-layer distributions of displacements and stresses. In addition to this, it can gives reliable results by satisfying transverse shear continuity conditions across the layer interfaces as well as shear free conditions at the top and bottom surfaces of the plates. This approach was further extended to analyze the coupled thermos-electric-mechanical behaviors of smart composite structures [35-38]. In EHOPT, however, C^1 shape function (slope continuity condition along the boundary of the element) is necessary in their finite element implementation to satisfy shear free conditions. This requires non-conventional shape function routine which is not available in commercial finite element software.

To avoid using the C^1 interpolation function in the finite element implementation, some post-process methods have been developed [15-20]. A new analysis model based on post-process methods is developed by Cho and Kim [16,17], in which the EHOPT displacement field is utilized as the postprocessor. However it still requires a cumbersome calculation of the shear correction factor. To circumvent this, Kim and Cho proposed enhanced first order shear deformation theory based on the strain energy transformation (EFSDT) for the efficient and accurate analysis of composite plates [18]. They

systematically establish the relationships between the independent displacement fields (EHOPT and FSDT) by transforming the strain energy of the EHOPT into the FSDT-like strain energy. On the basis of the relationships between them, EFSDT only requires C^0 interpolation function in their finite element implementation in a similar way to the conventional FSDT model. Once the EFSDT strain energy is solved, the EHOPT displacement field is also utilized as the post-process procedure to improve their accuracy. In EFSDT, however, equilibrium state of the transverse normal stress is not completely satisfied since the EFSDT is derived by minimizing the error between the theories in the least square sense. To complement this, a mixed variational theorem is newly introduced, in which the stress field comes from the EHOPT and the displacement field is taken as the FSDT. This is referred to as the EFSDTM [19]. This concept of the mixed variational theorem was extended to HSDT, enhanced higher order shear deformation theory based on the mixed formulation (EHSDTM) was sequentially proposed for the efficient and accurate analysis of laminated composite structures [20]. The main objective of EHSDTM is to systematically set-up the relationship between the higher order shear deformation theory and fifth order zig-zag model, so that EHSDTM can fulfill the simplicity by calculating conventional HSDT-like theory as well as the accuracy by utilizing the fifth order zig-zag model as means of the recovery procedure. These enhanced theories (EFSDT, EFSDTM, EHSDTM) are also attractive because they are able to describe accurate behavior of the laminated composite structures without heavy computational efforts. However, most of these enhanced theories have been developed to analyze mechanical response of

the composite structures. Thus, more research on the enhanced theory is necessary to accurately and efficiently analyze their thermo-mechanical and visco-elastic behavior.

The main objective of this dissertation is to develop a more enhanced theories to accurately model the thermo-mechanical and visco-elastic characteristics of laminated composite and sandwich structures. To achieve the above requirements, the concepts of mixed variational theorem and strain energy transformation are employed to derive the reasonable relationships between the independently assumed displacement fields. In addition, particular enhanced theory (EFSDT) is further extended to geometrically non-linear analysis by introducing co-rotational approach. The major product of the objectives can be summarized as follows:

- EFSDTM_TN (EFSDTM including transverse normal effect): enhanced first-order model to analyze the thermo-mechanical behavior.
- EFSDT in Laplace domain: enhanced first-order model to analyze the visco-elastic response.
- EFSDT_CR (EFSDT based on co-rotational formulation): enhanced first-order model to predict the geometrically non-linear characteristics.
- EHSDTM (analytical and FEM approach): enhanced higher-order model to predict mechanical response and their edge effect.
- ELCWM (Enhanced Lo-Christensen-Wu theory): enhanced higher-order

model to analyze the thermo-mechanical behavior.

- Enhanced C^0-type EHOZT: enhanced zig-zag model to analyze the thermo-mechanical behavior.

1.2. Basic Concept of the Strain Energy Matching Scheme

In this dissertation, a generic laminated composite and sandwich plates of thickness *h* is considered in order to illustrated the proposed numerical model. Geometry and coordinates of the laminated composite plate is given in **Fig. 1.1**. The number of layers and sequence of fiber angles are arbitrarily designed according to the case of numerical example model. Greek indices written in this paper will take values in the set 1, 2, whereas Latin indices will be regarded as the values in 1, 2, 3. The summation rule of repeated indices will also be used. The reference two-dimensional (2D) plane of the laminated composite plates is referred as x_α, and the transverse displacement position is denoted by x_3.

1.2.1. Mixed Variational Theorem

The relationships between the independently assumed displacement fields can be derived by employing the mixed variational theorem (MVT). In the MVT, displacement and transverse stress fields are independently assumed for the reliable thermo-mechanical analysis of the laminated composite plates. The

three-dimensional Hellinger-Reissner functional for a linear thermo-elasticity is expressed by [19,20]:

$$\begin{aligned}&\int_V \left[\sigma_{\alpha\beta}\delta\varepsilon_{\alpha\beta} + \sigma^*_{\alpha 3}\delta\gamma_{\alpha 3} + \sigma^*_{33}\delta\varepsilon_{33}\right]dV \\ &+\int_V \left[(\gamma_{\alpha 3} - \gamma^*_{\alpha 3})\delta\sigma^*_{\alpha 3} + (\varepsilon_{33} - \varepsilon^*_{33})\delta\sigma^*_{33}\right]dV \\ &-\int_{S_\sigma} \tilde{t}^*_i \delta u_i dS_\sigma - \int_{S_u} \delta\tilde{t}^*_i (u_i - \tilde{u}_i)dS_u = 0,\end{aligned} \tag{1.2.1}$$

where $(\,)^*$ denotes the stress and strain tensor from the independent stress field, and the quantities with a tilde are the prescribed values. S_u and S_σ denote the boundaries with prescribed displacements($\tilde{u}_i$) and tractions($\tilde{t}^*_i$), respectively. The mixed term in Eq. (1.2.1), which is variationally enforces the compatibility of the transverse shear forces, will be vanished to derive governing equations.

The three-dimensional constitutive equation for a thermal expansion problem is given by

$$\sigma_{ij} = C_{ijkl}\left(\varepsilon_{kl} - \alpha_{kl}\theta\right),\ \theta = T - T_o, \tag{1.2.2}$$

in which θ is the temperature rise from the initial temperature T_o. C_{ijkl} is the component of elasticity tensor, ε_{kl} denote strain tensor and α_{ij} is the thermal expansion coefficient. The strain-displacement relationship is given as:

$$\varepsilon_{kl} = \tfrac{1}{2}\left(u_{k,l} + u_{l,k}\right). \tag{1.2.3}$$

From the three-dimensional Hellinger-Reissner (HR) functional, one can derive the first variation of two-dimensional HR functional by taking variations only with respect to the displacement u_i and the independent transverse stress $\sigma^*_{\alpha 3}$ and applying the plane stress condition (i.e., σ_{33}= 0) as follows [19,20]:

$$\delta\Pi^{2D}_R = \int_\Omega \left\langle \sigma^{2D}_{\alpha\beta}\delta\varepsilon_{\alpha\beta} + \sigma^*_{\alpha 3}\delta\gamma_{3\alpha}\right\rangle d\Omega - \int_{S_\sigma} \tilde{t}_i \delta u_i dS_\sigma = 0. \tag{1.2.4}$$

Equation (1.2.4) is subjected to

$$\delta\Pi_R^{2D} = \int_\Omega \left\langle (\gamma_{3\alpha} - \gamma_{3\alpha}^*)\delta\sigma_{3\alpha}^* \right\rangle d\Omega + \int_{S_u} \delta t_i^* (\mathrm{u}_i - \tilde{\mathrm{u}}_i) dS_u = 0, \tag{1.2.5}$$

where

$$\begin{gathered} \langle \bullet \rangle = \int_{-h/2}^{+h/2} [\bullet] dx_3, \quad \sigma_{\alpha\beta} = Q_{\alpha\beta\gamma\omega}\varepsilon_{\gamma\omega}, \quad Q_{\alpha\beta\gamma\omega} = C_{\alpha\beta\gamma\omega} - \frac{C_{\alpha\beta 33}\cdot C_{\gamma\omega 33}}{C_{3333}} \\ \gamma_{3\alpha} = u_{\alpha,3} + u_{3,\alpha}, \quad \gamma_{3\alpha}^* = C_{3\alpha 3\beta}^{-1}\sigma_{3\beta}^*, \quad t_\alpha^* = \sigma_{\alpha 3}^* n_\alpha, \quad t_3^* = \sigma_{\alpha 3}^* n_{3,} \end{gathered} \tag{1.2.6}$$

in which n_i is the direction cosine to be projected on x_i axis. It should be noted that $\sigma_{\alpha\beta}$ is the in-plane stress based on displacement u_i, whereas $\sigma_{\alpha 3}^*$ is the independently assumed transverse shear stress.

1.2.2. Strain Energy Transformation

Another way to establish the relationships between the independent two fields is the strain energy transformation. According to the asymptotic analysis, the general form of 3D displacement fields can be given as [18]:

$$\begin{aligned} u_\alpha^{3D}(x_i) &= u_\alpha^o(x_\beta) - x_3 \cdot u_{3,\alpha}^o(x_\beta) + W_\alpha(x_i), \\ u_3^{3D}(x_i) &= u_3^o(x_\beta) + W_3(x_i), \end{aligned} \tag{1.2.7}$$

where the superscript $(\bullet)^o$ indicates the displacement components in the reference plane, and $W_\alpha(x_i)$ and $W_3(x_i)$ represent the through-the-thickness warping functions. Complexities in three-dimensional analysis arise from warping function ($W_i(x_i)$ in Eq. (1.2.7)). To circumvent these complexities, the averaged displacement fields based on plate theory ($u_i^{2D}(x_i)$) are independently introduced to approximate the warping function. The averaged displacements can

be defined by applying the least-square approximation as follows:

$$\min \left\langle \left\| u_i^{3D} - u_i^{2D} \right\|_2 \right\rangle = 0 , \tag{1.2.8}$$

which yields the displacement relations between the independent two fields.

By using the displacement relations, the strain energy of three-dimensional displacement fields (U^{3D}) can be transformed into averaged displacement type strain energy (U^{2D}) as [18]:

$$U^{3D} \approx U^{2D} + U_{Error}. \tag{1.2.9}$$

The U_{Error} indicates the strain energy difference between the two fields. Then, the relations of these strain energies (U^{3D} and U^{2D}) are reasonably defined by minimizing U_{Error} as close to be zero as possible.

1.3. Thesis outline

The present thesis is organized as follows. The development of an enhanced first-order shear deformation theories will be introduced in chapter 2. The EFSDTM including transverse normal effect (EFSDTM_TN) and EFSDT in Laplace domain are presented in this chapter for the thermo-mechanical and visco-elastic analysis of the laminated composite and sandwich plates. At the beginning of each analysis model, previous works are reviewed. In chapter 3, enhanced higher-order shear deformation theories are developed by enhancing conventional higher-order shear deformation theories. EHSDTM will be proposed to accurately analyze mechanical response of the laminated composite and sandwich plates and their boundary edge effect. In addition, ELCWM will be also introduced in chapter 3 to

precisely predict their thermo-mechanical behavior. Chapter 4 present enhanced zig-zag theory by introducing the enhanced C^0-type EHOZT for the accurate and efficient thermo-mechanical analysis of the laminated composite and sandwich plates. Chapter 5 introduces EFSDT based on co-rotational formulation. In this chapter, the EFSDT which is linear-elastic based model will be extended to the geometrically non-linear finite element implementation by applying the co-rotational frame to the EFSDT. In each chapter, the performance of the proposed theories will be demonstrated by investigating various numerical results of the laminated structures. Finally, conclusions and recommendations for the future work are provided in Chapter 6.

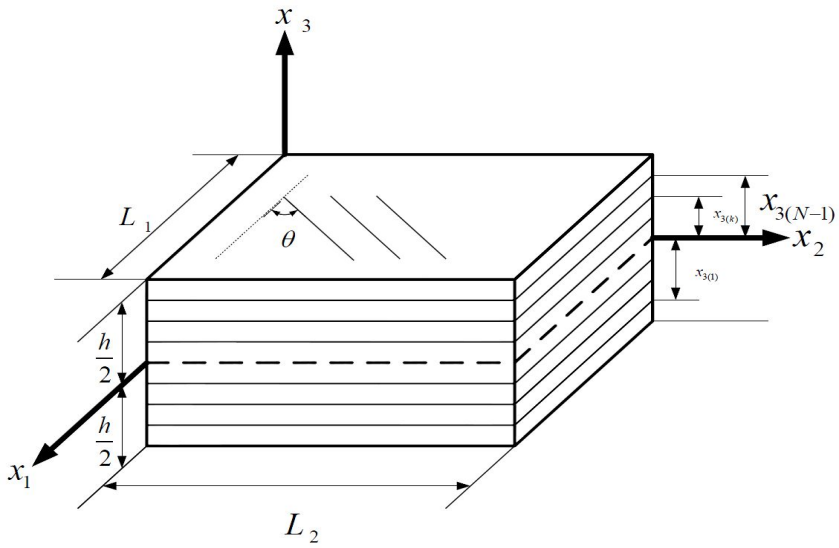

Fig. 1.1. Geometry and coordinates of laminated plate

Chapter 2

Enhanced First-order

Shear Deformation Theory

2.1. Enhanced First-order Shear Deformation Theory including Transverse Normal Effect via the MVT

2.1.1. Literature Review

With the improvement of technology, composite structures can be applied to wider range of engineering field, so that it can be consequently faced with severe environment such as high temperature situations. The thermal loading based on rising temperature may give rise to significant thermal deformation and stresses due to their different thermal expansion properties of adjacent layers of the laminated structures. Thus, productive research on composite and sandwich plates under thermal loading is highly required to accurately predict their thermo-elastic response.

Previous conventional works (CLPT, FSDT) are inapplicable to accurate

analysis of the thermo-elastic behavior for the relatively thick plates because they assumed shear strain to be zero or constant value. In addition, conventional theories are based on the plane stress assumption in which transverse normal strain effect is neglected. However, transverse normal strain effect plays a significant role for the analysis of thick multilayered structures under thermal environment. Therefore, many researchers focus on their interest in refined higher order as well as zig-zag shear deformation theories to accurately predict the thermos-elastic response of the thick laminated composite and sandwich structures [23-41].

Reviewing on previous works, these mentioned higher-order and zig-zag theories can provide reliable thermo-elastic response of the composite structures in thermal environment. Conventional FSDT, however, is estimated an in adequate approach to demonstrate thermo-elastic analysis, although it has explicit advantages such as computational profits as well as C^0 finite element implementation. EFSDT, which contains advantages of the conventional FSDT, is somewhat reliable for the elasto-static problems. However, it is not appropriate for thermo-elastic problems due to the significant effect of the transverse normal strain. To settle this problem, Oh et al developed an enhanced lower order shear deformation theory (ELSDT) for the electro-thermo-mechanical coupled analysis of a smart composite structures [42]. This model is efficient and accurate tool for the analysis of smart structures under complex loading conditions by extending transverse displacement field to be smooth parabolic distribution. The ELSDT, however, requires more degrees of freedom and three dimensional governing equation which will lead to heavy

computational efforts. This bring us to develop a modified method that can take the benefits of using conventional FSDT and accurately predict the thermo-elastic behavior of the laminated composite and sandwich plates.

As a new way to address the aforementioned issues, enhanced first order shear deformation theory including transverse normal effect based on mixed variational theorem (EFSDTM_TN) is proposed. By modifying the transverse displacement field, present model can consider transverse normal strain effect without additional displacement variables. Moreover, in-plane correction factors which is introduced to satisfy the in-plane equilibrium equations are newly considered to more accurately predict thermo-elastic responses for the general configuration of the structures. The main objective herein is to systematically establish the relationship between FSDT_TN (FSDT including transverse normal effect) and EHOPT_TN (EHOPT including transverse normal effect), so that modified EFSDTM_TN can fulfill the simplicity by calculating conventional FSDT-like theory as well as the accuracy by utilizing the third order zig-zag model as means of the recovery procedure. The temperature field assumed the form of a uniform or linear distribution through the thickness of the structures. Finally the accuracy and efficiency of the results obtained in this paper is demonstrated by comparing them to those of other theories including three dimensional elasticity solutions.

2.1.2. Mixed Formulation

To accurately and efficiently analyze the thermo-mechanical responses of the laminated composite and sandwich plates, EFSDTM_TN is developed in this

dissertation via the mixed variational theorem. In the MVT, the first variation of two-dimensional HR functional, which is given in Eqs. (1.2.4) and (1.2.5), is employed to derive the relationships between the independent two fields.

2.1.2.1. Improvement of transverse displacement field

In this chapter, a modified transverse displacement field which can effectively consider the transverse normal strain effect is introduced for the efficient and accurate prediction of the thermo-elastic responses of the laminated composite structures.

Many of the composite plate and shell theories proposed until now are based on plane stress assumption. In pure bending problem, they can provide relatively accurate results for the elasto-static responses of the laminated composite and sandwich plates. In thermo-mechanical problem, however, the transverse normal strain effect should be considered for the reliable thermo-elastic analysis. In the open literature, it has been also well known that both transverse normal and shear deformation shouldn't be neglected for the reasonable prediction of the thermal stresses under uniform temperature condition.

Among the possible approaches to efficiently consider the contribution of the transverse normal strain effect, a basic concept is to increase the order of transverse displacement field such like the form of parabolic variational field. This concept has accurately predicted thermo-elastic responses of the laminated structures because it can consider the transverse normal strain effect. However, more degrees of freedom accompanied by increasing transverse displacement components will lead to heavy computational efforts. Moreover, the parabolic

form of transverse displacement field requires three dimensional governing equations. Thus, the transverse displacement field is newly modified in this paper to improve the computational efficiency as well as the accuracy for the thermo-elastic analysis of the laminated composite structures. The modified displacement fields are introduced as follows

$$\begin{aligned} u_\alpha &= \sum_{k=0}^{i} u_\alpha^{(k)} x_3^{(k)} + j \bullet \sum_{k=1}^{N-1} S_\alpha^{(k)} (x_3 - x_{3(k)}) H(x_3 - x_{3(k)}), \\ u_3 &= u_3^{(0)} + \varphi^{(i)} T_o x_3 + \frac{1}{2} \varphi^{(i)} T_1 x_3^2 + \sum_{k=1}^{N-1} S_3^{(k)} H(x_3 - x_{3(k)}). \end{aligned} \tag{2.1.1}$$

$\varphi^{(i)}$ is layer-wise constant to satisfy the plane stress assumption, and T_o, T_1 represent a prescribed uniform or linear temperature distributions through the thickness. The explicit derivation of $\varphi^{(i)}$ can be found in **Appendix A**.

N is the number of layers, $S_i^{(k)}$ and $H(x_3 - x_{3(k)})$ are the linear zig-zag terms and the Heaviside unit step function, respectively. Some modified theories, which are FSDT_TN (i=1, j=0), HSDT_TN (i=3, j=0) and EHOPT_TN (i=3, j=1), is expressed in Eq. (2.1.1). These modified displacement fields will allow us to accurately analyze the thermo-mechanical behavior of the laminated composite and sandwich plates by considering transverse normal strain effect. In addition, it also allow us to simplify the calculation process by applying two dimensional governing equations under plane stress assumption.

2.1.2.2. Independent transverse shear stress fields

In the MVT, two independent displacement fields (u_i) and transverse shear stress fields ($\sigma^*_{3\alpha}$) are assumed in the MVT. In this section, a third order zig-zag model based on EHOPT_TN is introduced to derive independent transverse shear stress fields which are to be used as $\sigma^*_{3\alpha}$ in MVT. A reliable displacement fields should satisfies the shear free conditions on the surface of the structures and the shear stress continuity conditions at the interfaces between each layers without losing the accuracy and efficiency. These conditions can be satisfied by superimposing linear zig-zag fields, which have different slopes in each layer, to the globally cubic varying displacement fields. The starting third order zig-zag displacement fields can be written as follows

$$\begin{aligned} u_\alpha &= u_\alpha^{(0)} + u_\alpha^{(1)} x_3 + u_\alpha^{(2)} x_3^2 + u_\alpha^{(3)} x_3^3 + \sum_{k=1}^{N-1} S_\alpha^{(k)} (x_3 - x_{3(k)}) H(x_3 - x_{3(k)}), \\ u_3 &= u_3^{(0)} + \varphi^{(i)} T_o x_3 + \frac{1}{2} \varphi^{(i)} T_1 x_3^2 + \sum_{k=1}^{N-1} S_3^{(k)} H(x_3 - x_{3(k)}). \end{aligned} \tag{2.1.2}$$

$u_i^{(i)}$ denote displacement components at the reference plane. By applying shear stress free conditions on the top and bottom surface of the structures, two set of equations are derived as follows [12, 13]:

$$\begin{aligned} \gamma_{\alpha 3}\big|_{z=\frac{h}{2}} = \; & u_\alpha^{(1)} + u_\alpha^{(2)} h + \frac{3}{4} h^2 u_\alpha^{(3)} + \sum_{k=1}^{N-1} S_\alpha^k + u_{3,\alpha}^{(0)} \\ & + \varphi^{(N)} T_{o,\alpha} \frac{h}{2} + \varphi^{(N)} \frac{1}{2} T_{1,\alpha} \frac{h^2}{4} + \sum_{k=1}^{N-1} S_{3,\alpha}^k = 0, \\ \gamma_{\alpha 3}\big|_{z=-\frac{h}{2}} = \; & u_\alpha^{(1)} - u_\alpha^{(2)} h + \frac{3}{4} h^2 u_\alpha^{(3)} + u_{3,\alpha}^{(0)} \\ & - \varphi^{(1)} T_{o,\alpha} \frac{h}{2} + \varphi^{(1)} \frac{1}{2} T_{1,\alpha} \frac{h^2}{4} = 0. \end{aligned} \tag{2.1.3}$$

These equation can be satisfied by following relationships

$$u_\alpha^{(1)} = -\left(\begin{array}{l} u_{3,\alpha}^{(0)} + \frac{3}{4}h^2 u_\alpha^{(3)} + \frac{1}{2}\sum_{k=1}^{N-1}(S_\alpha^{(k)} + S_{3,\alpha}^{(k)}) \\ + \frac{h}{2}\frac{\left(\varphi^{(N)} - \varphi^{(1)}\right)}{2}T_{o,\alpha} + \frac{h^2}{4}\frac{\left(\varphi^{(N)} + \varphi^{(1)}\right)}{2}\left(\frac{1}{2}T_{1,\alpha}\right) \end{array} \right),$$

$$u_\alpha^{(2)} = -\left(\begin{array}{l} \frac{1}{2h}\sum_{k=1}^{N-1}(S_\alpha^{(k)} + S_{3,\alpha}^{(k)}) \\ + \frac{h}{2}\frac{\left(\varphi^{(N)} + \varphi^{(1)}\right)}{2h}T_{o,\alpha} + \frac{h^2}{4}\frac{\left(\varphi^{(N)} - \varphi^{(1)}\right)}{2h}\left(\frac{1}{2}T_{1,\alpha}\right) \end{array} \right). \quad (2.1.4)$$

Thus, the transverse shear strains is then expressed as follows:

$$\begin{aligned} \gamma_{\alpha 3} = & \left(3x_3^2 - \frac{3}{4}h^2\right)u_\alpha^{(3)} + \left(-\frac{1}{2} - \frac{x_3}{h} + H(x_3 - x_{3(k)})\right)\sum_{k=1}^{N-1}(S_\alpha^{(k)} + S_{3,\alpha}^{(k)}) \\ & + \left(-\frac{h}{2}\left(\frac{\left(\varphi^{(N)} - \varphi^{(1)}\right)}{2} + \frac{\left(\varphi^{(N)} + \varphi^{(1)}\right)}{h}x_3\right) + \varphi^{(i)}x_3\right)T_{o,\alpha} \\ & + \left(-\frac{h^2}{4}\left(\frac{\left(\varphi^{(N)} + \varphi^{(1)}\right)}{2} + \frac{\left(\varphi^{(N)} - \varphi^{(1)}\right)}{h}x_3\right) + \varphi^{(i)}x_3^2\right)\frac{1}{2}T_{1,\alpha}. \end{aligned} \quad (2.1.5)$$

The $S_\alpha^{(k)}$ and $S_3^{(k)}$ are slope change at the layer interface which can be determined in terms of the primary variables of the reference plane and prescribed thermal values. They can be expressed as following form [12, 13]:

$$S_\alpha^{(k)} = a_{\alpha\beta}^{(k)}u_\beta^{(3)} + b_{\alpha\beta}^{(k)}T_{o,\beta} + c_{\alpha\beta}^{(k)}\frac{1}{2}T_{1,\beta}, \quad S_3^{(k)} = b_{33}^{(k)}T_o + c_{33}^{(k)}\frac{1}{2}T_1. \quad (2.1.6)$$

The term $a_{\alpha\gamma}^{(k)}$, $b_{\alpha\gamma}^{(k)}$ and $c_{\alpha\gamma}^{(k)}$ are functions of the material properties that account for the transverse shear stress continuity conditions at, while $b_{33}^{(k)}$, $c_{33}^{(k)}$

are the functions of layer-wise constant ($\varphi^{(k)}$) to satisfy the transverse displacement continuity conditions at the layer interfaces. The explicit calculations of $a_{\alpha\gamma}^{(k)}$, $b_{ij}^{(k)}$ and $c_{ij}^{(k)}$ can be found in **Appendix B**.

Substituting of Eqs. (2.1.4) and (2.1.6) into Eqs. (2.1.2) and (2.1.5), final expression of the displacement fields and their transverse shear fields of EHOPT_TN can be expressed as,

Displacement fields:

$$\begin{aligned} u_\alpha &= u_\alpha^{(0)} - u_{3,\alpha}^{(0)} x_3 + \Phi_{\alpha\beta}^{(1)} u_\beta^{(3)} + \Phi_{\alpha\beta}^{(2)} T_{o,\beta} + \Phi_{\alpha\beta}^{(3)} \frac{1}{2} T_{1,\beta}, \\ u_3 &= u_3^{(0)} + \left[\varphi^{(i)} x_3 + \sum_{k=1}^{N-1} b_{33}^{(k)} H(x_3 - x_{3(k)}) \right] T_o \\ &\quad + \left[\varphi^{(i)} x_3^2 + \sum_{k=1}^{N-1} c_{33}^{(k)} H(x_3 - x_{3(k)}) \right] \frac{1}{2} T_1. \end{aligned} \tag{2.1.7}$$

In which

$$\begin{aligned} \Phi_{\alpha\beta}^{(1)} &= \left(x_3^3 - \frac{3h^2}{4} x_3 \right) \delta_{\alpha\beta} + \left(-\frac{x_3}{2} - \frac{x_3^2}{2h} + (x_3 - x_{3(k)}) H(x_3 - x_{3(k)}) \right) \sum_{k=1}^{N-1} a_{\alpha\beta}^{(k)}, \\ \Phi_{\alpha\beta}^{(2)} &= \begin{pmatrix} \left[-\frac{h}{2} \left(\frac{\left(\varphi^{(N)} - \varphi^{(1)}\right)}{2} x_3 + \frac{\left(\varphi^{(N)} + \varphi^{(1)}\right)}{h} \frac{x_3^2}{2} \right) \right] \delta_{\alpha\beta} \\ + \left(-\frac{x_3}{2} - \frac{x_3^2}{2h} \right) \sum_{k=1}^{N-1} \left(b_{\alpha\beta}^{(k)} + \delta_{\alpha\beta} b_{33}^{(k)} \right) + (x_3 - x_{3(k)}) H(x_3 - x_{3(k)}) \sum_{k=1}^{N-1} b_{\alpha\beta}^{(k)} \end{pmatrix}, \\ \Phi_{\alpha\beta}^{(3)} &= \begin{pmatrix} \left[-\frac{h^2}{4} \left(\frac{\left(\varphi^{(N)} + \varphi^{(1)}\right)}{2} x_3 + \frac{\left(\varphi^{(N)} - \varphi^{(1)}\right)}{h} \frac{x_3^2}{2} \right) \right] \delta_{\alpha\beta} \\ + \left(-\frac{x_3}{2} - \frac{x_3^2}{2h} \right) \sum_{k=1}^{N-1} \left(c_{\alpha\beta}^{(k)} + \delta_{\alpha\beta} c_{33}^{(k)} \right) + (x_3 - x_{3(k)}) H(x_3 - x_{3(k)}) \sum_{k=1}^{N-1} c_{\alpha\beta}^{(k)} \end{pmatrix}. \end{aligned} \tag{2.1.8}$$

Transverse shear strain and stress fields:

$$\begin{aligned}\gamma_{3\alpha} &= \mathscr{A}_{\alpha\beta}u_{\beta}^{(3)} + \mathscr{B}_{\alpha\beta}T_{o,\beta} + \mathscr{C}_{\alpha\beta}\frac{1}{2}T_{1,\beta} \cong \gamma_{\alpha 3}^{*} \quad , \\ \sigma_{\alpha 3} &= C_{\alpha 3\beta 3}\left[\mathscr{A}_{\beta\gamma}u_{\gamma}^{(3)} + \mathscr{B}_{\beta\gamma}T_{o,\gamma} + \mathscr{C}_{\beta\gamma}\frac{1}{2}T_{1,\gamma}\right] \cong \sigma_{\alpha 3}^{*}.\end{aligned} \tag{2.1.9}$$

In which

$$\begin{aligned}\mathscr{A}_{\alpha\beta} &= \left(3x_3^2 - \frac{3}{4}h^2\right)\delta_{\alpha\beta} + \left(-\frac{1}{2} - \frac{x_3}{h} + H(x_3 - x_{3(k)})\right)\sum_{k=1}^{N-1}a_{\alpha\beta}^{(k)}, \\ \mathscr{B}_{\alpha\beta} &= \left(\begin{array}{l}\left[-\frac{h}{2}\left(\frac{\left(\varphi^{(N)} - \varphi^{(1)}\right)}{2} + \frac{\left(\varphi^{(N)} + \varphi^{(1)}\right)}{h}x_3\right) + \varphi^{(i)}x_3\right]\delta_{\alpha\beta} \\ + \left(-\frac{1}{2} - \frac{x_3}{h} + H(x_3 - x_{3(k)})\right)\sum_{k=1}^{N-1}\left(b_{\alpha\beta}^{(k)} + \delta_{\alpha\beta}b_{33}^{(k)}\right)\end{array}\right), \\ \mathscr{C}_{\alpha\beta} &= \left(\begin{array}{l}\left[-\frac{h^2}{4}\left(\frac{\left(\varphi^{(N)} + \varphi^{(1)}\right)}{2} + \frac{\left(\varphi^{(N)} - \varphi^{(1)}\right)}{h}x_3\right) + \varphi^{(i)}x_3^2\right]\delta_{\alpha\beta} \\ + \left(-\frac{1}{2} - \frac{x_3}{h} + H(x_3 - x_{3(k)})\right)\sum_{k=1}^{N-1}\left(c_{\alpha\beta}^{(k)} + \delta_{\alpha\beta}c_{33}^{(k)}\right)\end{array}\right).\end{aligned} \tag{2.1.10}$$

$\delta_{\alpha\beta}$ is the Kronecker delta function.

To find the more reasonable relationships between the independent two fields for the general configuration of the structure, in-plane shear correction factors are newly considered in EHOPT_TN to satisfy their self-equilibrium states. The displacement and transverse shear stress fields which additionally consider the in-plane correction factors can be expressed as

Displacement fields:

$$
\begin{aligned}
u_\alpha &= u_\alpha^{(0)} - u_{3,\alpha}^{(0)} x_3 + \Phi_{\alpha\beta}^{(1)} u_\beta^{(3)} + \Phi_{\alpha\beta}^{(2)} T_{o,\beta} + \Phi_{\alpha\beta}^{(3)} \frac{1}{2} T_{1,\beta} - C_\alpha^N - C_\alpha^M x_3, \\
u_3 &= u_3^{(0)} + \left[\varphi^{(i)} x_3 + \sum_{k=1}^{N-1} b_{33}^{(k)} H(x_3 - x_{3(k)}) \right] T_o \\
&\quad + \left[\varphi^{(i)} x_3^2 + \sum_{k=1}^{N-1} c_{33}^{(k)} H(x_3 - x_{3(k)}) \right] \frac{1}{2} T_1.
\end{aligned}
\tag{2.1.11}
$$

Transverse shear strain and stress fields:

$$
\begin{aligned}
\gamma_{3\alpha} &= \mathscr{A}_{\alpha\beta} u_\beta^{(3)} + \mathscr{B}_{\alpha\beta} T_{o,\beta} + \mathscr{C}_{\alpha\beta} \frac{1}{2} T_{1,\beta} - C_\alpha^M \cong \gamma_{\alpha 3}^* \quad , \\
\sigma_{\alpha 3} &= C_{\alpha 3 \beta 3} \left[\mathscr{A}_{\beta\gamma} u_\gamma^{(3)} + \mathscr{B}_{\beta\gamma} T_{o,\gamma} + \mathscr{C}_{\beta\gamma} \frac{1}{2} T_{1,\gamma} - C_\alpha^M \right] \cong \sigma_{\alpha 3}^*,
\end{aligned}
\tag{2.1.12}
$$

where

$$
\begin{aligned}
C_\alpha^N &= c_{\alpha\beta}^{N(\phi)} \phi_\beta + c_{\alpha\beta}^{N(T_o)} T_{o,\beta} + c_{\alpha\beta}^{N(T_1)} \left(\frac{1}{2} T_{1,\beta} \right), \\
C_\alpha^M &= c_{\alpha\beta}^{M(\phi)} \phi_\beta + c_{\alpha\beta}^{M(T_o)} T_{o,\beta} + c_{\alpha\beta}^{M(T_1)} \left(\frac{1}{2} T_{1,\beta} \right).
\end{aligned}
\tag{2.1.13}
$$

C_α^N, C_α^M are the in-plane correction factors in terms of the $u_\alpha^{(3)}$, T_o and T_1 which can't be derived in initial statement. These in-plane correction factors can be derived by matching resultant force and moment of both assumed theories based on Saint-Venant principle. The detailed expression for the derivation process of the in-plane correction factors are given in the **Appendix C**.

The variables in the final form of the displacement and transverse shear stress fields are defined at the reference plane. Thus, primary unknown variables of the

EHOPT_TN, which is expressed as $u_1^{(0)}, u_2^{(0)}, u_1^{(3)}, u_2^{(3)}, u_3^{(0)}$, does not depend on the number of layers. These independent transverse shear strains and stresses make it possible to find the reasonable relationships between FSDT_TN and EHOPT_TN, and the relationships play an important role as the shear correction factor in deriving governing equations of the FSDT_TN.

2.1.2.3. Displacement fields

The displacement fields of the FSDT_TN, which are used for the displacement and strain fields in MVT, is given as following forms

$$\begin{aligned} \overline{u}_\alpha &= \overline{u}_\alpha^{(0)} + \overline{u}_\alpha^{(1)} x_3, \\ \overline{u}_3 &= \overline{u}_3^{(0)} + \varphi^{(i)} T_o x_3 + \frac{1}{2}\varphi^{(i)} T_1 x_3^2 + \sum_{k=1}^{N-1} S_3^{(k)} H(x_3 - x_{3(k)}). \end{aligned} \tag{2.1.14}$$

To achieve clear comparison between displacement fields of FSDT_TN and EHOPT_TN, the components of the FSDT_TN are given with overbar. And the mid-plane displacement $\overline{u}_\alpha^{(0)}$ denotes the mean displacement of the plate. Through the displacement fields of Eq. (2.1.14), the strains can be subsequently derived as follows:

$$\begin{aligned} \overline{\varepsilon}_{\alpha\beta} &= \overline{\varepsilon}_{\alpha\beta}^{(0)} + \overline{\varepsilon}_{\alpha\beta}^{(1)} x_3, \\ \overline{\gamma}_{3\alpha} &= \overline{\gamma}_{3\alpha}^{(0)} + \left[\varphi^{(i)} x_3 + \sum_{k=1}^{N-1} b_{33}^{(k)} H(x_3 - x_{3(k)}) \right] T_{o,\alpha} \\ &\quad + \left[\varphi^{(i)} x_3^2 + \sum_{k=1}^{N-1} c_{33}^{(k)} H(x_3 - x_{3(k)}) \right] \frac{1}{2} T_{1,\alpha}. \end{aligned} \tag{2.1.15}$$

And the in-plane stress to be used in MVT, in Ep. (1.2.4), can be given as

$$\sigma_{\alpha\beta} = Q_{\alpha\beta\gamma\omega}(\overline{\varepsilon}_{\gamma\omega} - \alpha_{\gamma\omega}\Delta T), \tag{2.1.16}$$

where $Q_{\alpha\beta\gamma\omega}$ are the reduced elastic stiffness tensor, as expressed in Eq. (1.2.6); $\alpha_{\gamma\omega}$ are the thermal expansion coefficients in the plate coordinates; and ΔT is the temperature distribution.

2.1.3. Enhanced First-order Shear Deformation Theory including Transverse normal effect via the MVT

Independently assumed transverse shear stresses and displacement fields are described in the previous section. In this section, an enhanced first order shear deformation theory including transverse normal strain effect is derived. The relationships between independent two fields can be systematically established via the MVT. Thus, governing equation of the present theory is based on the FSDT_TN. In addition, recovery process is also considered in this section to more accurately predict the thermo-elastic response of the laminated composite structures.

2.1.3.1. Relationships between the two theories

Substituting displacement and strain fields (Eqs. (2.1.14) and (2.1.15)) into

MVT (Eq. (1.2.4)) yields

$$\delta\Pi_R^{2D} = \bar{N}_{\alpha\beta}\delta\bar{u}^o_{\alpha,\beta} + \bar{M}_{\alpha\beta}\delta\bar{u}^{(1)}_{\alpha,\beta} + Q^*_\alpha\delta(\bar{\gamma}^{(0)}_{3\alpha}). \tag{2.1.17}$$

and the third 'mixed' term in Eq. (1.2.5), which is used as the constraint equations, is expressed as

$$\left\langle \left(\bar{\gamma}^{(0)}_{3\alpha} - S_{3\alpha3\beta}\sigma^*_{3\beta}\right)\delta\sigma^*_{3\alpha} \right\rangle = 0, \tag{2.1.18}$$

where

$$\bar{\gamma}^{(0)}_{3\alpha} = \bar{u}^{(1)}_\alpha + \bar{u}^o_{3,\alpha}\ , [\bar{N}_{\alpha\beta}, \bar{M}_{\alpha\beta}, Q^*_\alpha] = \left\langle \bar{\sigma}^{2D}_{\alpha\beta}[1, x_3], \sigma^*_{3\alpha} \right\rangle. \tag{2.1.19}$$

The independent transverse shear force Q^*_α considering in-plane correction factor can be expressed as:

$$Q^*_\alpha = \hat{A}^{(0)}_{\alpha3\beta3}u^{(3)}_\beta + \hat{A}^{(1)}_{\alpha3\beta3}\left(\varphi T_{o,\beta}\right) + \hat{A}^{(2)}_{\alpha3\beta3}\left(\frac{1}{2}\varphi T_{1,\beta}\right), \tag{2.1.20}$$

where

$$\begin{aligned}
\hat{A}^{(0)}_{\alpha3\beta3} &= \left\langle C_{\alpha3\gamma3}\left(\mathscr{A}_{\gamma\beta} - c^{M(\phi)}_{\gamma\beta}\right)\right\rangle, \\
\hat{A}^{(1)}_{\alpha3\beta3} &= \left\langle C_{\alpha3\gamma3}\left(\mathscr{B}_{\gamma\beta} - c^{M(T_o)}_{\gamma\beta}\right)\right\rangle, \\
\hat{A}^{(2)}_{\alpha3\beta3} &= \left\langle C_{\alpha3\gamma3}\left(\mathscr{C}_{\gamma\beta} - c^{M(T_1)}_{\gamma\beta}\right)\right\rangle.
\end{aligned} \tag{2.1.21}$$

From the constraint conditions expressed as Eq. (2.1.18), the component of the independent transverse shear stresses based on the EHOPT_TN ($u^{(3)}_\alpha$) can be expressed in terms of the variables from assumed displacement fields of the

FSDT_TN ($\overline{\gamma}_{\alpha 3}$) as follows [19]:

$$\begin{aligned}&\hat{A}^{(0)}_{\alpha 3\gamma 3}\overline{\gamma}^{(0)}_{\gamma 3}+\hat{B}^{(0)}_{\alpha 3\gamma 3}\left(\varphi T_{o,\gamma}\right)+\hat{D}^{(0)}_{\alpha 3\gamma 3}\left(\frac{1}{2}\varphi T_{1,\gamma}\right)\\&=\tilde{A}^{(0)}_{\alpha 3\beta 3}u^{(3)}_{\beta}+\tilde{A}^{(1)}_{\alpha 3\beta 3}\left(\varphi T_{o,\beta}\right)+\tilde{A}^{(2)}_{\alpha 3\beta 3}\left(\frac{1}{2}\varphi T_{1,\beta}\right),\end{aligned} \tag{2.1.22}$$

where

$$\begin{aligned}\begin{bmatrix}\hat{B}^{(0)}_{\gamma 3\beta 3}\\ \hat{D}^{(0)}_{\gamma 3\beta 3}\end{bmatrix}&=\left\langle\left(\hat{\mathscr{A}}^{(0)}_{\gamma\alpha}-c^{M(\phi)}_{\gamma\alpha}\right)C_{\alpha 3\beta 3}\begin{bmatrix}\left(\varphi^{(i)}x_3+\sum_{k=1}^{N-1}b^{(k)}_{33}H(x_3-x_{3(k)})\right)\\ \left(\varphi^{(i)}x_3^2+\sum_{k=1}^{N-1}c^{(k)}_{33}H(x_3-x_{3(k)})\right)\end{bmatrix}\right\rangle,\\ \begin{bmatrix}\tilde{A}^{(0)}_{\gamma 3\beta 3}\\ \tilde{A}^{(1)}_{\gamma 3\beta 3}\\ \tilde{A}^{(2)}_{\gamma 3\beta 3}\end{bmatrix}&=\left\langle\left(\hat{\mathscr{A}}^{(0)}_{\gamma\alpha}-c^{M(\phi)}_{\gamma\alpha}\right)C_{\alpha 3\mu 3}\begin{bmatrix}\left(\hat{\mathscr{A}}^{(0)}_{\mu\beta}-c^{M(\phi)}_{\mu\beta}\right)\\ \left(\hat{\mathscr{A}}^{(1)}_{\mu\beta}-c^{M(T_0)}_{\mu\beta}\right)\\ \left(\hat{\mathscr{A}}^{(2)}_{\mu\beta}-c^{M(T_1)}_{\mu\beta}\right)\end{bmatrix}\right\rangle,\end{aligned} \tag{2.1.23}$$

which renders final form of the relationship as follows:

$$u^{(3)}_{\beta}=\Gamma^{(1)}_{\beta\alpha}\overline{\gamma}^{(0)}_{\alpha 3}+\Gamma^{(2)}_{\beta\alpha}\left(T_{o,\alpha}\right)+\Gamma^{(3)}_{\beta\alpha}\left(\frac{1}{2}T_{1,\alpha}\right), \tag{2.1.24}$$

where

$$\begin{aligned}\Gamma^{(1)}_{\beta\alpha}&=\left(\tilde{A}^{(0)}_{\beta 3\gamma 3}\right)^{-1}\left[\hat{A}^{(0)}_{\gamma 3\alpha 3}\right],\\ \Gamma^{(2)}_{\beta\alpha}&=\left(\tilde{A}^{(0)}_{\beta 3\gamma 3}\right)^{-1}\left[\hat{B}^{(0)}_{\gamma 3\alpha 3}-\tilde{A}^{(1)}_{\gamma 3\alpha 3}\right],\\ \Gamma^{(3)}_{\beta\alpha}&=\left(\tilde{A}^{(0)}_{\beta 3\gamma 3}\right)^{-1}\left[\hat{D}^{(0)}_{\gamma 3\alpha 3}-\tilde{A}^{(2)}_{\gamma 3\alpha 3}\right].\end{aligned} \tag{2.1.25}$$

Substituting Eq. (2.1.24) into Eq. (2.1.20), transverse shear forces can be expressed as [19]:

$$Q_{\alpha}^{*} = A_{\alpha 3\beta 3}^{*}\overline{\gamma}_{\beta 3}^{(0)} + B_{\alpha 3\beta 3}^{*}\left(\varphi T_{o,\beta}\right) + D_{\alpha 3\beta 3}^{*}\left(\frac{1}{2}\varphi T_{1,\beta}\right), \tag{2.1.26}$$

where

$$\begin{aligned} A_{\alpha 3\beta 3}^{*} &= \hat{A}_{\alpha 3\mu 3}^{(0)}\left(\tilde{A}_{\mu 3\gamma 3}^{(0)}\right)^{-1}\hat{A}_{\gamma 3\beta 3}^{(0)}, \\ B_{\alpha 3\beta 3}^{*} &= \hat{A}_{\alpha 3\mu 3}^{(0)}\left(\tilde{A}_{\mu 3\gamma 3}^{(0)}\right)^{-1}\left[\hat{B}_{\gamma 3\beta 3}^{(0)} - \tilde{A}_{\gamma 3\beta 3}^{(1)}\right] + \hat{A}_{\alpha 3\beta 3}^{(1)}, \\ D_{\alpha 3\beta 3}^{*} &= \hat{A}_{\alpha 3\mu 3}^{(0)}\left(\tilde{A}_{\mu 3\gamma 3}^{(0)}\right)^{-1}\left[\hat{D}_{\gamma 3\beta 3}^{(0)} - \tilde{A}_{\gamma 3\beta 3}^{(2)}\right] + \hat{A}_{\alpha 3\beta 3}^{(2)}. \end{aligned} \tag{2.1.27}$$

In Eq. (2.1.26), $A_{\alpha 3\beta 3}^{*}$, $B_{\alpha 3\beta 3}^{*}$ and $D_{\alpha 3\beta 3}^{*}$ will play a major role in deriving FSDT_TN-like governing equations as modified shear correction factors, which renders a so-called 'effective shear stiffness modulus'. These effective shear modulus can't be directly obtained in the initial statement because the in-plane correction factors depend on the transverse shear relations. Thus repeated computational process is required to derive reasonable in-plane correction factors and effective shear stiffness modulus. The detailed expression for the computational process is given in **Fig. 2.1.1**. Using the final relationships, FSDT_TN-like governing equations can be derived in which it is the same with the FSDT_TN governing equations except for the transverse shear stiffness modulus.

2.1.3.2. Equilibrium equations and boundary conditions of the EFSDTM_TN

The constraint equations, which play a major role in matching process, are

solved in previous section and then mixed terms are dismissed in MVT. Thus, the two-dimensional Hellinger-Reissner functional given in Eq. (2.1.17) can be reasonably applied to solve the problem. From Eq. (2.1.17), the governing equations for the present model can be derived as follows:

$$\begin{aligned} &\delta\bar{u}_{\alpha}^{(0)}: \bar{N}_{\alpha\beta,\beta} = 0, \\ &\delta\bar{u}_{\alpha}^{(1)}: \bar{M}_{\alpha\beta,\beta} - Q_{\alpha}^{*} = 0, \\ &\delta\bar{u}_{3}^{(0)}: Q_{\alpha,a}^{*} = -q. \end{aligned} \tag{2.1.28}$$

Their associated boundary conditions are given as:

$$\begin{aligned} &\delta\bar{u}_{\alpha}^{(0)} = 0 \quad or \quad \bar{N}_{\alpha\beta}v_{\beta} = 0, \\ &\delta\bar{u}_{\alpha}^{(1)} = 0 \quad or \quad \bar{M}_{\alpha\beta}v_{\beta} = 0, \\ &\delta\bar{u}_{3}^{(0)} = 0 \quad or \quad Q_{\alpha}^{*}v_{\alpha} = 0. \end{aligned} \tag{2.1.29}$$

Note that the terms of the uniform and linear distributed temperature loading in modified transverse shear forces act like the external loading.

2.1.3.3. Displacement and stress recovery

Once the governing equations for the EFSDTM_TN are solved, accuracy of their local distributions through the thickness of the plate can be improved by using the recovery process. In this paper, EHOPT_TN is used as the post-processor to restore their results. This can be achieved by expressing the displacement fields of EHOPT_TN in terms of the variables of the EFSDTM_TN.

The mid-plane stretching component of the EHOPT_TN can be approximated

by using the least square sense. The relationship of the mid-plane stretching component can be given as follows:

$$\min_{\bar{u}_\alpha^{(0)}} \left\langle \left\| u_a - \bar{u}_\alpha \right\|_2 \right\rangle = 0, \tag{2.1.30}$$

where u_α are based on the Eq. (2.1.7) which are not including in-plane correction factor to find a reasonable kinematical relation. The least square approximation for the in-plane displacement fields will render as following forms:

$$u_\alpha^{(0)} = \bar{u}_\alpha^{(0)} - \frac{1}{h}\left\langle \Phi_{\alpha\beta}^{(1)} \right\rangle u_\beta^{(3)} - \frac{1}{h}\left\langle \Phi_{\alpha\beta}^{(2)} \right\rangle T_{o,\beta} - \frac{1}{h}\left\langle \Phi_{\alpha\beta}^{(2)} \right\rangle \left(\frac{1}{2} T_{1,\beta} \right). \tag{2.1.31}$$

Substituting Eq. (2.1.31) into Eq. (2.1.11), displacement fields of the EHOPT_TN can be rewritten as follows [18, 19]:

$$\begin{aligned} u_\alpha &= \bar{u}_\alpha^{(0)} - \bar{u}_{3,\alpha}^{(0)} x_3 + \left[\Phi_{\alpha\beta}^{(1)} - \frac{1}{h}\left\langle \Phi_{\alpha\beta}^{(1)} \right\rangle \right] u_\beta^{(3)} + \left[\Phi_{\alpha\beta}^{(2)} - \frac{1}{h}\left\langle \Phi_{\alpha\beta}^{(2)} \right\rangle \right] T_{o,\beta} \\ &\quad + \left[\Phi_{\alpha\beta}^{(3)} - \frac{1}{h}\left\langle \Phi_{\alpha\beta}^{(3)} \right\rangle \right] \frac{1}{2} T_{1,\beta} - C_\alpha^N - C_\alpha^M x_3, \\ u_3 &= \bar{u}_3^{(0)} + \varphi^{(i)} T_o x_3 + \frac{1}{2}\varphi^{(i)} T_1 x_3^2 + \sum_{k=1}^{N-1} S_3^{(k)} H(x_3 - x_{3(k)}). \end{aligned} \tag{2.1.32}$$

According to the relationships of the transverse shear forces (Eq. (2.1.24)), the terms $u_\alpha^{(3)}$ can be expressed by EFSDTM_TN variables.

Thus, one can now express the EHOPT_TN in terms of the variables of the EFSDTM_TN as given by:

$$u_\alpha = \bar{u}_\alpha^{(0)} - \bar{u}_{3,\alpha}^{(0)} x_3 + \left[\Phi_{\alpha\beta}^{*(1)}\right]\Gamma_{\beta\gamma}^{(1)}\bar{\gamma}_{\gamma 3}^{(0)} + \left\{\left[\Phi_{\alpha\beta}^{*(1)}\right]\Gamma_{\beta\gamma}^{(2)} + \left[\Phi_{\alpha\gamma}^{*(2)}\right]\right\} T_{o,\gamma}$$
$$+ \left\{\left[\Phi_{\alpha\beta}^{*(1)}\right]\Gamma_{\beta\gamma}^{(3)} + \left[\Phi_{\alpha\gamma}^{*(3)}\right]\right\}\frac{1}{2} T_{1,\gamma} - C_\alpha^N - C_\alpha^M x_3, \qquad (2.1.33)$$
$$u_3 = \bar{u}_3^{(0)} + \varphi^{(i)} T_o x_3 + \frac{1}{2}\varphi^{(i)} T_1 x_3^2 + \sum_{k=1}^{N-1} S_3^{(k)} H(x_3 - x_{3(k)}),$$

where

$$\Phi_{\alpha\beta}^{*(i)} = \Phi_{\alpha\beta}^{(i)} - \frac{1}{h}\left\langle \Phi_{\alpha\beta}^{(i)} \right\rangle. \qquad (2.1.34)$$

For the calculation of the transverse stresses, the transverse normal stress can't be directly calculated by the constitutive relation approach because plane stress condition is assumed in this model. To derive this one, the equilibrium approach should be utilized. Thus, three dimensional equilibrium equations are additionally considered to more accurately predict the distribution of the transverse shear and normal stresses. From the Eq. (2.1.16), the three-dimensional equilibrium equations can be given as:

$$\sigma_{\alpha 3}^e = -\int_{-\frac{h}{2}}^{x_3} \sigma_{\alpha\beta,\beta}^c dx_3,$$
$$\sigma_{33}^e = -\int_{-\frac{h}{2}}^{x_3} \sigma_{\alpha 3,\alpha}^e dx_3. \qquad (2.1.35)$$

In Eq. (2.1.35), superscripts, $(\bullet)^e$ and $(\bullet)^c$, denote the results calculated by the equilibrium approach and constitutive one, respectively. The results based on equilibrium approach can obviously improve their accuracy for the local distribution, and makes it mathematically more reasonable.

2.1.4. Numerical examples and discussion

In order to verify the efficiency and accuracy of the present model (i.e. EFSDTM_TN), several thermo-elastic problems for the laminated composite and sandwich plates are analyzed in this section. The analytical solutions are obtained for a plate that is formed of length a, width b, and height h. The results of present model are compared to the solutions obtained by FSDT_TN as well as the three-dimensional elasticity solutions. The Pagano solutions for the simply-supported rectangular plates under thermal loadings are used as the benchmark solutions. In the FSDT_TN, a shear correction factor is assumed to be 5/6.

The ply material properties of composite and sandwich plates considered herein are given as follows:

Material properties for composite plates:

$$\begin{aligned} &E_L / E_T = 25, \quad G_{LT} / E_T = 0.5, \\ &G_{TT} / E_T = 0.3356, \quad E_T = 10 Gpa, \\ &v_{LT} = 0.3, \quad v_{TT} = 0.49, \\ &\alpha_L = 0.015 \cdot 10^{-6} / K, \quad \alpha_T = 10^{-6} / K. \end{aligned} \tag{2.1.36}$$

Material properties for sandwich plates:

-Face sheets (h/5 x 2)

$$\begin{aligned} &E_L = 200\, Gpa, \quad E_T = 8\, Gpa, \\ &G_{LT} = 5\, Gpa, \quad G_{TT} = 2.2\, Gpa, \\ &v_{LT} = 0.25, \quad v_{TT} = 0.35, \\ &\alpha_L = -2 \cdot 10^{-6} / K, \quad \alpha_T = 50 \cdot 10^{-6} / K. \end{aligned} \tag{2.1.37}$$

-Core material (3h/5)

$$\begin{aligned} &E_1 = E_2 = 1Gpa, \quad E_3 = 2Gpa, \\ &G_{12} = 3.7Gpa, \quad G_{13} = G_{23} = 0.8Gpa, \\ &v_{12} = 0.35, \quad v_{13} = v_{23} = 0.25, \\ &\alpha_1 = \alpha_2 = \alpha_3 = 30 \cdot 10^{-6} / K. \end{aligned} \tag{2.1.38}$$

Where L represents a parallel direction to the fiber, while T denotes a perpendicular direction to the fiber.

For all of the problems, thermal loading is linearly prescribed through the thickness direction of the plate, which is expressed as follows:

$$T(x_i) = \left[T_o + x_3 T_1\right] \sin(px_1) \sin(qx_2), \tag{2.1.39}$$

Where

$$p = \frac{\pi}{L_1} \ , \ q = \frac{\pi}{L_2}. \tag{2.1.40}$$

The primary variables of the EFSDTM_TN are assumed to be a double trigonometric series to satisfy the simply supported boundary conditions, which is given as follows:

$$\begin{aligned} &\left[\bar{u}_1^{(0)}, \bar{u}_1^{(1)}\right] = \left[\bar{U}_1^{(0)}, \bar{U}_1^{(1)}\right] \cos(px_1) \sin(qx_2), \\ &\left[\bar{u}_2^{(0)}, \bar{u}_2^{(1)}\right] = \left[\bar{U}_2^{(0)}, \bar{U}_2^{(1)}\right] \sin(px_1) \cos(qx_2), \\ &\left[\bar{u}_3^{o}\right] = \bar{U}_3^{o} \sin(px_1) \sin(qx_2), \end{aligned} \tag{2.1.41}$$

To compare the results obtained by present model with those of other theories,

the results reported herein are normalized as following forms:

$$\left[u_\alpha\right]=\left[\overline{u}_\alpha\right]\cdot\frac{1}{\alpha_T},\quad \left[\sigma_{\alpha\beta}\ ,\sigma_{3\alpha}\ ,\sigma_{33}\right]=\left[\overline{\sigma}_{\alpha\beta}\ ,\overline{\sigma}_{3\alpha}\ ,\overline{\sigma}_{33}\right]\cdot\frac{1}{\alpha_T\cdot E_T}, \tag{2.1.42}$$

where the in-plane stresses are obtained by using the constitutive equations, whereas the transverse shear and normal stresses are calculated by integrating the three-dimensional equilibrium equations.

2.1.4.1. Uniform temperature loading case

Considering thermal loading with uniform temperature, several cases of laminated composite and sandwich plates are analyzed. The uniform temperature can be expressed as $\Delta T(x_1,x_2,x_3)=T_0\sin(px_1)\sin(px_2)$. Following assumptions are used for all cases of the laminated composite and sandwich plates: aspect ratio as $L_1=L_2$ and length-to-thickness ratio as $S=L_1/h=5$.

Firstly, the normalized transverse shear and normal stresses for a single layer composite plate are shown in **Figs. 2.1.2 and 2.1.3**. Distribution of the transverse shear stresses depicted in **Fig. 2.1.2** shows the roughly cubic shape, and transverse normal stresses depicted in **Fig. 2.1.3** shows compression at the plate center which is based on the lentil-like deformation. The present EFSDTM_TN, as shown in **Figs. 2.1.2 and 2.1.3**, yields relatively accurate cubic shape of the transverse shear stresses as well as lentil-like deformation of the transverse normal stress with comparison to the exact solutions, although

providing slightly over-estimated distributions. But results of FSDT_TN, which delivers zero values for the transverse stresses, entirely fail to describe transverse shear and normal stresses for the single layer composite plate under uniform temperature loading. In particular, it is noteworthy that EFSDTM_TN can predict accurate results which are in good agreement with those obtained by exact solutions just by solving FSDT_TN-like governing equations.

Figs. 2.1.4-2.1.6 show the normalized in-plane and transverse stresses for a symmetric cross-ply [0/90/0] composite plates. The present EFSDTM_TN agree well with the exact solutions for the distribution of the in-plane stress σ_{22} in **Fig. 2.1.4**, whereas FSDT_TN can't describe accurate distribution. The distributions of the transverse shear stress through the thickness of the plates are depicted in **Fig. 2.1.5**. In this result, it can be found that present model provides fairly accurate semi-cubic variation in σ_{13}, whereas FSDT_TN cannot. **Fig. 2.1.6** compares distributions of the normalized transverse normal stress. In the results of transverse normal stress, FSDT_TN fail to accurately predict biquadratic variation for the distribution of the transverse normal stress; however, it can be found that present EFSDTM _TN accurately describe the shape of biquadratic variation precisely.

The distribution of the in-plane displacement for an anti-symmetric cross-ply [0/90/0/90] composite plates are presented in **Fig. 2.1.7**. From this result, it can be observed that the EFSDTM_TN can provides reliable result by capturing their unsymmetrical parabolic distribution. In the anti-symmetric case, sudden changes of the elastic stiffness modulus between adjacent layers lead to zig-zag shape for the transverse shear stress. This distribution is reflected by **Fig. 2.1.8**.

The present model and FSDT_TN somewhat agree well with the exact solution.

Results of transverse shear and normal stresses for the many layer symmetric cross-ply $[0/90/0/90/0]_s$ composite plates are given in **Figs. 2.1.9 and 2.1.10**. In the many layer plates case, distributions of the transverse shear stress exist in the shape of a zig-zag mode because of the sharp change of their stiffness between adjacent layers in case of the cross-ply. As shown in **Fig. 2.1.9**, present model gives best compromised results which can predict the distribution of the zig-zag shape of the σ_{13} through the thickness, whereas the result of FSDT_TN gives imprecise distribution. The distribution of the transverse normal stress are compared in **Fig. 2.1.10**. In the distribution of the transverse normal stress, it can be shown that the result is compressive at the plate center. While this lentil-like deformation can be fairly well described by the EFSDTM_TN, the result of the FSDT_TN, which provides tensile value, is totally inaccurate compared to the exact solutions.

When it comes to sandwich plates, a square [0/core/0] sandwich plates is considered to validate the performance of the present model. In-plane and transverse stresses for the uniform thermal loading are shown in **Figs. 2.1.11-2.1.13**. As shown in **Fig. 2.1.11**, present model can accurately predict non-continuous distribution of the in-plane stress. From the results of transverse stresses (**Figs. 2.1.12 and 2.1.13**), it can be seen that the results obtained by present model are in excellent agreement with the exact solution. FSDT_TN, however, fails to describe kink shape of the transverse shear stress and provides over-estimated value for the transverse normal stress.

2.1.4.2. Linear temperature loading case

Just like the previous chapter, several cases of laminated composite and sandwich plates under linear temperature loading ($\Delta T(x_1, x_2, x_3) = x_3 T_1 \sin(px_1)\sin(px_2)$) are also analyzed.

The distributions of the transverse shear and normal stress for a single layer composite plate are depicted in **Figs. 2.1.14 and 2.1.15**. Linear distributed thermal loading lead to a bending deflection for the single layer plate. From **Fig. 2.1.14**, it can be described that the present EFSDTM_TN yields relatively accurate prediction for the bending deformation of the transverse shear stress as compared to that of FSDT_TN. In the case of transverse normal stress (**Fig. 2.1.15**), EFSDTM_TN can accurately capture the roughly cubic variation which contains compressive stress in the upper half and tensile one in the lower half of the plate. FSDT_TN, however, entirely fail to describe transverse normal stress distributions for the single layer plate under linear distributed thermal loading. The point which special attention should be paid is that EFSDTM_TN can accurately predict distribution of the transverse normal stress, which can't be obtained by FSDT_TN, just by solving similar procedure as that of FSDT_TN.

The normalized in-plane and transverse normal stresses for a symmetric cross-ply composite plates are presented in **Figs. 2.1.16 and 2.1.17**. For distribution of the in-plane stress as shown in **Fig. 2.1.16**, the result based on the present model is in good accord with the exact solution, whereas FSDT_TN can't describe precise distribution. The distributions of the transverse normal stress is depicted in **Fig. 2.1.17**. From this result, it can be found that present EFSDTM_TN

precisely describes the shape of quintic variation which can't be captured by FSDT_TN.

For the case of an anti-symmetric cross-ply composite plates, **Fig. 2.1.18** shows the distribution of the transverse shear stress which have value of opposite sign in the upper and lower half of the plate. This shape can be fairly well captured by the present model as well as FSDT_TN. The results of the transverse normal stress are compared in **Fig. 2.1.19**. The result of present model can accurately describe the roughly cubic variation of the transverse normal stress, whereas FSDT_TN provides somewhat over-estimated value.

The case of the many layers which are stacked as the symmetric cross-ply lay-up composite plates is considered. **Fig. 2.1.20** compares normalized transverse shear stress for a $[0/90/0/90/0]_2$. From **Fig. 2.1.20**, it can be observed that present EFSDTM_TN provides almost same distribution as compared with the FSDT_TN, and their results can accurately describe the distribution shape of the exact solution. In the distribution of the transverse normal stress given in **Fig. 2.1.21**, present model gives best compromised results by precisely describing the shape of exact solution, whereas FSDT_TN provides entirely opposite distribution.

Finally, the distributions of the in-plane and transverse stresses for a [0/core/0] sandwich plates are presented in **Figs. 2.1.22-2.1.24**. As shown in **Fig. 2.1.22**, present model provides accurate result of the in-plane stress by precisely describing the non-continuous shape of the exact solution. From the distribution of the transverse shear stress given in **Fig. 2.1.23**, it can be observed that present model can fairly well capture the kink shape, whereas FSDT_TN can't take

account. The result of transverse normal stress is plotted in **Fig. 2.1.24**. The present model shows excellent agreement with the exact solution. FSDT_TN, however, provides quite under-estimated distribution of the transverse normal stress.

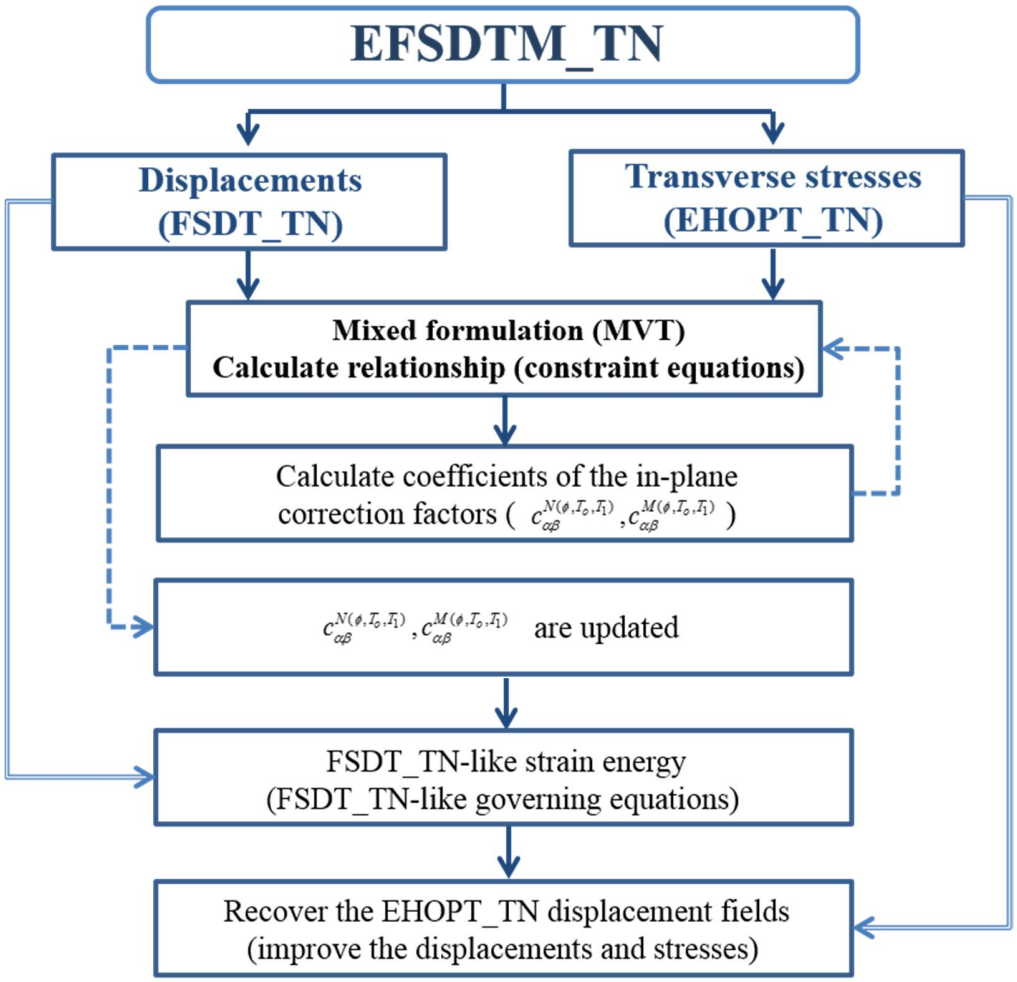

Fig. 2.1.1. Flowchart of the EFSDTM_TN

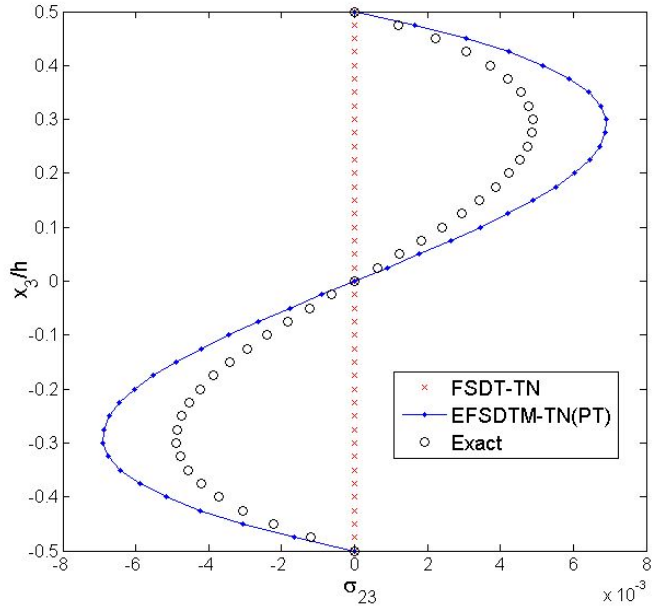

Fig. 2.1.2. Transverse shear stress of a single layer composite plate ($T_0 \neq 0$)

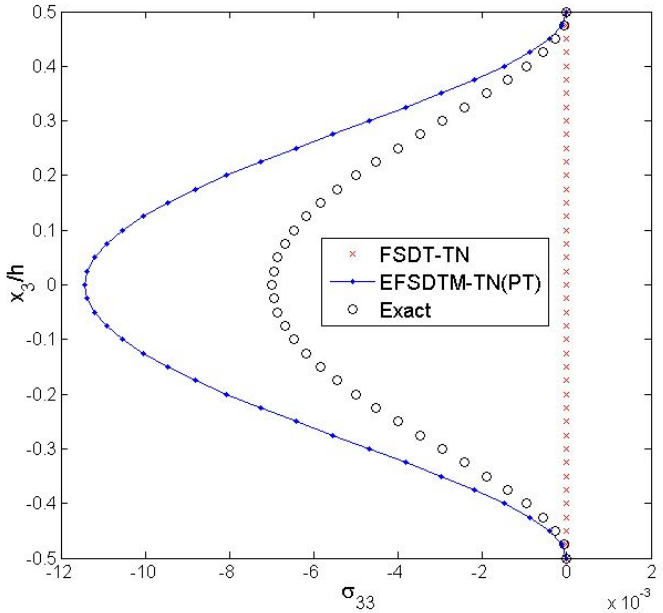

Fig. 2.1.3. Transverse normal stress of a single layer composite plate ($T_0 \neq 0$)

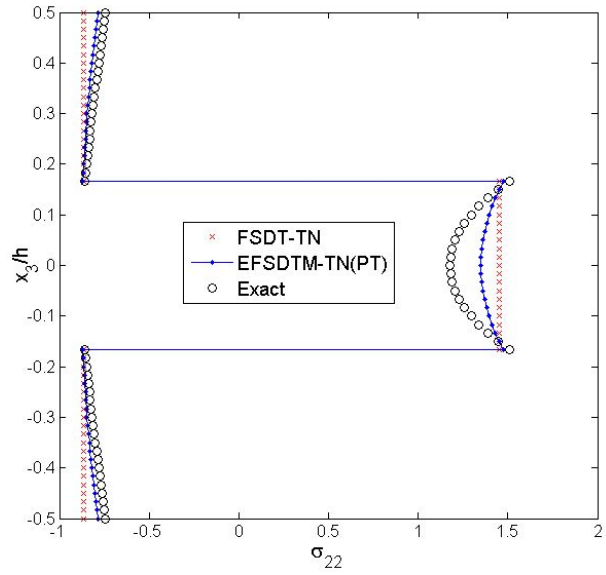

Fig. 2.1.4. In-plane stress of a [0/90/0] composite plates ($T_0 \neq 0$)

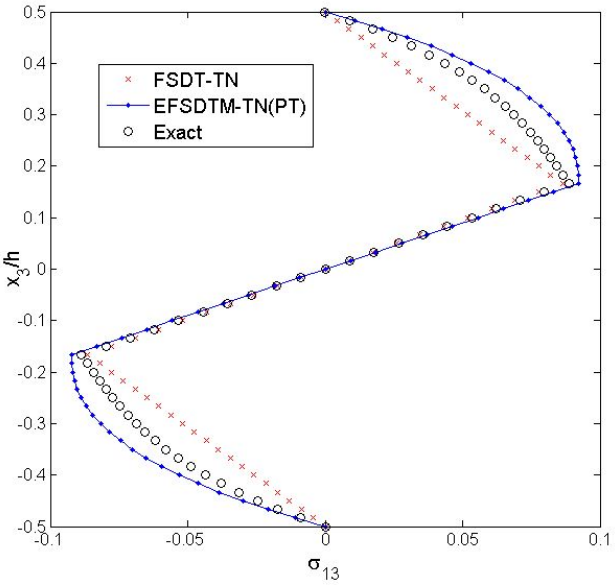

Fig. 2.1.5. Transverse shear stress of a [0/90/0] composite plates ($T_0 \neq 0$)

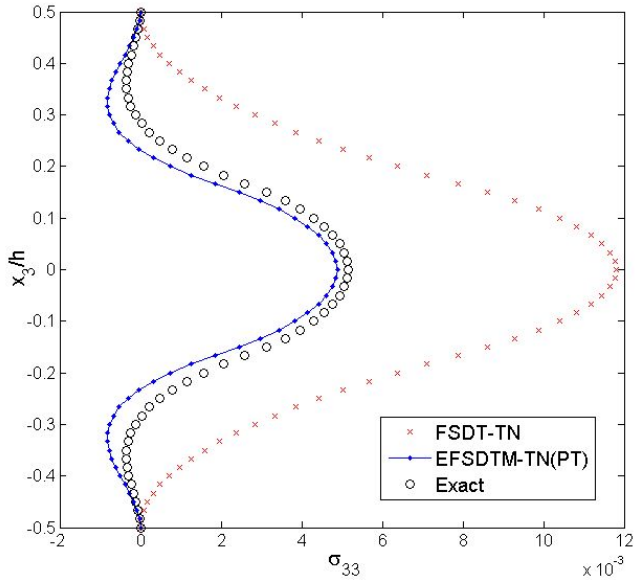

Fig. 2.1.6. Transverse normal stress of a [0/90/0] composite plates ($T_0 \neq 0$)

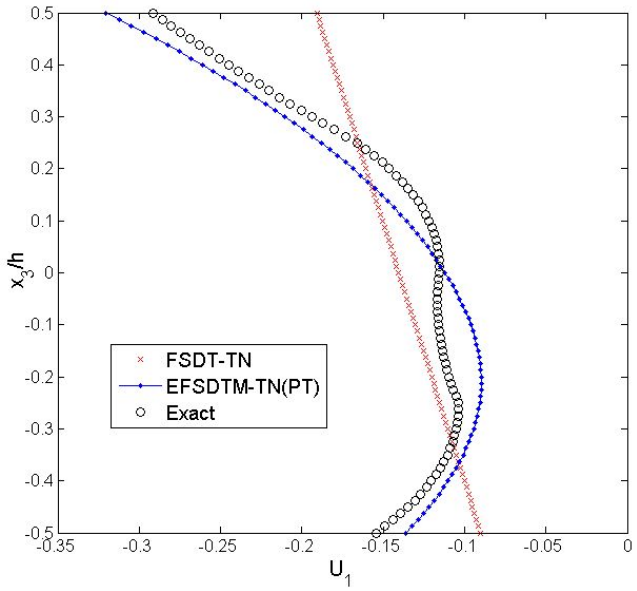

Fig. 2.1.7. In-plane displacement of a [0/90/0/90] composite plates ($T_0 \neq 0$)

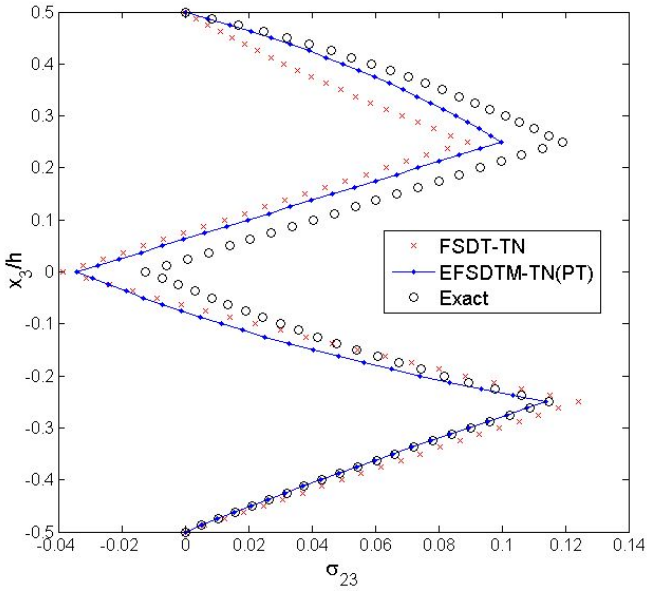

Fig. 2.1.8. Transverse shear stress of a [0/90/0/90] composite plates ($T_0 \neq 0$)

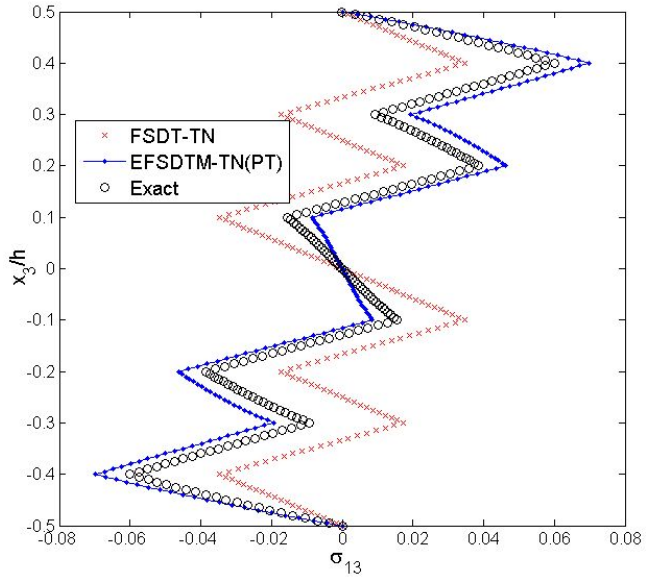

Fig. 2.1.9. Transverse shear stress of a $[0/90/0/90/0]_s$ composite plates ($T_0 \neq 0$)

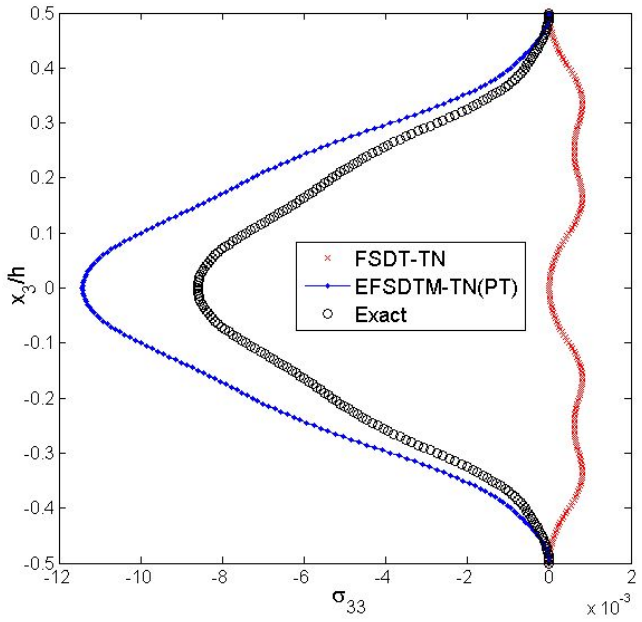

Fig. 2.1.10. Transverse normal stress of a $[0/90/0/90/0]_s$ composite plates ($T_0 \neq 0$)

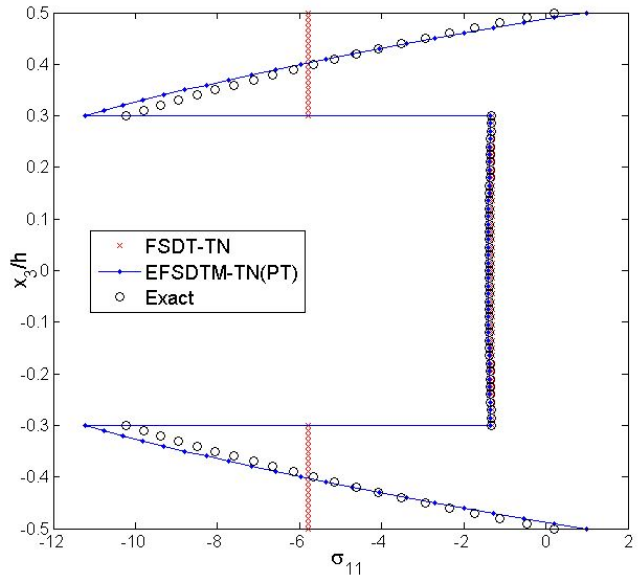

Fig. 2.1.11. In-plane stress of a [0/Core/0] sandwich plates ($T_0 \neq 0$)

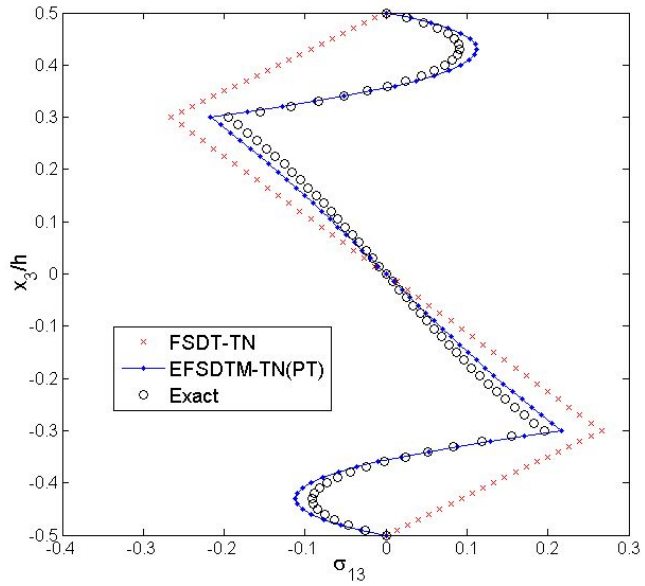

Fig. 2.1.12. Transverse shear stress of a [0/Core/0] sandwich plates ($T_0 \neq 0$)

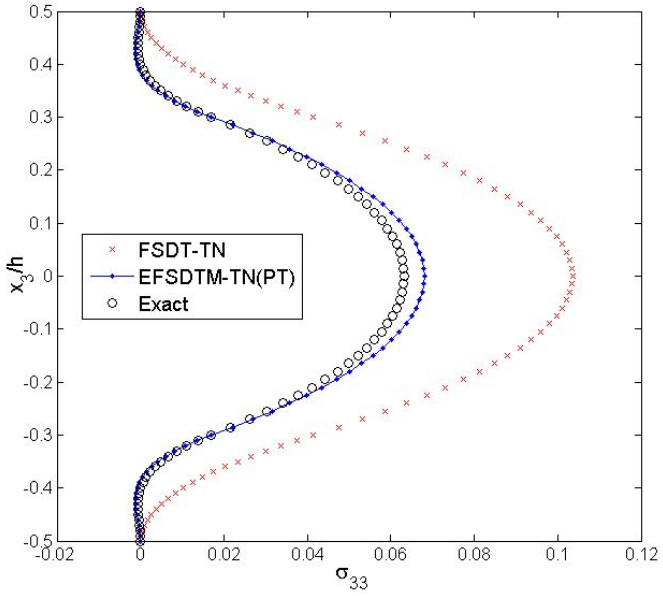

Fig. 2.1.13. Transverse normal stress of a [0/Core/0] sandwich plates ($T_0 \neq 0$)

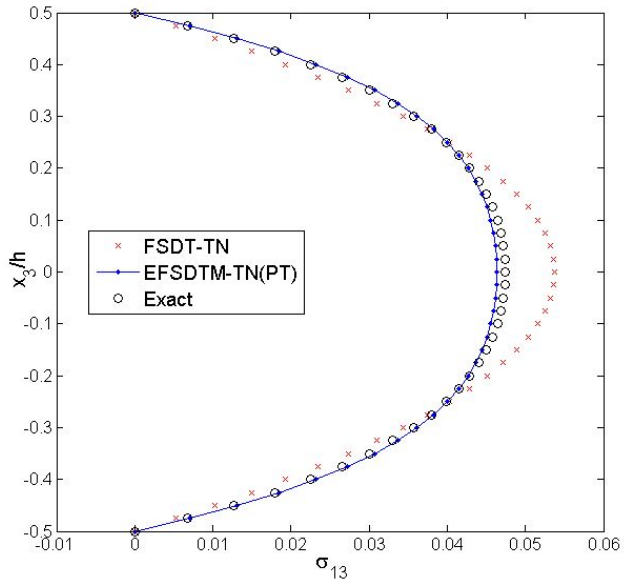

Fig. 2.1.14. Transverse shear stress of a single layer composite plate ($T_1 \neq 0$)

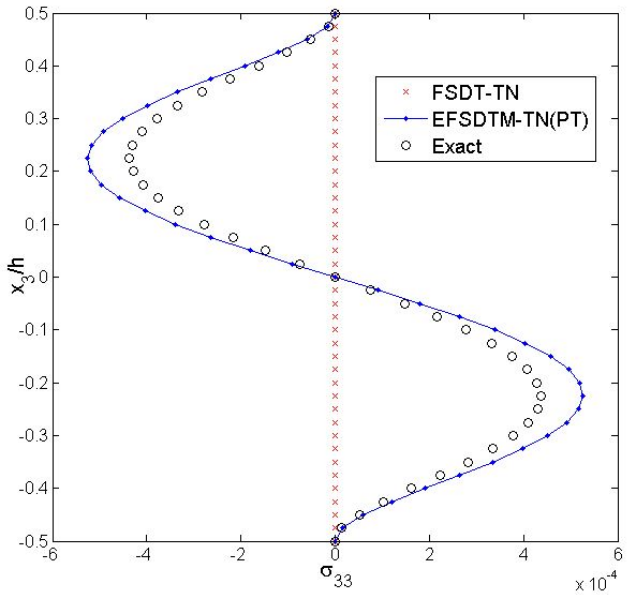

Fig. 2.1.15. Transverse normal stress of a single layer composite plate ($T_1 \neq 0$)

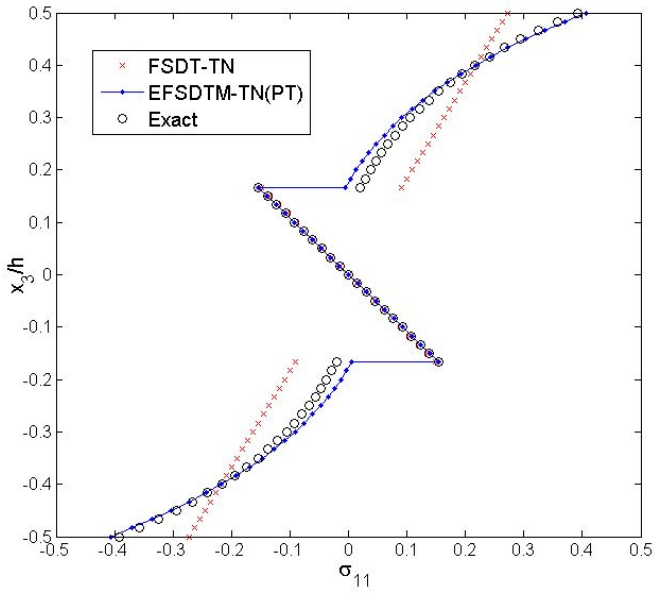

Fig. 2.1.16. In-plane stress of a [0/90/0] composite plates ($T_1 \neq 0$)

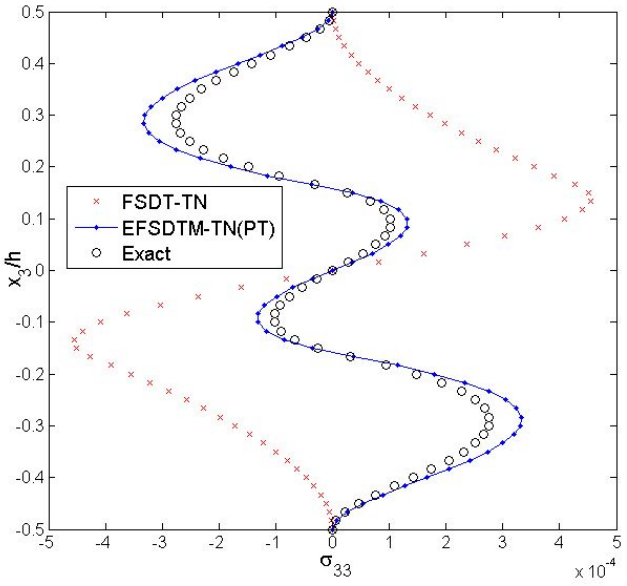

Fig. 2.1.17. Transverse normal stress of a [0/90/0] composite plates ($T_1 \neq 0$)

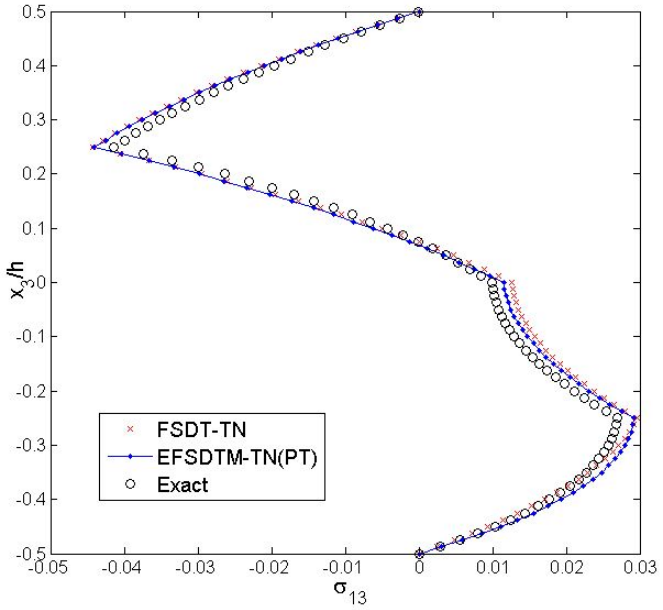

Fig. 2.1.18. Transverse shear stress of a [0/90/0/90] composite plates ($T_1 \neq 0$)

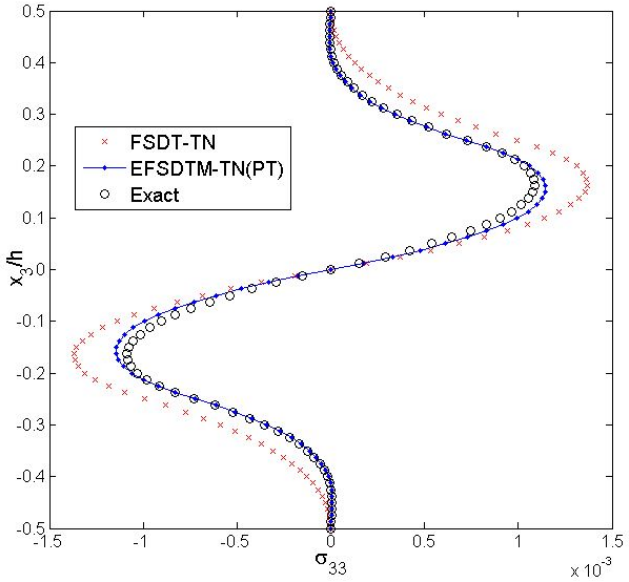

Fig. 2.1.19. Transverse normal stress of a [0/90/0/90] composite plates ($T_1 \neq 0$)

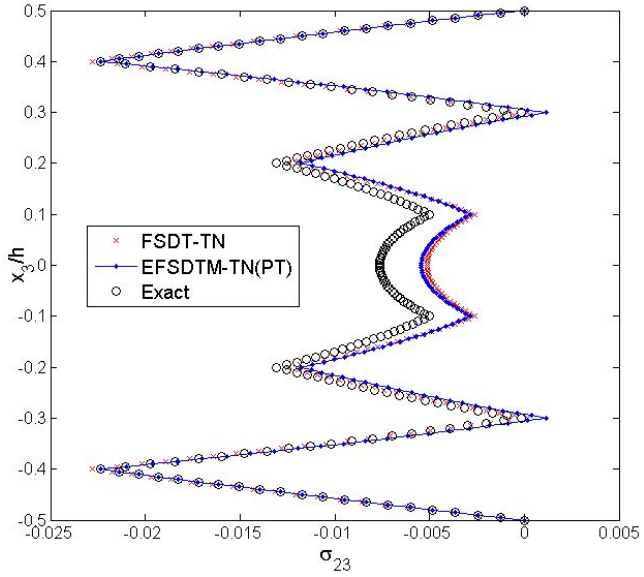

Fig. 2.1.20. Transverse shear stress of a $[0/90/0/90/0]_s$ composite plates ($T_1 \neq 0$)

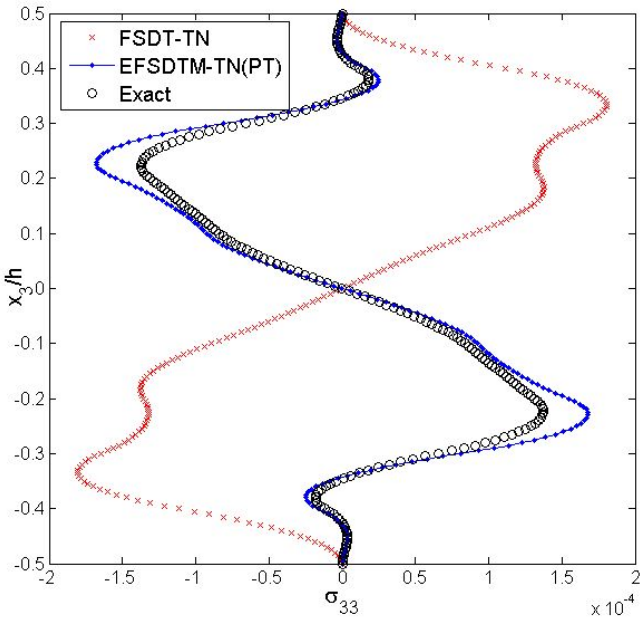

Fig. 2.1.21. Transverse normal stress of a $[0/90/0/90/0]_s$ composite plates ($T_1 \neq 0$)

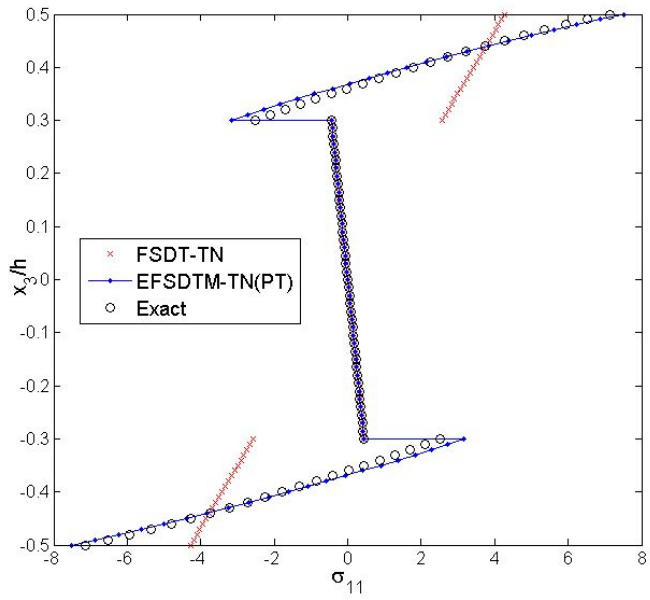

Fig. 2.1.22. In-plane stress of a [0/Core/0] sandwich plates ($T_1 \neq 0$)

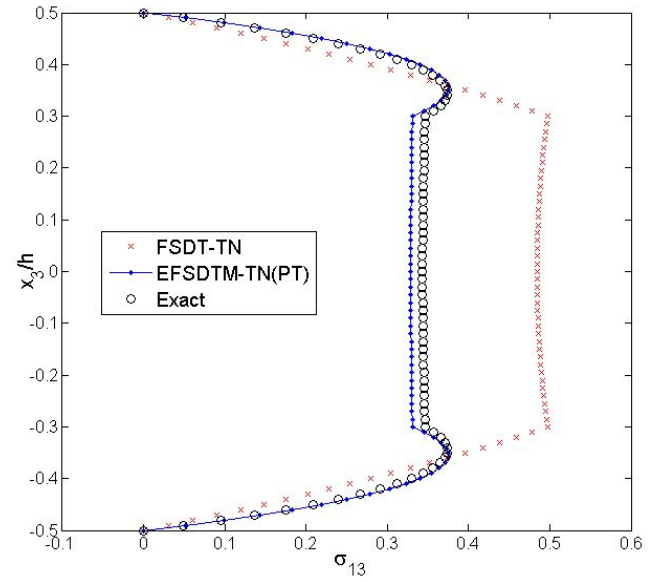

Fig. 2.1.23. Transverse shear stress of a [0/Core/0] sandwich plates ($T_1 \neq 0$)

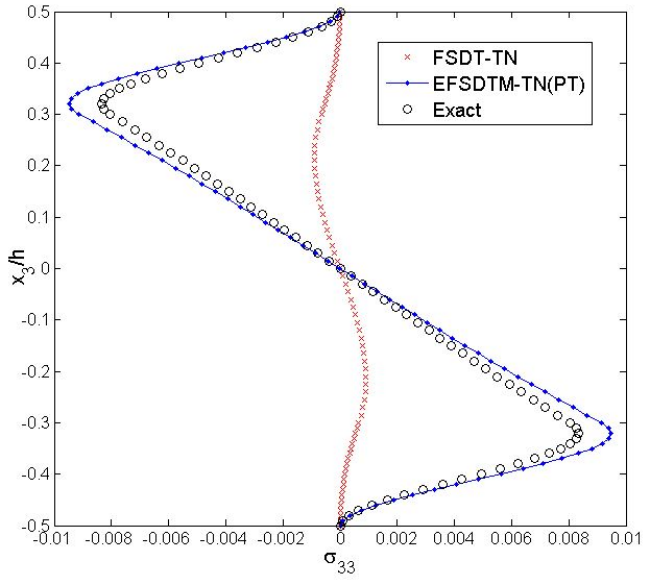

Fig. 2.1.24. Transverse normal stress of a [0/Core/0] sandwich plates ($T_1 \neq 0$)

2.2. Enhanced First-order Shear Deformation Theory in Laplace domain

2.2.1. Literature Review

Recently, many branches of the engineering fields still demand light-weighted and high-stiffened structures. The advanced laminated composite and sandwich structures can satisfy high stiffness-to-weight characteristics by reasonably stacking sequence of laminates. So, they have been widely used in automobile, marine, aerospace and many other industrial facilities due to their advantages. With the increased use of laminated composite structures, a number of analysis models are therefore developed to accurately predict their static and dynamic responses.

Meanwhile, most of the mentioned composite plate models (FSDT, EHOPT, EFSDT, etc.) have been used to analyze the linear elastic behavior of composite structures. Composite materials, however, are inhomogeneous materials composed of reinforced elastic fibers and temperature-sensitive viscoelastic matrix. Thus, fiber-reinforced composite materials have viscoelastic characteristics such as creep strain, stress relaxation and time-dependent failure. These viscoelastic behaviors can lead to critical problems when the composite structures are in high hygro-thermal conditions. For this reason, the viscoelastic effects of composite materials should be considered for reliable analysis in high temperature environments [43, 44].

To accurately analyze the time-dependent behaviors of laminated composite and

sandwich plates, several studies on their viscoelastic responses were performed over the past three decades. Some researchers employed numerical procedures based on the Taylor method [45-48] to solve the linear viscoelastic Boltzmann superposition integral equation. Zak [49] proposed an iterative numerical procedure to circumvent storage of the solutions over all time steps. Vallala et al [50] predicted the geometrically nonlinear deformations for linear viscoelastic materials by applying a trapezoidal rule. Other researchers [51, 52] proposed nonlinear constitutive models to analyze the nonlinear viscoelastic materials.

Another interesting scheme, which is based on the Laplace or Fourier transformations [53-58], is applied to linear viscoelastic materials in order to examine their dynamic and quasi-static responses. The Laplace transformation was not applied to nonlinear viscoelastic constitutive equations in the literature, because extremely complicated equations can be introduced during the transformation process. Thus the transformation was restricted to linear viscoelastic materials. Once the linear viscoelastic problem is solved in the Laplace domain, results in the real time domain can be obtained by applying the inverse Laplace transformation based on numerical inversion techniques. Since this method only requires a simple calculation process without time integration, it can be an effective approach for long-term simulation. Recently, Nguyen et al. [57, 58] presented the method of using Laplace transformation for FSDT, HSDT and EHOPT to investigate the viscoelastic behavior of laminated composite and sandwich plates. Especially for the EHOPT model, their approach [58] provides one important benefit in that the transverse shear continuity conditions can be easily implemented. It is extremely complicated to enforce the continuity

conditions on the linear viscoelastic materials in the real-time domain. In order to take advantage of the accuracy of EHOPT and the simplicity of FSDT, the Laplace transformation can be applied to both shear stress continuity conditions (EHOPT) and strain energy transformation (EFSDT) in order to develop a simple yet accurate linear viscoelastic model. This will allow us to efficiently analyze the laminated composite plates under mechanical loadings and to investigate the time-responded results for the viscoelastic behaviors.

In this section, as a new way to address the aforementioned issues, EFSDT via strain energy transformation is applied to the linear viscoelastic problem in the Laplace domain and tested numerically. The main objective herein is to systematically establish the relationships between the two theories (conventional FSDT and EHOPT) in the Laplace domain via strain energy transformation as well as the least-square sense approximation. According to the relationships, the FSDT-like theory incorporating the efficiency of the conventional FSDT as well as the accuracy of the EHOPT for linear viscoelastic analysis can be derived. In addition, the time-integral form of the Boltzmann superposition equation can be simplified by employing Laplace transformation. Hence, the calculation process can be further improved as compared to the linear elastic counterpart. Furthermore, transverse shear continuity conditions at layer interfaces can be easily enforced in the Laplace domain. Several numerical examples are given to show the performance of the proposed method and the results for the present theory are compared with data available in the open literature to demonstrate their accuracy and efficiency.

2.2.2. Constitutive equation for linear viscoelastic materials

The constitutive equation for linear viscoelastic materials can be obtained from the time-integral equation as follows:

$$\begin{aligned}\sigma_{ij}(t) &= \int_0^t Q_{ijkl}(t-\tau)\dot{\varepsilon}_{kl}(\tau)d\tau, \\ \varepsilon_{ij}(t) &= \int_0^t J_{ijkl}(t-\tau)\dot{\sigma}_{kl}(\tau)d\tau,\end{aligned} \tag{2.2.1}$$

where t is time, τ denotes a dummy variable for time integration, and $\sigma_{ij}(t)$ and $\varepsilon_{ij}(t)$ are time-dependent stress and strain, respectively. The time-dependent compliance and relaxation modulus based on a prony series of decaying exponentials can be expressed as [44]:

$$Q_{ijkl}(t) = Q^0_{(ijkl)}\varphi_{(ijkl)} = Q^0_{(ijkl)}\left[\sum_{p=0}^{m} b^p_{(ijkl)} \cdot e^{-\frac{t}{a^p_{(ijkl)}}}\right], \tag{2.2.2}$$

where Q^0_{ijkl} denotes the relaxation modulus at the initial time, which can be obtained from the linear elastic material properties. The viscoelastic coefficient b^p_{ijkl} and characteristic time constant a^p_{ijkl} are determined from the experimental relaxation curve.

Several experimental works have been conducted to investigate the time-dependent relaxation moduli of some real composite materials such as

GY70/339, T300/5209 and T300/934. According to previous work by Crossmann et al [44], to reflect the experimental master curves for the realistic viscoelastic behavior of composite materials, the prony series needs to be extended to higher-order terms.

In this study, viscoelastic responses based on the real composite material GY70/339 are investigated at room temperature (T=75^{o}F) with a moisture condition of M=0.1%. Detailed expression of the time-dependent material properties for the GY70/339 will be described in the section on numerical examples and discussion.

By applying the convolution theorem of the Laplace transformation to Eq. (2.2.1), the constitutive equation for the linear viscoelastic materials can be simplified as follows [57, 58]:

$$\begin{aligned} \sigma_{ij}^{*}(s) &= Q_{ijkl}^{*}(s)\cdot s\cdot \varepsilon_{kl}^{*}(s), \\ \varepsilon_{ij}^{*}(s) &= J_{ijkl}^{*}(s)\cdot s\cdot \sigma_{kl}^{*}(s), \end{aligned} \tag{2.2.3}$$

where superscript $(\ )^{*}$ represents the parameters in the Laplace domain.

From Eq. (2.2.3) in the Laplace domain, it is apparent that the simplified forms of the constitutive equation for the linear viscoelastic materials are similar to those of the generalized Hook's law for linear elastic materials. Therefore, we can solve the linear viscoelastic problem as compared with the linear elastic counterpart.

2.2.3. Enhanced first order shear deformation theory for the

linear viscoelastic model

In this section, a new type of model based on the enhanced first order shear deformation theory (EFSDT) is derived to analyze the linear viscoelastic problem by employing the strain energy relationships and Laplace transformation. The main feature of the proposed theory is to systematically derive an improved strain energy expression for conventional FSDT via the scheme of strain energy transformation in the Laplace domain, and then provide a way to recover the stresses and displacements in the real-time domain to improve their accuracy.

2.2.3.1. Displacement and strain fields

When it comes to the interior solution, the general form of time-dependent 3-D displacement based on the asymptotic approach can be expressed by

$$\begin{aligned} u_\alpha^{3D}(x_i) &= u_\alpha^o(x_\beta) - x_3 \cdot u_{3,\alpha}^o(x_\beta) + W_\alpha(x_i), \\ u_3^{3D}(x_i) &= u_3^o(x_\beta) + W_3(x_i). \end{aligned} \tag{2.2.4}$$

In addition, those of FSDT are given as follows:

$$\begin{aligned} \overline{u}_\alpha(x_i) &= \overline{u}_\alpha^o(x_\beta) + x_3 \cdot \overline{\theta}_\alpha(x_\beta), \\ \overline{u}_3(x_i) &= \overline{u}_3^o(x_\beta), \end{aligned} \tag{2.2.5}$$

where the superscript $(\bullet)^o$ indicates the displacement components in the reference plane, the over-bar $(\overline{\bullet})$ denotes the averaged values, respectively.

$W_\alpha(x_i)$ and $W_3(x_i)$ represent the through-the-thickness warping functions. In order to simplify the problem, in-plane warping function can be split into the through-the-thickness function (Φ) and the effective transverse shear strain (ϕ) as follows [18]:

$$W_\alpha(x_i) = \Phi_{\alpha\gamma}(x_3) \cdot \phi_\gamma(x_\beta). \tag{2.2.6}$$

In general, it is hard to determine an appropriate in-plane warping function for accurate analysis of the laminated composite plates. Thus, some refined plate theories are considered to extract in-plane warping function. Among many refined higher-order plate theories, the EHOPT is utilized to obtain the in-plane warping functions due to their simplicity and accuracy. The in-plane displacement fields of the EHOPT are composed of global and layer-local components, in which layer-local zig-zag displacement is superimposed to a smooth globally cubic varying displacement to satisfy the static as well as the geometric continuity conditions. It can be expressed in terms of the only five primary D.O.F by enforcing the transverse shear stress conditions (transverse shear free conditions at top and bottom surfaces and transverse shear stress continuity conditions across the laminate interfaces). Thus, the final form of time-dependent displacement fields of the EHOPT can be given as follows [18]:

$$\begin{aligned} u_\alpha(x_i) &= u_\alpha^o(x_\beta) - x_3 \cdot u_{3,\alpha}^o(x_\beta) + \Phi_{\alpha\gamma}(x_3) \cdot \phi_\gamma(x_\beta), \\ u_3(x_i) &= u_3^o(x_\beta) + W_3(x_i), \end{aligned} \tag{2.2.7}$$

in which

$$\Phi_{\alpha\gamma}(x_3) = -x_3 \cdot \left(\frac{3}{4} h^2 \delta_{\alpha\gamma} + \frac{1}{2} \cdot \sum_{k=1}^{N-1} a_{\alpha\gamma}^{(k)} \right) - x_3^2 \cdot \frac{1}{2h} \cdot \sum_{k=1}^{N-1} a_{\alpha\gamma}^{(k)} + x_3^3 \delta_{a\gamma} + \sum_{k=1}^{N-1} a_{\alpha\gamma}^{(k)} (x_3 - x_{3(k)}) H(x_3 - x_{3(k)}), \tag{2.2.8}$$

where N is the number of layers, $\delta_{a\gamma}$ denotes the Kronecker delta function, and $H(x_3 - x_{3(k)})$ is the Heaviside unit step function. The coefficient $a_{\alpha\gamma}^{(k)}$, which depends upon the material properties of each layer, can be obtained from the interface continuity conditions [12,13].

The time-dependent in-plane warping functions can be explicitly determined from those of EHOPT given in Eq. (2.2.7), so that the general form of 3-D displacement fields can be expressed in the compact form:

$$\begin{aligned} u_\alpha^{3D}(x_i) &\approx u_\alpha(x_i) = u_\alpha^o(x_\beta) - x_3 \cdot u_{3,\alpha}^o(x_\beta) + \Phi_{\alpha\gamma}(x_3) \cdot \phi_\gamma(x_\alpha), \\ u_3^{3D}(x_i) &\approx u_3(x_i) = u_3^o(x_\beta) + W_3(x_i) \approx u_3^o(x_\beta), \end{aligned} \tag{2.2.9}$$

where the out-of-plane warping function $W_3(x_i)$ can be negligible in Eq. (2.2.9) because it is considerably small as compared to the effective transverse shear strains, ϕ_α, for moderately thick plate in general [18].

By applying the Laplace transformation to the time-dependent displacement fields, displacement fields in Laplace domain can be given by the following relationship:

$$\begin{aligned} u_\alpha^*(x_i) &= u_\alpha^{o*}(x_\beta) - x_3 \cdot u_{3,\alpha}^{o*}(x_\beta) + \Phi_{\alpha\gamma}^*(x_3) \cdot \phi_\gamma^*(x_\beta), \\ u_3^*(x_i) &= u_3^{o*}(x_\beta), \end{aligned} \tag{2.2.10}$$

in which

$$\Phi^*_{\alpha\gamma}(x_3) = -x_3 \cdot \left(\frac{3}{4} h^2 \delta_{\alpha\gamma} + \frac{1}{2} \cdot \sum_{k=1}^{N-1} a^{*(k)}_{\alpha\gamma} \right) - x_3^2 \cdot \frac{1}{2h} \cdot \sum_{k=1}^{N-1} a^{*(k)}_{\alpha\gamma} + x_3^3 \delta_{a\gamma} + \sum_{k=1}^{N-1} a^{*(k)}_{\alpha\gamma} (x_3 - x_{3(k)}) H(x_3 - x_{3(k)}), \tag{2.2.11}$$

where the superscript $(\bullet)^*$ denotes the variables in the Laplace domain, $a^{*(k)}_{\alpha\gamma}$ represents the change of the slope angle at each layer in the Laplace domain to satisfy the transverse shear continuities [12, 13, 58]. The detailed expression of $a^{*(k)}_{\alpha\gamma}$ can be found in **Appendix D.**

The displacement fields of FSDT in the Laplace domain are given by:

$$\begin{aligned} \overline{u}^*_\alpha(x_i) &= \overline{u}^{o*}_\alpha(x_\beta) + x_3 \cdot \overline{\theta}^*_\alpha(x_\beta), \\ \overline{u}^*_3(x_i) &= \overline{u}^{o*}_3(x_\beta). \end{aligned} \tag{2.2.12}$$

From Eqs. (2.2.10) and (2.2.12), the corresponding in-plane and transverse shear strains are subsequently given as:

$$\begin{aligned} \varepsilon^*_{\alpha\beta}(x_i) &= \varepsilon^{o*}_{\alpha\beta}(x_\beta) + x_3 \cdot \varepsilon^{(1)*}_{\alpha\beta}(x_\beta) + \varepsilon^{(w)*}_{\alpha\beta}(x_i), \\ \gamma^*_{3\alpha}(x_i) &= \Phi^*_{\alpha\gamma,3}(x_3) \cdot \phi^*_\gamma(x_\beta), \\ \overline{\varepsilon}^*_{\alpha\beta}(x_i) &= \overline{\varepsilon}^{o*}_{\alpha\beta}(x_\beta) + x_3 \cdot \overline{\varepsilon}^{(1)*}_{\alpha\beta}(x_\beta), \\ \overline{\gamma}^*_{3\alpha}(x_i) &= \overline{\theta}^*_\alpha(x_\beta) + \overline{u}^{o*}_{3,\alpha}(x_\beta), \end{aligned} \tag{2.2.13}$$

in which

$$\varepsilon_{\alpha\beta}^{o*} = \frac{1}{2}(u_{\alpha,\beta}^{o*} + u_{\beta,\alpha}^{o*}), \quad \varepsilon_{\alpha\beta}^{(1)*} = -\frac{1}{2}(u_{3,\alpha\beta}^{o*} + u_{3,\beta\alpha}^{o*}),$$
$$\varepsilon_{\alpha\beta}^{(w)*} = \frac{1}{2}(\Phi_{\alpha\gamma}^{*}(x_3)\cdot\phi_{\gamma,\beta}^{*}(x_\alpha) + \Phi_{\beta\gamma}^{*}(x_3)\cdot\phi_{\gamma,\alpha}^{*}(x_\alpha)), \tag{2.2.14}$$
$$\overline{\varepsilon}_{\alpha\beta}^{o*} = \frac{1}{2}(\overline{u}_{\alpha,\beta}^{o*} + \overline{u}_{\beta,\alpha}^{o*}), \quad \overline{\varepsilon}_{\alpha\beta}^{(1)*} = \frac{1}{2}(\overline{\theta}_{\alpha,\beta}^{*} + \overline{\theta}_{\beta,\alpha}^{*}).$$

2.2.3.2. Relationships between the two theories (EHOPT and FSDT) in the Laplace domain

Although conventional FSDT is attractive due to its simplicity and efficiency, it requires appropriate shear correction factors and fails to provide accurate results for the through-the-thickness local distribution of stress and deformations. In order to compensate for the aforementioned drawbacks, the conventional FSDT is reconstructed via the proper strategies.

In the proposed approach, the displacement field assumptions of the conventional FSDT are retained so that extensional and bending strain energy is the same as those of the conventional FSDT. However, the transverse shear strain energy will be derived from that of EHOPT by introducing the averaged strain concept in this subsection.

In order to derive the relationships between the EHOPT and FSDT, the least-square sense approximation is applied to the displacement fields in the Laplace domain (Eqs. (2.2.10) and (2.2.12)). Consequently, the least-square sense minimization of error between EHOPT and FSDT yields the following relationships [18]:

$$
\begin{aligned}
&\min_{\bar{\varepsilon}^{o*}_{\alpha\beta}} \left\langle \left\| \varepsilon^{o*}_{\alpha\beta} - \bar{\varepsilon}^{o*}_{\alpha\beta} \right\|_2 \right\rangle = 0 \rightarrow \bar{\varepsilon}^{o*}_{\alpha\beta} = \varepsilon^{o*}_{\alpha\beta} + \frac{1}{h}\left\langle \varepsilon^{(w)*}_{\alpha\beta} \right\rangle, \\
&\min_{\bar{\varepsilon}^{(1)*}_{\alpha\beta}} \left\langle \left\| \varepsilon^{o*}_{\alpha\beta} - \bar{\varepsilon}^{o*}_{\alpha\beta} \right\|_2 \right\rangle = 0 \rightarrow \bar{\varepsilon}^{(1)*}_{\alpha\beta} = \varepsilon^{(1)*}_{\alpha\beta} + \frac{12}{h^3}\left\langle x_3 \cdot \varepsilon^{(w)*}_{\alpha\beta} \right\rangle, \\
&\min_{\bar{u}^{o*}_{\alpha}} \left\langle \left\| u^{*}_{\alpha} - \bar{u}^{*}_{\alpha} \right\|_2 \right\rangle = 0 \rightarrow \bar{u}^{o*}_{\alpha} = u^{o*}_{\alpha} + C^{*}_{\alpha\gamma} \cdot \phi^{*}_{\gamma}, \\
&\min_{\bar{\theta}^{*}_{\alpha}} \left\langle \left\| u^{*}_{\alpha} - \bar{u}^{*}_{\alpha} \right\|_2 \right\rangle = 0 \rightarrow \bar{\theta}^{*}_{\alpha} = -u^{o*}_{3,\alpha} + \Gamma^{*}_{\alpha\gamma} \cdot \phi^{*}_{\gamma}, \\
&\min_{\bar{u}^{o*}_{3}} \left\langle \left\| u^{*}_{3} - \bar{u}^{*}_{3} \right\|_2 \right\rangle = 0 \rightarrow \bar{u}^{o*}_{3} = u^{o*}_{3} + \frac{1}{h}\left\langle W_3 \right\rangle,
\end{aligned}
\tag{2.2.15}
$$

in which

$$
C^{*}_{\alpha\gamma} = \frac{1}{h}\left\langle \Phi^{*}_{\alpha\gamma} \right\rangle, \quad \Gamma^{*}_{\alpha\gamma} = \frac{12}{h^3}\left\langle x_3 \cdot \Phi^{*}_{\alpha\gamma} \right\rangle. \tag{2.2.16}
$$

From Eq. (2.2.15) and the out-of-plane warping condition $\langle W_3 \rangle \approx 0$, the averaged transverse shear strain, $\bar{\theta}^{*}_{\alpha} + \bar{u}^{o*}_{3,\alpha}$ from Eq. (2.2.12), can be expressed in terms of the effective transverse shear strain ϕ^{*}_{α} as follows:

$$
\bar{\gamma}^{*}_{3\alpha} = \bar{\theta}^{*}_{\alpha} + \bar{u}^{o*}_{3,\alpha} = \Gamma^{*}_{\alpha\gamma} \cdot \phi^{*}_{\gamma}. \tag{2.2.17}
$$

On the other hand, the relationships for the in-plane strain fields can be expressed in the form of a matrix:

$$
\begin{aligned}
\bar{E}^{*}_{o} &= E^{*}_{o} + \tilde{C}^{*} \cdot K^{*}_{h}, \\
\bar{K}^{*}_{o} &= K^{*}_{o} + \tilde{\Gamma}^{*} \cdot K^{*}_{h},
\end{aligned}
\tag{2.2.18}
$$

$\bar{E}^{*}_{o}$, $\bar{K}^{*}_{o}$ etc. are defined in **Appendix E**.

From Eqs. (2.2.17) and (2.2.18), the strain energy for the EHOPT can be

transformed into that of conventional FSDT because the strain relationships between the two theories are defined.

In contrast with the linear elastic model, the strain energy expression for the linear viscoelastic model is considerably complicated because it contains the process of time integration. Thus, we use a compact expression for the reduced strain energy in the Laplace domain as follows:

$$U^* = \mathop{\mathrm{I}}_{\eta}\left[\left\langle Q^*_{\alpha\beta\gamma\mu}(\eta)\varepsilon^*_{\gamma\mu}(\eta)\varepsilon^*_{\alpha\beta}(s-\eta) + Q^*_{3\alpha 3\beta}(\eta)\gamma^*_{3\beta}(\eta)\gamma^*_{3\alpha}(s-\eta)\right\rangle\right], \tag{2.2.19}$$

where

$$\mathop{\mathrm{I}}_{\eta}\left[F(\eta)\right] = \left(\frac{1}{s}\right)\frac{1}{2\pi i}\lim_{T\to\infty}\int_{c-iT}^{c+iT}\left[\eta(s-\eta)\cdot F(\eta)\right]d\eta. \tag{2.2.20}$$

The complex variable in Eq. (2.2.20) is only used to define the strain energy relationships between the two theories, so it is not involved in deriving the governing equation for the present theory. The detailed procedure for Eq. (2.2.19) is presented in **Appendix F**.

The reduced strain energy of EHOPT for the linear viscoelastic problem can be written by substituting Eq. (2.2.13) into Eq. (2.2.19):

$$U^*_{EHOPT} = \mathop{\mathrm{I}}_{\eta}\begin{bmatrix} E_o^{*T}(\eta)A^*E_o^*(s-\eta) + E_o^{*T}(\eta)B^*K_o^*(s-\eta) \\ +E_o^{*T}(\eta)E^*K_h^*(s-\eta) + K_o^{*T}(\eta)B^*E_o^*(s-\eta) \\ +K_o^{*T}(\eta)D^*K_o^*(s-\eta) + K_o^{*T}(\eta)F^*K_h^*(s-\eta) \\ +K_h^{*T}(\eta)E^{*T}E_o^*(s-\eta) + K_h^{*T}(\eta)F^{*T}K_o^*(s-\eta) \\ +K_h^{*T}(\eta)H^*K_h^*(s-\eta) + \phi^{*T}(\eta)G^*\phi^*(s-\eta) \end{bmatrix}, \tag{2.2.21}$$

The stiffness matrices are defined in **Appendix E**.

To utilize the variables of the conventional FSDT, the reduced strain energy of EHOPT should be rewritten based on the strain relationships of Eqs. (2.2.17) and (2.2.18). Substituting the previously mentioned strain relationships (Eqs. (2.2.17) and (2.2.18)) into the above expression of the strain energy (Eq. (2.2.21)) yields the following equation.

$$U^*_{EHOPT} = \mathop{\mathrm{I}}_{\eta}\left[\begin{pmatrix} \left(\bar{E}^*_o(\eta)-\tilde{C}^*K^*_h(\eta)\right)^T A^*\left(\bar{E}^*_o(s-\eta)-\tilde{C}^*K^*_h(s-\eta)\right) \\ +\left(\bar{E}^*_o(\eta)-\tilde{C}^*K^*_h(\eta)\right)^T B^*\left(\bar{K}^*_o(s-\eta)-\tilde{\Gamma}^*K^*_h(s-\eta)\right) \\ +\left(\bar{E}^*_o(\eta)-\tilde{C}^*K^*_h(\eta)\right)^T E^*K^*_h(s-\eta) \\ +\left(\bar{K}^*_o(\eta)-\tilde{\Gamma}^*K^*_h(\eta)\right)^T B^*\left(\bar{E}^*_o(s-\eta)-\tilde{C}^*K^*_h(s-\eta)\right) \\ +\left(\bar{K}^*_o(\eta)-\tilde{\Gamma}^*K^*_h(\eta)\right)^T D^*\left(\bar{K}^*_o(s-\eta)-\tilde{\Gamma}^*K^*_h(s-\eta)\right) \\ +\left(\bar{K}^*_o(\eta)-\tilde{\Gamma}^*K^*_h(\eta)\right)^T F^*K^*_h(s-\eta) \\ +K^{*T}_h(\eta)E^{*T}\left(\bar{E}^*_o(s-\eta)-\tilde{C}^*K^*_h(s-\eta)\right) \\ +K^{*T}_h(\eta)F^{*T}\left(\bar{K}^*_o(s-\eta)-\tilde{\Gamma}^*K^*_h(s-\eta)\right) \\ +K^{*T}_h(\eta)H^*K^*_h(s-\eta)+\bar{\gamma}^{*T}(\eta)\left(\hat{\Gamma}^{*T}G^*\hat{\Gamma}^*\right)\bar{\gamma}^*(s-\eta) \end{pmatrix}\right]. \tag{2.2.22}$$

After rearranging the strain energy expression of Eq. (2.2.22), one can decompose U^*_{EHOPT} into those of the conventional FSDT-like theory and error energy as follows:

$$U^*_{EHOPT} = U^*_{FSDT-like} + U^*_{Error}, \tag{2.2.23}$$

The detailed expression for $U^*_{FSDT-like}$ and U^*_{Error} is given by

$$U^*_{FSDT-like} = \mathop{\mathrm{I}}_{\eta}\begin{bmatrix} \bar{E}^*_o(\eta)A^*\bar{E}^*_o(s-\eta) + \bar{E}^*_o(\eta)B^*\bar{K}^*_o(s-\eta)] \\ +\bar{K}^*_o(\eta)B^*\bar{E}^*_o(s-\eta) + \bar{K}^*_o(\eta)D^*\bar{K}^*_o(s-\eta) \\ +\bar{\gamma}^*(\eta)\hat{G}^*\bar{\gamma}^*(s-\eta) \end{bmatrix}, \tag{2.2.24}$$

$$U^*_{Error} = \mathop{\mathrm{I}}_{\eta}\begin{bmatrix} \bar{E}^{*T}_o(\eta)\cdot[R_1]\cdot K^*_h(s-\eta) \\ +K^{*T}_h(\eta)\cdot[R^T_1]\cdot\bar{E}^*_o(s-\eta) \\ +\bar{K}^{*T}_o(\eta)\cdot[R_2]\cdot K^*_h(s-\eta) \\ +K^{*T}_h(\eta)\cdot[R^T_2]\cdot\bar{K}^*_o(s-\eta) \\ +K^{*T}_h(\eta)\cdot[R_3]\cdot K^*_h(s-\eta) \end{bmatrix}, \tag{2.2.25}$$

Where

$$\begin{aligned} R_1 &= -A^*\tilde{C}^* - B^*\tilde{\Gamma}^* + E^*, \\ R_2 &= -B^*\tilde{C}^* - D^*\tilde{\Gamma}^* + F^*, \\ R_3 &= -\tilde{C}^{*T}\cdot R_1 - \tilde{\Gamma}^{*T}\cdot R_2 - E^{*T}\tilde{C}^* - F^{*T}\tilde{\Gamma}^* + H^*. \end{aligned} \tag{2.2.26}$$

U_{Error} indicates the strain energy difference between the two theories. Then, the relationship matrices $\tilde{C}$ and $\tilde{\Gamma}$ are determined by minimizing U_{Error} to be as close to zero as possible under the condition where $R_1, R_2 \approx 0$. Once we have found the solution for minimizing the error energy ($U_{Error} \approx 0$), the strain energy of EHOPT can be successfully expressed in terms of the variables of conventional FSDT-like theory and their effective transverse shear stiffness can be obtained by

$$\hat{G}^* = \hat{\Gamma}^{*T}\cdot G^*\cdot\hat{\Gamma}^*, \quad \hat{\Gamma}^* = \begin{bmatrix} \Gamma^*_{11} & \Gamma^*_{12} \\ \Gamma^*_{21} & \Gamma^*_{22} \end{bmatrix}^{-1}. \tag{2.2.27}$$

Note that the stiffness matrices coincide with those of conventional FSDT except for the transverse shear stiffness matrix. Matrices A^*, B^* and D^* are the well-known transformed reduced stiffness of the conventional FSDT in the Laplace domain, whereas the transverse shear stiffness moduli are modified by applying the strain energy transformation. Therefore, the effect of the shear correction factor is automatically identified through mechanics-based consideration in the present model.

2.2.3.3. Recovery process

Once the linear viscoelastic behavior was examined with the conventional FSDT-like theory, the displacement fields of EHOPT in the Laplace domain could be recovered by substituting the relationships of Eq. (2.2.15) into the displacement fields of Eq. (2.2.10) as follows [18]:

$$\begin{aligned} u_\alpha^*(x_i) &= \overline{u}_\alpha^{o*}(x_\beta) - x_3 \cdot \overline{u}_{3,\alpha}^{o*}(x_\beta) + \left\{\Phi_{\alpha\gamma}^*(x_3) - C_{\alpha\gamma}^*\right\} \cdot \left(\Gamma_{\gamma\mu}^*\right)^{-1} \cdot \overline{\gamma}_{3\mu}^*(x_\beta), \\ u_3^*(x_i) &= \overline{u}_3^{o*}(x_\beta). \end{aligned} \tag{2.2.28}$$

Consequently, In-plane and transverse stresses are estimated based on the recovered EHOPT displacements. Note that the averaged values, which are expressed as $(\overline{\bullet})$, are obtained from the FSDT-like theory with the effective transverse shear stiffness $\hat{G}$ instead of the conventional FSDT with $\hat{G}$, where $\hat{G} = \left\langle Q_{\alpha 3 \beta 3} \right\rangle$.

Theoretical calculation results for the present theory in the Laplace domain should be converted into those of the real-time domain to examine the time-dependent behaviors. Several numerical techniques have been proposed to conduct inverse Laplace transformations and some researchers have listed and compared the numerical algorithms for that inverse process [58-63].

In this study, we use the fast Fourier transform (FFT) method to convert the results in the Laplace domain back into the real-time domain. The inversion technique based on the Fourier series method is given as follows:

$$f(t)=\frac{e^{at}}{t}\left\{\frac{1}{2}F(a)+\mathrm{Re}\sum_{k=1}^{m}F\left(a+j\frac{k\pi}{t}\right)(-1)^{k}\right\}. \tag{2.2.29}$$

$F(s)$ is a function in the Laplace domain, whereas $f(t)$ is a converted function in the real-time domain. The parameters, α and m, should be optimized to improve their accuracy for the Laplace inversion. The accuracy of FFT techniques for complicated functions is less than desirable. For the polynomial based displacement field, however, inversion using FFT techniques can provide accurate results for both dynamic and quasi-static problems, and the accuracy can be further improved by optimizing the parameters used in Eq. (2.2.29). From the FFT techniques, one can analyze the linear viscoelastic behaviors in the real-time domain [58].

2.2.4. Numerical examples and discussion

In order to verify the efficiency and accuracy of the present theory (EFSDT in

the Laplace domain), rectangular composite and sandwich plates with cross-ply layup configurations are evaluated. As mentioned previously, Laplace transformation is still limited for application to the nonlinear viscoelastic constitutive equation. Thus, quasi-static analysis results for linear viscoelastic materials are taken into account in this work as numerical examples. The quasi-static bending problem of the plates subjected to doubly sinusoidal loading is used as a test-bed, in which the Pagano solution is labeled as "exact". The results of the present theory are compared to the exact solution as well as those of conventional FSDT and EHOPT. The real composite material considered herein is GY70/339 and the material properties are measured at room temperature (T=75^{o}F) and low moisture conditions (M=0.1%) to determine the linear viscoelastic behavior. The linear elastic material properties of GY70/339 are given as:

$$\begin{aligned} E_L / E_T &= 47.73, \quad G_{LT} / E_T = 0.68, \\ G_{TT} / E_T &= 0.34, \quad v_{LT} = v_{TT} = 0.31. \end{aligned} \tag{2.2.30}$$

where the subscript $(\bullet)_L$ and $(\bullet)_T$ represent a fiber direction and a perpendicular direction to the fibers, respectively. The time-dependent linear viscoelastic function, $\varphi_{ijkl}(t)$, for the material GY70/339 is listed in **Table 2.2.1**, which can be obtained from the master curve of Crossmann's experimental data [44]. For the carbon-fiber reinforced composite materials, one can assume that the modulus $Q_{1111}(t)$ is time-independent (i.e., $\varphi_{1111}(t)=1$), because the fiber modulus is dominant. On the other hand, it is assumed that the other moduli

have the same time-dependent linear viscoelastic function ($\varphi_{ijkl}(t)=\varphi(t)$) due to their matrix-dominant characteristics.

For the sandwich plates, the linear elastic material properties of a face sheet are the same as Eq. (2.2.30), and those of the core material are taken as

$$\begin{aligned} &E_1 = E_2 = E_3 = E_L / 2890, \\ &G_{12} = G_{23} = G_{13} = E_L / 7225, \\ &v_{12} = v_{23} = v_{13} = 0.25, \end{aligned} \tag{2.2.31}$$

As given in **Table 2.2.2**, the decaying rate of the time-dependent linear viscoelastic function in the core material is relatively faster than that of GY70/339 mainly due to the softness of the core portion.

For all of the examples considered herein, simply supported boundary conditions are applied. The mechanical loading is prescribed on the top surface of the plates, such that

$$p(x_\alpha, \tfrac{h}{2}; t) = p_o \sin(\tfrac{\pi}{L_1}\cdot x)\cdot \sin(\tfrac{\pi}{L_2}\cdot y)\cdot H(t_0 - t), \tag{2.2.32}$$

where $H(t_0 - t)$ is the Heaviside unit step function which accounts for linear viscoelastic creep ($t_0 > t$) and relaxation ($t_0 < t$) processes.

The normalized values reported in **Figs. 2.2.1-2.2.10** are defined by

$$\begin{aligned} &\tilde{u}_\alpha = \frac{E_T \cdot u_\alpha}{p\cdot h\cdot S^3}, \quad \tilde{u}_3 = \frac{100\cdot E_T \cdot u_3}{p\cdot h\cdot S^4}, \\ &\tilde{\sigma}_{\alpha\beta} = \frac{\sigma_{\alpha\beta}}{p\cdot S^2}, \quad \tilde{\sigma}_{3\alpha} = \frac{\sigma_{3\alpha}}{p\cdot S}, \quad S = \frac{L_1}{h} = \frac{L_2}{h}, \end{aligned} \tag{2.2.33}$$

where the length-to-thickness ratio, S, are selected for both the laminated composite and sandwich plates (S=4 or 6 for composite plates, S=10 for sandwich plates), and indicates that the plate is considerably thick.

The following six different cases are investigated to demonstrate the accuracy and efficiency of the present theory.

- Case 1: A four-layered symmetric cross-ply [0/90/0] composite square plate. Each layer has the same thickness h/3.

- Case 2: A four-layered anti-symmetric cross-ply [90/0/90/0] composite square plate. Each layer has the same thickness h/4.

- Case 3: A ten-layered symmetric cross-ply $[0/90/0/90/0]_s$ composite square plate. Each layer has the same thickness h/10.

- Case 4: An eight-layered anti-symmetric cross-ply $[90/0/90/0]_2$ composite square plate. Each layer has the same thickness h/8.

- Case 5: A symmetric cross-ply [0/Core/0] sandwich square plate, the thickness of each face sheet is equal to h/10.

- Case 6: An anti-symmetric cross-ply [90/Core/0] sandwich square plate, the thickness of each face sheet is equal to h/10.

The two types of well-known processes for the linear viscoelastic behavior are considered; these are the creep and relaxation processes.

2.2.4.1. Creep strain and stress distribution

In the creep process, we investigate the time-dependent creep strains and stress distributions under steady-state external loading conditions (i.e., $p(t)$=const).

The normalized deflections of the linear elastic and linear viscoelastic responses are presented in **Table 2.2.3** for the laminated composite plates (Case 1-4). The results obtained herein are compared to those of the conventional FSDT and EHOPT proposed by Nguyen Sy et al [35, 36]. From **Table 2.2.3**, it can be seen that the linear elastic deflections are constant over the elapsed time, because the time-dependent effect is not considered in linear elastic analysis. In contrast, the viscoelastic deflections increase over time. For the composite plates (Case 1-4), the viscoelastic deflections have the same value as the linear elastic solutions at the initial time. Subsequently, the deflections vary from the linear elastic solutions to 7.98-8.98% after 10^6 s (over 11 days) and to 19.71-22.25% after 10^8s (approximately over 3 years). This tendency is dependent upon the viscoelastic decaying rate of the relaxation moduli or the damping effect. In addition, it is observed that the linear elastic deflections of the present theory and EHOPT give the best compromised results as compared to the exact solution when both symmetric and anti-symmetric laminated composite plates are considered. The linear elastic and linear viscoelastic deflections for the sandwich plates are presented in **Table 2.2.4**. For the sandwich plates (Case 5-6), it is found that the variation rate of viscoelastic deflections increase faster than those of the composite plates due to their flexible core material. They are sequentially increased by 10.21-54.85% after 10^6 s and 24.67-114.94% after 10^8s. As shown in **Table 2.2.4**, the linear elastic deflections predicted by the conventional FSDT shows very poor performance, while those of the present

theory and EHOPT provide reliable results compared to the exact solution. Even for the very thin sandwich plate, S=100, the conventional FSDT has a significant error [18, 19]. It is noteworthy that the first-order theory is not a satisfactory method to analyze the global response of sandwich plates.

To further investigate the linear viscoelastic creep strain, the distributions of in-plane displacements as well as transverse shear stresses are considered for both laminated composite plates (S=4) and sandwich plates (S=10). The variations of normalized viscoelastic in-plane displacements with respect to the elapse of time are illustrated in **Figs. 2.2.1-2.2.3**. The results obtained herein are compared to the exact solutions as well as those predicted by conventional FSDT and EHOPT. In all the plots shown below, the black lines represent the exact solution, while the red lines denote the results of EHOPT and the magenta lines represent those of conventional FSDT. Results from the present theory are shown in blue lines, and variations in their viscoelastic behavior are expressed using symbolic markers. The in-plane displacements of cross-ply composite plates (Case 1 and 2) are plotted in **Figs. 2.2.1 and 2.2.2**. From the results, one can see that the present theory and EHOPT show good agreement with the exact solution. Zig-zag variations of in-plane displacement are suitably captured by the present theory and EHOPT, while conventional FSDT is unable to represent the zig-zag distribution. To assess the present theory further for sandwich plates, the in-plane displacements of a sandwich plate (Case 5) is presented in **Fig. 2.2.3**. A sandwich plate is a challenging problem due to its flexible core material. From **Fig. 2.2.3**, the result of conventional FSDT shows inaccurate distribution as it cannot describe the severe zig-zag distribution with slop discontinuities at the

layer interfaces, whereas the present theory and EHOPT can.

When it comes to dealing with viscoelastic responses, these theories provide flexible solutions over time. For the carbon-fiber reinforced laminated plates, the out-of-plane responses are more likely to be influenced by viscoelastic effects than the in-plane responses.

This tendency is natural in arbitrary layup laminates since viscoelastic characteristics are attributed to matrix-dominant behavior that is prominent in the out-of-plane direction. It is important to note that in the present theory and EHOPT, the in-plane displacement fields contain the u_3^o component. Thus, both models predict fairly flexible deformations as time progresses.

Unlikely both theories, the conventional FSDT exhibits only slight variations of in-plane responses since FSDT does not account for the u_3^o component in its in-plane displacement fields.

The variations in the normalized transverse shear stresses with the elapsed time for the creep process are presented in **Figs. 2.2.4 and 2.2.5**, where the results of transverse shear stresses are obtained using the equilibrium approach. **Figures 2.2.4 and 2.2.5** compare the transverse shear stresses of symmetric cross-ply composite (Case 1) and sandwich plates (Case 5). **Figures. 2.2.4 and 2.2.5** show that the present theory and EHOPT are capable of providing considerably accurate transverse shear stresses for both the laminated composite plates (**Fig. 2.2.4**) and the sandwich plates (**Fig. 2.2.5**). The kink shapes of transverse shear stress can be accurately captured by the present theory and EHOPT, whereas

conventional FSDT cannot represent the kink shape. In simple viscoelastic models such as the Maxwell and Kelvin model, distributions of stresses are time-independent for the creep process. However, as shown in **Figs. 2.2.4 and 2.2.5**, the individual ply stresses can change over time for the general viscoelastic model because of their different viscoelastic characteristics according to the direction of the fibers. **Figures 2.2.4 and 2.2.5** show that the kink shapes of the transverse shear stresses become significant as time passes due to variations in their individual ply stresses. The transverse shear forces, however, remain consistent with the passage of time for the creep process because the external loading applied is constant.

2.2.4.2. Stress relaxation

We also investigate the time-dependent stress relaxation under the steady deflection condition (u_3 =const) assigned. In the relaxation process, the distributions of the stresses tend to decrease as time passes due to the viscoelastic effect of the decayed relaxation modulus. This statement is explicitly demonstrated in **Figs. 2.2.6-2.2.10**.

To investigate the stress relaxation, the distributions of in-plane and transverse shear stresses are evaluated for the laminated composite plates (S=4) as well as the sandwich plates (S=10).

Figures 2.2.6 and 2.2.7 show the linear-elastic as well as the viscoelastic distributions of the normalized in-plane stresses over time for the relaxation

process. With regard to prediction of in-plane stresses, one can see that the present theory and EHOPT can accurately predict sudden change at the layer interface whereas the predictions by the conventional FSDT deviate significantly from the exact solution. Especially for the sandwich plate (**Fig. 2.2.7**), conventional FSDT provides excessively underestimated results for the in-plane stress distribution. This means that conventional FSDT may not be an appropriate model to analyze the mechanical response of sandwich plates. As far as viscoelastic behavior is concerned, it can be observed that the viscoelastic responses of the in-plane stresses are increased in the upper-half of the plates, whereas they are decreased in the lower-half over time. It is noteworthy that the bending moment decreases gradually with the elapsed time for the relaxation process.

The through-the-thickness distributions of the normalized transverse shear stresses over time for the relaxation process are plotted in **Figs. 2.2.8-2.2.10**. The transverse shear stresses of the cross-ply composite plates (Case 2 and 4) are shown in **Fig. 2.2.8 and 2.2.9**. The present theory and EHOPT show excellent agreement with the exact solution for the transverse shear stresses. They are able to accurately capture the severe kink shape in the vicinity of the layer interfaces, whereas the conventional FSDT does not. **Fig. 2.2.10** presents the transverse shear stress results for a sandwich plate (Case 6). Even if the sandwich plates are considerably thick (S=10), it can be observed that their unsymmetrical kink shape is precisely described by the present theory and EHOPT. For the viscoelastic behavior, it can be seen that the transverse shear stress decreases over time. In contrast to the creep process, in which the shear

force is almost constant, the transverse shear forces during the relaxation process gradually decrease as time passes because of the viscoelastic effect of the decayed relaxation modulus.

Table 2.2.3. The time-dependent function of relaxation modulus of GY70/399 composite material

p	b_p	a_p
0	0.669825e-1	∞
1	0.813977e-2	5.516602214e+02
2	0.484272e-1	1.494783951e+04
3	0.710360e-1	5.288067476e+05
4	0.114155e+0	1.846670914e+07
5	0.102892e+0	5.253922053e+08
6	0.146757e+0	1.799163029e+10
7	0.148508e+0	4.761315266e+11
8	0.150514e+0	1.477467149e+13
9	0.696426e-1	4.976486103e+14
10	0.729459e-1	8.174141919e+15

Table 2.2.2. The time-dependent function of relaxation modulus of the core of sandwich plate

p	b_p	a_p
0	0.3844	∞
1	0.0806	0.9196
2	0.0172	0.9812e+01
3	0.0429	0.9527e+02
4	0.0491	0.9432e+03
5	0.0647	0.9207e+04
6	0.0753	0.8997e+05
7	0.0888	0.8685e+06
8	0.0874	0.8514e+07
9	0.1096	0.7740e+08

Table 2.2.3. The value of time-dependent creep deflection W for the laminated composite plates

Lay-up case	Theory	Linear-elastic solution	Time (Viscoelastic solution)				
			$t=10^0$s	$t=10^2$s	$t=10^4$s	$t=10^6$s	$t=10^8$s
[0/90/0] (S=6)	Exact	0.7678	-	-	-	-	-
	FSDT	0.6981	0.6981	0.6989	0.7147	0.7649	0.8631
	EFSDT	0.7980	0.7980	0.7990	0.8179	0.8776	0.9940
	EHOPT	0.7656	0.7656	0.7664	0.7832	0.8360	0.9371
[90/0/90/0] (S=6)	Exact	0.7247	-	-	-	-	-
	FSDT	0.6138	0.6138	0.6144	0.6260	0.6628	0.7348
	EFSDT	0.7253	0.7253	0.7261	0.7415	0.7904	0.8867
	EHOPT	0.7052	0.7052	0.7060	0.7204	0.7662	0.8555
$[90/0/90/0]_2$ (S=6)	Exact	0.6300	-	-	-	-	-
	FSDT	0.5777	0.5777	0.5782	0.5896	0.6255	0.6963
	EFSDT	0.6374	0.6374	0.6381	0.6513	0.6936	0.7769
	EHOPT	0.6300	0.6300	0.6306	0.6435	0.6845	0.7648
$[0/90/0/90/0]_s$ (S=6)	Exact	0.6116	-	-	-	-	-
	FSDT	0.5736	0.5736	0.5742	0.5855	0.6217	0.6930
	EFSDT	0.6228	0.6228	0.6235	0.6365	0.6781	0.7600
	EHOPT	0.6158	0.6158	0.6165	0.6291	0.6694	0.7484

Table 2.2.4. The value of time-dependent creep deflection W for the sandwich plates

Lay-up case	Theory	Linear-elastic solution	Time (Viscoelastic solution)				
			$t=10^0$s	$t=10^2$s	$t=10^4$s	$t=10^6$s	$t=10^8$s
[0/Core/0] (S=10)	Exact	9.3868	-	-	-	-	-
	FSDT	1.2334	1.2350	1.2385	1.2685	1.3593	1.5377
	EFSDT	10.1579	10.6335	11.3698	12.7771	15.7295	21.8333
	EHOPT	9.4279	9.8346	10.4529	11.6234	14.0067	18.6344
[90/Core/0] (S=10)	Exact	10.3052	-	-	-	-	-
	FSDT	4.1526	4.1564	4.1678	4.3020	4.7190	5.5369
	EFSDT	10.5281	10.9281	11.5503	12.7760	15.3576	20.6926
	EHOPT	10.3501	10.7164	11.2814	12.4029	14.7509	19.3267

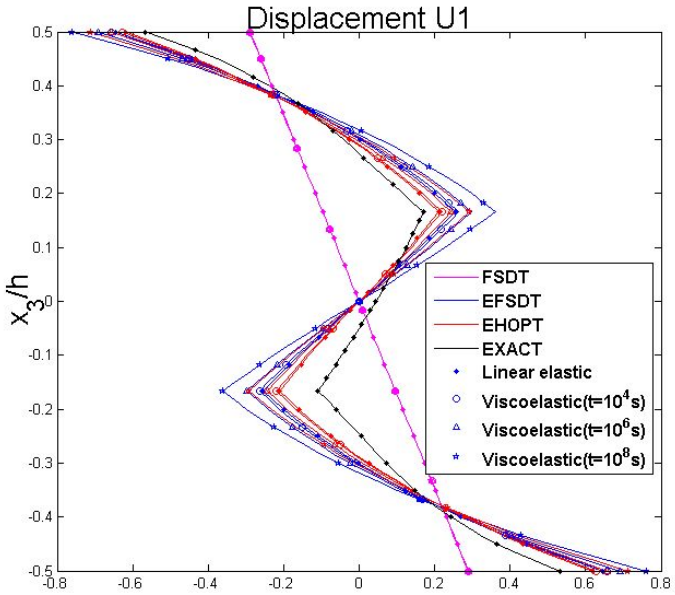

Fig. 2.2.1. [0/90/0]: time-dependent in-plane displacements for the creep process

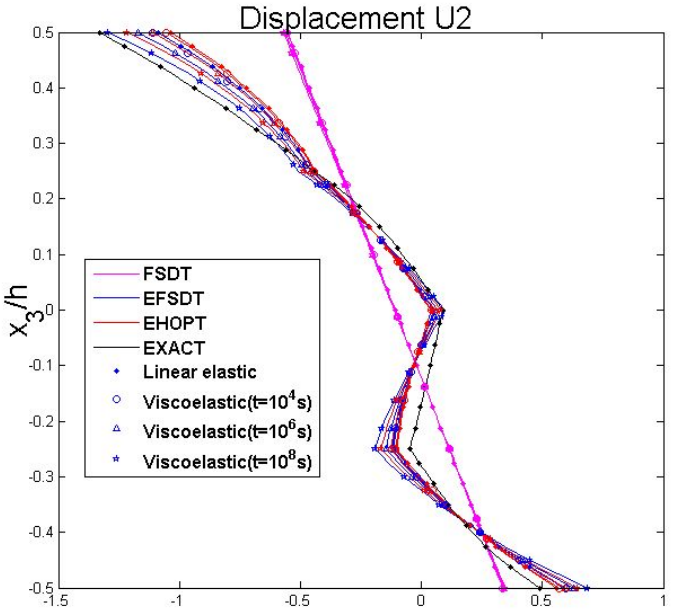

Fig. 2.2.2. [90/0/90/0]: time-dependent in-plane displacements for the creep process

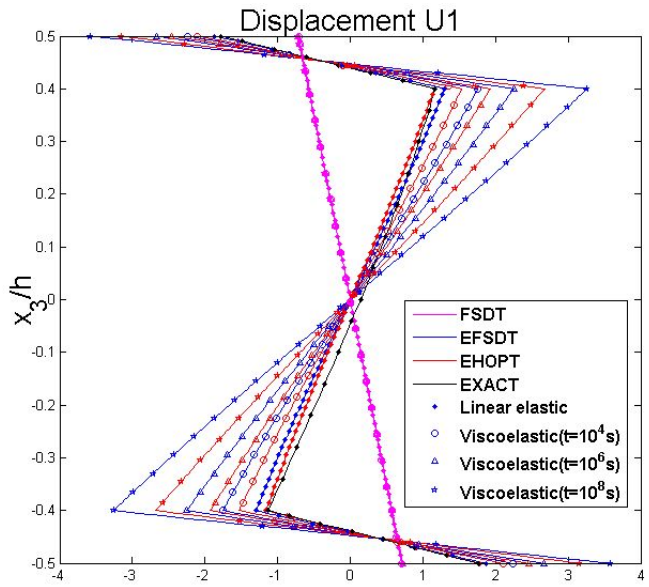

Fig. 2.2.3. [0/Core/0]: time-dependent in-plane displacements for the creep process

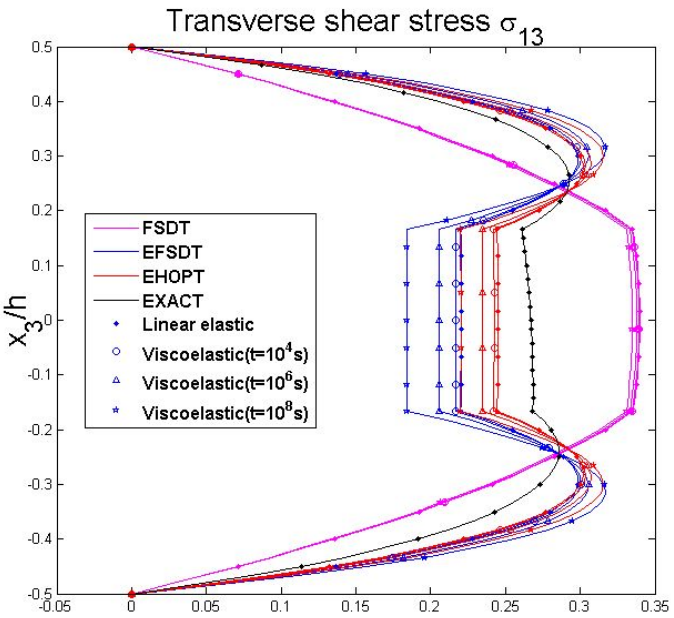

Fig. 2.2.4. [0/90/0]: time-dependent transverse shear stresses for the creep process

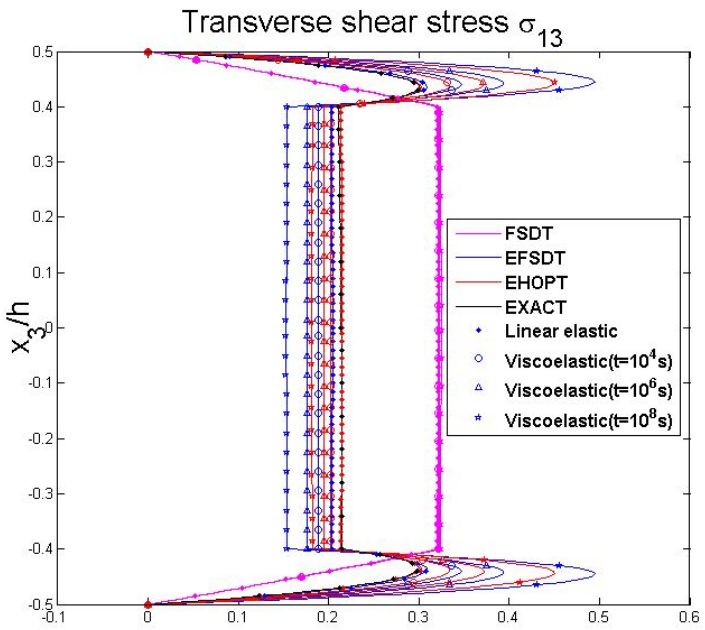

Fig. 2.2.5. [0/Core/0]: time-dependent transverse shear stresses for the creep process

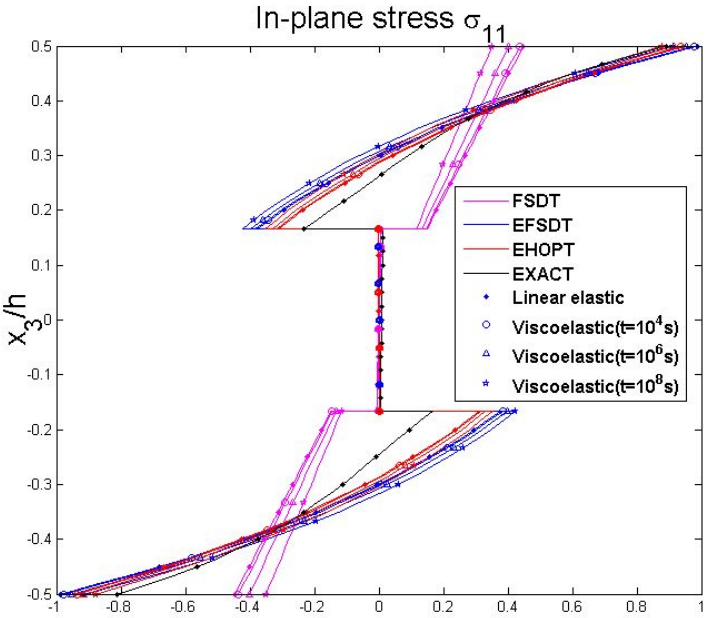

Fig. 2.2.6. [0/90/0]: time-dependent in-plane stresses for the relaxation process

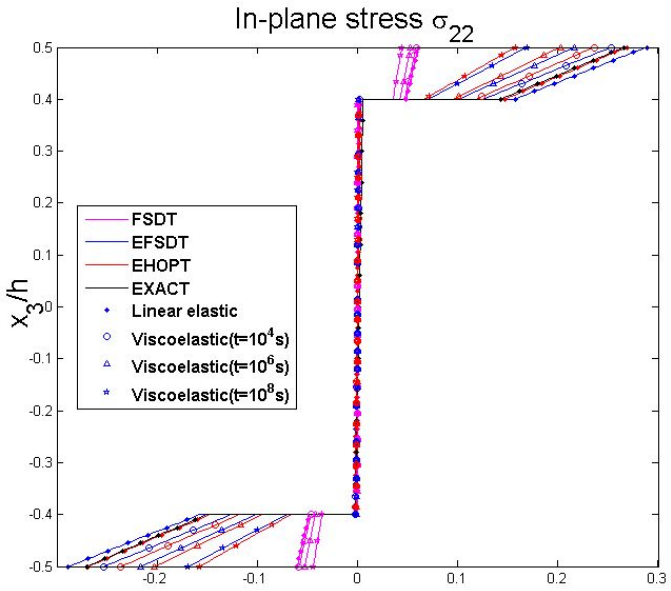

Fig. 2.2.7. [0/Core/0]: time-dependent in-plane stresses for the relaxation process

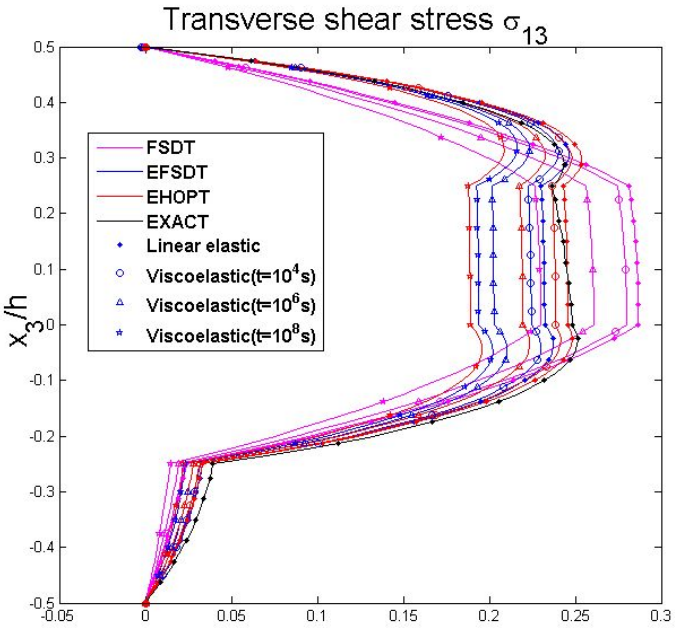

Fig. 2.2.8. [90/0/90/0]: time-dependent transverse shear stresses for the

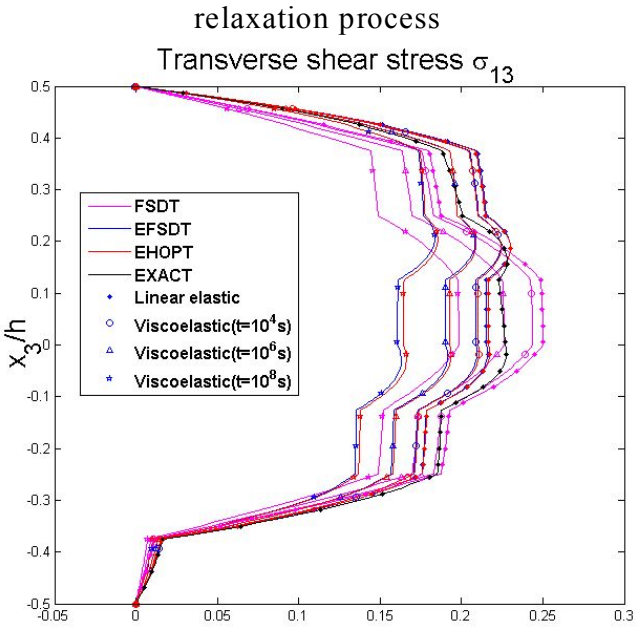

Fig. 2.2.9. $[90/0/90/0]_2$: time-dependent transverse shear stresses for the relaxation process

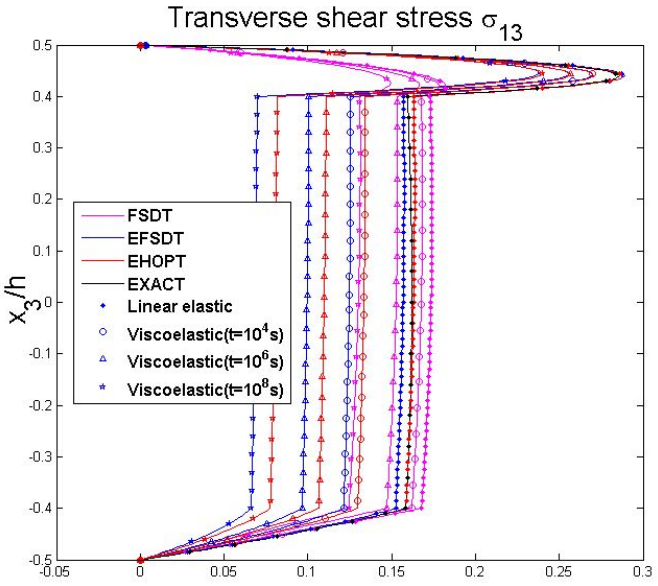

Fig. 2.2.10. [90/Core/0]: time-dependent transverse shear stresses for the relaxation process

Chapter 3

Enhanced Higher-order Shear Deformation Theory

3.1. Enhanced Higher-order Shear Deformation Theory based on the MVT

3.1.1. Literature Review

As mentioned in previous chapter 2, with the increased use of laminated composite structures, a number of analysis models are therefore developed to accurately predict their static and dynamic responses. Conventional theories (CLPT, FSDT), higher order theories (TSDT, HSDT, LCW), refined zig-zag theories (EHOPT, EHOZT) and analysis models based on post-process method (EFSDT, EFSDTM) have been sequentially developed. Among others, theories based on post-process method is very attractive because it can provide a reasonable compromise between solution accuracy as well as efficiency.

Moreover, they have the same primary variables as the FSDT, which is well suited for the implement to a commercial software. They however have a drawback in that the boundary layer effect is not properly captured. Even though both EFSDT and EFSDTM is capable to predict its qualitative behavior, they are still based on the FSDT and share the same fundamental characteristics as the FSDT.

There have also been the $C0$-based higher-order zigzag plate theories reported in literature to address the aforementioned issues. Averill [64] employed the penalty function concept to circumvent the $C1$ continuity while satisfying the shear stress continuity and free conditions. Tessler et al. [65] developed a refined zigzag plate theory, in which they did not enforce full continuity of the transverse stresses. However the results obtained therein were matched very well with elasticity and 3D FEM solutions for both simply supported and clamped-free boundary conditions, when the equilibrium approach is adopted. Petrolo et al. [66] developed the mixed plate theories based on the axiomatic/asympotic method [67] and the Carrera Unified Formulation [68]. Even though the models developed are highly accurate as compared to the elasticity approach, the number of degrees of freedom is relatively high.

In this section, the enhanced higher order shear deformation theory based on mixed variational theorem (EHSDTM), which was developed by Kim [20], is extended to the boundary layer state prediction for clamped and free boundaries. In the previous work [20], the in-plane correction factor did not considered in the analysis model, and thus the recovered stress fields cannot satisfy the self-equilibrium state. It plays a crucial role in the recovering process to improve the in-plane and transverse stresses. Thus, in-plane correction factor is additionally

introduced in the proposed model to satisfy the self-equilibrium state.

The present EHSDTM is able to provide the following features:

- The *C*0 characteristics for the favorable finite element implementation.
- The minimal number of degrees of freedom (the same as the classical HSDT).
- The accurate prediction of in-plane and transverse stresses including the boundary layer state

To achieve the main features of the present plate theory, three key ingredients are formulated as follows:

- The mixed variational theorem is employed. The transverse shear stress field is derived by employing the quantic zig-zag displacement field. The displacement field is taken as the same as the conventional HSDT.
- The strain energy transformation is carried out by expressing the variables of the stress field in terms of those of the conventional HSDT. This yields the refined HSDT model which is referred to as the EHSDTM.
- The stress recovery process is then applied, in which the quantic displacement field is expressed by the EHSDTM solution. The in-plane stress filed is corrected by introducing the factor that is calculated by minimizing the stress resultant variation between the two models. The transverse shear stress is subsequently computed by employing either the

constitutive or equilibrium approaches.

The transverse shear stresses via the constitutive approach requires only the first-order derivatives of the primary variables of the EHSDTM. Using the transverse shear stresses, the transverse normal stress can be calculated via the equilibrium approach. Consequently the highest-order of derivatives is just the second one while providing the comparable accuracy to the quintic zigzag model. Therefore proposed model makes it possible to predict the boundary layer state. For the purpose of the proper illustration of the EHSDT, two examples are considered, such as simply-supported and clamped-free boundary conditions. To demonstrate accuracy and efficiency of the present theory, the results obtained herein are compared to those of three-dimensional elasticity (3D exact), three-dimensional finite element method (3D FEM) and the models available results in the literature.

3.1.2. Mixed Formulation

To accurately and efficiently analyze the boundary layer state of the laminated composite and sandwich plates, EHSDTM is developed in this dissertation via the mixed variational theorem. In the MVT, the first variation of two-dimensional HR functional, which is given in Eqs. (1.2.4) and (1.2.5), is employed to derive the relationships between the independent two fields (HSDT and quantic zig-zag model).

3.1.2.1. Independent transverse shear stress fields

In the MVT, two independent displacement fields (u_i) and transverse shear stress fields ($\sigma^*_{3\alpha}$) are assumed in the MVT. In this subsection, a quintic zig-zag model is introduced to derive independent transverse shear stress fields which are to be used as $\sigma^*_{3\alpha}$ in MVT. A reliable transverse shear stress field, which fulfills the equilibrium conditions for transverse shear stresses (shear free conditions on the surface of the structures as well as shear continuity conditions at the layer interfaces), can be derived by employinga the displacement field that includes a quintic polynomial and a linear zigzag function.

The displacement field is initially assumed by

$$\begin{aligned} u_\alpha(x_i) &= u^0_\alpha(x_\alpha) + \sum_{i=1}^{5} \psi^{(i)}_\alpha(x_\alpha)\cdot x_3^{(i)} \\ &\quad + \sum_{k=1}^{N-1} S^{(k)}_\alpha(x_\alpha)(x_3 - x_{3(k)})H(x_3 - x_{3(k)}), \\ u_3(x_i) &= u^0_3(x_\alpha), \end{aligned} \tag{3.1.1}$$

where N is the number of layers, and $H(x_3 - x_{3(k)})$ is the Heaviside unit step function.

The continuity conditions of transverse shear stresses at layer interfaces are applied, as are the bounding traction-free conditions on the top and bottom surfaces. The transverse shear strain is then obtained as follows:

$$\gamma_{\alpha 3}(x_i) = u_{\alpha,3} + u_{3,\alpha} = \sum_{i=1}^{3} \mathscr{A}^{(i)}_{\alpha\beta}(x_3)\psi^{(i+2)}_\beta(x_\alpha), \tag{3.1.2}$$

in which

$$\mathscr{A}_{\alpha\beta}^{(1)}(x_3) = 3\left(x_3^2 - \frac{h^2}{4}\right)\delta_{\alpha\beta} + \sum_{k=1}^{N-1} a_{\alpha\beta}^{(k)} f(x_3, x_{3(k)}),$$
$$\mathscr{A}_{\alpha\beta}^{(2)}(x_3) = 4x_3\left(x_3^2 - \frac{h^2}{4}\right)\delta_{\alpha\beta} + \sum_{k=1}^{N-1} b_{\alpha\beta}^{(k)} f(x_3, x_{3(k)}), \tag{3.1.3}$$
$$\mathscr{A}_{\alpha\beta}^{(3)}(x_3) = 5\left(x_3^4 - \frac{h^4}{16}\right)\delta_{\alpha\beta} + \sum_{k=1}^{N-1} c_{\alpha\beta}^{(k)} f(x_3, x_{3(k)}),$$

where

$$f(x_3, x_{3(k)}) = -\frac{1}{2} - \frac{x_3}{h} + H(x_3 - x_{3(k)}). \tag{3.1.4}$$

$\delta_{\alpha\beta}$ is the Kronecker delta function. The terms of $a_{\alpha\beta}^{(k)}, b_{\alpha\beta}^{(k)}$ and $c_{\alpha\beta}^{(k)}$ are the functions of the material properties that account for the transverse shear stress continuity, and their explicit calculations can be found in Ref. [20].

By using the Eq. (3.1.2), the transverse shear stress to be used in Eqs. (1.2.4) and (1.2.5) can be calculated by

$$\sigma_{\alpha 3} = C_{\alpha 3 \beta 3}\gamma_{\beta 3}, \tag{3.1.5}$$

which the transverse shear strains has three independent variables $\psi_\gamma^{(i)}$ $(i = 3,4,5)$. Those variables are eventually expressed in terms of the variables used in the assumed displacement fields $(\overline{u}_i)$ that will be described in the next subsection. The independent transverse shear strains and stresses make it possible to find the reasonable relationships between the independently assumed displacement fields.

3.1.2.2. Displacement fields

The displacement fields to be used in Eqs. (1.2.4) and (1.2.5) is assumed to have the following form.

$$\begin{aligned} \overline{u}_\alpha(x_i) &= \overline{u}_\alpha^0(x_\alpha) + \sum_{i=1}^{3} \overline{\theta}_\alpha^{(i)}(x_\alpha) \cdot x_3^{(i)}, \\ \overline{u}_3(x_i) &= \overline{u}_3^0(x_\alpha), \end{aligned} \tag{3.1.6}$$

which is often referred to as a conventional higher-order shear deformation theory or simply HSDT. In what follows, it will shown that the variables given in Eq. (3.1.6) become the primary variables in the two-dimensional Hellinger-Reissner functional of Eq. (1.2.4). Additionally, the components of the conventional HSDT are given with overbar $(\overline{\bullet})$ to clear distinguish between those of quintic zig-zag model and conventional HSDT. By employing the displacement fields given in Eq. (3.1.6), corresponding strain fields can be subsequently derived as follows:

$$\begin{aligned} \overline{\varepsilon}_{\alpha\beta} &= \overline{\varepsilon}_{\alpha\beta}^0 + \sum_{i=1}^{3} \overline{\varepsilon}_{\alpha\beta}^{(i)}(x_\alpha) \cdot x_3^{(i)}, \\ \overline{\gamma}_{\alpha 3} &= \sum_{i=1}^{3} g_{\alpha 3}^{(i)} \cdot x_3^{(i-1)}, \end{aligned} \tag{3.1.7}$$

where

$$\begin{aligned} &\overline{\varepsilon}_{\alpha\beta}^0 = \frac{1}{2}\left(\overline{u}_{\alpha,\beta}^0 + \overline{u}_{\beta,\alpha}^0\right), \quad \overline{\varepsilon}_{\alpha\beta}^{(i)} = \frac{1}{2}\left(\overline{\theta}_{\alpha,\beta}^{(i)} + \overline{\theta}_{\beta,\alpha}^{(i)}\right), \\ &\overline{g}_{\alpha 3}^{(1)} = \overline{\theta}_\alpha^{(1)} + \overline{u}_{3,\alpha}^0, \quad \overline{g}_{\alpha 3}^{(2)} = 2\overline{\theta}_\alpha^{(2)}, \quad \overline{g}_{\alpha 3}^{(3)} = 3\overline{\theta}_\alpha^{(3)}. \end{aligned} \tag{3.1.8}$$

By using the Eq. (3.1.7), the in-plane stress to be used in Eqs. (1.2.4) can be calculated by

$$\bar{\sigma}_{\alpha\beta} = Q_{\alpha\beta\gamma\omega}\bar{\varepsilon}_{\gamma\omega}, \tag{3.1.9}$$

where $Q_{\alpha\beta\gamma\omega}$ are the reduced elastic stiffness tensor given in Eq. (1.2.6).

3.1.2.3. Relationships between the two theories

From the constraint equation in Eq. (1.2.5), the variables of quintic zig-zag model given in Eq. (3.1.2) can be expressed in terms of the variables of conventional HSDT given in Eq. (3.1.6). Substituting (3.1.2), (3.1.5) and (3.1.7) into the first term in Eq. (1.2.5) yields

$$\begin{bmatrix} \psi_\beta^{(3)} \\ \psi_\beta^{(2)} \\ \psi_\beta^{(1)} \end{bmatrix} = \left[D_{\beta 3\gamma 3}\right]^{-1}\left[B_{\gamma 3\lambda 3}\right]^{T}\begin{bmatrix} \bar{g}_{\lambda 3}^{(3)} \\ \bar{g}_{\lambda 3}^{(2)} \\ \bar{g}_{\lambda 3}^{(1)} \end{bmatrix}, \tag{3.1.10}$$

where

$$\begin{aligned} \left[D_{\beta 3\gamma 3}\right] &= \begin{bmatrix} D_{\beta 3\gamma 3}^{(1,1)} & D_{\beta 3\gamma 3}^{(1,2)} & D_{\beta 3\gamma 3}^{(1,3)} \\ D_{\beta 3\gamma 3}^{(2,1)} & D_{\beta 3\gamma 3}^{(2,2)} & D_{\beta 3\gamma 3}^{(2,3)} \\ D_{\beta 3\gamma 3}^{(3,1)} & D_{\beta 3\gamma 3}^{(3,2)} & D_{\beta 3\gamma 3}^{(3,3)} \end{bmatrix}, \\ \left[B_{\beta 3\gamma 3}\right] &= \begin{bmatrix} B_{\beta 3\gamma 3}^{(1,1)} & B_{\beta 3\gamma 3}^{(1,2)} & B_{\beta 3\gamma 3}^{(1,3)} \\ B_{\beta 3\gamma 3}^{(2,1)} & B_{\beta 3\gamma 3}^{(2,2)} & B_{\beta 3\gamma 3}^{(2,3)} \\ B_{\beta 3\gamma 3}^{(3,1)} & B_{\beta 3\gamma 3}^{(3,2)} & B_{\beta 3\gamma 3}^{(3,3)} \end{bmatrix}, \end{aligned} \tag{3.1.11}$$

in which

$$D_{\beta 3\gamma 3}^{(i,j)} = \left\langle \mathscr{A}_{\beta\lambda}^{(i)} C_{\lambda 3\mu 3} \mathscr{A}_{\mu\gamma}^{(j)} \right\rangle, \quad B_{\alpha 3\beta 3}^{(i,j)} = \left\langle x_3^{(i-1)} C_{\alpha 3\gamma 3} \mathscr{A}_{\gamma\beta}^{(j)} \right\rangle,$$
$$\langle \bullet \rangle = \int_{-h/2}^{h/2} (\bullet) dx_3. \tag{3.1.12}$$

Note that Eq. (3.1.10) plays a crucial role in deriving the enhanced higher-order shear deformation theory based on the MVT (EHSDTM) and recovering the stress and displacement fields. This will be described in detail in the following subsection.

3.1.3. Enhanced higher-order shear deformation theory based on the MVT

In this subsection, the enhanced higher-order shear deformation theory is derived by substituting the transverse shear stress field and the displacement fields obtained in the previous subsection into the two-dimensional Hellinger-Reissner functional of Eq. (1.2.4). Thus, governing equation of the present theory is based on the FSDT_TN. In addition, recovery process is also considered in this section to more accurately predict the thermo-elastic response of the laminated composite structures. Once we obtained the relationship between the independent two fields which is given in Eq. (3.1.10), the HR functional can be rewritten in terms of the primary variables of conventional HSDT as follows:

$$\int_{\Omega}\left[N_{\alpha\beta}\delta\overline{u}^{(0)}_{\alpha,\beta}+\sum_{i=1}^{3}\left(M^{(i)}_{\alpha\beta}\delta\overline{\theta}^{(i)}_{\alpha,\beta}+Q^{(i)}_{\alpha}\delta\overline{g}^{(i)}_{\alpha 3}\right)\right]d\Omega=\int_{S_\sigma}\tilde{t}_3\delta\overline{u}^{(0)}_3 dS, \tag{3.1.13}$$

where

$$N_{\alpha\beta}=\left\langle\overline{\sigma}_{\alpha\beta}\right\rangle,\ M^{(i)}_{\alpha\beta}=\left\langle x^i_3\overline{\sigma}_{\alpha\beta}\right\rangle,\ Q^{(i)}_{\alpha}=\left\langle x^{(i-1)}_3\sigma_{\alpha 3}\right\rangle, \tag{3.1.14}$$

in which the transverse shear force Q_α needs a special attention, because the transverse shear stress $\sigma_{\alpha 3}$ is not expressed in terms of the primary variables of conventional HSDT. By applying Eq. (3.1.10) to the transverse shear force, one can obtain as follows:

$$\begin{bmatrix}Q^{(1)}_{\alpha}\\ Q^{(2)}_{\alpha}\\ Q^{(3)}_{\alpha}\end{bmatrix}=\left[\hat{G}_{\alpha 3\lambda 3}\right]\begin{bmatrix}\overline{g}^{(1)}_{\lambda 3}\\ \overline{g}^{(2)}_{\lambda 3}\\ \overline{g}^{(3)}_{\lambda 3}\end{bmatrix}, \tag{3.1.15}$$

where

$$\left[\hat{G}_{\alpha 3\lambda 3}\right]=\left[B_{\alpha 3\beta 3}\right]\left[D_{\beta 3\gamma 3}\right]^{-1}\left[B_{\gamma 3\lambda 3}\right]^{T}, \tag{3.1.16}$$

which is the transverse shear stiffness of EHSDTM that differs from those obtained by either the fifth-order zig-zag theory (Eq. (3.1.3)) or conventional HSDT (Eq. (3.1.6)).

3.1.3.1. Governing equations and boundary conditions

The governing equations are obtained by applying the integration by parts to the Eq. (3.1.13). The governing equations of EHSDTM are then given as follows:

$$\begin{aligned} &\delta\bar{u}_{\alpha}^{(0)}: \ N_{\alpha\beta,\beta}=0, \\ &\delta\bar{\theta}_{\alpha}^{(n)}: \ M_{\alpha\beta,\beta}^{(n)}-nQ_{\alpha}^{(n)}=0, \quad (n=1,2,3) \\ &\delta\bar{u}_{3}^{(0)}: \ Q_{\alpha,\alpha}^{(1)}=-\tilde{t}_{3}, \end{aligned} \tag{3.1.17}$$

and the associated boundary conditions are given by

$$\begin{aligned} &\delta\bar{u}_{\alpha}^{(0)}=0 \quad or \quad N_{\alpha\beta}n_{\beta}=0, \\ &\delta\bar{\theta}_{\alpha}^{(n)}=0 \quad or \quad M_{\alpha\beta}^{(n)}n_{\beta}=0, \quad (n=1,2,3) \\ &\delta\bar{u}_{3}^{(0)}=0 \quad or \quad Q_{\alpha}^{(1)}n_{\alpha}=0, \end{aligned} \tag{3.1.18}$$

Here one can clearly see that the present EHSDTM does modify the transverse shear stress resultant only, as compared to a conventional HSDT. Thus a physical inconsistency (or anomaly) in the definition of the transverse shear force, which were discussed in Refs. [64, 65], dose not present in the proposed model.

3.1.3.2. Displacement and stress recovery

Once the governing equations of EHSDTM (Eq. (3.1.17)) is solved, one can recover the fifth-order zig-zag displacement field, Eq. (3.1.1), in terms of the variables of the EHSDTM. Utilizing the transverse shear strain given in Eq. (3.1.2), the displacement field can be rewritten as:

$$
\begin{aligned}
u_\alpha &= u_\alpha^{(0)} - x_3 \overline{u}_{3,\alpha}^{(0)} + \sum_{i=1}^{3} \Phi_{\alpha\beta}^{(i)} \psi_\beta^{(i+2)}, \\
u_3 &= \overline{u}_3^{(0)},
\end{aligned}
\tag{3.1.19}
$$

where

$$
\begin{aligned}
\Phi_{\alpha\beta}^{(1)} &= \int \mathscr{A}_{\alpha\beta}^{(1)} dx_3 = x_3 \left(x_3 - \frac{3h^2}{4} \right) \delta_{\alpha\beta} + \sum_{k=1}^{N-1} a_{\alpha\beta}^{(k)} F(x_3, x_{3(k)}), \\
\Phi_{\alpha\beta}^{(2)} &= \int \mathscr{A}_{\alpha\beta}^{(2)} dx_3 = x_3^2 \left(x_3^2 - \frac{h^2}{2} \right) \delta_{\alpha\beta} + \sum_{k=1}^{N-1} b_{\alpha\beta}^{(k)} F(x_3, x_{3(k)}), \\
\Phi_{\alpha\beta}^{(3)} &= \int \mathscr{A}_{\alpha\beta}^{(3)} dx_3 = x_3 \left(x_3^4 - \frac{5h^4}{16} \right) \delta_{\alpha\beta} + \sum_{k=1}^{N-1} c_{\alpha\beta}^{(k)} F(x_3, x_{3(k)}),
\end{aligned}
\tag{3.1.20}
$$

in which

$$
F(x_3, x_{3(k)}) = -\frac{1}{2} x_3 - \frac{x_3^2}{2h} + (x_3 - x_{3(k)}) H(x_3 - x_{3(k)}),
\tag{3.1.21}
$$

and $\psi_\beta^{(i+2)}$ can be expressed by the transverse shear strain of the EHSDTM, $\overline{g}_{\gamma 3}^{(i)}$, using the relationships of Eq. (3.1.10). The transverse displacement u_3 is assumed to be the same as the EHSDTM, since it is improved as compared to the conventional HSDT.

Now one needs to express the constant displacement $u_\alpha^{(0)}$ in terms of the variables of the EHSDTM. Unlike the constant displacement component in EHSDTM, the recovered one does not necessarily mean the displacement at the middle plane of a plate. This enforces us to employ an average matching between the EHSDTM and the recovered one. The least square minimization of

the difference between two displacement fields with respect to the unknown $u_\alpha^{(0)}$ is given by

$$\min_{\bar{u}_\alpha^{(0)}} \left\langle \left(u_\alpha - \bar{u}_\alpha \right)^2 \right\rangle = 0, \tag{3.1.22}$$

which yields

$$u_\alpha^{(0)} = \bar{u}_\alpha^{(0)} + \frac{h^2}{12}\bar{\theta}_\alpha^{(2)} - \frac{1}{h}\sum_{i=1}^{3}\left\langle \Phi_{\alpha\beta}^{(i)} \right\rangle \psi_\beta^{(i+2)} - c_\alpha, \tag{3.1.23}$$

where c_α is an unknown function to be determined later. This in-plane correction factors play a crucial role to calculate the stresses using three-dimensional stress equilibrium equations. The recovered displacement field is finally obtained by

$$u_\alpha = \bar{u}_\alpha^{(0)} - x_3\bar{u}_{3,\alpha}^{(0)} + \frac{h^2}{12}\bar{\theta}_\alpha^{(2)} + \sum_{i=1}^{3}\left(\Phi_{\alpha\beta}^{(i)} - \frac{1}{h}\left\langle \Phi_{\alpha\beta}^{(i)} \right\rangle \right)\psi_\beta^{(i+2)} - c_\alpha, \tag{3.1.24}$$

which include the first-order derivatives with respect to in-plane coordinates x_α. The determination procedure of the in-plane correction function c_α is given in **Appendix G**.

To obtain the improved stress components, strains are calculated first by using Eq. (3.1.24), subsequently stresses are manipulated via the two-dimensional constitutive equation given in Eq. (1.2.6). There are two ways to calculate transverse shear stresses, such as constitutive and equilibrium approaches. The constitutive approach is to use the transverse shear constitutive equation (Eq.

(3.1.5)), in which the shear strains are evaluated by the displacements of Eq. (3.1.24). The results obtained in this way are called 'EHSDTM(c)'. The equilibrium approach is to utilize the three-dimensional stress equilibrium equation such that

$$\hat{\sigma}_{\alpha 3} = -\int_{-h/2}^{x_3} \sigma_{\alpha\beta,\beta} dx_3. \tag{3.1.25}$$

Once the shear stresses of Eq. (3.1.25) are calculated, a transverse normal stress can be improved. This however requires fourth-order derivatives with respect to in-plane coordinates x_α. To circumvent this, the transverse shear stresses via the constitutive equation (Eq. (3.1.5)) are utilized, as the equilibrium approach is employed. That is,

$$\hat{\sigma}_{33} = -\int_{-h/2}^{x_3} \sigma_{\alpha 3,\alpha} dx_3. \tag{3.1.26}$$

Henceforth, the transverse shear and normal stresses predicted by the Eqs. (3.1.25) and (3.1.26) are referred to as 'EHSDTM(e)'.

3.1.4. Numerical results and discussion

To demonstrate the efficiency and accuracy of a present theory, semi-infinite laminated composite plates are considered in this study. Two boundary conditions are taken as test-beds, which are simply-supported (SS) and clamped-free (CF) boundary conditions (see **Fig. 3.1.1**). The SS conditions are useful when the accuracy assessment of proposed theories is needed, while the CF conditions are

essential for the investigation of edge-effects. The SS plates are subjected to a sinusoidal loading, and the CF plates are under an uniformly distributed pressure.

The material properties of each ply are assumed to have

$$\begin{aligned} &E_L = 172.4Gpa,\ E_T = 6.9Gpa,\ G_{LT} = 3.45Gpa, \\ &G_{TT} = 1.38Gpa,\ v_{LT} = v_{TT} = 0.25, \end{aligned} \tag{3.1.27}$$

where subscripts 'L' and 'T' denote the direction parallel to the fiber and the direction perpendicular to the fiber, respectively. For sandwich configurations, the material properties of face sheets are the same as those in Eq. (3.1.27), and the core material properties are given as:

$$\begin{aligned} &E_1 = 0.1Gpa,\ E_2 = E_3 = E_1,\ G_{12} = 0.4Gpa, \\ &G_{23} = G_{13} = G_{12},\ v_{12} = 0.25,\ v_{23} = v_{13} = v_{12}. \end{aligned} \tag{3.1.28}$$

Four different laminate configurations are considered, which are listed in **Table 3.1.1**. The fiber angle is misaligned in order to utilize the work of Pagano, and the exact solutions are reproduced, according to the fiber angles given in **Table 3.1.1**, in this paper.

For the purpose of comparison, the displacement and stresses reported herein are normalized as follows:

$$\begin{aligned} &\tilde{u}_\alpha = \frac{100 \cdot E_T \cdot u_\alpha}{q_0 \cdot h \cdot S^3},\ \tilde{u}_3 = \frac{100 \cdot E_T \cdot u_3}{q_0 \cdot h \cdot S^4}, \\ &\tilde{\sigma}_{\alpha\beta} = \frac{\sigma_{\alpha\beta}}{q_0 \cdot S^2},\ \tilde{\sigma}_{3\alpha} = \frac{\sigma_{3\alpha}}{q_0 \cdot S},\ \tilde{\sigma}_{33} = \frac{\sigma_{33}}{q_0}, \end{aligned} \tag{3.1.29}$$

where S is the length-to-thickness ratio, L_1/h, and q_0 is the maximum of an

applied pressure.

3.1.4.1. Interior solutions: simply-supported boundary conditions

Simply-supported conditions are analyzed first, in order to analytically asses the accuracy of interior solutions via the present EHSDTM theory. The results obtained herein are then compared to those of FSDT, HSDT, EFSDT [18], EFSDTM [19], FAMPA [69] as well as the elasticity approach. The results of FSDT, HSDT, EFSDT, EFSDTM and elasticity approach are reproduced in this work.

For the four cases, normalized center deflections are listed and compared to those of other theories in **Table 3.1.2**. Classical theories, such as FSDT and HSDT, tend to underestimate the deflections as the plate becomes thick (S=4). This tendency is significant when the sandwich configuration (case 4) is considered. The results of EFSDT and EFSDTM are comparable to those of the FAMPA2nd which is based on an asymptotic expansion method. The asymptotic method requires the iterative calculation that is computationally expensive. Their results still deviate from the exact solutions (about 40%), although they are much better than the classical theories. **Table 3.1.2** clearly indicates that the present EHSDTM is the best compromised theory in terms of the numerical efficiency and accuracy. Moreover, the EHSDTM has the same degrees of freedom as the conventional HSDT, and therefore it only requires the C^0 continuity without any additional numerical treatments.

In addition to the accurate prediction of global responses, the present

EHSDTM is able to predict precisely the through-the-thickness distributions of displacement and stress. The in-plane displacement of Case 1 and transverse shear stress of Case 2, for the very thick plate of $S = 4$, are plotted in **Fig. 3.1.2**. The conventional HSDT, EFSDTM and EHSDTM are able to capture the qualitative behavior of the displacement and transverse shear stress. Especially the present EHSDTM yields almost identical results with the elasticity approach. There are two ways for the calculation of transverse shear stresses, such as constitutive and equilibrium approaches, as described in subsection 3.1.3.2. The equilibrium approach, EHSDTM(e), shows a highly accurate prediction of σ_{13}, while the constitutive approach, EHSDTM(c), is comparable to HSDT(e). One should notice here that the EHSDTM(c) only requires the first-order derivatives of primary variables with respect to the in-plane coordinates x_α. This is a great feature when the theory is applied to a finite element method, which shall be addressed in next subsection. This feature subsequently leads to the accurate prediction of transverse normal stresses, which are of practical importance for the possible initiation of a delamination. The transverse normal stress distribution for antisymmetric cross-ply ($S = 4$) and sandwich ($S = 10$) configurations are illustrated in **Fig. 3.1.3**. One can see that only the EHSDTM has a high fidelity for the accurate prediction of the through-the-thickness distribution for both cases. In this regard, EHSDTM has a great advantage for analytical and numerical researches of composite plates including a sandwich plate.

3.1.4.2. Edge effects: clamped-free boundary conditions

Next the semi-infinite plates with clamped-free boundary conditions are considered to assess the performance of EHSDTM when the edge effects are presented. To this end, a three-noded element based on Lagrangian polynomials is employed, and 80 elements are used to calculate the stress distributions on various axial locations. The plate is assumed to be very thick, which allows us to emphasize the significance of edge effects for all the cases.

Normalized tip deflections of a clamped-free plate with varying the length-to-thickness ratio S are shown in **Fig. 3.1.4**. The conventional FSDT and HSDT underestimate the deflection, whereas EFSDTM overestimates it. In contrast to this, the present EHSDTM shows an excellent agreement with the 3D FEM, even for the very thick case of S = 4. As the length-to-thickness ratio increases, the conventional HSDT that has the same degrees of freedom with the EHSDTM still deviates from the 3D FEM. This clearly indicates that the present theory is a best-compromised theory in terms of accuracy and efficiency.

Local stress distributions are also investigated to assess the accuracy of EHSDTM near the boundaries. To this end, stresses are computed at the 10th element ($x_1 = 0.12L_1$) for the clamped end effect and at the 70th element ($x_1 = 0.87L_1$) for the free end effect. All the derivatives with respect to the axial coordinate are carried out at the mid-node. The in-plane stresses of the antisymmetric angle-ply plate with S = 4 are plotted in **Fig. 3.1.5**. The results obtained are compared to those of FSDT, HSDT, EFSDTM and 3D FEM, which are reproduced in this work. It can be seen that the conventional FSDT is not able to predict the boundary effect at all, especially for the free end. On the other hand, the EHSDTM can predict the stress distributions qualitatively as well as

quantitatively.

Transverse shear stresses are of great importance in composite plates. The stresses are also calculated at near both clamped and free ends. They can be calculated via either constitutive approach or equilibrium approach. Unlike the simply-supported boundary condition in the preceding section, there is a numerical difficulty in the calculation of higher-order derivatives. For this very reason, the constitutive approach is employed. The stresses calculated are then illustrated in **Fig. 3.1.6** for the nearly symmetric cross-ply (case 1) that is selected as a representative example. The theories considered herein are not able to capture the kinky shape of the stresses. The present EHSDTM is however well correlated with the 3D FEM. One should note that the transverse shear stress via the constitutive approach only requires the first-order derivatives with respect to the axial coordinate. This is one of the merits of using the EHSDTM. Now one can calculate transverse normal stresses via the equilibrium approach of Eq. (3.1.26) that require the second-order derivatives. The normal stresses are calculated and plotted in **Fig. 3.1.7** for the sandwich configuration (case 4) with $S = 4$. It is observed again that the present EHSDTM shows an excellent agreement with the 3D FEM. The results predicted by FSDT and EFSDTM significantly deviate from those of the 3D FEM. As amply demonstrated so far, the EHSDTM is capable of predicting the boundary layer states. In what follows, the boundary layer zone shall be calculated by using the present theory.

3.1.4.3. Boundary layer zone

It is of interest to investigate how far the edge effects propagate. To this end,

one needs to employ alternative definition of the stresses. For the clamped-free boundary condition, the stresses vary from one end to the other. In order to consider such a variation, the boundary coordinate x_b is introduced (see **Fig. 3.1.8**). In **Fig. 3.1.8**, L_c and L_f denote the boundary layer zone at clamped and free ends, respectively. The normalized stresses, which are defined in Eq. (3.1.29), are scaled in the following manner:

$$\breve{\sigma}_{\alpha\beta} = \frac{\tilde{\sigma}_{\alpha\beta}}{\left(x_b / L_1\right)^2}, \quad \breve{\sigma}_{3\alpha} = \frac{\tilde{\sigma}_{3\alpha}}{\left(x_b / L_1\right)}, \quad \breve{\sigma}_{33} = \tilde{\sigma}_{33}. \tag{3.1.30}$$

In addition, the change in the maximum value of stresses is introduced to determine the interior zone or the boundary layer zone.

$$\sigma_{ij}^{cr} = \frac{\max\left(\breve{\sigma}_{ij}^{(k+1)}\right) - \max\left(\breve{\sigma}_{ij}^{(k)}\right)}{\max\left(\breve{\sigma}_{ij}^{(k)}\right)} \times 100, \tag{3.1.31}$$

where the superscript '(k)' indicates the k-th element. It is assumed that the criteria of the interior zone is taken as:

$$\sigma_{ij}^{cr} \le 0.1 \tag{3.1.32}$$

For the comparison purpose, three cases are considered in this section, which include an isotropic plate as well as the symmetric cross-ply (case 1) and the sandwich plate (case 4) given in Table 1. The length-to-thickness ratio (*S*) is assumed to be 40, and the number of the elements is 200 to accurately calculate the stresses. The boundary layer zones for both clamped and free ends are estimated and listed in **Table 3.1.3** and illustrated in **Fig. 3.1.9**.

For the isotropic case, the interior zone is more than 90%, as expected. It is seen that the boundary layer state of the transverse shear stress decays faster than that of the in-plane normal stress. This is reasonable because the higher order states rapidly decay in general. This trend is observed in all the cases considered herein. For the sandwich plate, the boundary layer state of the in-plane normal stress deeply penetrates into the interior of the plate (see **Fig. 3.1.9**). In fact, there is no interior state for this case ($S = 40$). This implies that one should employ a higher-order theory with a proper shear correction (like the EHSDTM) to analyze the plate made of highly anisotropic materials.

To investigate the boundary layer states further, the through-the-thickness distributions are plotted in **Figs. 3.1.10-3.1.12**, for the isotropic, composite and sandwich plate. It is of interest to see that the signs of the stresses at the interface are changed. They have mean values at near the mid-span where the through-the-thickness distribution of the conventional FSDT is identical that of the EHSDTM. This indicates that the stress distribution of the conventional FSDT is invariant with respect to the axial coordinate. The change in the stresses estimated by the EHSDTM is very small near the mid-span, which is spotted by the dark area in **Fig. 3.1.10-3.1.12**, and indicates the interior zone. Although the conventional FSDT is a shear deformable theory, it is not able to predict the boundary layer stress state at all.

Table 3.1.1. A list of lamination sequence for laminated and sandwich plates

Case	Layup	x_3/h
1	$[0.5^o/90.5^o/90.5^o/0.5^o]$	[-1/2, -1/4, 0, 1/4, 1/2]
2	$[90.5^o/0.5^o/90.5^o/0.5^o]$	[-1/2, -1/4, 0, 1/4, 1/2]
3	$[-30^o/30^o/-30^o/30^o]$	[-1/2, -1/4, 0, 1/4, 1/2]
4	$[0.05^o/\text{Core}/0.05^o]$	[-1/2, -2/5, 0, 2/5, 1/2]

Table 3.1.2. Comparison of center deflections of simply-supported semi-infinite plates under a sinusoidal load

S	Models	Case 1	Case 2	Case 3	Case 4
4	Exact	3.336	4.181	3.291	75.59
	FAMPA 2nd	3.591	4.538	3.443	108.07
	FSDT	2.730	3.296	2.787	8.27
	HSDT	3.219	3.624	2.940	52.96
	EFSDT	3.594	4.336	3.350	108.08
	EFSDTM	3.707	3.920	3.171	108.40
	EHSDTM	3.364	4.408	3.385	82.57
10	Exact	1.036	1.659	1.385	17.01
	FAMPA 2nd	1.044	1.671	1.390	18.14
	FSDT	0.906	1.473	1.285	2.17
	HSDT	1.006	1.534	1.315	10.90
	EFSDT	1.044	1.639	1.375	18.14
	EFSDTM	1.062	1.572	1.346	18.19
	EHSDTM	1.037	1.672	1.391	17.23
20	Exact	0.679	1.261	1.096	5.22
	FAMPA 2nd	0.680	1.262	1.097	5.29
	FSDT	0.646	1.212	1.070	1.30
	HSDT	0.671	1.228	1.078	3.55
	EFSDT	0.680	1.254	1.093	5.29
	EFSDTM	0.684	1.237	1.086	5.30
	EHSDTM	0.680	1.263	1.097	5.22

Table 3.1.3. Comparison of boundary layer and interior zones of the clamped-free edge plates

Case		Characteristic length		Interior zone
		Clamped length	Free length	
		L_c/L (%)	L_f/L (%)	$100-(L_c+L_f)/L$ (%)
Isotropic	σ_{11}	1%	8%	91%
	σ_{13}	2.5%	2%	95.5%
[0/90/90/0] Composite	σ_{11}	5.5%	27.5%	67%
	σ_{13}	9%	7.5%	83.5%
Sandwich	σ_{11}	-	-	none
	σ_{13}	27%	20%	53%

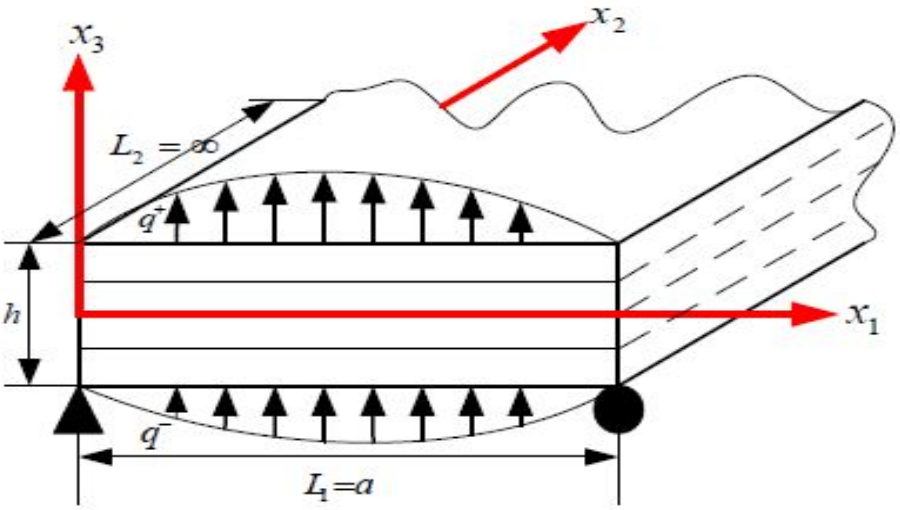

(a) Simply-supported plate under sinusoidal pressure

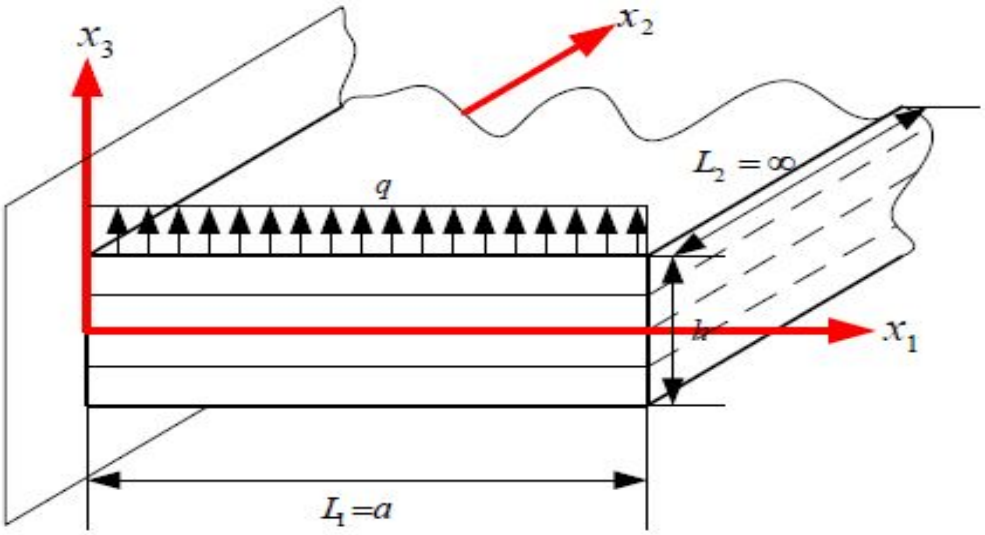

(b) Clamped-free plate under uniform pressure

Fig. 3.1.1. Loading and boundary conditions of semi-infinite plates

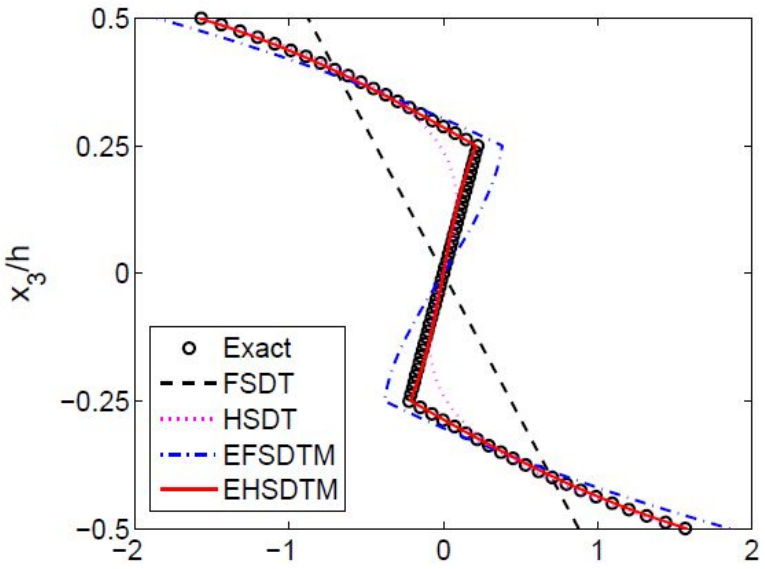

(a) Displacements of the symmetric cross-ply, Case 1

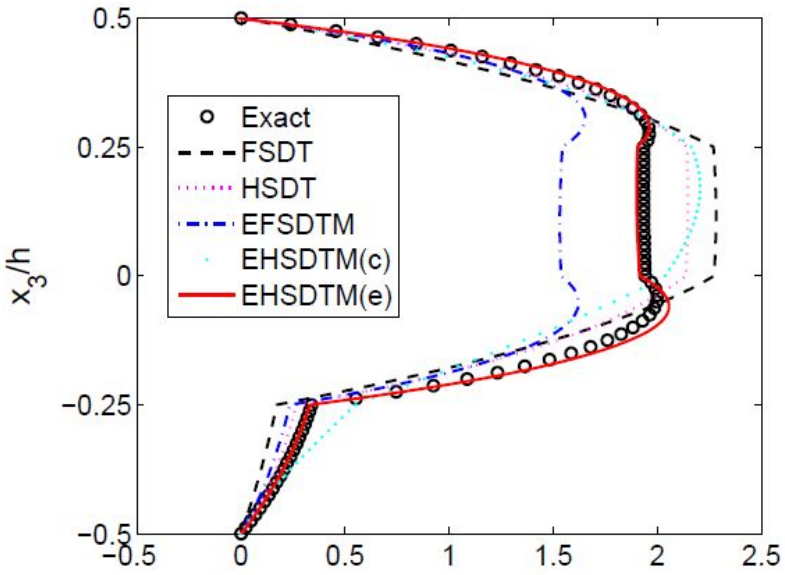

(b) Transverse shear stresses of the anti-symmetric cross-ply, Case 2

Fig. 3.1.2. Displacement and stress of a simply-supported plate, S=4

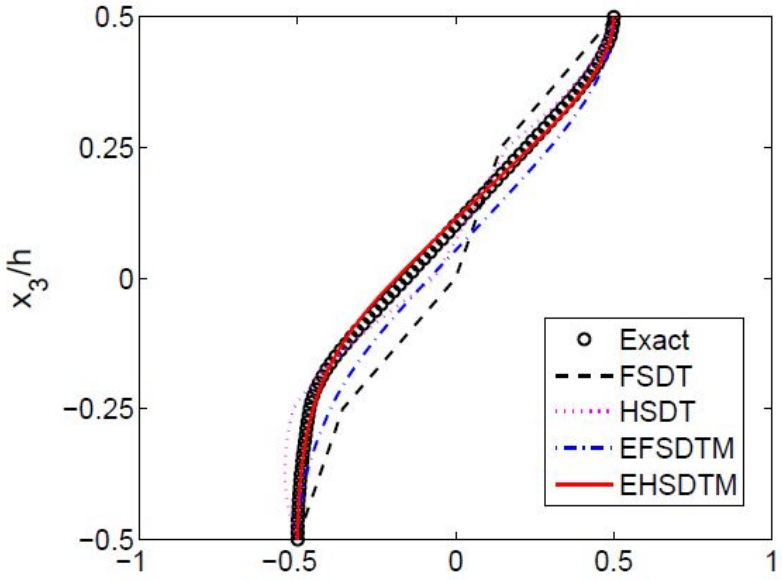

(a) Transverse normal stresses of the anti-symmetric cross-ply (S=4)

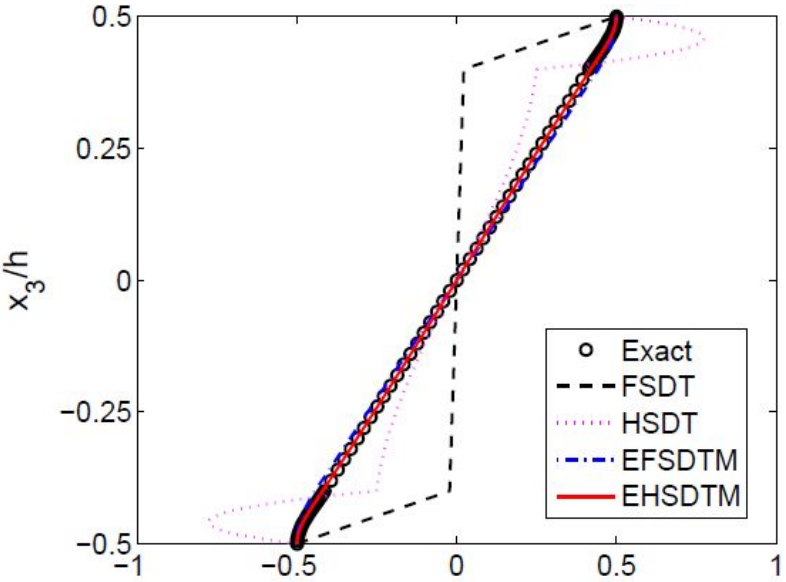

(b) Transverse normal stresses of the sandwich (S=10)

Fig. 3.1.3. Transverse normal stresses of a simply-supported plate, Case 2 and 4

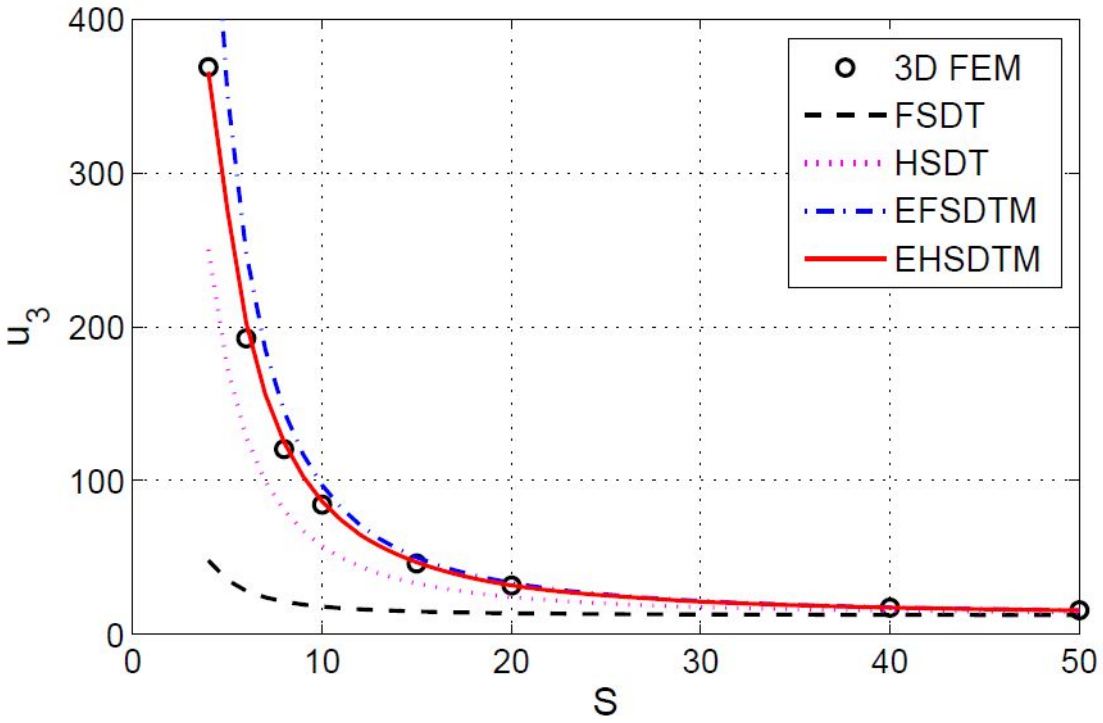

Fig. 3.1.4. Normalized tip deflections of the clamped-free sandwich plate

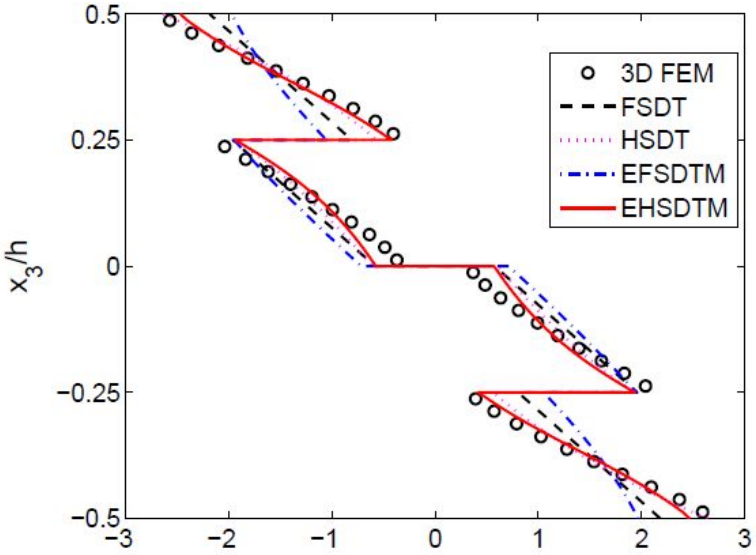

(a) In-plane stresses at near clamped end ($0.12L_1$)

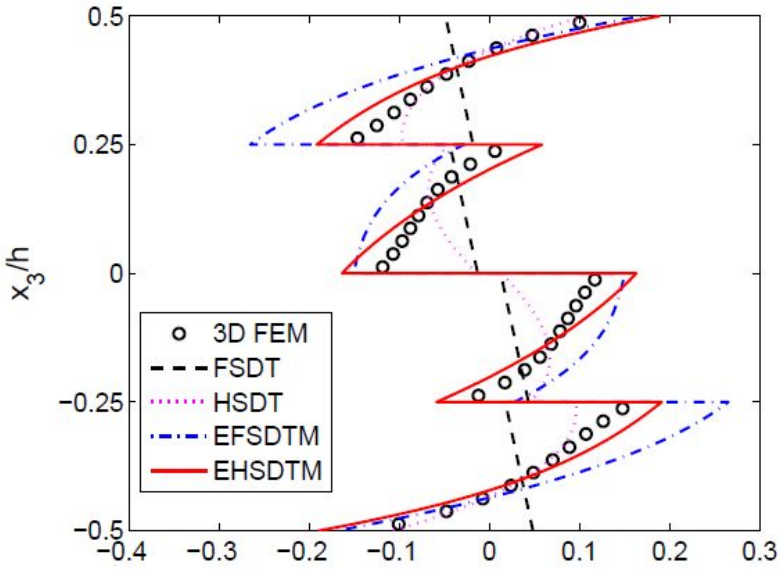

(b) In-plane stresses at near free end ($0.87L_1$)

Fig. 3.1.5. In-plane normal stresses of the clamped-free plate for the anti-symmetric angle-ply (Case 3), S=4

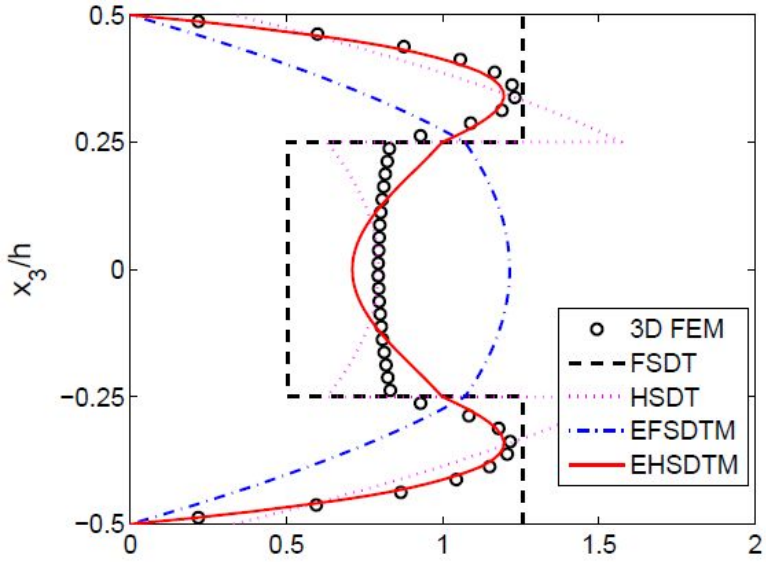

(a) Transverse shear stresses at near clamped end ($0.12L_1$)

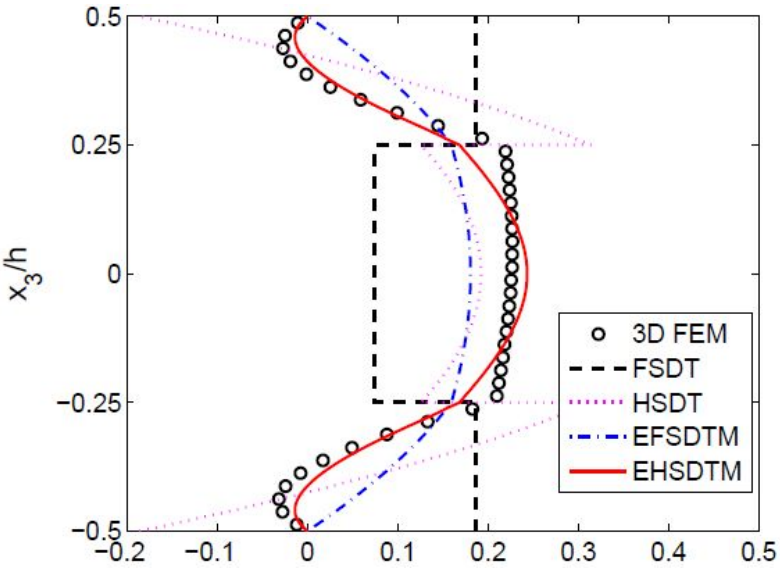

(b) Transverse shear stresses at near free end ($0.87L_1$)

Fig. 3.1.6. Transverse shear stresses of the clamped-free plate for the nearly symmetric cross-ply (Case 1), S=4

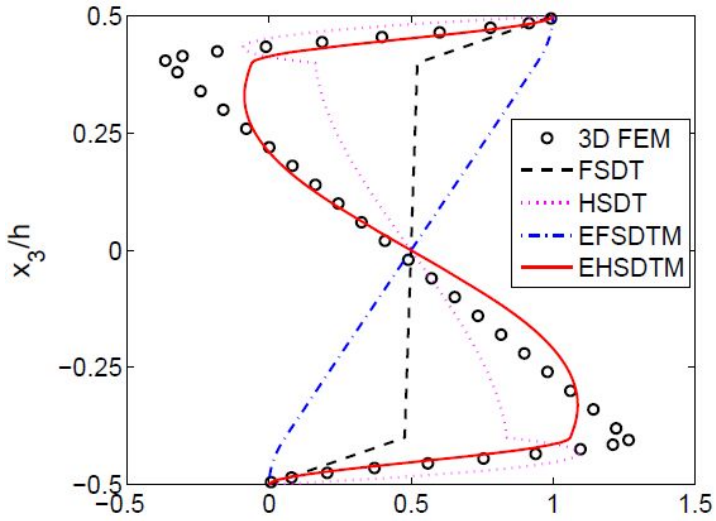

(a) Transverse normal stresses at near clamped end ($0.12L_1$)

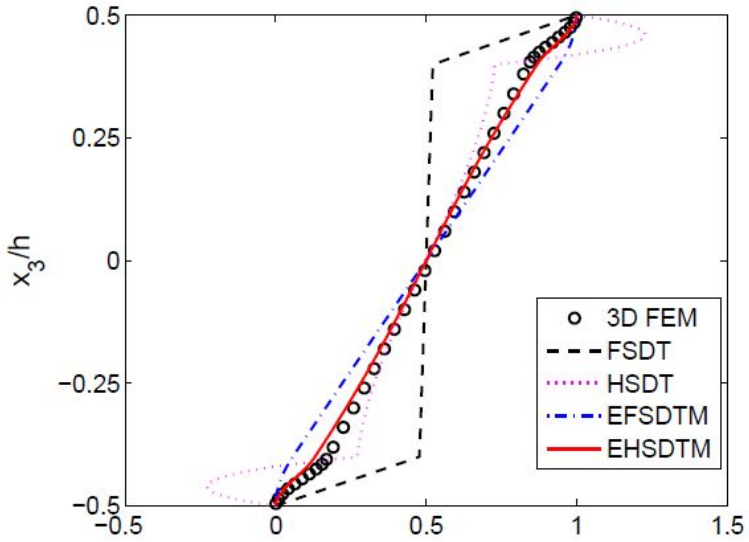

(b) Transverse normal stresses at near free end ($0.87L_1$)

Fig. 3.1.7. Transverse normal stresses of the clamped-free plate for the sandwich (Case 4), S=4

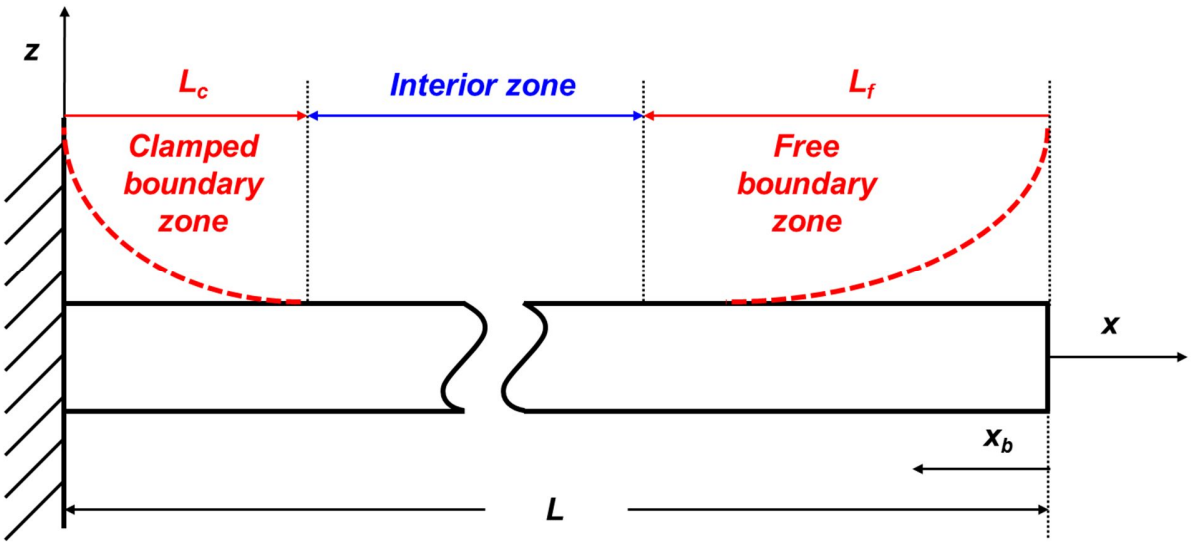

Fig. 3.1.8. Schematic of a semi-infinite clamped-free plate for the boundary layer and interior zone

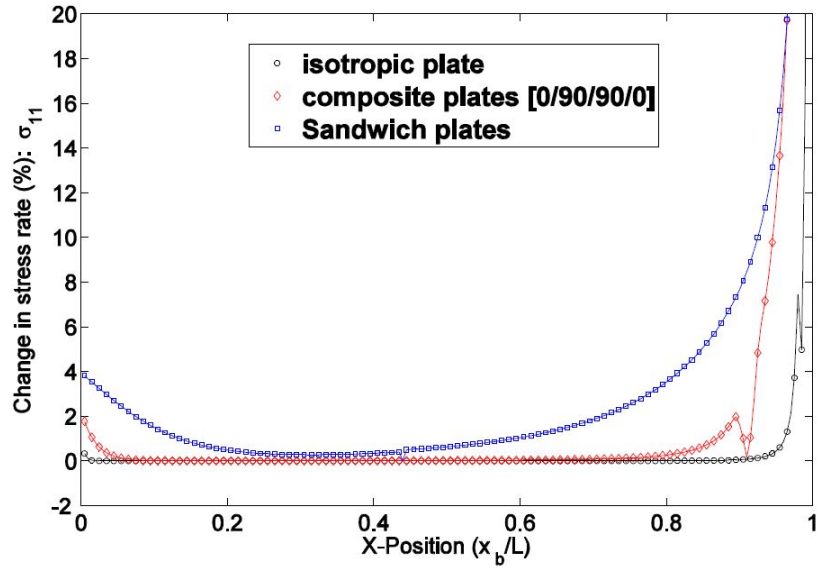

(a) The change in the maximum value of the in-plane stress

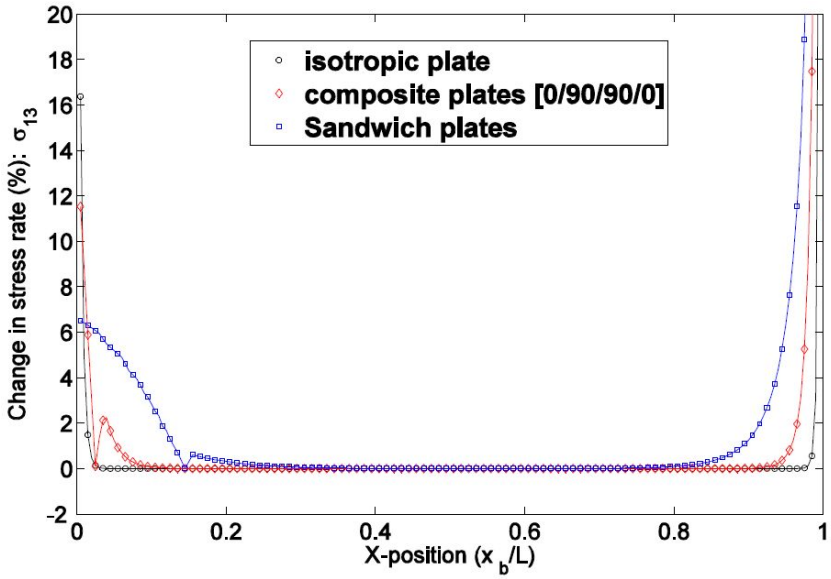

(b) The change in the maximum value of the transverse shear stress

Fig. 3.1.9. The change in the maximum value of the stresses along the axial coordinate (S=40)

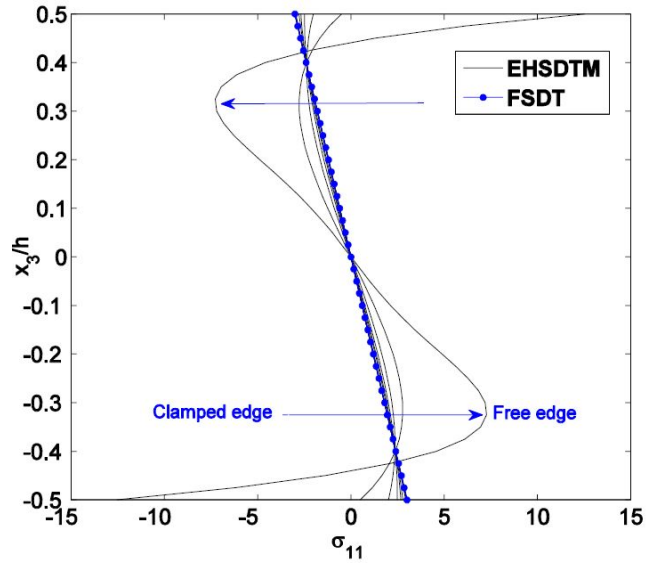

(a) Variations of the in-plane stress

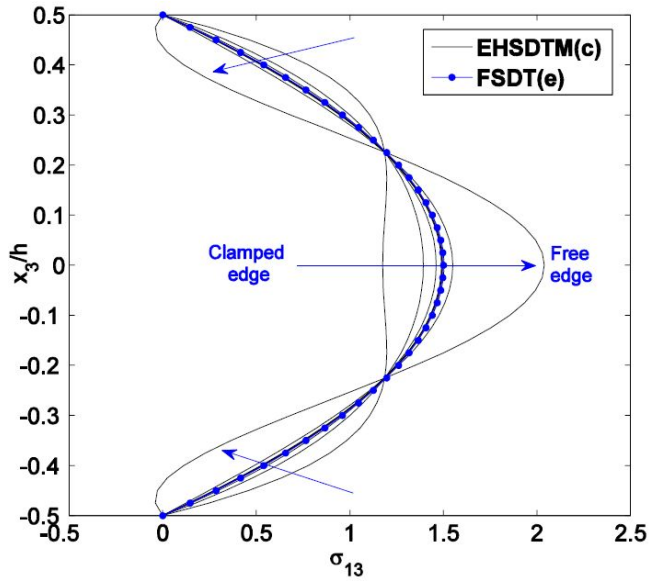

(b) Variations of the transverse shear stress

Fig. 3.1.10. Variations of the through-the-thickness stress distributions of the clamped-free isotropic plate (S=40)

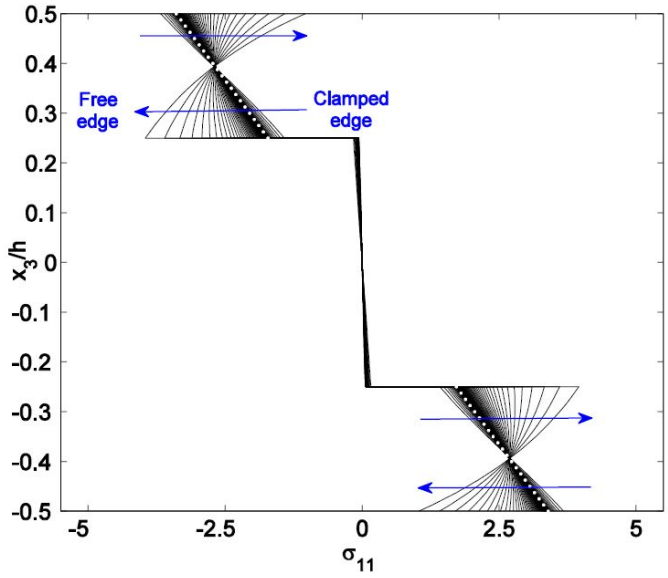

(a) Variations of the in-plane stress

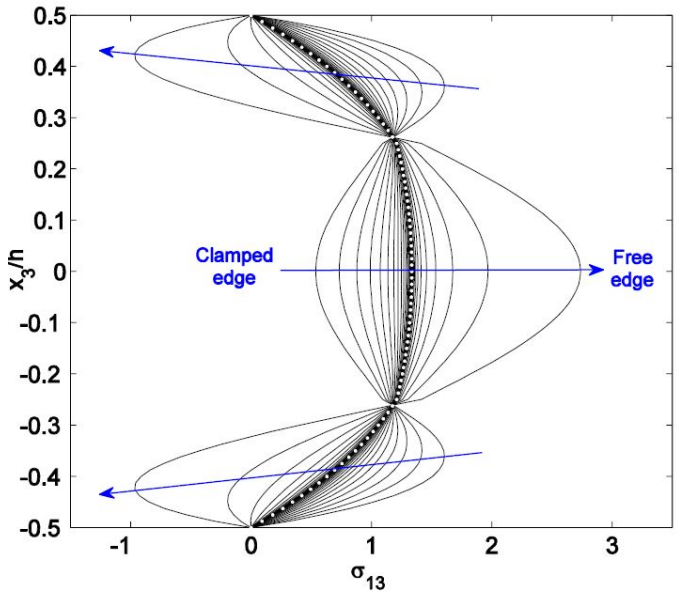

(b) Variations of the transverse shear stress

Fig. 3.1.11. Variations of the through-the-thickness stress distributions of the symmetric cross-ply composite plates (S=40)

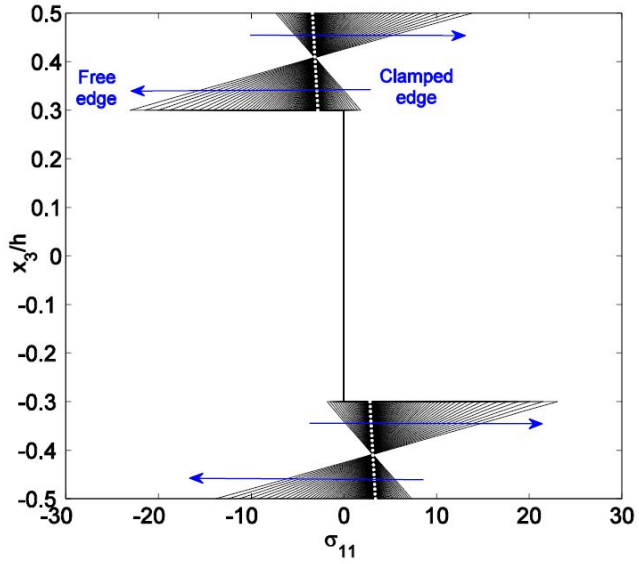

(a) Variations of the in-plane stress

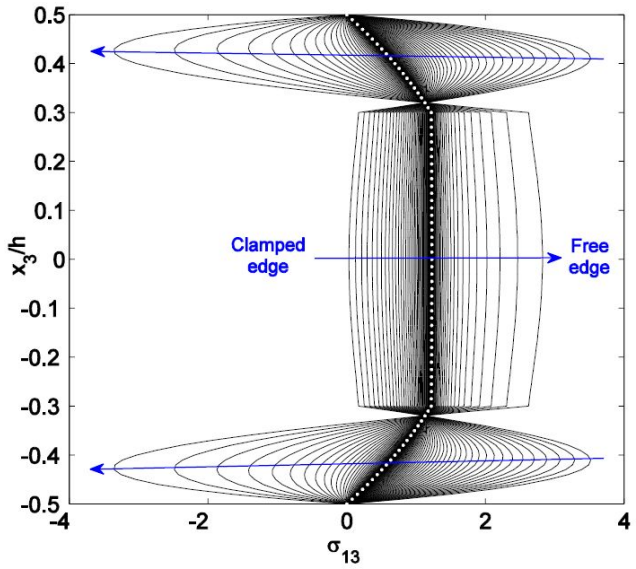

(b) Variations of the transverse shear stress

Fig. 3.1.12. Variations of the through-the-thickness stress distributions of the sandwich plates (S=40)

3.2. Enhanced Lo-Christensen-Wu Theory via the MVT

3.2.1. Literature Review

As mentioned above, with the improvement of technology, advanced composite materials can be applied to severe engineering environment such as high temperature situations. The thermal loading based on rising temperature often represent a crucial factor, which can give a rise to significant thermal deformation and stresses due to the transverse normal deformation effect. Thus, tremendous interest in the thermo-mechanical analysis of the laminated composite plates has emerged in many decades.

Because the previous conventional works (CLPT, FSDT) are inapplicable to accurate analysis of their thermo-elastic response, many researchers focus on their interest in refined higher order shear deformation theories to accurately predict the thermos-elastic response of the thick laminated composite and sandwich structures [23-41].

Rohwer et al estimate thermal stresses of the laminated composite structures under uniform and linear distributed temperature loading through the thickness by extending displacement fields to be third or fifth order [25]. They ascertain the relationships between accuracy of the results and order of the assumed displacement fields, and make sure that conventional FSDT is inadequate for the accurate prediction of the transverse shear stresses under thermal loading conditions.

Zenkour developed unified shear deformable plate theory and predicted the

bending response of the cross-ply laminated composite plates under thermo-mechanical loading conditions [26]. Zenkour showed that the thermo-mechanical behavior of the composite structures can be more accurately characterized by using the higher-order theories. However, the transverse shear stresses demonstrated by unified theory can't satisfy shear continuity conditions across the layer interface. Matsunaga introduced ninth-order theory to analyze thermos-elastic behavior of laminated composite and sandwich plates, and certified the effects of ninth-order displacement fields on predicting thermo-elastic responses [27-29]. Ninth-order theory provides more accurate results, while it needs much more computational resources with increasing the order of displacement fields. Other higher order composite theories which is not mentioned in this paper can be founded in refs. [30-34].

Likewise mechanical loading case, various zig-zag theories are introduced to improve aforementioned deficiencies in analyzing thermo-elastic response of the laminated structures [35-39]. Oh and Cho proposed efficient higher order zig-zag theory (EHOZT) to predict the electro-thermo-mechanical fully coupled behavior of the laminated composite plates [35, 36]. This theory satisfies transverse shear continuity conditions at the layer interfaces as well as shear free conditions at the surfaces of the structures. In addition, transverse displacement field is assumed to be a smooth parabolic distribution to quite well consider transverse normal strain effect. Oh and Cho subsequently applied the EHOZT to three node triangular finite element method, and further extended it to smart composite shell structures [37, 38].

Kapuria and Achary proposed an efficient two dimensional higher order zig-zag

theory for the thermal stress analysis of laminated composite structures by introducing thermal expansion coefficients in their transverse displacement field [39]. This model can consider contribution of the transverse normal strain effect without increasing unknown variables in their displacement fields. However, in case of sandwich plates which contain different thermal expansion coefficients in adjacent layers, transverse displacement continuity conditions at the layer interfaces can't be satisfied automatically.

Zhen et al are attempted to propose an efficient global-local higher order theory by considering global and local variables in their computational process [40, 41]. Thermal contribution can be reasonably considered in this theory by extending transverse displacement field, so it can accurately predict the thermo-elastic behavior of the laminated composite structures. Additionally, the displacement continuity conditions are enforced by using the local variables [41].

These mentioned higher-order theories achieve accurate and reliable prediction of the thermo-mechanical response of the composite structures. However, derivatives of the transverse displacement field were contained in the in-plane displacement fields of mentioned theories, so that these theories require C^1-continuous kinematic interpolation functions in their finite element implementation, which is not available on commercial finite element software. Furthermore, although the mentioned C^0-continuous theories, such as EFSDT, EFSDTM, EHSDTM, etc., are somewhat successful for elasto-static problems, it is not appropriate for thermo-mechanical problems because the significant transverse normal deformation effect is neglected in these theories. This brings us to develop a new enhanced higher-order shear deformation theory by

extending the concept of the strain energy transformation to the LCW. This will allow us to analyze accurately the laminated composite plates under thermal loadings and to investigate the transverse normal effects for the thermo-mechanical behavior.

In this subsection, to address the aforementioned issues, the enhanced LCW theory (ELCWM) via the mixed variational theorem is proposed and tested numerically. The main objective herein is to systematically establish the relationship between the LCW displacement field and the fifth-order zig-zag displacement field, so that one can come up with the LCW-like theory (i.e. ELCWM) incorporating the simplicity of LCW and the accuracy of the fifth-order zig-zag model. The temperature field takes the form of a linear distribution through the thickness of the plate. Finally the results obtained are assessed by comparing them to those reported in the open literature.

3.2.2. Mixed Formulation

To accurately and efficiently analyze the thermo-mechanical response of the laminated composite and sandwich plates, ELCWM is developed in this dissertation via the mixed variational theorem. In the MVT, the three-dimensional Hellinger-Reissner (HR) functional, which is given in Eqs. (1.2.1), is employed to derive the relationships between the independent two fields (conventional LCW and fifth-order zig-zag model).

3.2.2.1. Independent transverse stress fields

A fifth-order zig-zag model is introduced to derive the transverse stress field to be used in Eq. (1.2.1). The displacement field of the fifth-order zigzag model can be expressed as follows:

$$\begin{aligned} u_\alpha^* &= \hat{u}_\alpha^o + \sum_{i=1}^{5} \xi_\alpha^{(i)} x_3^i + \sum_{k=1}^{N-1} S_\alpha^{(k)} (x_3 - x_{3(k)}) H(x_3 - x_{3(k)}), \\ u_3^* &= \hat{u}_3^o + \hat{u}_3^{(1)} x_3 + \hat{u}_3^{(2)} x_3^2, \end{aligned} \tag{3.2.1}$$

where N is the number of layers, $S_\alpha^{(k)}$ and $\mathrm{H}(x_3 - x_{3(k)})$ are the linear zig-zag terms and Heaviside unit step function, respectively. The transverse displacement field of the fifth-order zig-zag model is assumed to be smooth parabolic distribution to efficiently consider contribution of the transverse normal deformation effect. Additionally, the components of the fifth-order zig-zag model are given with superscript $(\bullet)^*$ to clear distinguish between those of conventional LCW and fifth-order zig-zag model.

Applying the transverse shear stress free conditions on top and bottom surface as well as shear continuity conditions at the interfaces between layers [12, 13, 20, 35, 36], the following displacement fields can be derived as follows:.

$$\begin{aligned} u_\alpha^* &= \hat{u}_\alpha^o - \hat{u}_{3,\alpha}^o x_3 - \sum_{i=2}^{3} \frac{1}{i} \hat{u}_{3,\alpha}^{(i-1)} x_3^i + \sum_{i=1}^{3} \Phi_{\alpha\beta}^{(i)} \phi_\beta^{(i)}, \\ u_3^* &= \hat{u}_3^o + \hat{u}_3^{(1)} x_3 + \hat{u}_3^{(2)} x_3^2, \end{aligned} \tag{3.2.2}$$

where

$$\phi_\alpha^{(1)} = \left(3\xi_\alpha^{(3)} + \hat{u}_{3,\alpha}^{(2)}\right),\ \phi_\alpha^{(2)} = \xi_\alpha^{(4)},\ \phi_\alpha^{(3)} = \xi_\alpha^{(5)}, \tag{3.2.3}$$

and

$$\begin{aligned}
\Phi_{\alpha\beta}^{*(1)} &= x_3\left(\frac{1}{2}x_3^2 - \frac{h^2}{4}\right)\delta_{\alpha\beta} + \sum_{k=1}^{N-1} a_{\alpha\beta}^{(k)} f(x_3, x_{3(k)}),\\
\Phi_{\alpha\beta}^{*(2)} &= x_3^2\left(x_3^2 - \frac{h^2}{2}\right)\delta_{\alpha\beta} + \sum_{k=1}^{N-1} b_{\alpha\beta}^{(k)} f(x_3, x_{3(k)}),\\
\Phi_{\alpha\beta}^{*(3)} &= x_3\left(x_3^4 - \frac{5h^2}{16}\right)\delta_{\alpha\beta} + \sum_{k=1}^{N-1} c_{\alpha\beta}^{(k)} f(x_3, x_{3(k)}),\\
\Phi_{\alpha\beta}^{(i)} &= \Phi_{\alpha\beta}^{*(i)} - \frac{1}{h}\left\langle \Phi_{\alpha\beta}^{*(i)} \right\rangle, \quad \left\langle \bullet \right\rangle = \int_{-h/2}^{+h/2} \bullet\, dx_3,
\end{aligned} \tag{3.2.4}$$

where $\delta_{\alpha\beta}$ is the Kronecker delta function. The terms of $a_{\alpha\beta}^{(k)}, b_{\alpha\beta}^{(k)}$ and $c_{\alpha\beta}^{(k)}$ are function of the material properties which can enforce the transverse shear continuity conditions on layer interfaces, and the derivation of these coefficients can be found in Refs. [12, 13, 20, 35, 36], and

$$f(x_3, x_{3(k)}) = -\frac{x_3}{2} - \frac{x_3^2}{2h} + (x_3 - x_{3(k)})H(x_3 - x_{3(k)}). \tag{3.2.5}$$

From Eq. (3.2.2), one can now obtain the corresponding strains as follows:

$$\begin{aligned}
\varepsilon_{\alpha\beta}^{*} &= \varepsilon_{\alpha\beta}^{*(0)} + \sum_{i=1}^{3} \varepsilon_{\alpha\beta}^{*(i)} x_3^i + \frac{1}{2}\sum_{i=1}^{3}\left(\Phi_{\alpha\gamma}^{(i)}\phi_{\gamma,\beta}^{(i)} + \Phi_{\beta\omega}^{(i)}\phi_{\omega,\alpha}^{(i)}\right),\\
\gamma_{\alpha 3}^{*} &= \sum_{i=1}^{3} \Phi_{\alpha\beta,3}^{(i)}\phi_\beta^{(i)},\\
\varepsilon_{33}^{*} &= \varepsilon_{33}^{*(0)} + x_3\varepsilon_{33}^{*(1)}.
\end{aligned} \tag{3.2.6}$$

where

$$\varepsilon_{\alpha\beta}^{*(0)}=\frac{1}{2}\left(\hat{u}_{\alpha,\beta}^{o}+\hat{u}_{\beta,\alpha}^{o}\right),\quad \varepsilon_{\alpha\beta}^{*(i)}=-\frac{1}{i}\left(\hat{u}_{3,\alpha\beta}^{(i-1)}\right),$$
$$\varepsilon_{33}^{*(0)}=\hat{u}_{3}^{(1)},\quad \varepsilon_{33}^{*(1)}=2\hat{u}_{3}^{(2)}. \tag{3.2.7}$$

Equation (3.2.6) allows us to derive the transverse stress field via the constitutive equation in Eq. (1.2.2) as follows:

$$\sigma_{\alpha 3}^{*}=C_{\alpha 3\beta 3}\gamma_{\beta 3}^{*},$$
$$\sigma_{33}^{*}=C_{33\alpha\beta}\left(\varepsilon_{\alpha\beta}^{*}-\alpha_{\alpha\beta}\theta\right)+C_{3333}\left(\varepsilon_{33}^{*}-\alpha_{33}\theta\right). \tag{3.2.8}$$

3.2.2.2. Displacement fields

The displacement field of LCW [9], which is to be used for the strain and displacement fields in MVT, which is Eq. (1.2.1), is given as follows:

$$u_{\alpha}=u_{\alpha}^{o}+\sum_{i=1}^{3}\psi_{\alpha}^{(i)}x_{3}^{i},$$
$$u_{3}=u_{3}^{o}+u_{3}^{(1)}x_{3}+u_{3}^{(2)}x_{3}^{2}. \tag{3.2.9}$$

which is often referred to as a conventional Lo-Christensen-Wu theory or simply LCW. In what follows, it will be shown that the variables given in Eq. (3.2.9) become the primary variables in the three-dimensional Hellinger-Reissner functional of Eq. (1.2.1). By employing the displacement fields given in Eq. (3.2.9), corresponding strain fields can be subsequently derived as follows:

$$\varepsilon_{\alpha\beta}=\varepsilon_{\alpha\beta}^{(0)}+x_{3}\varepsilon_{\alpha\beta}^{(1)}+x_{3}^{2}\varepsilon_{\alpha\beta}^{(2)}+x_{3}^{3}\varepsilon_{\alpha\beta}^{(3)},$$
$$\gamma_{\alpha 3}=\gamma_{\alpha 3}^{(0)}+x_{3}\gamma_{\alpha 3}^{(1)}+x_{3}^{2}\gamma_{\alpha 3}^{(2)}, \tag{3.2.10}$$
$$\varepsilon_{33}=\varepsilon_{33}^{(0)}+x_{3}\varepsilon_{33}^{(1)}.$$

where

$$\varepsilon_{\alpha\beta}^{(0)} = \frac{1}{2}\left(u_{\alpha,\beta}^{o} + u_{\beta,\alpha}^{o}\right), \quad \varepsilon_{\alpha\beta}^{(i)} = \frac{1}{2}\left(\psi_{\alpha,\beta}^{(i)} + \psi_{\beta,\alpha}^{(i)}\right), \quad (i = 1,2,3)$$
$$\gamma_{\alpha 3}^{(0)} = \psi_{\alpha}^{(1)} + u_{3,\alpha}^{o}, \quad \gamma_{\alpha 3}^{(1)} = 2\psi_{\alpha}^{(1)} + u_{3,\alpha}^{(1)}, \quad \gamma_{\alpha 3}^{(2)} = 3\psi_{\alpha}^{(2)} + u_{3,\alpha}^{(2)}, \tag{3.2.11}$$
$$\varepsilon_{33}^{(0)} = u_{3}^{(1)}, \quad \varepsilon_{33}^{(1)} = 2u_{3}^{(2)}.$$

From the Eq. (3.2.9), in-plane stress to be used in Eq. (1.2.1) can be expressed by

$$\sigma_{\alpha\beta} = C_{\alpha\beta\gamma\omega}\left(\varepsilon_{\gamma\omega} - \alpha_{\gamma\omega}\theta\right) + C_{\alpha\beta 33}\left(\varepsilon_{33} - \alpha_{33}\theta\right). \tag{3.2.12}$$

3.2.2.3. Relationships between the two theories

The equation presented in the second line of Eq. (1.2.1) plays a crucial role to derive the enhanced LCW model. In fact, it provides the relationships between the two theories (i.e. conventional LCW and the fifth-order zigzag models) or the constraint to connect the displacement field and the transverse stress field.

This constraint equation is given by

$$\int_{V}\left[(\gamma_{\alpha 3} - \gamma_{\alpha 3}^{*})\delta\sigma_{\alpha 3}^{*} + (\varepsilon_{33} - \varepsilon_{33}^{*})\delta\sigma_{33}^{*}\right]dV = 0, \tag{3.2.13}$$

where the second term is zero because the transverse normal strains in the two theories are identical. This also implies that the transverse normal stress can be approximated by that of the conventional LCW. That is

$$\varepsilon_{33}^{*} = \varepsilon_{33} \rightarrow \sigma_{33}^{*} \approx \sigma_{33}. \tag{3.2.14}$$

Then we have the equation to be solved as follows:

$$\int_V \left[(\gamma_{\alpha 3} - \gamma^*_{\alpha 3}) \delta \sigma^*_{\alpha 3} \right] dV = 0, \tag{3.2.15}$$

in which the transverse shear strains based on the independent two theories are given in Eqs. (3.2.6) and (3.2.10), and the transverse shear stress of fifth-order zig-zag model is given in Eq. (3.2.8).

Substituting these equations into Eq. (3.2.15) yields

$$\begin{Bmatrix} \phi_\beta^{(1)} \\ \phi_\beta^{(2)} \\ \phi_\beta^{(3)} \end{Bmatrix} = [\Gamma_{\beta 3 \lambda 3}] \begin{Bmatrix} \gamma_{\lambda 3}^{(0)} \\ \gamma_{\lambda 3}^{(1)} \\ \gamma_{\lambda 3}^{(2)} \end{Bmatrix}, \tag{3.2.16}$$

where

$$\begin{aligned} &[\Gamma_{\beta 3 \lambda 3}] = [D_{\beta 3 \gamma 3}]^{-1} [B_{\gamma 3 \lambda 3}]^T, \\ &[D_{\beta 3 \gamma 3}]_{ij} = \left\langle \Phi^{(i)}_{\beta \lambda, 3} C_{\lambda 3 \mu 3} \Phi^{(j)}_{\mu \gamma, 3} \right\rangle, \\ &[B_{\gamma 3 \lambda 3}]_{ij} = \left\langle x_3^{i-1} C_{\gamma 3 \mu 3} \Phi^{(j)}_{\mu \lambda, 3} \right\rangle. \ (i, j = 1, 2, 3) \end{aligned} \tag{3.2.17}$$

Equation (3.2.16) implies that the variables of the fifth-order zig-zag theory can be expressed in terms of those of the conventional LCW.

In the displacement field of the fifth-order zig-zag model, there is still an unknown variable, i.e., the mid-plane stretching term. In order to express Eq. (1.2.1) in terms of the variables given in Eq. (3.2.9) completely, one needs to determine it in advance. Here we employ the least square approximation for the in-plane displacement [20]. Then one can write

$$\int_{-h/2}^{+h/2} \min_{u_\alpha^o} (u_\alpha^* - u_\alpha)^2 dx_3 = 0, \tag{3.2.18}$$

which will render relationship of the mid-plane stretching terms as following forms:

$$\hat{u}_\alpha^o = u_\alpha^o + \frac{h^2}{24}\gamma_{\alpha 3}^{(1)}, \tag{3.2.19}$$

where

$$\gamma_{\alpha 3}^{(1)} = \left(2\psi_\alpha^{(2)} + u_{3,\alpha}^{(1)}\right). \tag{3.2.20}$$

By substituting Eq. (3.2.19) into Eq. (3.2.2), one can now express all the variables in the fifth-order zigzag theory in terms of the variables of the conventional LCW.

3.2.3. Enhanced Lo-Christensen-Wu theory based on the MVT

In subsection 3.3.2, the constraint equations are solved, and therefore, they are dismissed in Eq. (1.2.1). By assuming that the prescribed traction is applied to x_3 direction only, the remaining equation is given by

$$\int_V \left[\sigma_{\alpha\beta}\delta\varepsilon_{\alpha\beta} + \sigma_{\alpha 3}^*\delta\gamma_{\alpha 3} + \sigma_{33}\delta\varepsilon_{33}\right]dV - \int_{S_\sigma} \tilde{t}_3\ \delta u_3 dS_\sigma = 0. \tag{3.2.21}$$

Notice here that the transverse normal stress is regarded as the displacement-based one because of Eq. (3.2.14). Thus the transverse shear stress only comes

from the independent stress field. This greatly simplifies the governing equations to be derived.

By applying the integration by parts and defining the stress resultants, the equilibrium equations for the problem are obtained as follows:

$$\begin{aligned}
\delta u_\alpha^o &: N_{\alpha\beta,\beta} = 0, \\
\delta \psi_\alpha^{(1)} &: M_{\alpha\beta,\beta} - Q_\alpha = 0, \\
\delta \psi_\alpha^{(2)} &: R_{\alpha\beta,\beta}^{(2)} - 2Q_\alpha^{(1)} = 0, \\
\delta \psi_\alpha^{(3)} &: R_{\alpha\beta,\beta}^{(3)} - 3Q_\alpha^{(2)} = 0, \\
\delta u_3^o &: Q_{\alpha,\alpha} + \tilde{t}_3 = 0, \\
\delta u_3^{(1)} &: Q_{\alpha,\alpha}^{(1)} + \tfrac{h}{2}\tilde{t}_3 - N_{33} = 0, \\
\delta u_3^{(2)} &: Q_{\alpha,\alpha}^{(2)} + \tfrac{h^2}{4}\tilde{t}_3 - 2M_{33} = 0.
\end{aligned} \tag{3.2.22}$$

In addition, the associated boundary conditions are given by

$$\begin{aligned}
\delta u_\alpha^o = 0 \ \text{ or } \ N_{\alpha\beta}\nu_\beta = 0, \\
\delta \psi_\alpha^{(1)} = 0 \ \text{ or } \ M_{\alpha\beta}\nu_\beta = 0, \\
\delta \psi_\alpha^{(2)} = 0 \ \text{ or } \ R_{\alpha\beta}^{(2)}\nu_\beta = 0, \\
\delta \psi_\alpha^{(3)} = 0 \ \text{ or } \ R_{\alpha\beta}^{(3)}\nu_\beta = 0, \\
\delta u_3^o = 0 \ \text{ or } \ Q_\alpha\nu_\alpha = 0, \\
\delta u_3^{(1)} = 0 \ \text{ or } \ Q_\alpha^{(1)}\nu_\alpha = 0, \\
\delta u_3^{(2)} = 0 \ \text{ or } \ Q_\alpha^{(2)}\nu_\alpha = 0.
\end{aligned} \tag{3.2.23}$$

3.2.3.1. Plate constitutive equations

As listed in Eq. (23.2.22, there are many stress resultants that should be expressed in terms of the variables of the conventional LCW. The constitutive equations are then summarized as follows:

$$
\begin{aligned}
N_{\alpha\beta} &= \sum_{i=0}^{3}\left\langle C_{\alpha\beta\gamma\omega}x_3^i\right\rangle\varepsilon_{\gamma\omega}^{(i)} + \sum_{j=0}^{2}\left\langle C_{\alpha\beta 33}x_3^j\right\rangle\varepsilon_{33}^{(j)} - N_{\alpha\beta}^{\theta},\\
M_{\alpha\beta} &= \sum_{i=0}^{3}\left\langle C_{\alpha\beta\gamma\omega}x_3^{i+1}\right\rangle\varepsilon_{\gamma\omega}^{(i)} + \sum_{j=0}^{2}\left\langle C_{\alpha\beta 33}x_3^{j+1}\right\rangle\varepsilon_{33}^{(j)} - M_{\alpha\beta}^{\theta},\\
R_{\alpha\beta}^{(2)} &= \sum_{i=0}^{3}\left\langle C_{\alpha\beta\gamma\omega}x_3^{i+2}\right\rangle\varepsilon_{\gamma\omega}^{(i)} + \sum_{j=0}^{2}\left\langle C_{\alpha\beta 33}x_3^{j+2}\right\rangle\varepsilon_{33}^{(j)} - R_{\alpha\beta}^{(2)\theta},\\
R_{\alpha\beta}^{(3)} &= \sum_{i=0}^{3}\left\langle C_{\alpha\beta\gamma\omega}x_3^{i+3}\right\rangle\varepsilon_{\gamma\omega}^{(i)} + \sum_{j=0}^{2}\left\langle C_{\alpha\beta 33}x_3^{j+3}\right\rangle\varepsilon_{33}^{(j)} - R_{\alpha\beta}^{(3)\theta},
\end{aligned}
\tag{3.2.24}
$$

where

$$
\begin{aligned}
N_{\alpha\beta}^{\theta} &= \left\langle C_{\alpha\beta\gamma\omega}\alpha_{\gamma\omega}\theta\right\rangle + \left\langle C_{\alpha\beta 33}\alpha_{33}\theta\right\rangle,\\
M_{\alpha\beta}^{\theta} &= \left\langle x_3 C_{\alpha\beta\gamma\omega}\alpha_{\gamma\omega}\theta\right\rangle + \left\langle x_3 C_{\alpha\beta 33}\alpha_{33}\theta\right\rangle,\\
R_{\alpha\beta}^{(2)\theta} &= \left\langle x_3^2 C_{\alpha\beta\gamma\omega}\alpha_{\gamma\omega}\theta\right\rangle + \left\langle x_3^2 C_{\alpha\beta 33}\alpha_{33}\theta\right\rangle,\\
R_{\alpha\beta}^{(3)\theta} &= \left\langle x_3^3 C_{\alpha\beta\gamma\omega}\alpha_{\gamma\omega}\theta\right\rangle + \left\langle x_3^3 C_{\alpha\beta 33}\alpha_{33}\theta\right\rangle.
\end{aligned}
\tag{3.2.25}
$$

These equations are the same as those defined in the conventional LCW, whereas the transverse shear stress resultants are not, which are given as follows:

$$
\begin{aligned}
Q_{\alpha} &= \sum_{j=0}^{2}[\hat{G}_{\alpha 3\beta 3}]_{1j}\gamma_{\beta 3}^{(j)},\\
Q_{\alpha}^{(i-1)} &= \sum_{j=0}^{2}[\hat{G}_{\alpha 3\beta 3}]_{ij}\gamma_{\beta 3}^{(j)},\ (i=2,3)
\end{aligned}
\tag{3.2.26}
$$

where

$$
[\hat{G}_{\alpha 3\beta 3}] = [B_{\alpha 3\mu 3}][D_{\mu 3\lambda 3}]^{-1}[B_{\lambda 3\beta 3}]^{T}. \tag{3.2.27}
$$

According to Eq. (3.2.14), the transverse normal stress resultants based on the conventional LCW are defined by

$$
\begin{aligned}
N_{33} &= \sum_{i=0}^{3} \left\langle C_{33\gamma\omega} x_3^i \right\rangle \varepsilon_{\gamma\omega}^{(i)} + \sum_{j=0}^{2} \left\langle C_{3333} x_3^j \right\rangle \varepsilon_{33}^{(j)} - N_{33}^{\theta}, \\
M_{33} &= \sum_{i=0}^{3} \left\langle C_{33\gamma\omega} x_3^{i+1} \right\rangle \varepsilon_{\gamma\omega}^{(i)} + \sum_{j=0}^{2} \left\langle C_{3333} x_3^{j+1} \right\rangle \varepsilon_{33}^{(j)} - M_{33}^{\theta},
\end{aligned}
\tag{3.2.28}
$$

where

$$
\begin{aligned}
N_{33}^{\theta} &= \left\langle C_{33\gamma\omega} \alpha_{\gamma\omega} \theta \right\rangle + \left\langle C_{3333} \alpha_{33} \theta \right\rangle, \\
M_{33}^{\theta} &= \left\langle x_3 C_{33\gamma\omega} \alpha_{\gamma\omega} \theta \right\rangle + \left\langle x_3 C_{3333} \alpha_{33} \theta \right\rangle.
\end{aligned}
\tag{3.2.29}
$$

3.2.3.2. Displacement and stress recovery

Substituting Eqs. (3.2.24), (3.2.26) and (3.2.28) into Eq. (3.2.22) yields the governing equations to be solved for the enhanced LCW theory. As compared to the conventional LCW, they take the complicated forms. However, the primary variables and the strain energy (except for the stiffness) are the same as those of the conventional LCW while enhancing its performance. Here it should be noted that the assumption we made is the equivalence of the transverse normal strain between the two theories, and therefore, the transverse normal stress. This does not necessarily mean that the transverse normal stresses obtained by the two theories are identical, since the transverse normal stress will be evaluated by using the three-dimensional stress equilibrium equations.

Once the governing equations of the enhanced LCW are solved, one can now recover the displacements and stresses to further improve the predictions. For instance, the displacement field of Eq. (3.2.2) and the transverse stress field of Eq. (3.2.8) can be obtained by employing the relationships between the two

theories (i.e. conventional LCW and the fifth-order zigzag models) as following forms

$$
\begin{aligned}
u_\alpha^* &= u_\alpha^o + \frac{h^2}{24}\gamma_{3\alpha}^{(1)} - u_{3,\alpha}^o x_3 - \sum_{i=2}^{3}\frac{1}{i}u_{3,\alpha}^{(i-1)}x_3^i + \sum_{i=1}^{3}\Phi_{\alpha\beta}^{(i)}\phi_\beta^{(i)} - c_\alpha, \\
u_3^* &= u_3^o + u_3^{(1)}x_3 + u_3^{(2)}x_3^2,
\end{aligned}
\tag{3.2.30}
$$

where the terms $\phi_\beta^{(i)}$, which are the variables of the fifth order zig-zag model, can be expressed in terms of the conventional LCW-based variables by using the constraint relationship of Eq. (3.2.16). In Eq. (3.2.30), in-plane correction factors, c_α, are newly considered to satisfy the in-plane equilibrium equations and their detailed expression for the derivation process of the in-plane correction factors are given in the **Appendix H**.

In this procedure, the constraint equations of Eq.(3.2.15) and the least square approximation of Eq.(3.2.19) play a significant role to recover both the stresses and displacements. This procedure is outlined in **Fig. 3.2.1**.

3.2.4. Numerical investigation and Discussion

For cross-ply lay-up rectangular composite and sandwich plates, the analytical solutions are derived in this section to demonstrate the efficiency and accuracy of the proposed theory (ELCWM). In these cases, there are no bending-shear and stretching-shear couplings. The temperature is linearly prescribed through the thickness of the plate, which is given as:

$$\theta(x_i) = \left(\overline{T}_0 + x_3\overline{T}_1\right)\sin(px)\sin(py), \tag{3.2.31}$$

where

$$p = \frac{\pi}{L_1},\ q = \frac{\pi}{L_2}. \tag{3.2.32}$$

The mechanical loading t_3 is prescribed on the top surface, which takes the form of

$$t_3(x_\alpha, \tfrac{h}{2}) = \bar{Q}\sin(px)\sin(py). \tag{3.2.33}$$

The primary variables of the enhanced LCW are assumed to have double trigonometric series for simply supported boundary conditions as follows:

$$\begin{aligned}
[u_1^o, \psi_1^{(i)}] &= [U, \Psi_1^{(i)}]\cos(px)\sin(py), \\
[u_2^o, \psi_2^{(i)}] &= [V, \Psi_2^{(i)}]\sin(px)\cos(py), \\
[u_3^o, u_3^{(\alpha)}] &= [W, W^{(\alpha)}]\sin(px)\sin(py),
\end{aligned} \tag{3.2.34}$$

where the superscript i takes the values of 1,2,3, while the superscript α takes the values of 1,2.

Substituting Eqs. (3.2.31), (3.2.33) and (3.2.34) into Eq. (3.2.22) via Eqs. (3.2.24), (3.2.26) and (3.2.28) yields the simultaneous algebraic equation as follows:

$$L_{ij}X_j = F_i, \quad (i, j = 1,2,\cdots,11) \tag{3.2.35}$$

where the X_j is the vector of unknown variables, and it can be expressed as follows:

$$X = \left\lfloor U, V, \Psi_1^{(1)}, \Psi_2^{(1)}, \Psi_1^{(2)}, \Psi_2^{(2)}, \Psi_1^{(3)}, \Psi_2^{(3)}, W, W^{(1)}, W^{(2)} \right\rfloor^T, \tag{3.2.36}$$

The detailed expression of the symmetric operator L_{ij} and loading vector F_i are given in the **Appendix I**.

To evaluate accuracy and efficiency of the thermo-mechanical prediction for rectangular laminated composite and sandwich plates using proposed theory, several cases of numerical examples are considered and discussed in this section. All of the example models assume the aspect ratio as $L_1 = L_2$, and the material properties of the laminated composite and sandwich plates which are used in this study are given as follows:

-Material(1) for the laminated composite plates:

$$\begin{aligned} &E_L / E_T = 25, \quad G_{LT} / E_T = 0.5, \quad G_{TT} / E_T = 0.2, \\ &v_{LT} = v_{TT} = 0.25, \quad \alpha_T / \alpha_L = 1125, \end{aligned} \tag{3.2.37}$$

-Material(2) for the laminated composite plates:

$$
\begin{aligned}
&E_L / E_T = 15, \quad G_{LT} / E_T = 0.5, \\
&G_{TT} / E_T = 0.3356, \quad v_{LT} = 0.3, \quad v_{TT} = 0.49, \\
&\alpha_L = 0.015 \cdot 10^{-6} / K, \quad \alpha_T = 10^{-6} / K,
\end{aligned}
\tag{3.2.38}
$$

- material(3) for the sandwich plates:

Face sheets:

$$
\begin{aligned}
&E_L = 200Gpa, \quad E_T = 8Gpa, \\
&G_{LT} = 5Gpa, \quad G_{TT} = 2.2Gpa, \\
&v_{LT} = 0.25, \quad v_{TT} = 0.35, \\
&\alpha_L = -2 \cdot 10^{-8} / K, \quad \alpha_T = 50 \cdot 10^{-6} / K,
\end{aligned}
\tag{3.2.39}
$$

Core material:

$$
\begin{aligned}
&E_x = E_y = 1Gpa, \quad E_z = 2Gpa, \\
&G_{xy} = 3.7Gpa, \quad G_{xz} = G_{yz} = 0.8Gpa, \\
&v_{xy} = 0.35, \quad v_{xz} = v_{yz} = 0.25, \\
&\alpha_x = \alpha_y = \alpha_z = 30 \cdot 10^{-6} / K,
\end{aligned}
\tag{3.2.40}
$$

where subscript L represents a parallel direction to the fibers, while T denotes a transverse direction to the fibers. v_{LT} is a Poisson's ratio, and α_L, α_T are the thermal expansion coefficients. The results of the proposed theory are compared with those obtained by other theories as well as the exact solutions. The exact solutions of the thermo-mechanical problems developed by Pagano are reproduced and used as the benchmark solutions. In conventional FSDT, a shear correction factor is assumed to be 5/6. In order to facilitate comparison of their

accuracy and performance, the results of displacement and stress are normalized according to the case of the numerical examples.

3.2.4.1. Mechanical loading problem

Several cases of laminated composite and sandwich plates subjected to a lateral sinusoidal upward mechanical loading ($\bar{Q} \neq 0, \bar{T}_0 = 0, \bar{T}_1 = 0$) are considered to validate accuracy of the present theory. The results are compared with those obtained by FSDT, HSDT, LCW, EHOPT, EFSDT and also with benchmark solutions (the exact solution developed by Pagano). In the pure mechanical loading problems, relatively thick plates models ($S = L_1/h = L_2/h = 4$) are considered and material properties are given according to material (1) or (3).
The results obtained herein are normalized as follows:

$$u_\alpha = \frac{E_T \cdot u_\alpha^*}{\bar{Q} \cdot h \cdot S^3},\ \sigma_{\alpha\beta} = \frac{\sigma_{\alpha\beta}^*}{\bar{Q} \cdot S^2},\ \sigma_{3\alpha} = \frac{\sigma_{3\alpha}^*}{\bar{Q} \cdot S}. \tag{3.2.41}$$

First of all, the normalized distributions of displacements and stresses for symmetric cross-ply laminated composite plates [$0^o/90^o/0^o$] of material (1) have been plotted in **Figs. 3.2.2-3.2.5**. The distributions of displacements are shown in **Fig. 3.2.2**. From **Fig. 3.2.2**, one can be observed that the result of displacement obtained by present theory (ELCWM) agree well with the exact solutions. Although zig-zag distributions with slope discontinuities at interfaces have been well described by EHOPT, EFSDT and ELCWM which are contained

zig-zag displacement fields, present ELCWM provides most accurate solution which is substantially coincides with the exact solutions. **Fig. 3.2.3** shows the distributions of in-plane stresses. As shown in **Fig. 3.2.3**, present result of σ_{11} yields indistinguishable result in compared with the exact solution which is discontinuous distribution at interfaces. And it can be also seen that results of the EHOPT and EFSDT are fairly well captured discontinuous distributions of in-plane stresses. However, LCW, HSDT and FSDT provide somewhat inaccurate distributions of in-plane stress. And the results of transverse shear stresses have been plotted in **Figs. 3.2.4 and 3.2.5**. Distributions of the transverse shear stresses can be obtained in a twofold manner: one way is based on the constitutive approach and the other way is based on equilibrium approach. Results of transverse shear stresses obtained by direct constitutive approach are presented in **Fig. 3.2.4**, and those obtained by equilibrium approach are shown in **Fig. 3.2.5**. The equilibrium approach can provides much more accurate results than direct constitutive approach, however it requires the higher derivative terms which cause a numerical problem in calculation process. From **Fig. 3.2.4**, it can be found that the results of EHOPT, EFSDT and ELCWM can satisfy the transverse shear stress conditions which are not satisfied by LCW, HSDT and FSDT. It is noteworthy that the present theory provides attractive advantage because the result of present theory based on direct constitutive equation gives quite accurate distributions of transverse shear stresses. The kinky distribution of transverse shear stress can be well captured by EHOPT, EFSDT and ELCWM in **Fig. 3.2.5**, while LCW, HSDT and FSDT cannot describe such a kinky

distribution. And the present theory gives a best compromised result which coincides with the exact solution.

In addition, mechanical behaviors of anti-symmetric cross-ply laminated composite plates $[0^o/90^o/0^o/90^o]$ of material (1) have been analyzed and corresponding results of displacements and stresses are plotted in **Figs. 3.2.6-3.2.9**. The distributions of displacements and in-plane stresses are shown in **Figs. 3.2.6 and 3.2.7**, respectively. As shown in **Figs. 3.2.6 and 3.2.7**, it can be observed that the results of EHOPT, EFSDT and ELCWM which are contained zig-zag displacement fields can provide reliable distributions by capturing the unsymmetrical zig-zag shape of displacement as well as the discontinuous shape of in-plane stresses. However, the results of LCW, HSDT and FSDT provide somewhat inaccurate results. Numerical results show that present results provide most accurate solution which is remarkably consistent with the exact solutions. Variations of the transverse shear stresses are illustrated in **Figs. 3.2.8 and 3.2.9**. **Fig. 3.2.8** represents distribution of the transverse shear stresses obtained by direct constitutive approach and those obtained by equilibrium approach are shown in **Fig. 3.2.9**. For results in **Fig. 3.2.8**, in common with symmetric cross-ply case, the results of LCW, HSDT and FSDT can't satisfy the transverse shear stress conditions. However, it can be seen that the results of the present theory provides quite accurate distributions of transverse shear stresses. In **Fig. 3.2.9**, results of EHOPT, EFSDT and ELCWM precisely describe the kinky distribution of transverse shear stress. Furthermore, it can be observed that the results of present theory match the exact solutions with excellent accuracy.

To further investigate the mechanical behavior of the laminated structures, a sandwich plate $[0^o/core/90^o]$ of material (3) with the thickness of each face

sheet that equals to h/5 is considered. **Figs. 3.2.10 and 3.2.11** compare normalized distributions of the displacements and in-plane stresses, respectively. From the results presented above, EHOPT, EFSDT and ELCWM among others capture well the severe zig-zag variation of displacement and discontinuous distribution of the in-plane stresses. It can be shown that the results of presented theory give best compromised performance in terms of accuracy and efficiency in compared with the exact solutions. Results of transverse shear stresses obtained by direct constitutive approach and equilibrium approach are plotted in **Figs. 3.2.12 and 3.2.13**, respectively. From these results, it can be found that the results of present ELCWM in **Figs. 3.2.12 and 3.2.13** are in excellent agreement with the exact solution and the results of EHOPT, EFSDT based on equilibrium approach are fairly-well capture the kinky shape of transverse shear stress.

3.2.4.2. Thermal loading problem

To validate accuracy of the present theory for the thermo-elastic response, some cases of laminated composite and sandwich plates under thermal loading are also analyzed. The results of present theory are compared to the exact solutions as well as to those obtained by some theories which are selected for comparison in the pure mechanical loading problem. In the thermal loading problem, relatively thick plates models ($S=L_1/h=L_2/h=5$) are considered and material properties are given according to material (2) or (3).

The results obtained herein are normalized as follows:

$$u_\alpha = \frac{u_\alpha^*}{\alpha_L \cdot h \cdot S}, \quad \sigma_{\alpha\beta} = \frac{\sigma_{\alpha\beta}^*}{\alpha_L \cdot E_T}, \quad \sigma_{3\alpha} = \frac{\sigma_{3\alpha}^*}{\alpha_L \cdot E_T}. \tag{3.2.42}$$

Laminated cross-ply composite and sandwich plates subjected to thermal loading of uniform temperature ($\bar{Q}=0, \bar{T}_0 \neq 0, \bar{T}_1 = 0$) are considered. Normalized distributions of in-plane and transverse shear stresses for a single layer composite plate of material (2) are shown in **Fig. 3.2.14 and 3.2.15**. The distributions of transverse shear stresses obtained by direct constitutive approach are omitted in thermal loading problems. From these figures, it can be seen that the results of LCW and present ELCWM can accurately predict both the cubic distribution of the transverse shear stress as well as the parabolic distribution of the in-plane stresses as compared to the exact solutions. However, results obtained by other theories, which neglected the contribution of the transverse normal deformation effect, entirely fail to describe distributions of in-plane and transverse shear stresses for the single layer composite plate under uniform temperature loading. **Fig. 3.2.16 and 3.2.17** present the normalized displacements and transverse shear stresses of anti-symmetric cross-ply laminated composite plates [$0^o / 90^o / 0^o / 90^o$] of material (2). From the results, the asymmetrical parabolic distributions of the displacements and zig-zag variation of transverse shear stresses are precisely captured by LCW and present ELCWM. Other numerical results, however, are unable to produce accurate distributions of displacements and transverse shear stresses because the effect of transverse normal deformation has been ignored. To demonstrate capability and accuracy of the present theory in predicting thermo-elastic response of the laminated sandwich plates, **Figs. 3.2.18 and 3.2.19** compare normalized

distributions of the in-plane stresses and transverse shear stresses for the laminated sandwich plates of material (3) under uniform temperature loading. In **Figs. 3.2.18 and 3.2.19**, LCW and present ELCWM give best compromised results which can precisely predict the local distribution of the laminated sandwich plates subjected to uniform temperature loading as compared to the exact solutions. Although other theories can describe global thermo-elastic behavior of the laminated sandwich plates, they fail to provide accurate local distribution of the laminated sandwich plates under uniform temperature loading. Additionally, laminated cross-ply composite plates subjected to thermal loading of temperature gradient ($\bar{Q}=0, \bar{T}_0=0, \bar{T}_1\neq 0$) are considered. The normalized distributions of in-plane and transverse shear stresses for symmetric cross-ply laminated composite plates [$0^o/90^o/0^o$] of material (2) have been presented in **Figs. 3.2.20 and 3.2.21**. For distributions of the in-plane and transverse shear stresses as shown in **Figs. 3.2.20 and 3.2.21**, it can be found that the results based on LCW and present ELCWM are in good accord with the exact solutions, whereas results obtained by other theories provide somewhat inaccurate distributions of in-plane and transverse shear stresses. And **Figs. 3.2.22 and 3.2.23** compare normalized distributions of the in-plane stresses and transverse shear stresses for the anti-symmetric cross-ply laminated composite plates [$0^o/90^o/0^o/90^o$] of material (2) under temperature gradient loading. As **Figs. 3.2.22 and 3.2.23** show, non-continuous distribution of in-plane stresses and zig-zag variation of transverse shear stresses are fairly well captured by LCW and present ELCWM, while the results of other theories provide slightly over-estimated values for the distribution of in-plane and transverse shear stresses.

In the thermo-elastic analysis, excellent agreements of results obtained by present theory with the exact solutions suggest that the present theory is capable to predict thermo-elastic responses of the laminated composite and sandwich plates. Whereas the point which special attention should be paid is that the theories which can't consider contribution of the transverse normal deformation effect fail to predict accurate thermo-elastic responses of the laminated composite and sandwich plates subjected to thermal loading, especially uniform temperature loading.

3.2.4.3. Thermo-mechanical coupled loading problem

To investigate the capability and accuracy of the present theory for the thermo-mechanical response, some case of laminated composite plates subjected to thermo-mechanical coupled loading are also analyzed. The results of present theory are compared to those obtained by LCW and exact solutions. In the thermo-mechanical coupled loading problem, relatively thick plates models ($S=L_1/h=L_2/h=4$) are considered and material properties are given according to material (1).

Laminated cross-ply composite plates subjected to uniform temperature-mechanical coupled loading ($\bar{Q}=10, \bar{T}_0=1, \bar{T}_1=0$) are considered. **Figs 3.2.24 and 3.2.25** show the normalized distributions of in-plane and transverse shear stresses for a symmetric cross-ply laminated composite plates [$0^o/90^o/0^o$]. As can be seen from **Figs. 3.2.24 and 3.2.25**, present ELCWM gives comparable results of in-plane and transverse shear stress as compared to the exact solutions,

whereas LCW fail to give accurate distributions of in-plane and transverse shear stress. Although LCW can describe relatively accurate global thermo-mechanical behavior, they can't provide accurate local distribution of the laminated composite plates under uniform temperature-mechanical coupled loading. The normalized distributions of in-plane and transverse shear stresses of an anti-symmetric cross-ply laminated composite plates $[0^o/90^o/0^o/90^o]$ are depicted in **Figs. 3.2.26 and 3.2.27**. From these figures, it can be seen that the results of in-plane and transverse shear stresses obtained by present ELCWM are in excellent agreement with the exact solutions, while LCW fail to describe accurate local distribution of the in-plane stress as shown in **Fig. 3.2.26** and provide somewhat inaccurate result of transverse shear stress as shown in **Fig. 3.2.27**.

Secondly, laminated cross-ply composite plates subjected to temperature gradient-mechanical coupled loading ($\bar{Q}=10, \bar{T}_0=0, \bar{T}_1=1$) are also considered. **Figs. 3.2.28 and 3.2.29** compare normalized distributions of in-plane and transverse shear stresses for a symmetric cross-ply laminated composite plates $[0^o/90^o/0^o]$. And the results of in-plane and transverse shear stresses for an anti-symmetric cross-ply laminated composite plates $[0^o/90^o/0^o/90^o]$ under temperature gradient-mechanical coupled loading are plotted in **Figs. 3.2.30 and 3.2.31**. As shown in **Fig. 3.2.30**, results of present ELCWM can match the exact solutions with excellent accuracy by capturing the shape of non-continuous zig-zag variation of in-plane stress precisely. The results of LCW, however, fail to provide accurate distributions of in-plane stresses because they can't describe non-continuous zig-zag variation. From the **Fig. 3.2.31**, it can be seen that

results of present ELCWM capture well the kinky variations in the transverse shear stresses, whereas LCW can't give reasonable results due to their inaccurate description on local variation of transverse shear stresses as compared to the exact solutions.

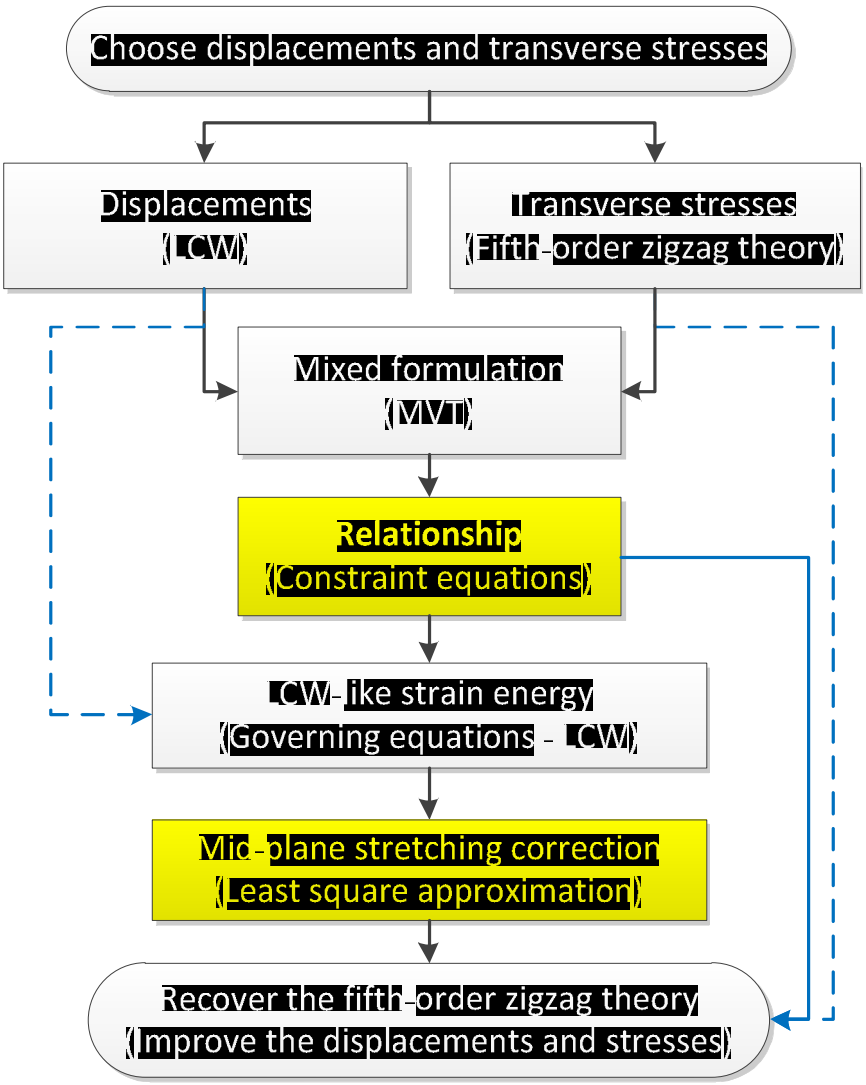

Fig. 3.2.1. Flowchart of the ELCWM

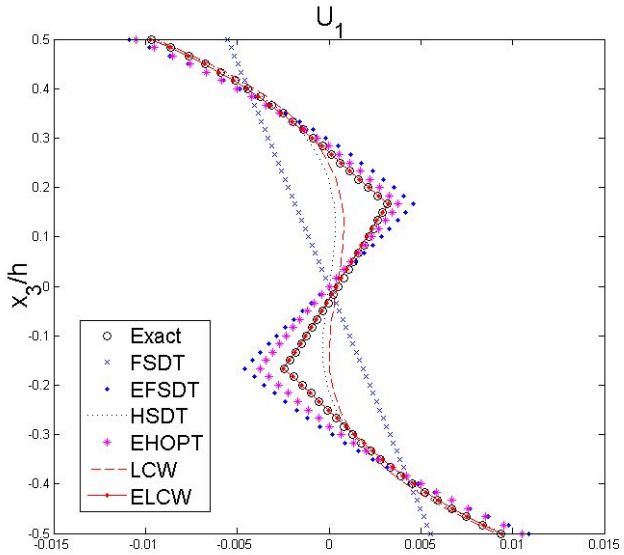

Fig. 3.2.2. In-plane displacements for [0^o / 90^o / 0^o] laminated plates under mechanical loading

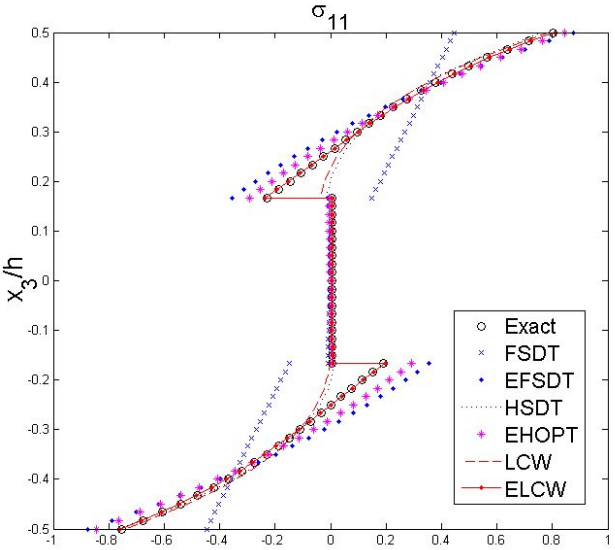

Fig.3.2.3. In-plane stresses for [0^o / 90^o / 0^o] laminated plates under mechanical loading

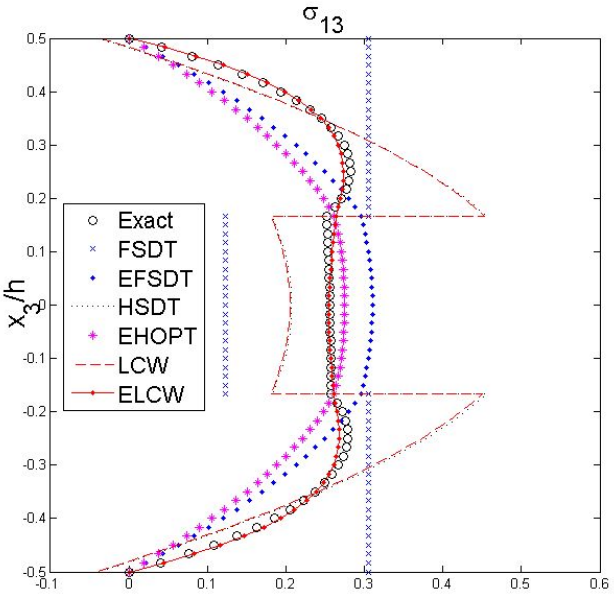

Fig. 3.2.4. Transverse shear stresses computed from constitutive equations for $[0^o/90^o/0^o]$ laminated plates under mechanical loading

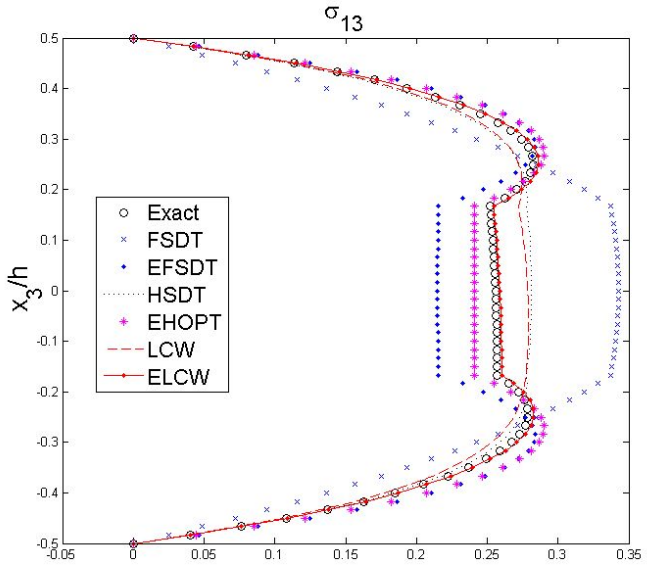

Fig. 3.2.5. Transverse shear stresses computed from equilibrium equations for $[0^o/90^o/0^o]$ laminated plates under mechanical loading

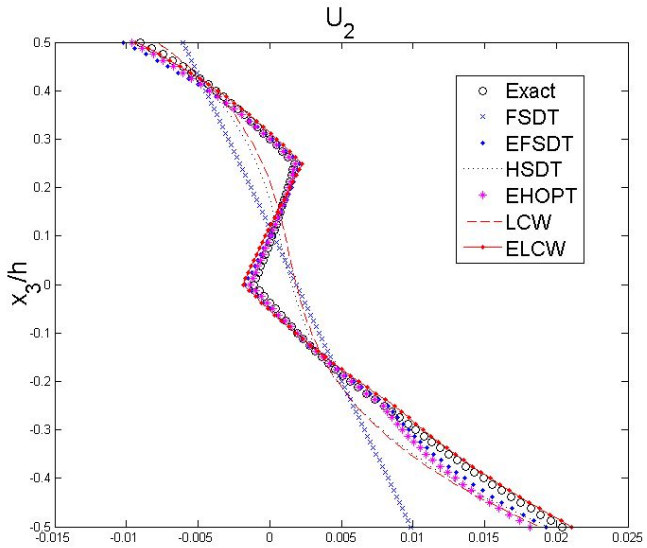

Fig. 3.2.6. In-plane displacements for [0^o / 90^o / 0^o / 90^o] laminated plates under mechanical loading

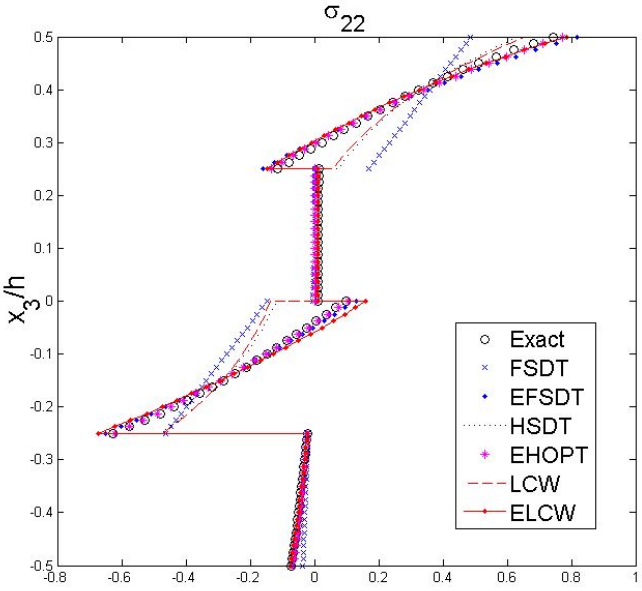

Fig. 3.2.7. In-plane stresses for [0^o / 90^o / 0^o / 90^o] laminated plates under mechanical loading

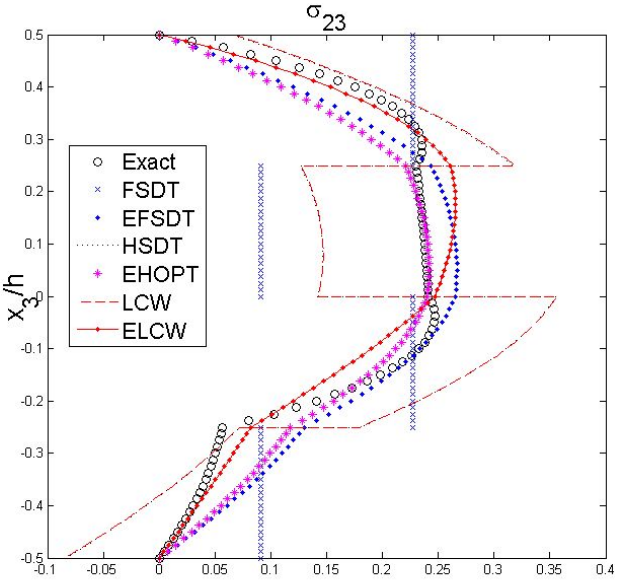

Fig. 3.2.8. Transverse shear stresses computed from constitutive equations for $[0^o/90^o/0^o/90^o]$ laminated plates under mechanical loading

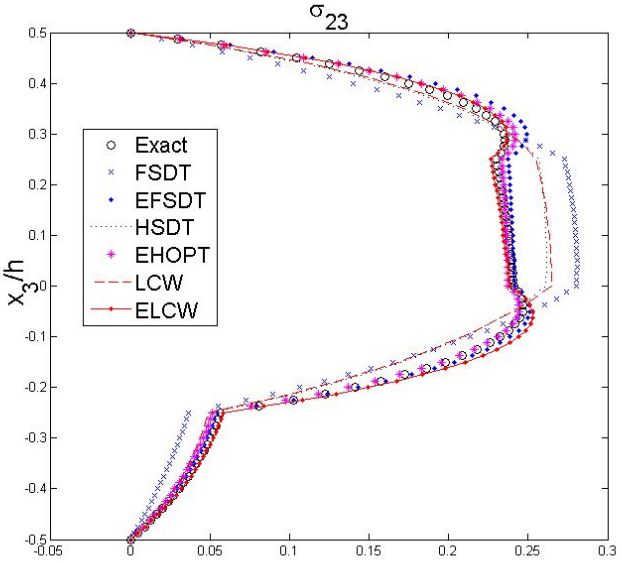

Fig. 3.2.9. Transverse shear stresses computed from equilibrium equations for $[0^o/90^o/0^o/90^o]$ laminated plates under mechanical loading

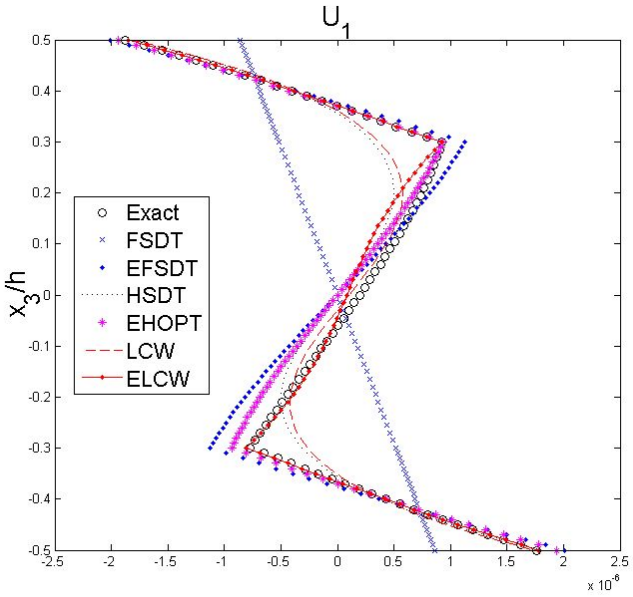

Fig. 3.2.10. In-plane displacements for $[0^o / core / 0^o]$ sandwich plates under mechanical loading

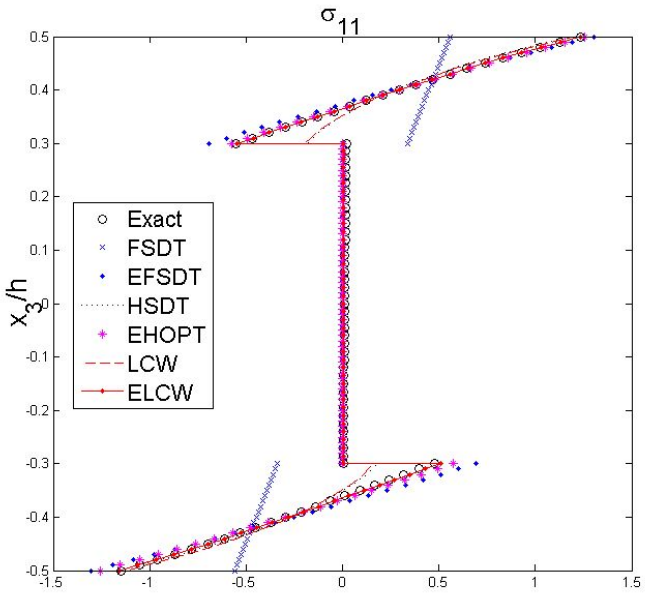

Fig. 3.2.11. In-plane stresses for $[0^o / core / 0^o]$ sandwich plates under mechanical loading

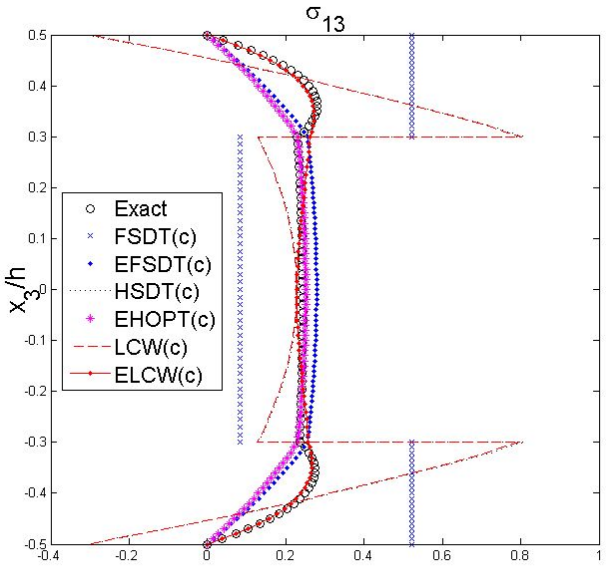

Fig. 3.2.12. Transverse shear stresses computed from constitutive equations for $[0^o / core / 0^o]$ sandwich plates under mechanical loading

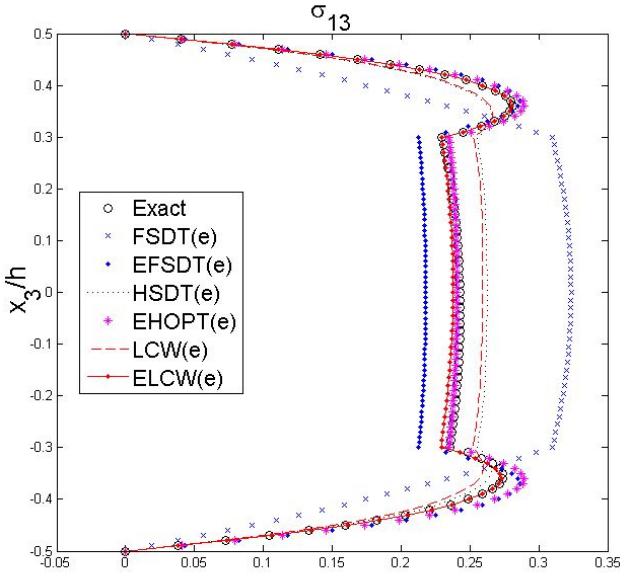

Fig. 3.2.13. Transverse shear stresses computed from equilibrium equations for $[0^o / core / 0^o]$ sandwich plates under mechanical loading

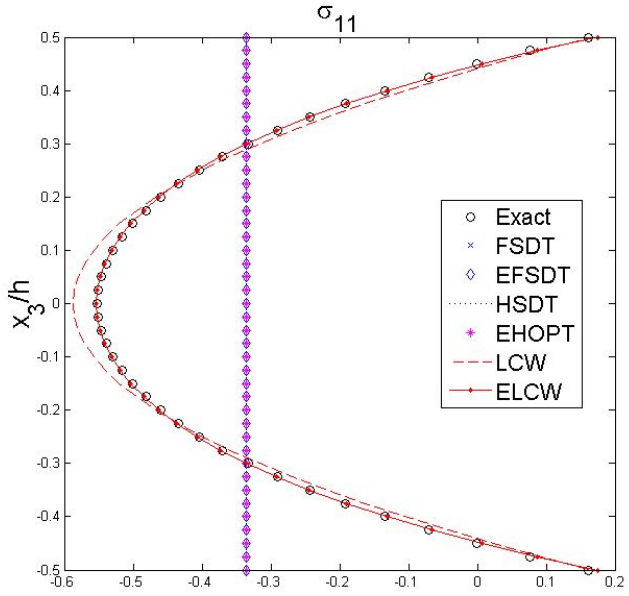

Fig. 3.2.14. In-plane stresses for a single layer plate under uniform temperature

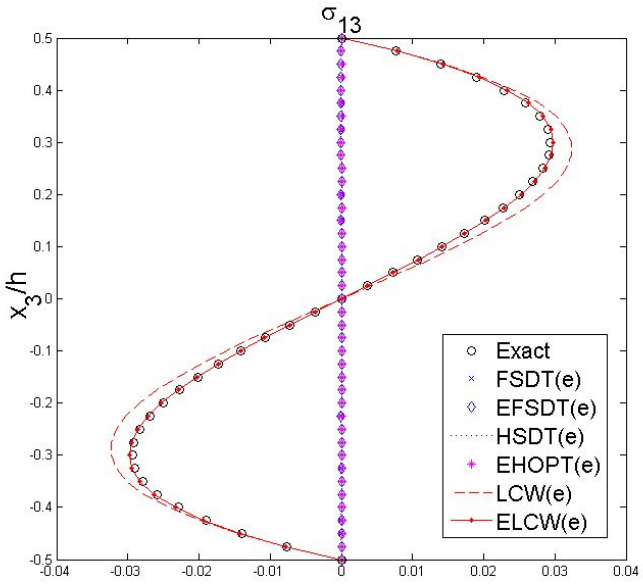

Fig. 3.2.15. Transverse shear stresses for a single layer plate under uniform temperature

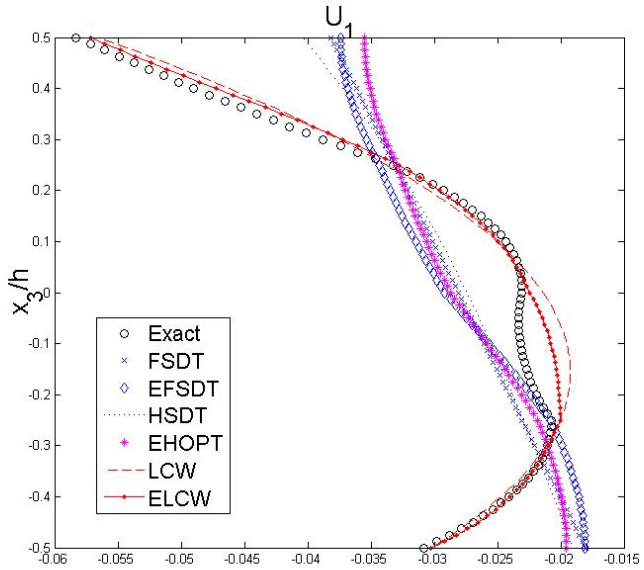

Fig. 3.2.16. In-plane displacements for $[0^o/90^o/0^o/90^o]$ laminated plates under uniform temperature

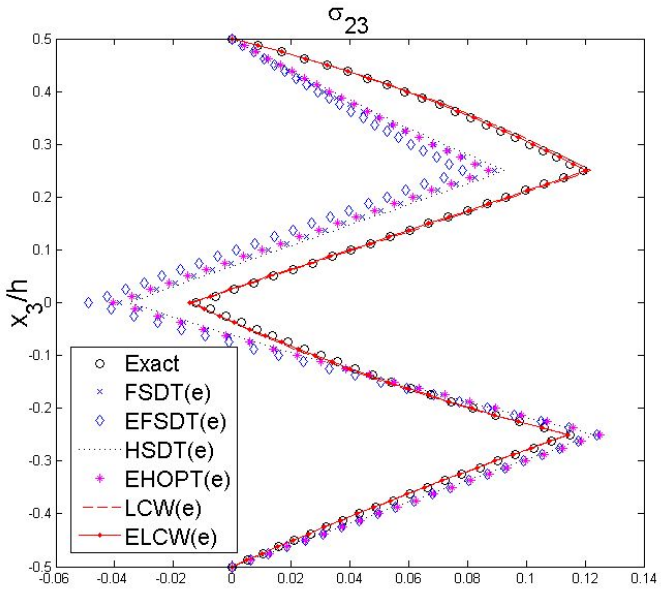

Fig. 3.2.17. Transverse shear stresses for $[0^o/90^o/0^o/90^o]$ laminated plates under uniform temperature

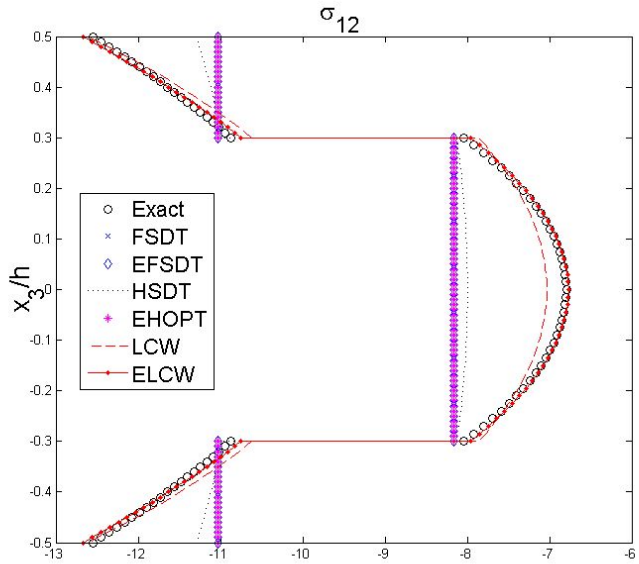

Fig. 3.2.18. In-plane stresses for $[0^o / core / 0^o]$ sandwich plates under uniform temperature

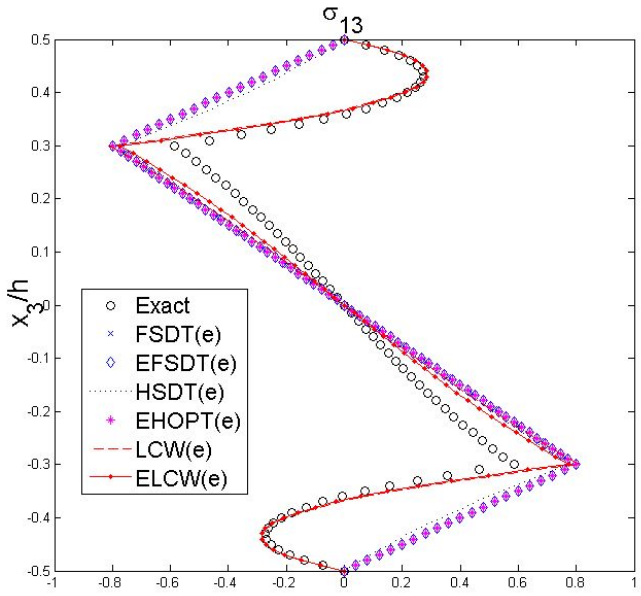

Fig. 3.2.19. Transverse shear stresses for $[0^o / core / 0^o]$ sandwich plates under uniform temperature

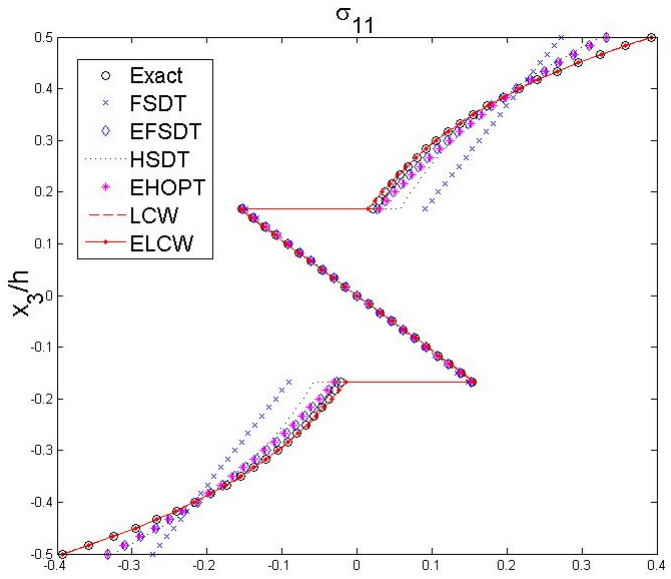

Fig. 3.2.20. In-plane stresses for [0^o / 90^o / 0^o] laminated plates under temperature gradient

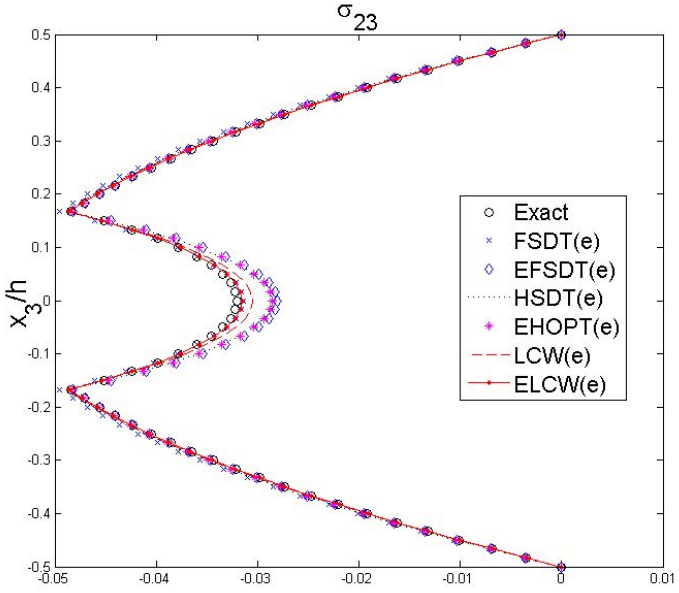

Fig. 3.2.21. Transverse shear stresses for [0^o / 90^o / 0^o] laminated plates under temperature gradient

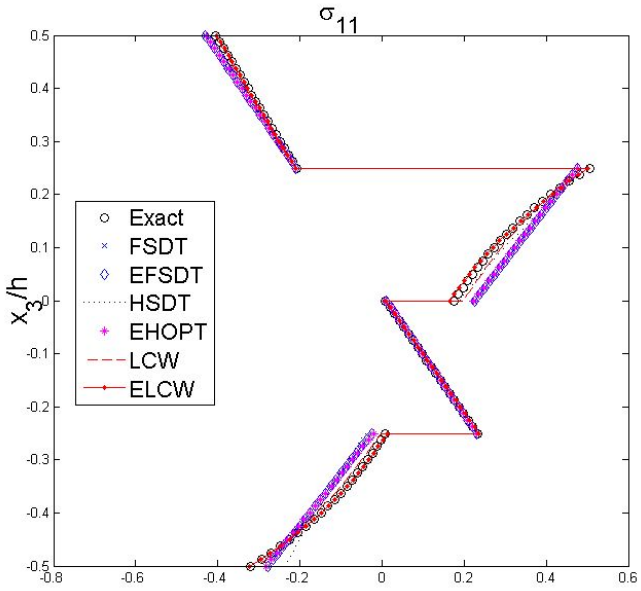

Fig. 3.2.22. In-plane stresses for [0^o / 90^o / 0^o / 90^o] laminated plates under temperature gradient

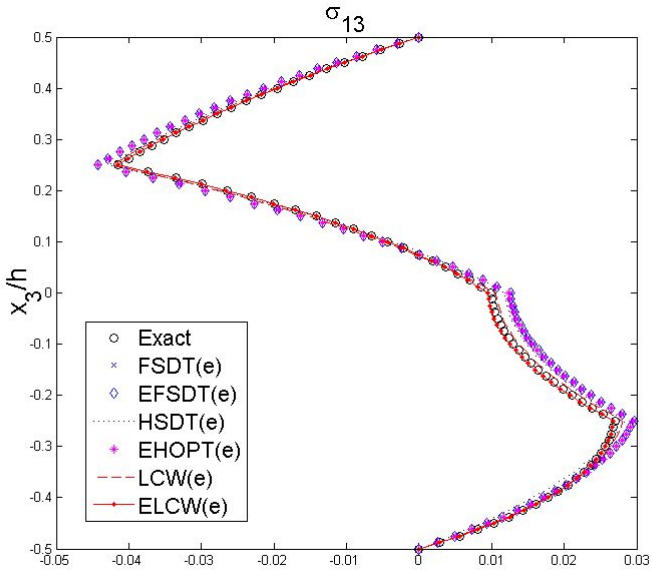

Fig. 3.2.23. Transverse shear stresses for [0^o / 90^o / 0^o / 90^o] laminated plates under temperature gradient

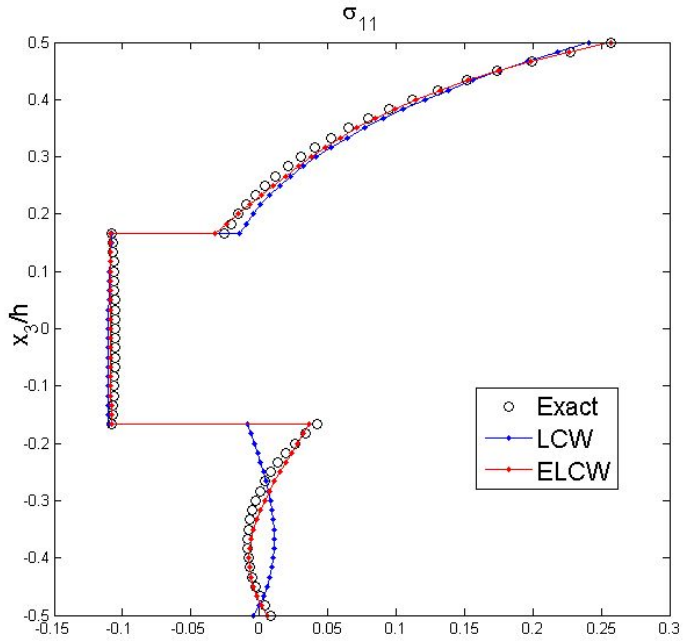

Fig. 3.2.24. In-plane stresses for $[0^o/90^o/0^o]$ laminated plates under uniform temperature-mechanical coupled load

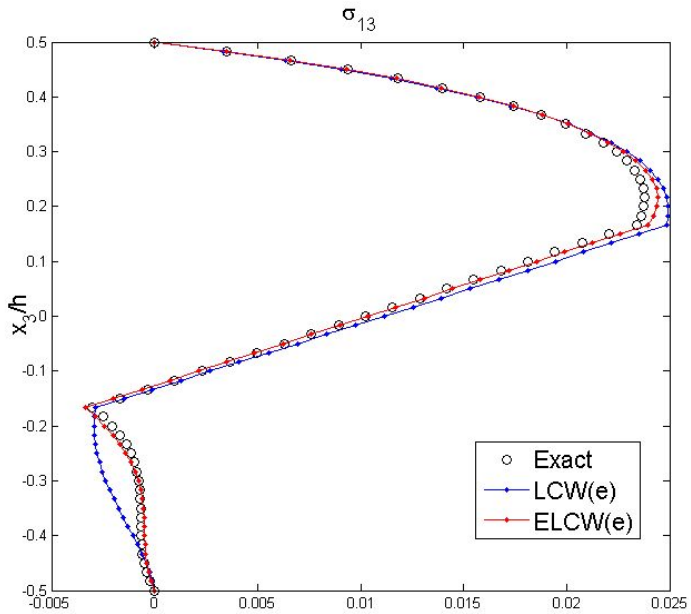

Fig. 3.2.25. Transverse shear stresses for $[0^o/90^o/0^o]$ laminated plates under uniform temperature-mechanical coupled load

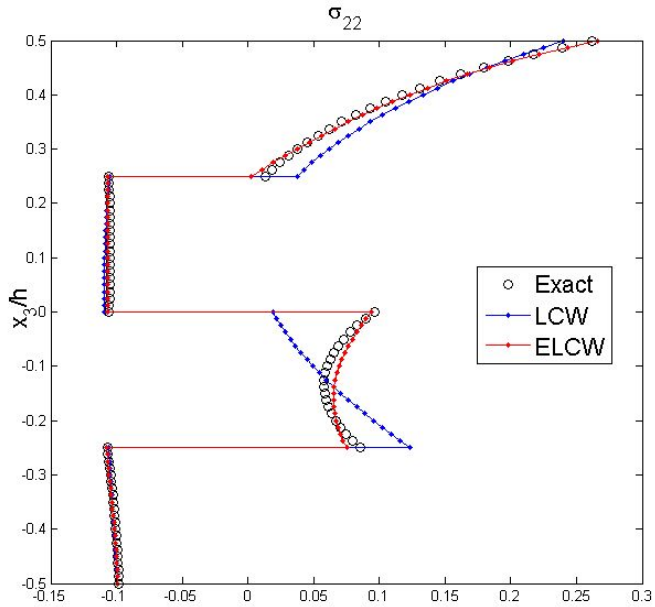

Fig. 3.2.26. In-plane stresses for $[0^o/90^o/0^o/90^o]$ laminated plates under uniform temperature-mechanical coupled load

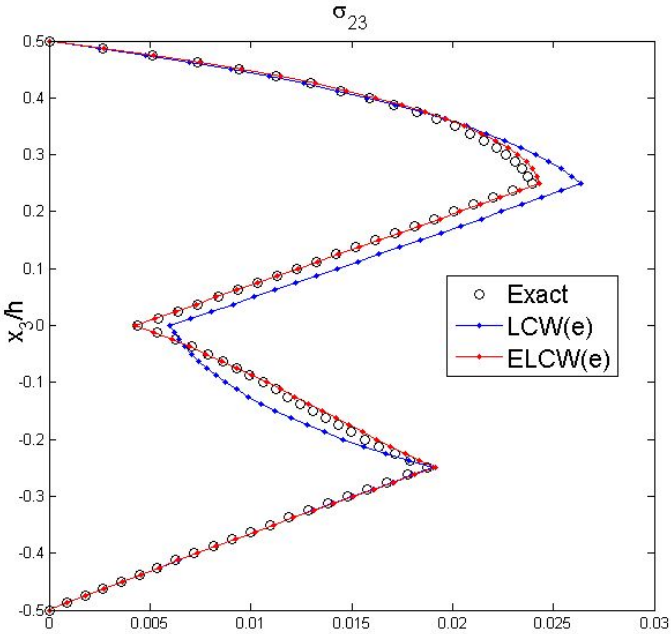

Fig. 3.2.27. Transverse shear stresses for $[0^o/90^o/0^o/90^o]$ laminated plates under uniform temperature-mechanical coupled load

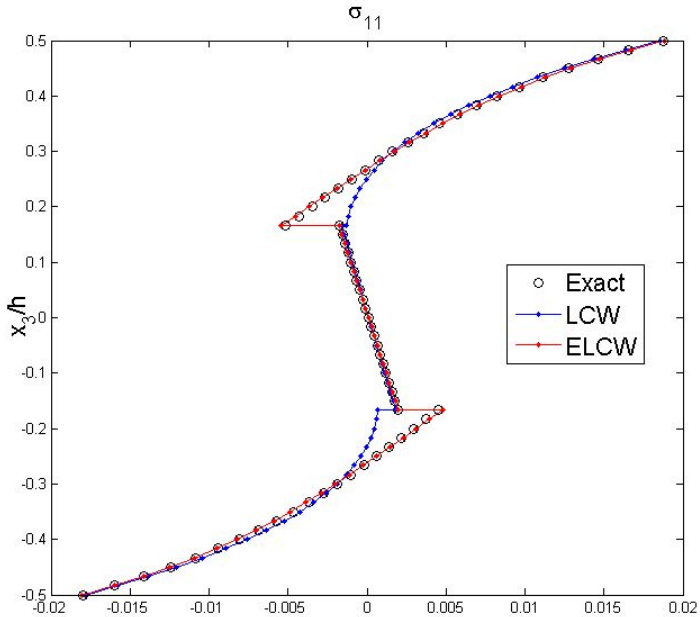

Fig. 3.2.28. In-plane stresses for [0^o / 90^o / 0^o] laminated plates under temperature gradient-mechanical coupled load

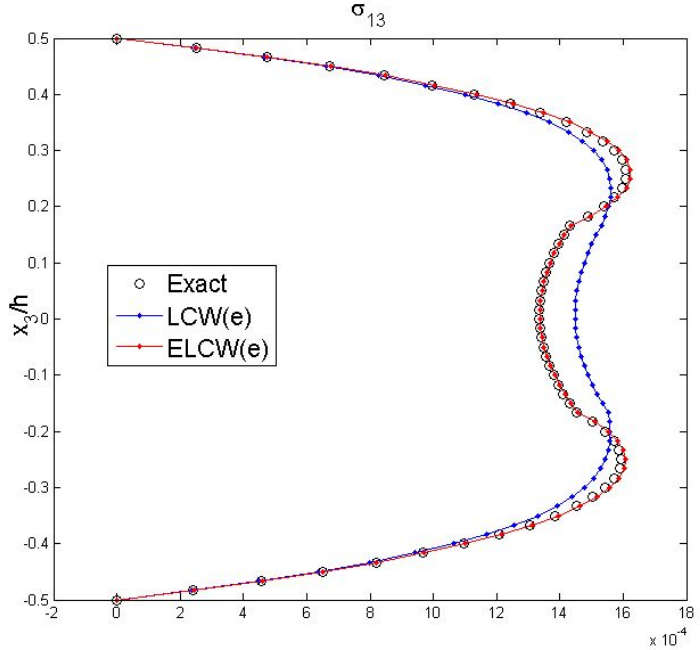

Fig. 3.2.29. In-plane stresses for [0^o / 90^o / 0^o] laminated plates under temperature gradient-mechanical coupled load

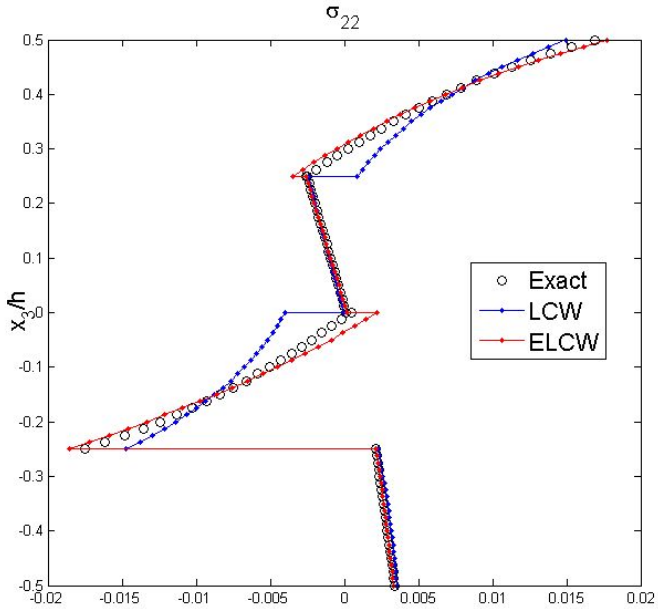

Fig. 3.2.30. In-plane stresses for $[0^o/90^o/0^o/90^o]$ laminated plates under temperature gradient-mechanical coupled load

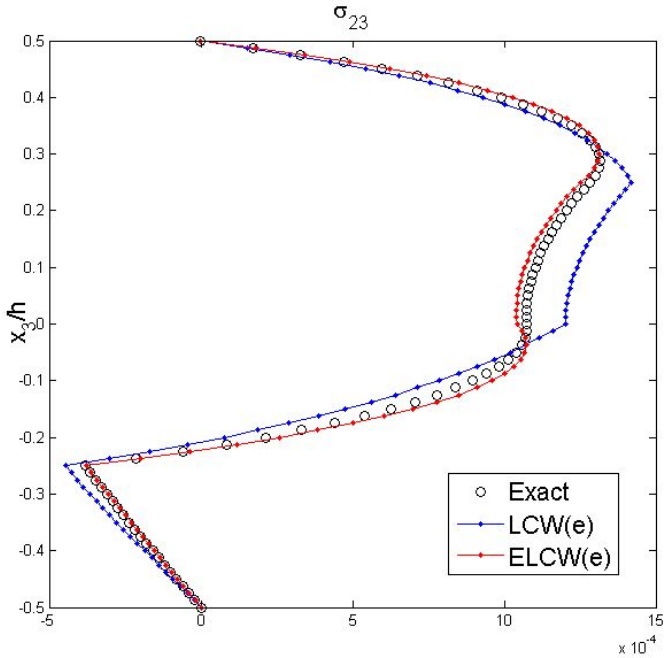

Fig. 3.2.31. In-plane stresses for $[0^o/90^o/0^o/90^o]$ laminated plates under temperature gradient-mechanical coupled load

Chapter 4

Enhanced Zig-zag

Shear Deformation Theory

4.1. Enhanced C^0-type Efficient Higher-Order Zig-zag Theory based on the MVT

4.1.1. Literature Review

As mentioned in previous subsections, a number of analysis models have been developed to accurately predict their static and dynamic responses. Conventional theories (CLPT, FSDT) and refined higher order theories (TSDT, HSDT, LCW) have been sequentially developed [1-10].

On the other hand, various zig-zag plate theories were also developed to improve their accuracy and compatibility [11-15]. Among others, the efficient higher-order plate theory(EHOPT) [12,13], which satisfy the transverse shear stress conditions (stress free at top and bottom surface and stress continuity at interfaces) by superimposing linear zig-zag field to the globally cubic in-plane

displacement field, has been considered as the best 5 D.O.F model. However, derivatives of transverse displacement field were contained in the in-plane displacement field of the EHOPT, so that it requires C^1-continuity conditions in their finite element implementation, which is not available in commercial finite element software.

To avoid using the C^1 interpolation function in the finite element implementation, C^0-type zig-zag theory was proposed by Xiaohui et al [70] for the accurate analysis of laminated composite and sandwich plates with general configuration. They give simple method to construct C^0-continuous finite element implementation based on C^0-type zig-zag theory by employing shear free conditions at the top and bottom surface to eliminate derivatives of transverse displacement field from the in-plane displacement fields. In addition, they can also provide accurate distributions of the transverse shear stress by integrating three-dimensional equilibrium equations.

Meanwhile, advanced composite materials can be applied to severe engineering environment such as high temperature situations. The thermal loading based on rising temperature often represent a crucial factor, which can give a rise to significant thermal deformation and stresses due to the transverse normal deformation effect. Thus, tremendous interest in the thermo-mechanical analysis of the laminated composite plates has emerged in many decades.

Although C^0-type zig-zag theory gives reliable results for the mechanical loading problems, it was developed under the plane stress assumption in which transverse normal strain effect is neglected. However, transverse normal strain effect plays a significant role in thermal loading problems [35, 36]. This brings

us to develop a new C^0-type composite plate theory for the accurate thermo-mechanical analysis of laminated composite and sandwich plates. By assuming transverse displacement field as smooth parabolic distribution [35, 36], proposed theory will allow us to analyze accurately the thermo-mechanical behavior of the laminated composite plates.

In this subsection, as a new way to address the aforementioned issues (C^0 interpolation function in the FE implementation as well as the accurate thermo-mechanical analysis), the C^0-type efficient higher-order zig-zag theory via the mixed formulation is developed and tested numerically. The main objective herein is to systematically set-up the relationships between the C^0-type efficient higher- order zig-zag theory and the seventh order zig-zag model. Transverse displacement field is assumed to be a smooth parabolic distribution through the thickness direction to consider transverse normal strain effect. And derivatives of transverse displacement field can be eliminated from the in-plane displacement fields of the C^0-type EHOZT by employing transverse shear stress conditions in a different way. Finally the results obtained herein are compared with those of other theories reported in the open literature.

4.1.2. Mixed Formulation

To accurately and efficiently analyze the thermo-mechanical response of the laminated composite and sandwich plates, Enhanced C^0-type EHOZT is developed in this dissertation via the mixed variational theorem. In the MVT, the three-dimensional Hellinger-Reissner (HR) functional, which is given in Eqs.

(1.2.1), is employed to derive the relationships between the independent two fields (C^0-type EHOZT and seventh-order zig-zag model).

4.1.2.1. Independent transverse stress fields

The independent transverse stress field, which is to be used in Eq. (1.2.1), is derived based on the seventh order zig-zag model including transverse normal strain effect. The initial displacement field of the seventh order zig-zag model is given as follows:

$$\begin{aligned} u_\alpha^* &= \hat{u}_\alpha^o + \sum_{k=1}^{7} \hat{u}_\alpha^{(k)} x_3^{(k)} + \sum_{k=1}^{N-1} S_\alpha^{(k)} (x_3 - x_{3(k)}) H(x_3 - x_{3(k)}), \\ u_3^* &= \hat{u}_3^o + \hat{u}_3^{(1)} x_3 + \hat{u}_3^{(2)} x_3^2, \end{aligned} \tag{4.1.1}$$

where N, $S_\alpha^{(k)}$ and $H(x_3 - x_{3(k)})$ represent the number of layers, change in slope at each layer interface and Heaviside unit step function, respectively. The superscript $(\ )^o$ denotes the variable on the reference plane. And transverse displacement is assumed to be a form of parabolic variational field to consider contribution of the transverse normal strain effect. For monoclinic layers, the transverse shear stresses depend only on the components of transverse shear strain. Thus some relationships can be calculated by applying the transverse shear stress conditions (stress free at top and bottom surface and stress continuity at interfaces) [12,13, 16-20, 35-38].

$$\hat{u}_\alpha^{(1)} = -\hat{u}_{3,\alpha}^{o} - \frac{h^2}{4}\left(3\hat{u}_\alpha^{(3)} + \hat{u}_{3,\alpha}^{(2)}\right) - \frac{5h^4}{16}\hat{u}_\alpha^{(5)} - \frac{7h^6}{64}\hat{u}_\alpha^{(7)} - \frac{1}{2}\sum_{k=1}^{N-1} S_\alpha^{(k)},$$
$$\hat{u}_\alpha^{(2)} = -\frac{1}{2}\hat{u}_{3,\alpha}^{(1)} - \frac{h^2}{2}\hat{u}_\alpha^{(4)} - \frac{3h^4}{16}\hat{u}_\alpha^{(6)} - \frac{1}{2h}\sum_{k=1}^{N-1} S_\alpha^{(k)}, \tag{4.1.2}$$
$$S_\alpha^{(k)} = a_{\alpha\beta}^{(k)}\left(3\hat{u}_\alpha^{(3)} + \hat{u}_{3,\alpha}^{(2)}\right) + b_{\alpha\beta}^{(k)}\hat{u}_\alpha^{(4)} + c_{\alpha\beta}^{(k)}\hat{u}_\alpha^{(5)} + d_{\alpha\beta}^{(k)}\hat{u}_\alpha^{(6)} + e_{\alpha\beta}^{(k)}\hat{u}_\alpha^{(7)}.$$

Substituting Eq. (4.1.2) into Eq. (4.1.1), initial displacement field can be rewritten as follows:

$$u_\alpha^* = \hat{u}_\alpha^o - \hat{u}_{3,\alpha}^o x_3 - \sum_{k=2}^{3}\frac{1}{k}\hat{u}_{3,\alpha}^{(k)} x_3^k + \sum_{k=1}^{5}\Phi_{\alpha\beta}^{(k)}\phi_\beta^{(k)},$$
$$u_3^* = \hat{u}_3^o + \hat{u}_3^{(1)} x_3 + \hat{u}_3^{(2)} x_3^2, \tag{4.1.3}$$

where

$$\phi_\alpha^{(1)} = \left(3\hat{u}_\alpha^{(3)} + \hat{u}_{3,\alpha}^{(2)}\right),\ \phi_\alpha^{(2)} = \hat{u}_\alpha^{(4)},$$
$$\phi_\alpha^{(3)} = \hat{u}_\alpha^{(5)},\ \phi_\alpha^{(4)} = \hat{u}_\alpha^{(6)},\ \phi_\alpha^{(5)} = \hat{u}_\alpha^{(7)}, \tag{4.1.4}$$

In the displacement fields of Eq. (4.1.3), the in-plane warping functions ($\Phi_{\alpha\beta}^{(k)}$) can be defined as follows:

$$\Phi_{\alpha\beta}^{*(1)} = x_3\left(\tfrac{1}{3}x_3^2 - \tfrac{h^2}{4}\right)\delta_{\alpha\beta} + \sum_{k=1}^{N-1} a_{\alpha\beta}^{(k)} f(x_3, x_{3(k)}),$$
$$\Phi_{\alpha\beta}^{*(2)} = x_3^2\left(x_3^2 - \tfrac{h^2}{2}\right)\delta_{\alpha\beta} + \sum_{k=1}^{N-1} b_{\alpha\beta}^{(k)} f(x_3, x_{3(k)}),$$
$$\Phi_{\alpha\beta}^{*(3)} = x_3\left(x_3^4 - \tfrac{5h^4}{16}\right)\delta_{\alpha\beta} + \sum_{k=1}^{N-1} c_{\alpha\beta}^{(k)} f(x_3, x_{3(k)}), \tag{4.1.5}$$
$$\Phi_{\alpha\beta}^{*(4)} = x_3^2\left(x_3^4 - \tfrac{3h^4}{16}\right)\delta_{\alpha\beta} + \sum_{k=1}^{N-1} d_{\alpha\beta}^{(k)} f(x_3, x_{3(k)}),$$
$$\Phi_{\alpha\beta}^{*(5)} = x_3\left(x_3^6 - \tfrac{7h^6}{64}\right)\delta_{\alpha\beta} + \sum_{k=1}^{N-1} e_{\alpha\beta}^{(k)} f(x_3, x_{3(k)}),$$

in which

$$f(x_3, x_{3(k)}) = -\tfrac{1}{2}x_3 - \tfrac{1}{2h}x_3^2 + (x_3 - x_{3(k)})H(x_3 - x_{3(k)}). \tag{4.1.6}$$

$\delta_{\alpha\beta}$ is the Kronecker delta function, and the terms of $a_{\alpha\beta}^{(k)}$, $b_{\alpha\beta}^{(k)}$, $c_{\alpha\beta}^{(k)}$, $d_{\alpha\beta}^{(k)}$ and $e_{\alpha\beta}^{(k)}$ are functions of the material properties which are based on the transverse shear continuity conditions.

From Eq. (4.1.3), corresponding in-plane and transverse strains are then obtained by:

$$\begin{aligned}
\varepsilon_{\alpha\beta}^{*} &= \varepsilon_{\alpha\beta}^{*(0)} + \sum_{k=1}^{3} \varepsilon_{\alpha\beta}^{*(k)} x_3^{(k)} + \tfrac{1}{2}\sum_{k=1}^{5}\left(\Phi_{\alpha\gamma}^{(k)}\phi_{\gamma,\beta}^{(k)} + \Phi_{\beta\omega}^{(k)}\phi_{\omega,\alpha}^{(k)}\right), \\
\gamma_{\alpha 3}^{*} &= \sum_{k=1}^{5} \Phi_{\alpha\beta,3}^{(k)}\phi_{\beta}^{(k)}, \\
\varepsilon_{33}^{*} &= \varepsilon_{33}^{*(0)} + x_3\varepsilon_{33}^{*(1)}.
\end{aligned} \tag{4.1.7}$$

Thus, independent transverse stress field based on the constitutive equation of Eq. (1.2.2) can be written as:

$$\begin{aligned}
\sigma_{\alpha 3}^{*} &= C_{\alpha 3\beta 3}\gamma_{\beta 3}^{*}, \\
\sigma_{33}^{*} &= C_{33\alpha\beta}\left(\varepsilon_{\alpha\beta}^{*} - \alpha_{\alpha\beta}\theta\right) + C_{3333}\left(\varepsilon_{33}^{*} - \alpha_{33}\theta\right).
\end{aligned} \tag{4.1.8}$$

4.1.2.2. Displacement fields

C^0-type efficient higher order plate theory (C^0-type EHOPT) is introduced to derive the displacement field to be used for the components of strain and displacement presented in Eq. (1.2.1). The initial displacement field of the third-

order zig-zag model including transverse normal strain effect can be written as follows:

$$
\begin{aligned}
u_\alpha &= u_\alpha^o + \sum_{k=1}^{3} \xi_\alpha^{(k)} x_3^{(k)} + \sum_{k=1}^{N-1} S_\alpha^{(k)} (x_3 - x_{3(k)}) H(x_3 - x_{3(k)}), \\
u_3 &= u_3^o + u_3^{(1)} x_3 + u_3^{(2)} x_3^2 .
\end{aligned}
\tag{4.1.9}
$$

The displacement field of Eq. (4.1.9) is quite distinguished from those based on the independent transverse stress field by superscript $(\,)^*$. By applying the shear free conditions at the top and bottom surfaces as well as the shear continuity condition at the $x_{3(1)}$ interface, the first derivatives of the transverse displacement field can be eliminated from the in-plane displacement field as following relationships:

$$
\begin{aligned}
u_{3,\alpha}^o &= -\xi_\alpha^{(1)} - \frac{3h^2}{4} \xi_\alpha^{(3)} - \frac{h^2}{4} u_{3,\alpha}^{(2)} - \frac{1}{2} \sum_{k=1}^{N-1} S_\alpha^{(k)}, \\
u_{3,\alpha}^{(1)} &= -2\xi_\alpha^{(2)} - \frac{1}{h} \sum_{k=1}^{N-1} S_\alpha^{(k)}, \\
u_{3,\alpha}^{(2)} &= a_{\alpha\gamma}^{(1)} \phi_\gamma + b_{\alpha\gamma}^{(1)} S_\gamma^{(1)} .
\end{aligned}
\tag{4.1.10}
$$

In addition, applying the shear continuity conditions at the interfaces other than $x_{3(1)}$ interface yield the following relationships:

$$
S_\alpha^{(k)} = a_{\alpha\gamma}^{(k)} \phi_\gamma + b_{\alpha\gamma}^{(k)} S_\gamma^{(1)} . \quad (2 \le k \le N-1)
\tag{4.1.11}
$$

Thus, the final displacement field of C^0-type efficient higher-order zig-zag theory (C^0-type EHOZT) can be obtained by substituting Eqs. (4.1.10) and (4.1.11) into Eq. (4.1.9) . This can be expressed as:

$$
\begin{aligned}
u_\alpha &= u_\alpha^o + \sum_{k=1}^{3} \xi_\alpha^{(k)} x_3^{(k)} + \Psi_{\alpha\beta}^{(1)} \varphi_\beta^{(1)} + \Psi_{\alpha\beta}^{(2)} \varphi_\beta^{(2)}, \\
u_3 &= u_3^o + u_3^{(1)} x_3 + u_3^{(2)} x_3^2,
\end{aligned}
\tag{4.1.12}
$$

where

$$
\varphi_\alpha^{(1)} = \xi_\alpha^{(3)}, \quad \varphi_\alpha^{(2)} = S_\alpha^{(1)}, \tag{4.1.13}
$$

and

$$
\begin{aligned}
\Psi_{\alpha\beta}^{(1)} &= \sum_{k=2}^{N-1} a_{\alpha\gamma}^{(k)} g(x_3, x_{3(k)}), \\
\Psi_{\alpha\beta}^{(2)} &= g(x_3, x_{3(1)}) + \sum_{k=2}^{N-1} b_{\alpha\gamma}^{(k)} g(x_3, x_{3(k)}), \\
g(x_3, x_{3(k)}) &= (x_3 - x_{3(k)}) H(x_3 - x_{3(k)}),
\end{aligned}
\tag{4.1.14}
$$

where the terms of $a_{\alpha\beta}^{(k)}$ and $b_{\alpha\beta}^{(k)}$, like the independent transverse stress field, are functions of the material properties which are derived from the transverse shear continuity conditions [12, 13].

Subsequently, in-plane and transverse strains can be obtained from the final displacement field given as Eq. (4.1.12) as follows:

$$
\begin{aligned}
\varepsilon_{\alpha\beta} &= \varepsilon_{\alpha\beta}^{(0)} + \sum_{k=1}^{3} \varepsilon_{\alpha\beta}^{(k)} x_3^{(k)} + \tfrac{1}{2} \sum_{k=1}^{2} \left(\Psi_{\alpha\gamma}^{(k)} \varphi_{\gamma,\beta}^{(k)} + \Psi_{\beta\omega}^{(k)} \varphi_{\omega,\alpha}^{(k)} \right), \\
\gamma_{\alpha 3} &= \gamma_{\alpha 3}^{(0)} + x_3 \gamma_{\alpha 3}^{(1)} + x_3^2 \gamma_{\alpha 3}^{(2)} + \sum_{k=1}^{2} \Psi_{\alpha\beta,3}^{(k)} \varphi_\beta^{(k)}, \\
\varepsilon_{33} &= \varepsilon_{33}^{(0)} + x_3 \varepsilon_{33}^{(1)}.
\end{aligned}
\tag{4.1.15}
$$

The in-plane stress to be used in Eq. (1.2.1) can be expressed as follows:

$$\sigma_{\alpha\beta} = C_{\alpha\beta\gamma\omega}\left(\varepsilon_{\gamma\omega} - \alpha_{\gamma\omega}\theta\right) + C_{\alpha\beta 33}\left(\varepsilon_{33} - \alpha_{33}\theta\right). \tag{4.1.16}$$

In the final displacement field of C^0-type EHOZT, the derivatives of transverse displacement field have been taken out from the in-plane displacement field, so that the C^0-continuous element is only required for their finite element implementation.

4.1.2.3. Relationships between the two theories

The displacement fields and independent transverse stress fields, which are required in the MVT, are independently defined in the previous subsections. In the MVT, the 'mixed' terms plays an important role to derive the Enhanced C^0-type EHOZT via the MVT. It is acting as constraint equation to connect the displacement fields and the independent transverse stress fields, thus it provides the reliable relationships between the two fields (i.e. C^0-type EHOZT and seventh-order zig-zag model including transverse normal strain effect).

Constraint equation in Eq. (1.2.1) is given by

$$\int_V \left[(\gamma_{\alpha 3} - \gamma^*_{\alpha 3})\delta\sigma^*_{\alpha 3} + (\varepsilon_{33} - \varepsilon^*_{33})\delta\sigma^*_{33}\right] dV = 0, \tag{4.1.17}$$

where the transverse normal strains based on displacement field is exactly equal to those obtained from independent transverse stress field, therefore the second term of the constraint equation become negligible. This also means that the transverse normal stress can be approximated by that of the C^0-type EHOZT.

$$\varepsilon_{33}^{*} = \varepsilon_{33} \rightarrow \sigma_{33}^{*} \approx \sigma_{33}. \tag{4.1.18}$$

Then constraint equation given as Eq. (4.1.17) can be simplified as follows:

$$\int_V \left[(\gamma_{\alpha 3} - \gamma_{\alpha 3}^{*}) \delta \sigma_{\alpha 3}^{*} \right] dV = 0, \tag{4.1.19}$$

in which the components of the transverse shear strains are given in Eqs. (4.1.7) and (4.1.15), and the transverse shear stress based on the seventh order zig-zag model is given in Eq. (4.1.8).

Relationships between the two fields can be derived by substituting these components of the transverse shear strains into the simplified constraint equation given in Eq. (4.1.19).

$$\begin{bmatrix} \phi_{\alpha}^{(1)} \\ \phi_{\alpha}^{(2)} \\ \phi_{\alpha}^{(3)} \\ \phi_{\alpha}^{(4)} \\ \phi_{\alpha}^{(5)} \end{bmatrix} = \left[\Gamma_{\alpha 3 \lambda 3} \right] \begin{bmatrix} \gamma_{\lambda 3}^{(1)} \\ \gamma_{\lambda 3}^{(2)} \\ \gamma_{\lambda 3}^{(3)} \\ \varphi_{\lambda}^{(1)} \\ \varphi_{\lambda}^{(2)} \end{bmatrix}, \tag{4.1.20}$$

where

$$\begin{aligned} &\left[\Gamma_{\alpha 3 \lambda 3} \right] = \left(A_{\alpha 3 \beta 3} \right)_{ij}^{-1} \left(B_{\beta 3 \lambda 3} \right)_{ij}^{T}, \\ &\left(A_{\alpha 3 \beta 3} \right)_{ij} = \left\langle \Phi_{\alpha \mu, 3}^{(i)} C_{\mu 3 \omega 3} \Phi_{\omega \beta, 3}^{(j)} \right\rangle \quad (i, j = 1 \sim 5), \\ &\left(B_{\beta 3 \lambda 3} \right)_{mj} = \left\langle x_3^{m-1} C_{\beta 3 \nu 3} \Phi_{\nu \lambda, 3}^{(j)} \right\rangle \quad (m = 1, 2, 3), \\ &\left(B_{\beta 3 \lambda 3} \right)_{mj} = \left\langle \Psi_{\beta \kappa, 3}^{(m-3)} C_{\kappa 3 \nu 3} \Phi_{\nu \lambda, 3}^{(j)} \right\rangle \quad (m = 4, 5), \end{aligned} \tag{4.1.21}$$

in which

$$\langle \bullet \rangle = \int_{-h/2}^{h/2} [\bullet] dx_3. \tag{4.1.22}$$

From Eq. (4.1.20), transverse shear stress based on the seventh order zig-zag model can be expressed in terms of those of the variables of C^0-type EHOZT. Thus, transverse shear stress resultants of C^0-type EHOZT can be improved by the relationships between the two theories.

4.1.3. Enhanced C^0-type Efficient Higher-Order Zig-zag Theory via the MVT

Independently assumed transverse shear stresses and displacement fields are described in the previous subsection. Additionally, the relationships between independent two fields was systematically established via the MVT. In this subsection, an enhanced C^0-type higher-order zig-zag theory is derived. The governing equation of the present model is based on the C^0-type higher-order zig-zag theory. In addition, recovery process is also considered in this subsection to more accurately predict the thermo-mechanical response of the laminated composite and sandwich structures.

4.1.3.1. Governing equations

The constraint equation, which plays a major role in deriving the relationships between the two theories, are systematically solved in previous subsection and therefore 'mixed terms' can be dismissed in the MVT. Thus, three-dimensional Hellinger-Reissner functional given in Eq. (1.2.1) can be rewritten as:

$$\int_V \left[\sigma_{\alpha\beta}\delta\varepsilon_{\alpha\beta} + \sigma^*_{\alpha 3}\delta\gamma_{\alpha 3} + \sigma_{33}\delta\varepsilon_{33} \right] dV - \int_{S_\sigma} \tilde{t}_3^{\,*}\delta u_3 dS_\sigma = 0, \tag{4.1.23}$$

where $\tilde{t}_3^*$ is the prescribed traction force which is applied to x_3 direction only, and the transverse normal stress is considered as the displacement field-based one because of Eq. (4.1.18). Thus the transverse shear stress is only derived from the independent transverse stress field.

Form Eq. (4.1.23), the governing equation for the enhanced C^0-type EHOZT via the MVT can be derived by applying the definition of the stress resultants as well as the integration by parts. This can be expressed as:

$$
\begin{aligned}
&\delta u_\alpha^o:\ N_{\alpha\beta,\beta}=0,\\
&\delta\xi_\alpha^{(1)}:\ M_{\alpha\beta,\beta}-Q_\alpha=0,\\
&\delta\xi_\alpha^{(2)}:\ R^{(2)}_{\alpha\beta,\beta}-2V_\alpha^{(1)}=0,\\
&\delta\xi_\alpha^{(3)}:\ R^{(3)}_{\alpha\beta,\beta}+\sum_{k=2}^{N-1}a_{\gamma\alpha}^{(k)}(M^{(k)}_{\gamma\beta,\beta}-x_{3(k)}N^{(k)}_{\gamma\beta,\beta})\\
&\qquad -3V_\alpha^{(2)}-\sum_{k=2}^{N-1}a_{\gamma\alpha}^{(k)}Q_\gamma^{(k)}=0,\\
&\delta S_\alpha^{(1)}:\ M^{(1)}_{\gamma\beta,\beta}-x_{3(1)}\cdot N^{(1)}_{\gamma\beta,\beta}+\sum_{k=2}^{N-1}b_{\gamma\alpha}^{(k)}(M^{(k)}_{\gamma\beta,\beta}-x_{3(k)}N^{(k)}_{\gamma\beta,\beta})\\
&\qquad -Q_\alpha^{(1)}-\sum_{k=2}^{N-1}b_{\gamma\alpha}^{(k)}Q_\gamma^{(k)}=0,\\
&\delta u_3^o:\ Q_{\alpha,\alpha}+\tilde{t}_3^*=0,\\
&\delta u_3^{(1)}:\ V^{(1)}_{\alpha,\alpha}-N_{33}+\tilde{t}_3^*(\frac{h}{2})=0,\\
&\delta u_3^{(2)}:\ V^{(2)}_{\alpha,\alpha}-2M_{33}+\tilde{t}_3^*(\frac{h^2}{4})=0,
\end{aligned}
\tag{4.1.24}
$$

where

$$
\begin{aligned}
&\left[N_{\alpha\beta},M_{\alpha\beta},R^{(2)}_{\alpha\beta},R^{(3)}_{\alpha\beta},N^{(k)}_{\alpha\beta},M^{(k)}_{\alpha\beta}\right]\\
&\quad=\left\langle\sigma_{\alpha\beta}\left[1,,x_3,x_3^2,x_3^3,H(x_3-x_{3(k)}),x_3H(x_3-x_{3(k)})\right]\right\rangle,\\
&\left[Q_\alpha,V_\alpha^{(1)},V_\alpha^{(2)},Q_\alpha^{(k)}\right]=\left\langle\sigma^*_{\alpha3}\left[1,,x_3,x_3^2,H(x_3-x_{3(k)})\right]\right\rangle,\\
&\left[N_{33},M_{33}\right]=\left\langle\sigma_{33}\left[1,x_3\right]\right\rangle.
\end{aligned}
\tag{4.1.25}
$$

4.1.3.2. Transverse shear stress recovery

Once the governing equations of the present theory (enhanced C^0-type

EHOZT via MVT) are solved, accuracy of the transverse shear stresses can be improved by using the recovery process. The independent transverse stress fields can be utilized to increase the accuracy of the prediction. This can be achieved by expressing the independent transverse stress fields in terms of the variables obtained by solving the governing equations. In this procedure, the relationships between the two fields given in Eq. (4.1.20) plays a significant role to recover the transverse shear stresses. Substituting Eqs. (4.1.7) and (4.1.20) into Eq. (4.1.8), the independent transverse stress fields can be rewritten as follows:

$$\sigma^{*}_{\alpha 3} = \left(T_{\alpha 3\beta 3}\right)_{1k}\left[\Gamma_{\beta 3\lambda 3}\right]\left[\hat{\gamma}_{\lambda 3}\right], \tag{4.1.26}$$

where

$$\begin{aligned} &\left(T_{\alpha 3\beta 3}\right)_{1k} = C_{\alpha 3\beta 3}\Phi^{(k)}_{\alpha\beta,3}, \ (k = 1 \sim 5) \\ &\left[\hat{\gamma}_{\lambda 3}\right] = \left[\gamma^{(1)}_{\lambda 3} \quad \gamma^{(2)}_{\lambda 3} \quad \gamma^{(3)}_{\lambda 3} \quad \varphi^{(1)}_{\lambda} \quad \varphi^{(2)}_{\lambda}\right]^{T}. \end{aligned} \tag{4.1.27}$$

Thus, transverse shear stresses are completely recovered in terms of variables of the present theory and accuracy of the results can be systematically improved.

4.1.4. Numerical investigation and Discussion

In order to verify the efficiency and accuracy of the present theory (enhanced C^0-type EHOZT via MVT), cross-ply lay-up rectangular composite plates are analyzed in this section. The mechanical loading is prescribed on the top surface, which is expressed as follows:

$$\tilde{t}_3^*(x_\alpha, \tfrac{h}{2}) = P_3 \sin(px)\sin(qy), \tag{4.1.28}$$

where

$$p = \frac{\pi}{L_1},\ q = \frac{\pi}{L_2}. \tag{4.1.29}$$

The thermal loading is linearly prescribed through the thickness of the plates, which take the form of

$$\theta(x_i) = \left(T_0 + x_3 T_1\right)\sin(px)\sin(qy). \tag{4.1.30}$$

The primary variables of the enhanced C^0-type EHOZT via MVT are assumed to be a double trigonometric series to satisfy the simply supported boundary conditions as follows:

$$\begin{aligned}
&[u_1^o, \xi_1^{(i)}, S_1^{(1)}] = [U_1, \Psi_1^{(i)}, \Theta_1]\cos(px)\sin(qy),\\
&[u_2^o, \xi_2^{(i)}, S_2^{(1)}] = [U_2, \Psi_2^{(i)}, \Theta_2]\sin(px)\cos(qy),\\
&[u_3^o, u_3^{(\alpha)}] = [U_3, U_3^{(\alpha)}]\sin(px)\sin(qy).
\end{aligned} \tag{4.1.31}$$

Example models assume the aspect ratio as $L_1 = L_2$, length-to-thickness ratio as $S = L_1/h = L_2/h = 4$ for the mechanical analysis and $S = L_1/h = L_2/h = 5$ for the pure thermal analysis.

The material properties of the composite plates are given as follows:

-material (1) for the mechanical loading problem:

$$E_L / E_T = 25, \quad G_{LT} / E_T = 0.5,$$
$$G_{TT} / E_T = 0.2, \; v_{LT} = v_{TT} = 0.25. \tag{4.1.32}$$

-material (2) for the thermal loading problem:

$$E_L / E_T = 15, \quad G_{LT} / E_T = 0.5,$$
$$G_{TT} / E_T = 0.3356, \; v_{LT} = 0.3, \quad v_{TT} = 0.49, \tag{4.1.33}$$
$$\alpha_L = 0.015 \cdot 10^{-6} / K, \quad \alpha_T = 10^{-6} / K.$$

where the subscript $(\,)_L$ represents a parallel direction, while $(\,)_T$ denotes a transverse direction to the fibers.

The results obtained herein are normalized as follows:

-Mechanical analysis:

$$u_\alpha = \frac{E_T \cdot u_\alpha^*}{\bar{Q} \cdot h \cdot S^3}, \; \sigma_{\alpha\beta} = \frac{\sigma_{\alpha\beta}^*}{\bar{Q} \cdot S^2}, \; \sigma_{3\alpha} = \frac{\sigma_{3\alpha}^*}{\bar{Q} \cdot S}. \tag{4.1.34}$$

-Thermal analysis:

$$u_\alpha = \frac{u_\alpha^*}{\alpha_L \cdot h \cdot S}, \quad \sigma_{\alpha\beta} = \frac{\sigma_{\alpha\beta}^*}{\alpha_L \cdot E_T}, \quad \sigma_{3\alpha} = \frac{\sigma_{3\alpha}^*}{\alpha_L \cdot E_T}. \tag{4.1.35}$$

4.1.4.1. Symmetric Cross-ply Layup case

Symmetric cross-ply $[0^o/90^o/0^o]$ laminated composite plates subjected to thermo-mechanical loading is considered.

In the uniform thermal loading case ($\overline{Q}=0, \overline{T}_0 \neq 0, \overline{T}_1 = 0$), normalized distributions of displacement and stresses of material (2) are shown in **Figs. 4.1.1-4.1.4**. The result of in-plane displacement for a symmetric cross-ply composite plates is plotted in **Fig. 4.1.1**. For the results of in-plane displacement, it can be observed that the present model and LCW give a best compromised results as compared with the exact solution. FSDT and EHOPT, however, provide constant distribution, and HSDT fail to accurately describe the parabolic distribution of in-plane displacement. **Figs. 4.1.2 and 4.1.3** represent normalized distributions of in-plane stresses. It can be seen that the present model and LCW can provide reliable result by capturing its non-continuous distributions of in-plane stresses. However, results obtained by other theories, which neglected the contribution of the transverse normal strain effect, entirely fail to give accurate distributions as compared with the exact solution. Normalized distribution of transverse shear stress is given in Fig. 4.1.4. In this result, it can be found that present model and LCW provide fairly accurate semi-cubic variation in transverse shear stress, whereas other theories cannot.

Figs. 4.1.5-4.1.7 show the normalized distributions of displacement and stresses of material (2) subjected to the temperature gradient ($\overline{Q}=0, \overline{T}_0 = 0, \overline{T}_1 \neq 0$). For the distribution of the in-plane displacement, as shown in **Fig. 4.1.5**, it can be found that present model and LCW yield almost identical results with the exact solution. In addition, the FSDT, HSDT and EHOPT are

able to capture the qualitative response of the in-plane displacement. The results of in-plane and transverse shear stresses are depicted in **Figs. 4.1.6 and 4.1.7**. From the results of stresses, it can be seen that the results of present model and LCW are well correlated with those of the exact solution. HSDT and EHOPT can provide somewhat accurate result of in-plane and transverse shear stresses. FSDT, however, fails to accurately capture the shape of exact solution.

To demonstrate the mechanical responses ($\bar{Q} \neq 0, \bar{T}_0 = 0, \bar{T}_1 = 0$) of composite plates, normalized displacement and stresses of material (1) are given in **Figs. 4.1.8-4.1.11**. Normalized distribution of in-plane displacements is shown in **Fig. 4.1.8**. From the result of in-plane displacement, one can be observed that the result obtained by present model agree well with the exact solutions. Although zig-zag distributions with slope discontinuities at interfaces have been well described by EHOPT which are contained zig-zag displacement fields, present model provides most accurate solution which is substantially coincides with the exact solutions. **Fig. 4.1.9** shows the distributions of in-plane stresses. As shown in **Fig. 4.1.9**, present result of σ_{11} gives best compromised result in compared with the exact solution which is discontinuous distribution at interfaces. In addition, it can be also seen that result of the EHOPT provides relatively accurate distributions of in-plane stresses. LCW, HSDT and FSDT, however, give somewhat inaccurate results for the distribution of in-plane stress. The results of transverse shear stresses have been plotted in **Figs. 4.1.10 and 4.1.11**. Distributions of the transverse shear stresses are obtained by equilibrium approach. As shown in **Figs. 4.1.10 and 4.1.11**, the kinky distribution of transverse shear stress can be well captured by present model and EHOPT (**Fig.**

4.1.10), while LCW, HSDT and FSDT cannot describe such a kinky distribution. Additionally, it can be observed that the present model can gives identical results with the exact solution.

4.1.4.2. Anti-symmetric Cross-ply Layup case

To further investigate the thermo-mechanical behaviors of composite plates, anti-symmetric cross-ply $[0^o/90^o/0^o/90^o]$ laminated composite is also considered.

Figs. 4.1.12-4.1.15 show the normalized distributions of displacement and stresses of material (2) subjected to the uniform temperature. **Figs. 4.1.12** present the normalized distributions of in-plane displacement. The asymmetric parabolic distribution of in-plane displacement (**Fig. 4.1.12**) is fairly well captured by present theory and LCW. The other theories, however, entirely fail to describe such a asymmetric parabolic shape because the transverse normal strain effect has been ignored in FSDT, HSDT and EHOPT. Normalized distributions of in-plane stresses are illustrated in **Figs. 4.1.13 and 4.1.14**. From the results, it can be seen that the present model and LCW show a highly accurate prediction of in-plane stresses by capturing discontinuous distribution of σ_{11} as well as symmetric parabolic shape of σ_{12}. The results obtained by other theories, however, significantly deviate from the exact solution. **Fig. 4.1.15** shows the normalized distribution of transverse shear stress. Form the **Fig. 4.1.15**, one can see that the present model and LCW have a highly fidelity for

the accurate predict the distribution of transverse shear stress. Zig-zag variation of σ_{13} is precisely described by present model and LCW.

Next the anti-symmetric cross-ply composite plates of material (2) subjected to the gradient temperature are considered to assess the performance of present model. **Fig. 4.1.16** shows the result of in-plane displacement. As one can see form **Fig. 4.1.16**, the results obtained by present model and LCW show excellent agreement with the exact solution. FSDT, HSDT and EHOPT, however, provide somewhat inaccurate result of in-plane displacement. Normalized distributions of in-plane and transverse shear stresses are plotted in **Figs. 4.1.17 and 4.1.18**. From the results, it can be observed that the results of present model and LCW match the exact solution with excellent accuracy, while the other theories provide slightly over-estimated results for the distributions of in-plane and transverse shear stresses.

For the mechanical loading case, normalized distributions of displacement and stresses of material (1) are shown in **Figs. 4.1.19-4.1.21**. Normalized distribution of the in-plane displacement is presented and examined in **Fig. 4.1.19**. As shown in **Fig. 4.1.19**, the results of the present model show excellent agreement with the exact solution. In addition, a good agreement between the EHOPT and exact solution is found for the in-plane displacement under mechanical loading. Present model and EHOPT can provide reliable distributions by accurately capturing the asymmetrical zig-zag shape of in-plane displacement. The results of FSDT, HSDT and LCW, however, provide somewhat inaccurate results. Variations of the in-plane and transverse shear stresses are illustrated in **Figs. 4.1.20 and 4.1.21**. For results in **Figs. 4.1.20 and**

4.1.21, the results of present model and EHOPT provide a best compromised results as compared with the exact solution. In **Fig. 4.1.21**, results of present model and EHOPT can precisely describe the kinky distribution of transverse shear stress. Especially the present model yields almost identical results with the exact solution. This clearly indicates that the present model has a great advantages in terms of accuracy and efficiency.

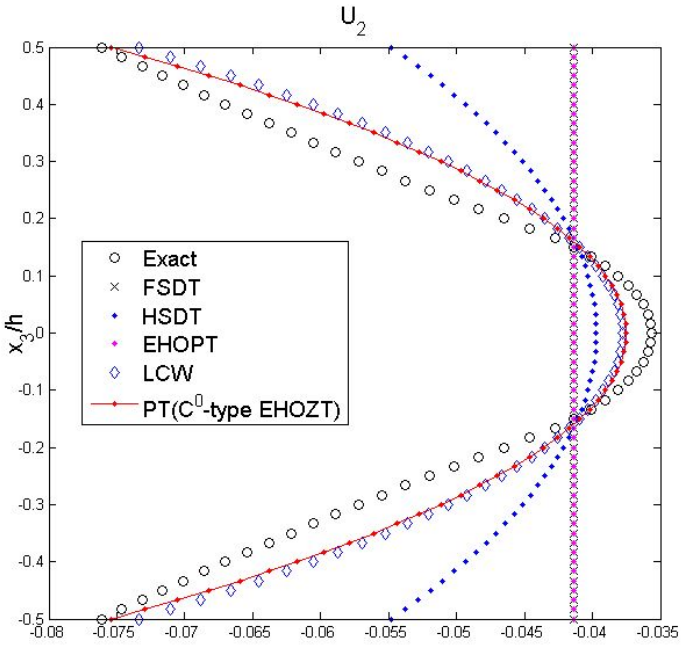

Fig. 4.1.1. In-plane displacements for [0^o / 90^o / 0^o] laminated plates under uniform temperature

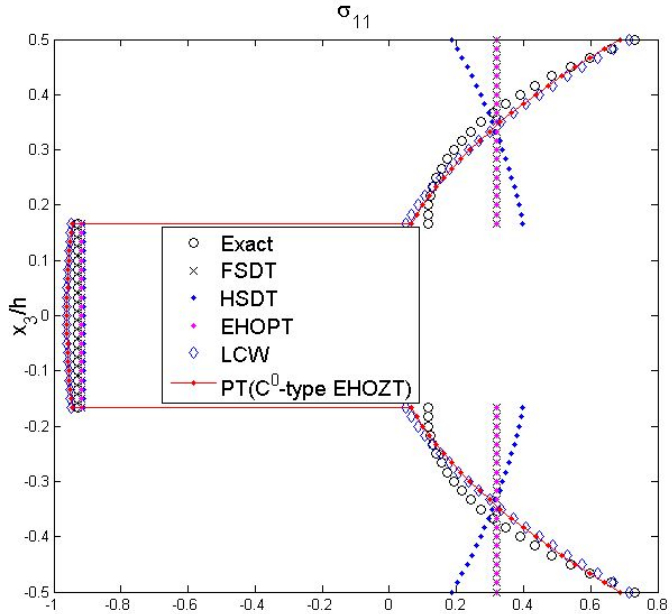

Fig. 4.1.2. In-plane stresses for [0^o / 90^o / 0^o] laminated plates under uniform temperature

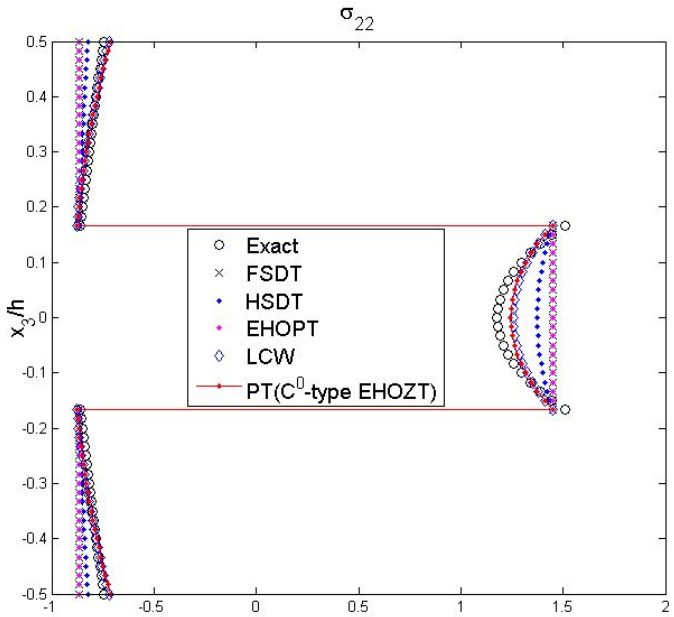

Fig. 4.1.3. In-plane stresses for [0^o / 90^o / 0^o] laminated plates under uniform temperature

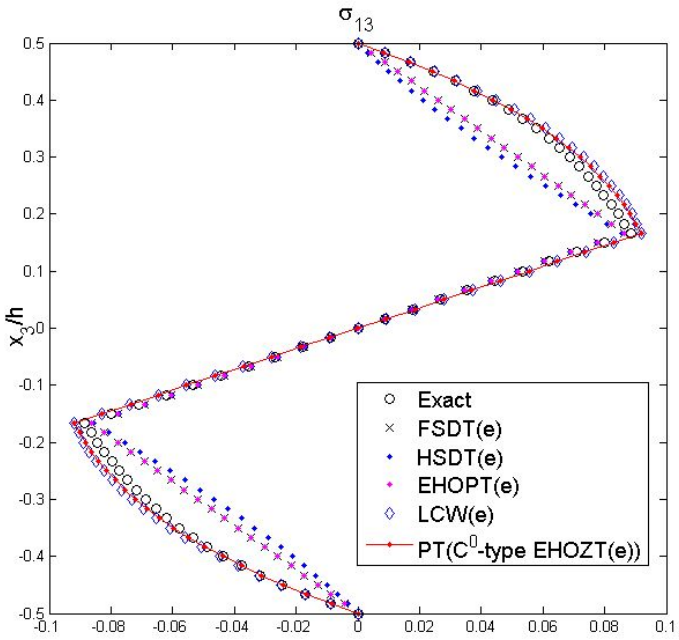

Fig. 4.1.4. Transverse shear stresses for [0^o / 90^o / 0^o] laminated plates under uniform temperature

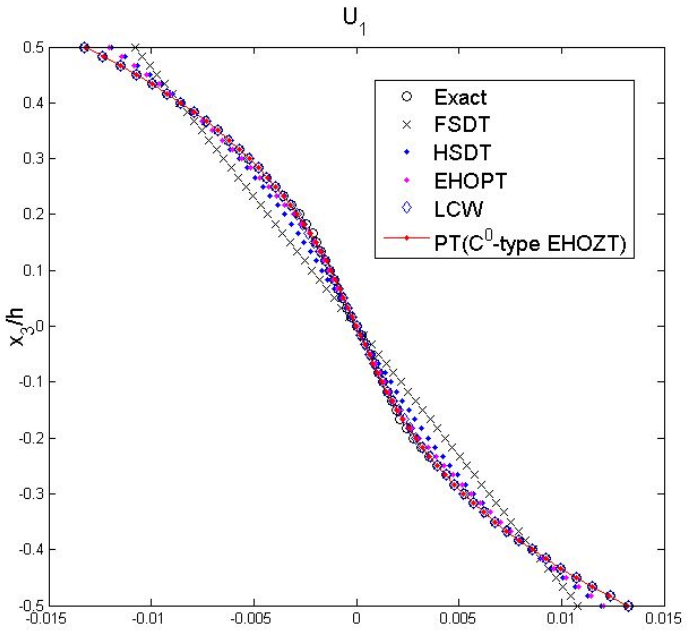

Fig. 4.1.5. In-plane displacements for [0^o / 90^o / 0^o] laminated plates under temperature gradient

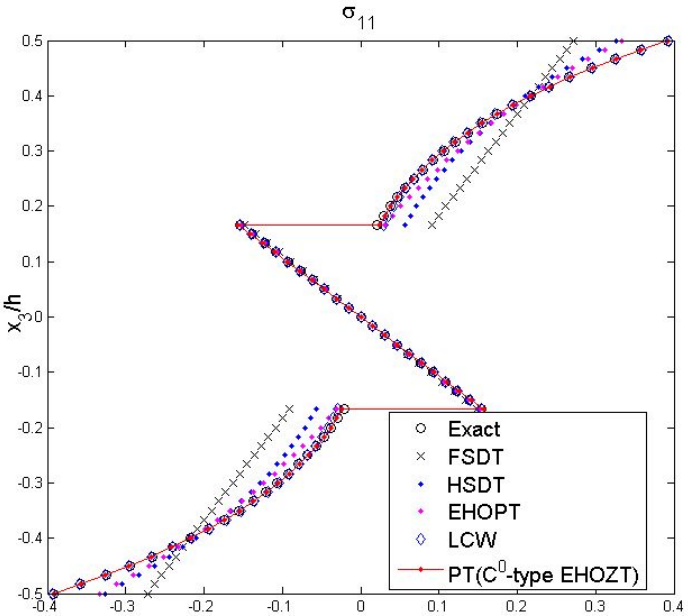

Fig. 4.1.6. In-plane stresses for [0^o / 90^o / 0^o] laminated plates under temperature gradient

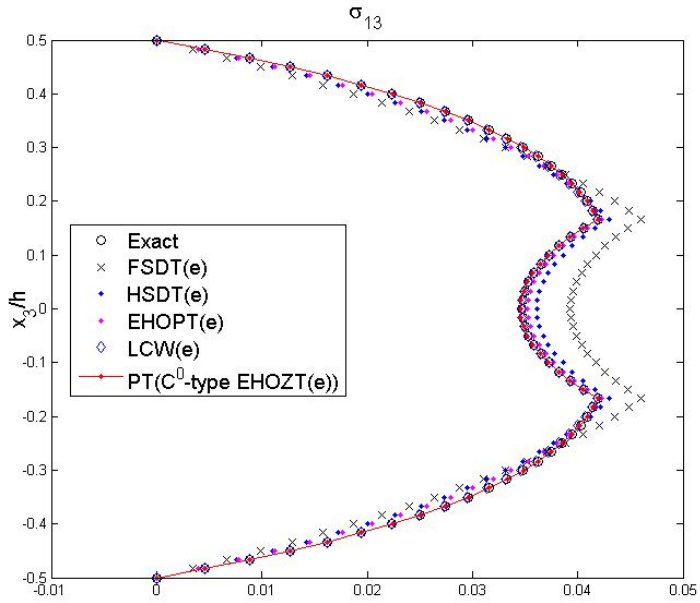

Fig. 4.1.7. Transverse shear stresses for $[0^o/90^o/0^o]$ laminated plates under temperature gradient

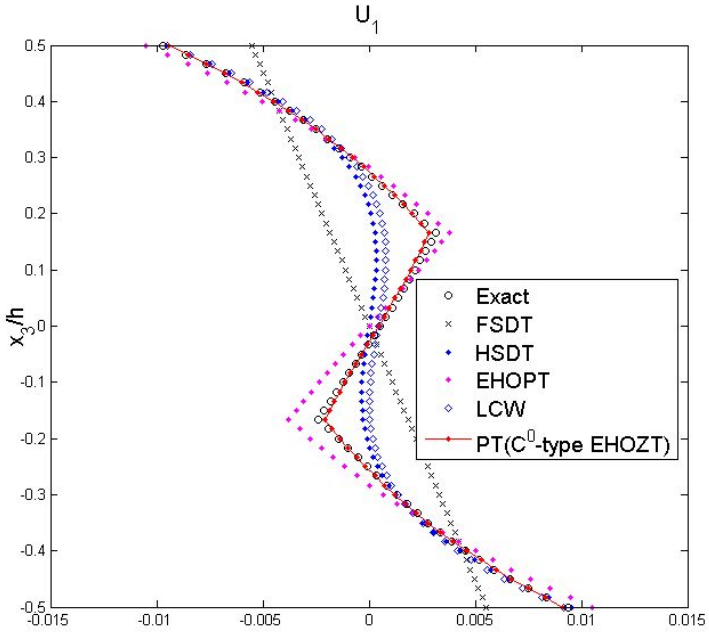

Fig. 4.1.8. In-plane displacements for $[0^o/90^o/0^o]$ laminated plates under mechanical loading

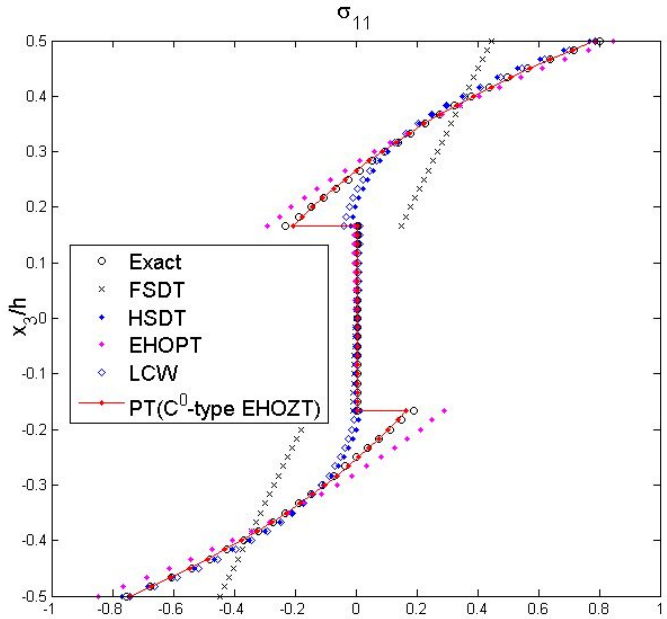

Fig. 4.1.9. In-plane stresses for [0^o / 90^o / 0^o] laminated plates under mechanical loading

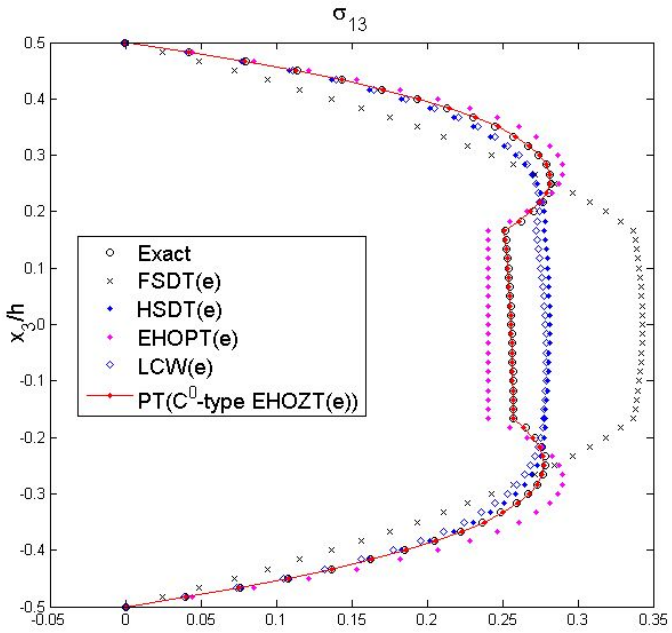

Fig. 4.1.10. Transverse shear stresses for [0^o / 90^o / 0^o] laminated plates under mechanical loading

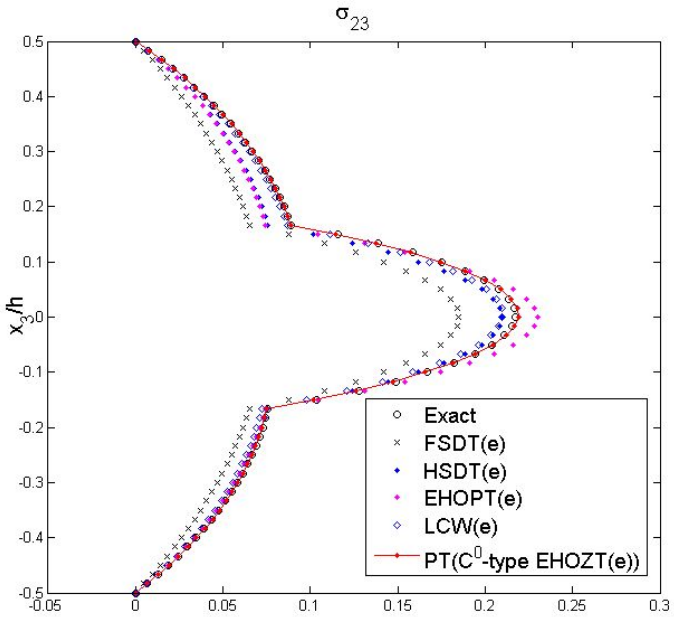

Fig. 4.1.11. Transverse shear stresses for [0^o / 90^o / 0^o] laminated plates under mechanical loading

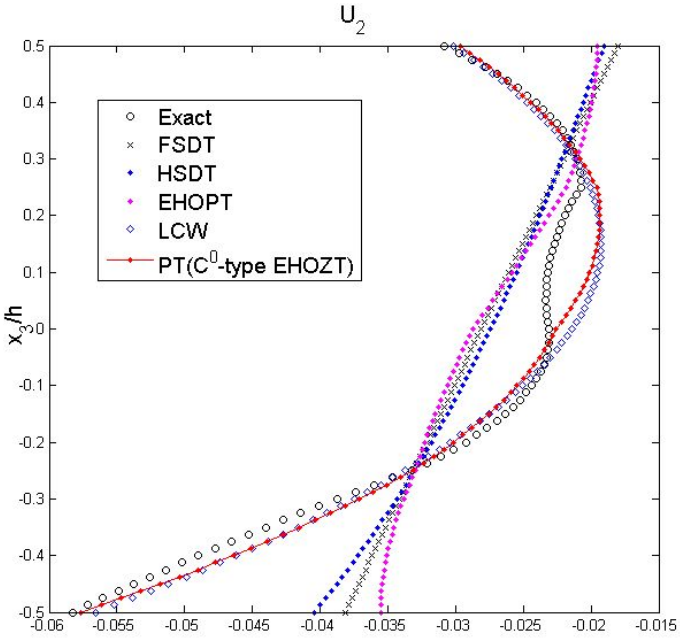

Fig. 4.1.12. In-plane displacements for [0^o / 90^o / 0^o / 90^o] laminated plates under uniform temperature

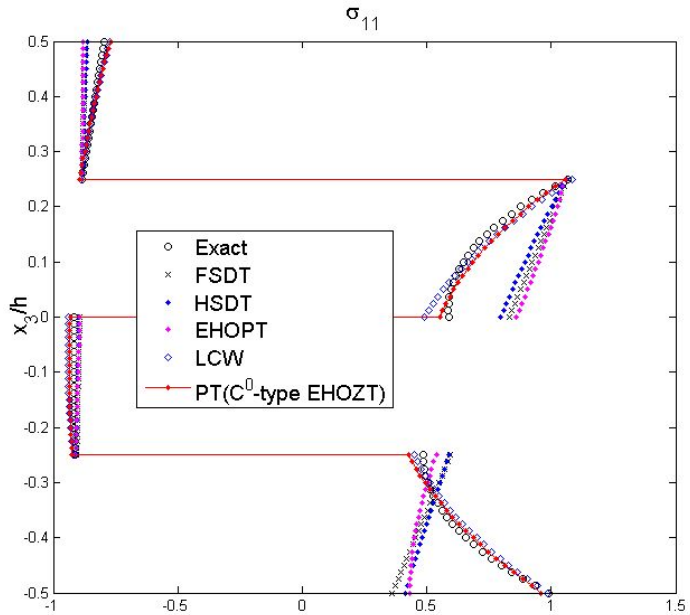

Fig. 4.1.13. In-plane stresses for [0^o / 90^o / 0^o / 90^o] laminated plates under uniform temperature

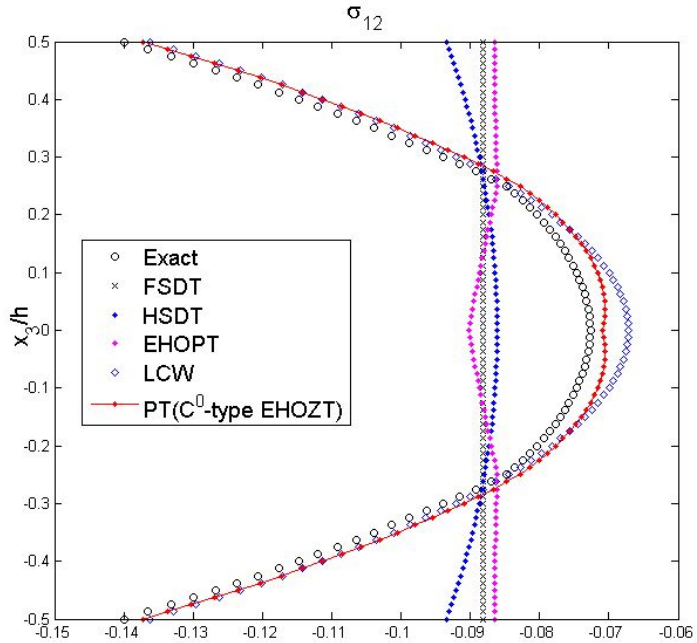

Fig. 4.1.14. In-plane stresses for [0^o / 90^o / 0^o / 90^o] laminated plates under uniform temperature

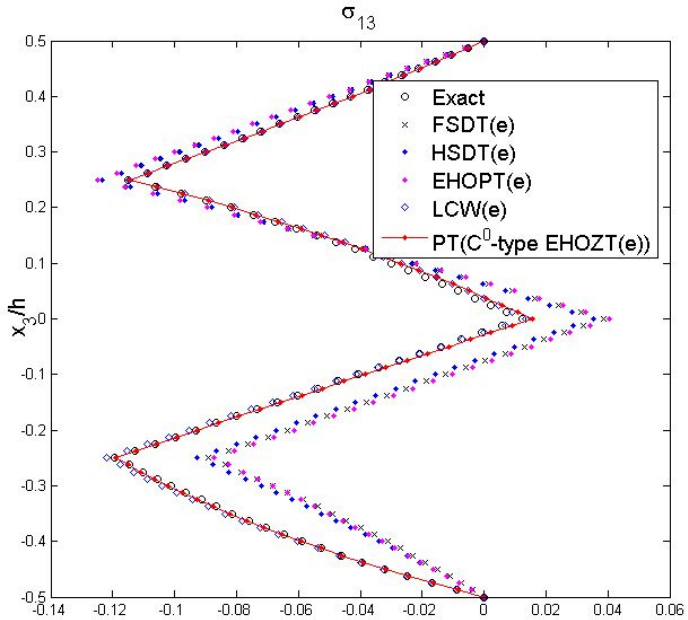

Fig. 4.1.15. Transverse shear stresses for [0^o / 90^o / 0^o / 90^o] laminated plates under uniform temperature

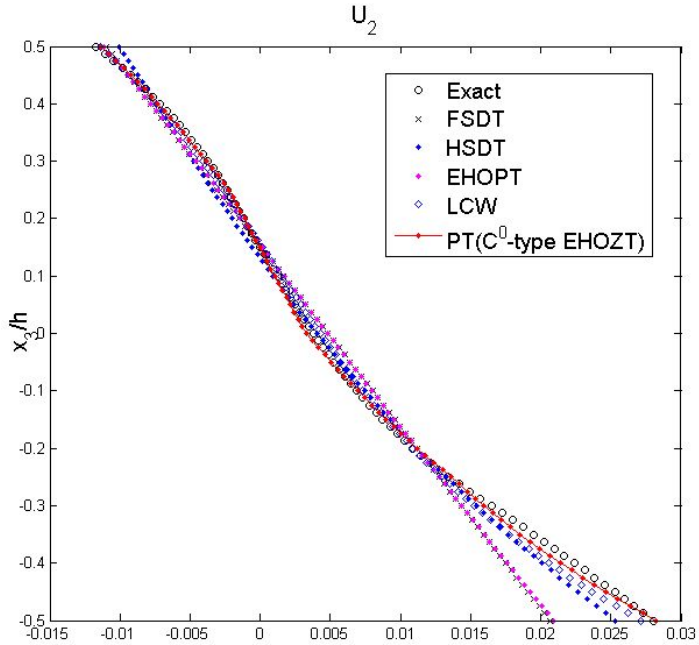

Fig. 4.1.16. In-plane displacements for [0^o / 90^o / 0^o / 90^o] laminated plates under temperature gradient

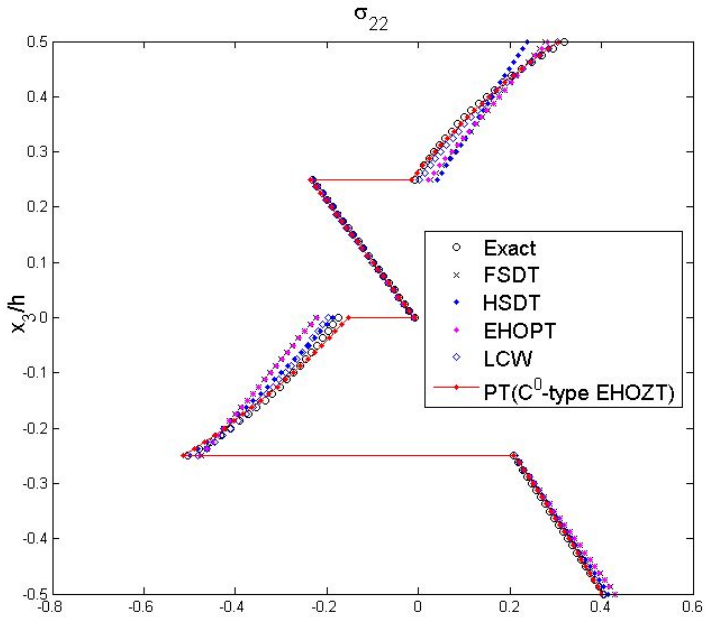

Fig. 4.1.17. In-plane stresses for [0^o / 90^o / 0^o / 90^o] laminated plates under temperature gradient

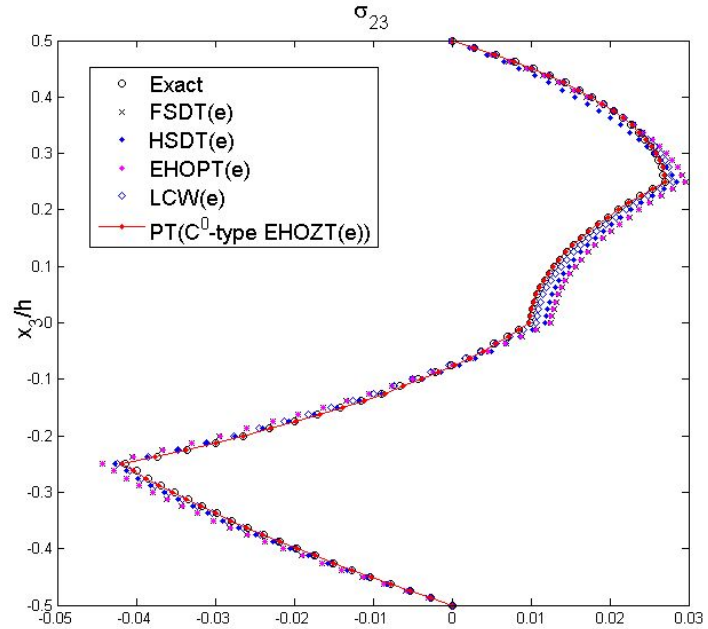

Fig. 4.1.18. Transverse shear stresses for [0^o / 90^o / 0^o / 90^o] laminated plates under temperature gradient

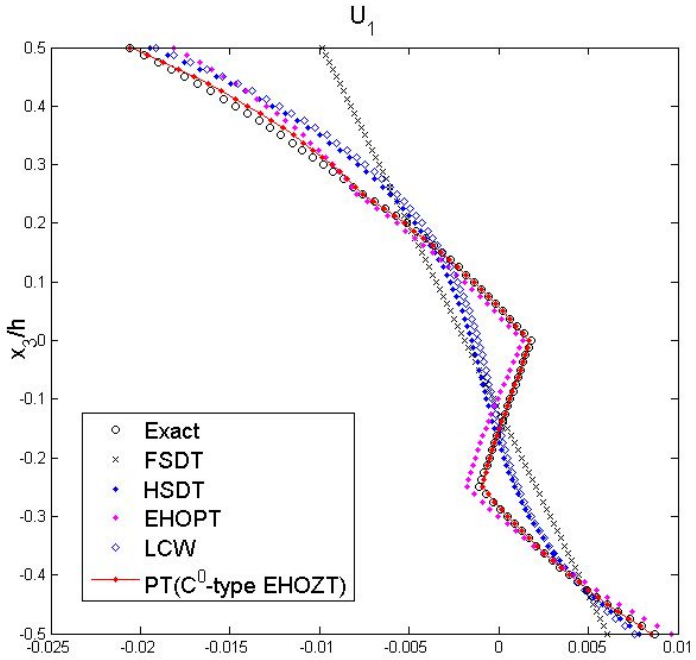

Fig. 4.1.19. In-plane displacements for [0^o / 90^o / 0^o / 90^o] laminated plates under mechanical loading

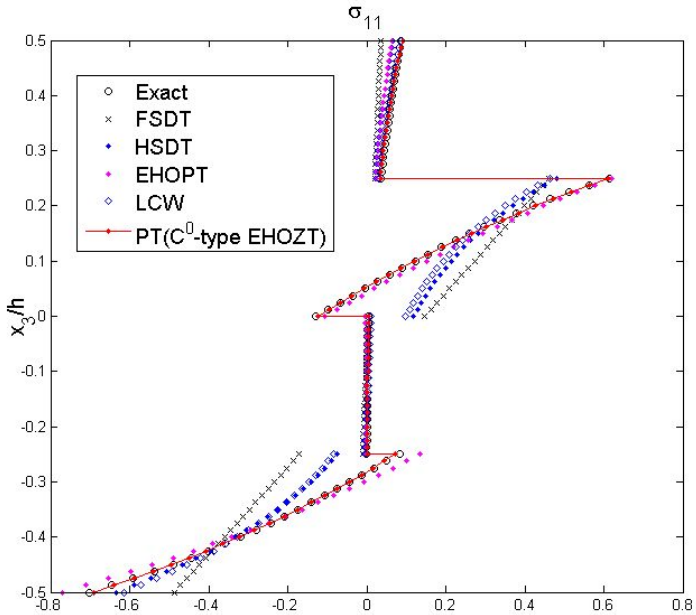

Fig. 4.1.20. In-plane stresses for [0^o / 90^o / 0^o / 90^o] laminated plates under mechanical loading

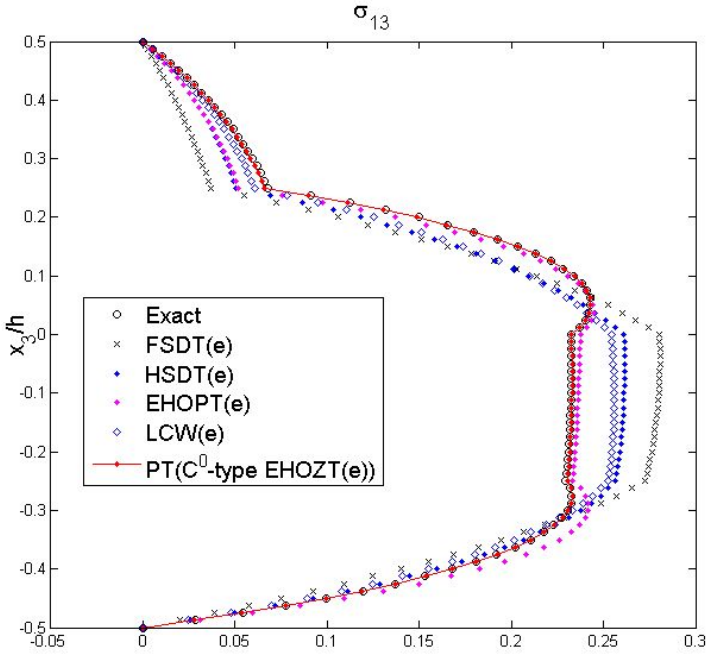

Fig. 4.1.21. Transverse shear stresses for [0^o / 90^o / 0^o / 90^o] laminated plates under mechanical loading

Chapter 5

Geometrically Nonlinear Analysis Based on Enhanced FSDT

5.1. Co-rotational Geometrically Nonlinear Formulation based on EFSDT

5.1.1. Literature Review

Thin and moderately thick laminated composite and sandwich plates with their excellent mechanical performance have been increasingly used in various fields of structural engineering. When the loading is applied, this type of structures is prone to geometrically nonlinear phenomena which is large displacement and rotation. So, geometrically nonlinear analysis should be considered in order to accurately predict their large deformed behavior as well as optimally design the laminated structures. The geometrically nonlinear analysis of laminated shell and plate structures is a complicated problem because their equilibrium state should be defined in the deformed configuration. According to the description

method for each element motion, the existing Lagrangian kinematic descriptions for geometrically nonlinear finite element method can be divided into three categories: (1) Total Lagrangian (TL), (2) Updated Lagrangian (UL) and Co-rotational (CR) formulation. For the TL formulation, equilibrium equations are established with respect to the initial configuration. For the UL formulation, those are referred to a deformed configuration which is based on the last converged solution. The CR formulation, which is based on the fixed configuration as in the TL formulation with a co-rotational configuration, is another efficient method to analyze the geometrically nonlinear behavior with large rotation and small strain.

Along these lines, the concept of an element independent co-rotational (EICR) formulation was introduced by Rankin and Brogan [71]. Further works on the EICR formulation were done by Rankin and Nour-Omid [72, 73] by considering a rotational projector matrix into the EICR formulation. Pacoste and Battini [74-76] employed the concept of rotational pseudo-vector in the EICR formulation to accurately describe the total rotation of element node. In addition, they provide the schemes to improve computational efficiency. Felippa and Haugen [77] summarized the existing EICR formulation and presented a unified CR formulation with small strain for geometrically nonlinear analysis. They also introduced the consistent symmetrizable equilibrated (CSE) CR formulation including the translational projection matrix to improve their numerical stability. Based on the CSE CR formulation, geometrically nonlinear dynamic analysis of laminated composite shell structures were carried out by Almeida and Awruch [78]. Furthermore, Yang and Xia [79] conducted nonlinear analysis for the thin shell structures with large rotation by employing the CSE CR formulation.

The main feature of the CR formulation is to extract pure elastic deformational motion from the total motion by introducing the CR frame which continuously translates and rotates with the element but does not deform with it. Due to the assumption of the small strain in the local CR frame, total deformation of each element can be decomposed into two parts: the rigid body motion of element and the pure elastic deformational motion based on the local CR configuration. Thus, element stiffness matrix and internal force vector of element can be established in the local CR frame by using the linear elastic finite element formulation, while the geometrically nonlinear effects are considered by transforming the element stiffness matrix and internal force vector in the local CR frame to those in the global coordinate system. Consequently, the main advantage of the CR formulation is that the existing excellent performance of linear elastic element can be transformed to a geometrically nonlinear one with just a little extra work. In addition, another advantage is that the transformation matrices are independent of the assumptions made for elements. This is to say that CR formulation for arbitrary element with the same geometry and node degrees of freedom (DOFs), the CR framework is exactly the same. Hence, the CR formulation is element independent.

In this subsection, to predict the geometrically nonlinear behavior of the relatively thick and thin laminated composite structures, the EFSDT based on co-rotational formulation is proposed and tested numerically. By applying the co-rotational configuration, the strain energy relationships between two theories (conventional FSDT and EHOPT) for the geometrically nonlinear analysis can be defined with similar manner as that of linear analysis model in the local CR frame. Therefore, one can come up with the conventional FSDT-like theory (i.e.

EFSDT) incorporating the simplicity of conventional FSDT and the accuracy of the third-order zig-zag model. Finally the results obtained are assessed by comparing them to those reported in the open literature.

5.1.2. Co-rotational Formulation

To analyze the geometrically nonlinear behavior of the laminated composite and sandwich plates, enhanced first-order shear deformation theory (EFSDT) based on the co-rotational formulation is considered in this subsection. The main feature of the co-rotational formulation is to decompose the motion of an element into the pure elastic deformational motion based on the local CR frame and the rigid-body translational and rotational motion. In EICR [77], decomposition of the total motion is purely based on its kinematic relations; the pure linear elastic deformational motion can be completely extracted from nonlinear deformational motion by applying EICR formulation to the local element (i.e., element independent formulation). Therefore, we efficiently implement the enhanced plate element based on EFSDT, which improve not only the accuracy of the geometrically nonlinear solution but also the efficiency of the computational process. Therefore, EICR is the effective method to analyze the geometric nonlinear behavior of the plate and shell structures. The matrix notation for the EICR formulation follows that of Ref. [79].

5.1.2.1. Co-rotational Kinematics of element

To enable kinematic extraction of rigid-body motions from the total element motion, co-rotational formulation requires different three configurations in terms of the before and after deformation of element, as shown in **Fig. 5.1.1**. These are the initial C^0, deformed C^D, and co-rotational C^R configurations. The initial configuration, C^0, is related to the undeformed condition without any motion of each element. The latter, C^R, is a theoretical concept introduced to intermediate phase between the initial and deformed configuration, which is based on the configuration of element after rigid-body translational and rotational motion before the elastic deformation. The deformed configuration, C^D, refers to the deformed condition of each element after pure elastic deformation in the local CR frame.

To describe the total motion of element, two kinds of coordinate systems (global and local coordinate system) are defined. C^R and C^D are defined the same local frame, as shown in **Fig. 5.1.1**, because the local frame is not translates and rotates during the linear elastic deformation. The local frame (e_i^0, e_i) and the local-to-global transformation matrix (T_0, T) are calculated in each element. Located at the centroid of each element, the local axis of e_1 can be defined as parallel to side 1-2 of each element, whereas e_3 is perpendicular vector to the plane of element. Based on the above definition of local axis, the local-to-global transformation matrix of the initial coordinate system can be given by:

$$
\begin{aligned}
&e_1^0 = \frac{x_{21}^0}{\left\| x_{21}^0 \right\|},\ e_3^0 = \frac{x_{21}^0 \times x_{31}^0}{\left\| x_{21}^0 \times x_{31}^0 \right\|},\ e_2^0 = e_3^0 \times e_1^0, \\
&T_0^T = \left[e_1^0 \quad e_2^0 \quad e_3^0 \right].
\end{aligned} \tag{5.1.1}
$$

where $x_{21}^0 = x_2^0 - x_1^0$, x_a^0 is the global coordinate-based position vector of the element node a in the initial configuration C^0. The transformation matrix of the element in the co-rotated coordinate system is then obtained with similar manner as that of the initial coordinate system as follows:

$$
\begin{aligned}
&e_1 = \frac{x_{21}}{\left\| x_{21} \right\|},\ e_3 = \frac{x_{21} \times x_{31}}{\left\| x_{21} \times x_{31} \right\|},\ e_2 = e_3 \times e_1, \\
&T^T = \left[e_1 \quad e_2 \quad e_3 \right].
\end{aligned} \tag{5.1.2}
$$

Based on the Eqs. (5.1.1) and (5.1.2), the transformation relationships between the vectors in the global and local coordinate system can be defined as

$$
\begin{aligned}
&\bar{x}_{C^0 a}^0 = T_0 x_{C^0 a}^0 = T_0 \left(x_a^0 - x_{C^0}^0 \right), \\
&\bar{x}_{Ca}^0 = T_0 x_{Ca} = T_0 \left(x_a - x_C \right),
\end{aligned} \tag{5.1.3}
$$

where $x_{C^0}^0 = \frac{1}{3}\sum_{a=1}^{3} x_a^0,\ x_C = \frac{1}{3}\sum_{a=1}^{3} x_a.$

The total deformational motion process of the element from the initial to deformed state needs two steps in terms of the intermediate configuration (local CR frame). In the first step, the element based on the initial configuration (C^0) is converted to the co-rotated configuration by the rigid body translational and rotational motion. The rigid body translation can be defined by the displacement vector in the global coordinate system, and the rigid body rotation can be described by the continuous rotation matrix. The second step is to extract the pure

elastic translation and rotation of element in the co-rotated coordinate system. Based on the above two steps, total deformation of each element can be decomposed into independent two parts: the rigid body translational and rotational motion of element and the pure elastic deformational motion in the local CR frame. So, elastic translation ($\bar{u}_{da}$) and rotation ($\bar{R}_{da}$) in the local coordinate system can be defined according to the geometric consideration.

In the global coordinate system, the pure elastic translation of node a can be defined by vector operation relationships as follows:

$$u_{da} = x_a - x_a^R = u_a + x_a^0 - u_C - x_{C^0}^0 - x_{Ca}^R. \tag{5.1.4}$$

The pure elastic rotation of node a in the global coordinate system can be obtained by the rotational matrix (R_a) as well as the transformation relationship for continuous rotation ($R_a = R_{da} R_o$):

$$R_{da} = R_a R_0^T. \tag{5.1.5}$$

From the deformational components in the global coordinate system (u_{da} and R_{da}), the pure elastic displacement in the local CR frame can be obtained by using the transformation relationship between the global and local coordinate system:

$$\begin{aligned} \bar{u}_{da} &= T u_{da} = T\left(u_a + x_a^0 - u_C - x_{C^0}^0\right) - \bar{x}_{C^0 a}^0, \\ \bar{R}_{da} &= T R_{da} T^T = T R_a T_0^T. \end{aligned} \tag{5.1.6}$$

5.1.2.2. Nodal Degrees of Freedom

In the process of EICR formulation, the rotation matrix (R) and the rotational pseudo-vector (θ) are assumed to describe the finite rotation. The rotational pseudo-vector can be obtained from the rotation matrix because the rotation matrix is a nonlinear function of the rotational pseudo-vector.

$$\bar{\theta}_{da} = \frac{\left\|\bar{\theta}_{da}\right\|}{2\sin\left\|\bar{\theta}_{da}\right\|}\begin{bmatrix} R_{32} - R_{23} \\ R_{13} - R_{31} \\ R_{21} - R_{12} \end{bmatrix}. \tag{5.1.7}$$

where R_{ij} are the component of the rotational matrix.

In the iterative process for solving geometrically nonlinear problem, the iterative incremental solutions are updated by additional infinitesimal incremental rotation ($\delta\bar{\omega}_{da}$). This infinitesimal incremental rotation is based on the finite rotation which can be obtained by the rotational pseudo-vector ($\delta\bar{\theta}_{da}$). Because $\delta\bar{\omega}_{da}$ and $\delta\bar{\theta}_{da}$, however, are not exactly same ($\bar{\theta}_{da} + \delta\bar{\omega}_{da} \neq \bar{\theta}_{da} + \delta\bar{\theta}_{da}$), the rotational pseudo-vector of the finite rotation cannot be directly calculated as $\bar{\theta}_{da} + \delta\bar{\omega}_{da}$ in updating the rotational degrees of freedom of each node. Therefore, transformation process between $\delta\bar{\omega}_{da}$ and $\delta\bar{\theta}_{da}$ is firstly required to express the same incremental rotation with the superposition characteristic.

The transformation relationship in the local coordinate system can be given by:

$$\begin{aligned}
&\delta\bar{\theta}_{da} = \bar{H}\left(\delta\bar{\theta}_{da}\right)\delta\bar{\omega}_{da}, \\
&\bar{H}\left(\delta\bar{\theta}_{da}\right) = I_3 - \frac{1}{2}spin\left(\delta\bar{\theta}_{da}\right) + \eta\, pin\left(\delta\bar{\theta}_{da}\right)^2,
\end{aligned} \tag{5.1.8}$$

where I_3 is a 3×3 identity matrix and the spinor matrix operator is

$$\begin{aligned}
spin\left(\delta\bar{\theta}_{da}\right) &= \begin{bmatrix} 0 & -\delta\bar{\theta}_{daz} & \delta\bar{\theta}_{day} \\ \delta\bar{\theta}_{daz} & 0 & -\delta\bar{\theta}_{dax} \\ -\delta\bar{\theta}_{day} & \delta\bar{\theta}_{dax} & 0 \end{bmatrix}, \\
\eta &= \frac{1-\frac{1}{2}\bar{\theta}_{da}\cot\left(\frac{1}{2}\bar{\theta}_{da}\right)}{\left(\bar{\theta}_{da}\right)^2} \\
&= \frac{1}{12} + \frac{1}{720}\bar{\theta}_{da}^2 + \frac{1}{30240}\bar{\theta}_{da}^4 + \frac{1}{1209600}\bar{\theta}_{da}^6 + \ldots..,
\end{aligned} \tag{5.1.9}$$

Where for the small angle ($\bar{\theta}_{da} \approx 0$), the coefficient η can be obtained by the power series expansion to improve their numerical stability.

The total displacement of the node in the global coordinate system is given as following vector:

$$d_a = \begin{bmatrix} u_a^T & R_a^T \end{bmatrix}^T. \tag{5.1.10}$$

In the solving process, the increment of total displacement vector of node a expressed by translation and incremental rotation ($\delta d_a = \begin{bmatrix} \delta u_a & \delta\omega_a \end{bmatrix}$). One essential step for the nonlinear analysis is to updating the nodal increment at the end of each iteration. Thus, the increment of rotational pseudo-vector $\delta\omega_a$ is used to update the rotational matrix R_a in the global coordinate system in each

iteration.

The procedure can be given as follows:

$$
\begin{aligned}
&R_{a,new} = R(\delta\omega_a)\,\mathrm{R}_{a,old}, \\
&R(\delta\omega_a) = I_3 + \frac{\sin(\delta\omega_a)}{\delta\omega_a} spin(\delta\omega_a) \\
&\qquad + \frac{1}{2}\left[\frac{\sin(\delta\omega_a/2)}{\delta\omega_a/2}\right]^2 spin(\delta\omega_a)^2 \\
&\qquad = I_3 + \left[1 - \frac{\|\delta\omega_a\|^2}{6} + \frac{\|\delta\omega_a\|^4}{120} - \frac{\|\delta\omega_a\|^6}{5040}\right] pin(\delta\omega_a) \\
&\qquad + \frac{1}{2}\left[1 - \frac{\|\delta\omega_a\|^2}{12} + \frac{\|\delta\omega_a\|^4}{3600}\right] spin(\delta\omega_a)^2
\end{aligned}
\tag{5.1.11}
$$

where $\delta\omega_a = \sqrt{\delta\omega_{ax}^2 + \delta\omega_{ay}^2 + \delta\omega_{az}^2}$.

5.1.2.3. Variation of Displacement Vector

In the global coordinate system, the consistent tangent stiffness matrix K_T of the element is obtained by the variation of the global internal force vector f relative to the global degrees of freedom.

$$
\delta f = K_T \delta d, \quad K_T = \frac{\partial f}{\partial d}. \tag{5.1.12}
$$

In order to calculate the K_T of the element, it is necessary to extract the increment of the elastic displacement vector in the local coordinate system

($\left[\delta\bar{u}_d \quad \delta\bar{\theta}_d\right]^T$) from the increment of the total displacement vector in the global coordinate system ($\left[\delta u \quad \delta\omega\right]^T$).

The relationship between the variation of the total and elastic deformational displacement vector of node a can be defined by:

$$\delta\begin{bmatrix}\bar{u}_{da}\\ \bar{\omega}_{da}\end{bmatrix}=\sum_{b=1}^{3}\bar{P}_{ab}\delta\begin{bmatrix}\bar{u}_b\\ \bar{\omega}_b\end{bmatrix},\quad \bar{P}_{ab}=\begin{bmatrix}U_{ab}+\bar{S}_a\bar{G}_{u,b} & 0_3\\ -\bar{G}_{u,b} & \delta_{ab}I_3\end{bmatrix}. \tag{5.1.13}$$

where

$$\begin{aligned}
&U_{ab}=\left(\delta_{ab}-\frac{1}{3}\right)I_3,\quad \bar{S}_a=spin\left(\bar{x}_a\right),\\
&\bar{G}_{u,1}=\frac{1}{2A}\begin{bmatrix} & \bar{x}_{32}\\ & \bar{y}_{32}\\ -2A/l_{12} & \end{bmatrix},\\
&\bar{G}_{u,2}=\frac{1}{2A}\begin{bmatrix} & \bar{x}_{13}\\ & \bar{y}_{13}\\ 2A/l_{12} & \end{bmatrix},\bar{G}_{u,3}=\frac{1}{2A}\begin{bmatrix} & \bar{x}_{21}\\ & \bar{y}_{21}\\ & \end{bmatrix}.
\end{aligned} \tag{5.1.14}$$

$\bar{P}_{ab}$ is a sub-block matrix of the projector matrix $\bar{P}$. Projector matrix plays a role in preservation of pure deformational motion, while discarding the rigid body motion. Through the projector matrix, the increment of pure elastic deformational displacement can be extracted from the increment of total displacement in the local coordinate system.

Final expression for the variation of pure elastic displacement vector can be given as follows:

$$
\begin{aligned}
&\delta\begin{bmatrix}\bar{u}_d\\ \bar{\theta}_d\end{bmatrix}=\begin{bmatrix}I & \\ & \bar{H}\end{bmatrix}\delta\begin{bmatrix}\bar{u}_d\\ \bar{\omega}_d\end{bmatrix}\\
&\delta\begin{bmatrix}\bar{u}_d\\ \bar{\omega}_d\end{bmatrix}=\bar{P}\delta\begin{bmatrix}\bar{u}\\ \bar{\omega}\end{bmatrix},\\
&\delta\begin{bmatrix}\bar{u}\\ \bar{\omega}\end{bmatrix}=T\delta\begin{bmatrix}u\\ \omega\end{bmatrix},\\
&\therefore\delta\begin{bmatrix}\bar{u}_d\\ \bar{\theta}_d\end{bmatrix}=\bar{H}\bar{P}T\delta\begin{bmatrix}u\\ \omega\end{bmatrix}.
\end{aligned}
\tag{5.1.15}
$$

5.1.3. Enhanced First-order Shear Deformation Theory

In this subsection, finite element model based on enhanced first-order shear deformation theory is considered in CR formulation to accurately and efficiently analyze the geometrically nonlinear behavior of laminated composite and sandwich plates. The main feature of the EFSDT is to systematically derive an improved strain energy expression for conventional FSDT in the co-rotated coordinate system, and then provide a way to recover the stresses and displacements to improve their accuracy. In EFSDT, the displacement fields of EHOPT and FSDT are independently assumed. The displacement fields based on EHOPT in the co-rotated coordinate system can be expressed as:

$$
\begin{aligned}
&u_\alpha^{(CR)}(x_i)=u_\alpha^{o(CR)}(x_\beta)-x_3\cdot u_{3,\alpha}^{o(CR)}(x_\beta)+\Phi_{\alpha\gamma}(x_3)\cdot\phi_\gamma^{(CR)}(x_\beta),\\
&u_3^{(CR)}(x_i)=u_3^{o(CR)}(x_\beta),
\end{aligned}
\tag{5.1.16}
$$

The displacement fields of conventional FSDT in the co-rotated coordinated

system are given as:

$$\begin{aligned}\hat{u}_\alpha^{(CR)}(x_i) &= \hat{u}_\alpha^{o(CR)}(x_\beta) + x_3 \cdot \hat{\theta}_\alpha^{(CR)}(x_\beta), \\ \hat{u}_3^{(CR)}(x_i) &= \hat{u}_3^{o(CR)}(x_\beta),\end{aligned} \tag{5.1.17}$$

The improved strain energy expression of EFSDT are systematically derived in co-rotated coordinated system. In order to derive the relationships between the EHOPT and conventional FSDT, the least-square sense approximation is applied to the displacements in co-rotated coordinate system (Eqs. (5.1.16) and (5.1.17)). Consequently, the least-square sense minimization of error between EHOPT and conventional FSDT yields the following relationships:

$$\begin{aligned}&\min_{\hat{u}_{(0)}^{(CR)}} \left\langle \left\| u^{(\mathrm{CR})} - \hat{u}^{(\mathrm{CR})} \right\|_2 \right\rangle = 0 \rightarrow \hat{u}_\alpha^{o(CR)} = u_\alpha^{o(CR)} + C_{\alpha\gamma} \cdot \phi_\gamma^{(CR)}, \\ &\min_{\hat{u}_{(1)}^{(CR)}} \left\langle \left\| u^{(\mathrm{CR})} - \hat{u}^{(\mathrm{CR})} \right\|_2 \right\rangle = 0 \rightarrow \hat{\theta}_\alpha^{(CR)} = -u_{3,\alpha}^{o(CR)} + \Gamma_{\alpha\gamma} \cdot \phi_\gamma^{(CR)},\end{aligned} \tag{5.1.18}$$

$$C_{\alpha\gamma} = \frac{1}{h}\left\langle \Phi_{\alpha\gamma} \right\rangle, \quad \Gamma_{\alpha\gamma} = \frac{12}{h^3}\left\langle x_3 \cdot \Phi_{\alpha\gamma} \right\rangle.$$

From Eq. (5.1.18), the relationships for the in-plane strain and effective transverse shear strain vectors can be expressed in the following form:

$$\begin{aligned}\hat{E}_o^{(CR)} &= \left(E_o^{(CR)} + \tilde{C} \cdot K_h^{(CR)} \right), \\ \hat{K}_o^{(CR)} &= \left(K_o^{(CR)} + \tilde{\Gamma} \cdot K_h^{(CR)} \right), \\ \overline{\phi} &= \hat{\Gamma}\overline{\gamma},\end{aligned} \tag{5.1.19}$$

$$\overline{\phi} = \begin{bmatrix} \phi_1 \\ \phi_2 \end{bmatrix}, \quad \hat{\Gamma} = \begin{bmatrix} \Gamma_{11} & \Gamma_{12} \\ \Gamma_{21} & \Gamma_{22} \end{bmatrix}^{-1} \quad \overline{\gamma} = \begin{bmatrix} \hat{\gamma}_{31}^{(CR)} \\ \hat{\gamma}_{32}^{(CR)} \end{bmatrix}.$$

From the eq. (5.1.19), the strain energy of the EHOPT can be transformed into that of conventional FSDT because the strain relationships between the two theories are defined. The reduced strain energy expression of EHOPT can be written as:

$$\begin{aligned} 2U_{EHOPT}^{(\mathrm{CR})} &= E_o^{(CR)T} A E_o^{(CR)} + 2E_o^{(CR)T} B K_o^{(CR)} + K_o^{(CR)T} D K_o^{(CR)} \\ &+ 2E_o^{(CR)T} E K_h^{(CR)} + 2K_o^{(CR)T} F K_h^{(CR)} + K_h^{(CR)T} H K_h^{(CR)} \\ &+ \overline{\phi}^T G\, \overline{\phi}\ . \end{aligned} \tag{5.1.20}$$

To utilize the variables of the conventional FSDT, the reduced strain energy expression of EHOPT should be rewritten based on the strain relationships of Eq. (5.1.19). Substituting the Eq. (5.1.19) into the above expression for the strain energy of EHOPT yields

$$\begin{aligned} 2U_{EHOPT}^{(\mathrm{CR})} &= \left(\hat{E}_o^{(CR)} - \tilde{C}\cdot K_h^{(CR)}\right)^T A \left(\hat{E}_o^{(CR)} - \tilde{C}\cdot K_h^{(CR)}\right) \\ &+ 2\left(\hat{E}_o^{(CR)} - \tilde{C}\cdot K_h^{(CR)}\right)^T B \left(\hat{K}_o^{(CR)} - \tilde{\Gamma}\cdot K_h^{(CR)}\right) \\ &+ \left(\hat{K}_o^{(CR)} - \tilde{\Gamma}\cdot K_h^{(CR)}\right)^T D \left(\hat{K}_o^{(CR)} - \tilde{\Gamma}\cdot K_h^{(CR)}\right) \\ &+ 2\left(\hat{E}_o^{(CR)} - \tilde{C}\cdot K_h^{(CR)}\right)^T E K_h^{(CR)} \\ &+ 2\left(\hat{K}_o^{(CR)} - \tilde{\Gamma}\cdot K_h^{(CR)}\right)^T F K_h^{(CR)} \\ &+ K_h^{(CR)T} H K_h^{(CR)} + \overline{\gamma}\left(\hat{\Gamma}^T G \hat{\Gamma}\right)\overline{\gamma}. \end{aligned} \tag{5.1.21}$$

After rearranging the strain energy expression of Eq. (5.1.21), one can decompose $U_{EHOPT}^{(\mathrm{CR})}$ into those of the conventional FSDT-like theory and error energy as follows:

$$2U_{EHOPT}^{(\mathrm{CR})} = 2U_{FSDT-like}^{(\mathrm{CR})} + 2U_{Error}^{(\mathrm{CR})}, \tag{5.1.22}$$

The detailed expression of $U_{FSDT-like}^{(\mathrm{CR})}$ and $U_{Error}^{(\mathrm{CR})}$ is given by:

$$\begin{aligned} 2U_{FSDT-like}^{(\mathrm{CR})} = \hat{E}_o^{(CR)\mathrm{T}} A \hat{E}_o^{(CR)} + 2\hat{E}_o^{(CR)\mathrm{T}} B \hat{K}_o^{(CR)} \\ + \hat{K}_o^{(CR)\mathrm{T}} D \hat{K}_o^{(CR)} + \overline{\gamma}^T \hat{G} \overline{\gamma}, \end{aligned} \tag{5.1.23}$$

$$\begin{aligned} 2U_{Error}^{(\mathrm{CR})} &= 2\hat{E}_o^{(CR)T} \cdot \left[-A\tilde{C} - B\tilde{\Gamma} + E \right] \cdot K_h^{(CR)} \\ &+ 2\hat{K}_o^{(CR)T} \cdot \left[-B^T \tilde{C} - D\tilde{\Gamma} + F \right] \cdot K_h^{(CR)} \\ &+ K_h^{(CR)T} \begin{bmatrix} \tilde{C}^T A \tilde{C} + 2\tilde{C}^T B \tilde{\Gamma} + \tilde{\Gamma}^T D \tilde{\Gamma} \\ -2\tilde{C}^T E - 2\tilde{\Gamma} F + H \end{bmatrix} K_h^{(CR)}. \end{aligned} \tag{5.1.24}$$

The U_{Error} indicates the strain energy difference between the two theories. Then, the relationship matrices $\tilde{C}$ and $\tilde{\Gamma}$ are determined by minimizing U_{Error} as close to be zero as possible. That can be fulfilled by satisfying the following relationships:

$$\begin{aligned} -A\tilde{C} - B\tilde{\Gamma} + E = 0, \\ -B^T \tilde{C} - D\tilde{\Gamma} + F = 0. \end{aligned} \tag{5.1.25}$$

Once we have found the solution for minimizing the error energy ($U_{Error} \approx 0$), the strain energy of EHOPT can be successfully expressed in terms of the variables of conventional FSDT-like theory and their effective transverse shear stiffness can be obtained by

$$\hat{G} = \hat{\Gamma}^T \cdot G \cdot \hat{\Gamma}. \tag{5.1.26}$$

Note that the stiffness matrices coincide with that of conventional FSDT except the transverse shear stiffness matrix. Matrices A, B and D are the well-

known transformed reduced stiffness of the conventional FSDT, whereas the transverse shear stiffness modulus are modified by applying the strain energy transformation. Therefore, the effect of shear correction factor automatically identified through mechanics-based consideration in the present model.

5.1.3.1. Tangent Stiffness Matrix and Internal Force

A conventional Newton-Raphson algorithm is used to solve the geometrically nonlinear finite element equations. An adaptive step-size control scheme depending on the stiffness matrix conditions [80] is also used to improve their iteration stability. The tangent stiffness matrix of the element in the global coordinate system can be given by:

$$
\begin{aligned}
&K = K_{GR} + K_{GP} + K_{GM} + K_{M},\\
&K_{M} = T^{T}\bar{P}^{T}\bar{H}^{T}\bar{K}^{e}\bar{H}\bar{P}T,\\
&K_{GR} = -T^{T}\bar{F}_{nm}\bar{G}T,\\
&K_{GM} = T^{T}\bar{P}^{T}\bar{M}\bar{P}T,\\
&K_{GP} = -T^{T}\bar{G}^{T}\bar{F}_{n}\bar{P}T.
\end{aligned}
\tag{5.1.27}
$$

where K_M is the material stiffness matrix in the global coordinate system, in which local stiffness matrix based on EFSDT ($\bar{K}^e$) is employed to derive K_M. K_{GR}, K_{GM} and K_{GP} are the geometric stiffness matrices.

The internal force vector of the element in the global coordinate system can be

expressed as:

$$\Delta f = T^T \bar{P}^T \bar{H}^T \bar{f}^e = T^T \bar{P}^T \bar{H}^T (\bar{\mathrm{K}}^e \bar{\mathrm{d}}_d). \tag{5.1.28}$$

As shown in Eq. (5.1.27), the material and geometric stiffness matrices are categorized according to the geometric nonlinearity; (K_{GR}: rotational geometric stiffness, K_{GM} : moment correction geometric stiffness, K_{GP} : eauilibrium projection geometric stiffness). The subscripts M, GR, GM and GP are related to the variations of matrices f, T, H and P, respectively. The assembled global tangent stiffness matrix is expressed as K. From Eq. (5.1.27), it can be seen that the tangent stiffness matrix of the element is a non-symmetric matrix.

5.1.3.2. Linear triangular element based on OPT and EFSDT

The finite element formulation of the linear elastic element is defined based on the virtual work variational principle; its derivation can be given by:

$$\begin{aligned} \delta W = \int_V \delta u_i \sigma_{ij,j} dV &= \int_V \left[\nabla \left(\delta u_i \sigma_{ij} \right) - \delta u_{i,j} \sigma_{ij} \right] dV \\ &= \int_S \delta u_i t_i dS - \int_V \delta u_{i,j} \sigma_{ij} dV. \end{aligned} \tag{5.1.29}$$

The first term on the right-hand side accounts for the prescribed boundary state; thus the stiffness matrix can be constructed by employing the second term in Eq. (5.1.29) as follow:

$$\begin{aligned}\int_V \delta u_{i,j}\sigma_{ij}dV &= \int_V \delta u_{i,j}\left(\sigma_{ij}^{\varepsilon}+\sigma_{ij}^{\omega}\right)dV \\ &= \int_V \delta\varepsilon_{ij}\sigma_{ij}^{\varepsilon}dV + \int_V \delta\omega_{ij}\sigma_{ij}^{\omega}dV,\end{aligned} \tag{5.1.30}$$

with $\omega_{ij}=\left(u_{i,j}-u_{j,i}\right)/2$. Because the element rotation tensor is skew-symmetric matrix ($\sigma_{ij}^{w}=-\sigma_{ij}^{w}$), component of strain-rotation coupling can be negligible in their finite element equation. Therefore, the formulation for each plate element given as follows:

$$\delta W = \delta\overline{d}_d \cdot \overline{K}^e \cdot \overline{d}_d, \tag{5.1.31}$$

with

$$\overline{K}^e = \left[\overline{K}^m + \overline{K}^b + 2\overline{K}^{mb}\right] + \left[\overline{K}^s\right], \tag{5.1.32}$$

in which

$$\begin{aligned}\overline{K}^m &= \int_A B^{\varepsilon T}\cdot\hat{A}\cdot B^{\varepsilon}dA, \quad \overline{K}^b = \int_A B^{\kappa T}\cdot\hat{D}\cdot B^{\kappa}dA, \\ \overline{K}^{mb} &= \int_A B^{\varepsilon T}\cdot\hat{B}\cdot B^{\kappa}dA, \ \overline{K}^s = \int_A B^{\phi T}\cdot\hat{G}\cdot B^{\phi}dA.\end{aligned} \tag{5.1.33}$$

The superscripts ε, κ and ϕ in the series of B matrices in Eq. (5.1.33) stand for the strain, curvature, and rotation, respectively. In this subsection, linear triangular elements with 18 degrees of freedom is employed to analyze geometrically nonlinear behavior of the composite and sandwich plates, which is illustrated in **Fig. 5.1.2**. In this plate element, the optimal membrane triangular (OPT) element proposed by Felippa [81] is used to construct the membrane and membrane-bending coupling stiffness of the element ($\overline{K}^m$ and $\overline{K}^{mb}$). It is based on the ANDES natural strain, especially optimized for in-plane bending behavior and numerically circumvent the aspect-ratio locking problem. The OPT elements

are used to calculate the membrane strain and drilling rotation in terms of u_x, u_y, θ_z.

For the bending and transverse shear behavior of the plate, mindlin triangular elements based on the enhanced first-order shear deformation theory [18] are utilized. The bending and transverse shear part of the motion is denoted by the superscript *b* and *s*, respectively. Curvature-related strain ($\kappa_{\alpha\beta}$ and $\gamma_{3\alpha}$) in terms of u_z, θ_x and θ_y are calculated by using the EFSDT element. To circumvent shear locking problem, adequate scheme proposed by Kim et al [82] is considered in mindlin triangular element. It should be point out that the material stiffness matrix can be established in the initial configuration because the local coordinate system in each element are exactly same. In addition, it should be emphasized that the plate element based on EFSDT only needs to replace the material stiffness matrix $\bar{K}^e$ of the element to consider other elements with 3 nodes and 18 DOF.

5.1.4. Numerical results and Discussion

The ability of combining the EICR formulation with the EFSDT plate elements to solve geometrically nonlinear problems of laminated composite and sandwich structures is demonstrated in this subsection. To investigate the capability of the proposed model (CR formulation with the EFSDT) and to identify its limitation, some geometric nonlinear problems were tested. The results used for comparison in the following are mainly taken from the popular benchmark problems for

geometric nonlinear analysis proposed by Sze et al [80]. For the numerical example, (1) cantilever isotropic plate (thickness is assumed to be thin), (2) cantilever laminated composite plates (thickness is assumed to be thin) and (3) moderately thick sandwich plate with simply supported as well as all clamped boundary conditions are considered.

5.1.4.1. Cantilever isotropic plate

A narrow cantilever isotropic plate subjected to the end shear force is considered as shown in **Fig. 5.1.3**. The material properties and its length, width and thickness are given as follows:

$$\begin{aligned} &E = 1.2\times 10^{6}, \quad v = 0, \\ &L = 10, \quad b = 1, \quad h = 0.1, \\ &P_o = \frac{EI}{L^2} = 1, \; P_{\max} = 4P_o. \end{aligned} \tag{5.1.34}$$

The cantilever isotropic plate is modeled with 32 x 4 x 2 triangular element in the CR formulation based on EFSDT, 32 x 4 rectangular element in the 2-D FEM solution and 200 x 20 x 6 solid element in 3-D FEM solution by using the commercial software (ANSYS and ABAQUS). The results obtained by present model are compared with those calculated by 3-D and 2-D FEM solution as well as CR formulation based on conventional FSDT. **Fig. 5.1.4** plots the end shear force against the vertical and horizontal tip deflections. In addition, **Fig. 5.1.5** shows the middle axis displacements at each step of the end shear force. Form the results plotted in **Figs. 5.1.4 and 5.1.5**, it can be observed that the result

obtained by present model are in good agreement with those of commercial software (3-D and 2-D FEM solution) and CR formulation based on conventional FSDT.

As the second numerical example, a narrow cantilever isotropic plate subjected to the end moment is considered (**Fig. 5.1.6**). The material properties and its length, width and thickness are given as follows:

$$\begin{aligned} &E = 1.2\times 10^{6}, \quad \nu = 0, \\ &L = 12, \quad b = 1, \quad h = 0.1, \\ &M_o = \frac{EI}{L} = \frac{25}{3}, \; M_{\max} = 2\pi M_o. \end{aligned} \tag{5.1.35}$$

Using the classical flexural formula $R = EI/M$, the analytical normalized deflections for the cantilever bending problem can be derived as follows:

$$\frac{U}{L} = \frac{M_o}{M}\sin\frac{M}{M_o} - 1, \quad \frac{W}{L} = \frac{M_o}{M}\left(1 - \cos\frac{M}{M_o}\right). \tag{5.1.36}$$

where $M_o = EI/L$. The maximum $M_{\max}$ is taken to be $2\pi M_o$ at which the cantilever beam will be bent into a circle. In this problem, **Fig. 5.1.7** plots the end moment against the vertical and horizontal tip deflections. Additionally, middle axis deformations at each step of the end moment is depicted in **Fig. 5.1.8**. As can be seen in **Figs. 5.1.7 and 5.1.8**, the result obtained by present model agrees well with the analytical solution as well as those of 2-D FEM solution and CR formulation based on conventional FSDT.

5.1.4.2. Cantilever composite plates

A narrow cantilever orthotropic composite plates is considered. The material properties of the composite plates and it's length, width and thickness are given as follows:

$$\begin{aligned} &E_L / E_T = 25, \quad G_{LT} / E_T = 0.5, \quad E_T = 1\times 10^6, \\ &G_{TT} / E_T = 0.2, \; v_{LT} = v_{TT} = 0.25, \\ &L = 10, \quad b = 1, \quad L/h = 100, \quad P_{\max} = 50. \end{aligned} \tag{5.1.37}$$

The cantilever composite plate is modeled with 32 x 4 x 2 triangular element in the CR formulation based on EFSDT and 200 x 20 x 6 solid element in 3-D FEM solution. The results obtained by present model are compared with those calculated by 3-D FEM solution as well as CR formulation based on conventional FSDT.

Fig. 5.1.9 plots the end shear force against the vertical and horizontal tip deflections for the symmetric cross-ply $[0^o / 90^o / 90^o / 0^o]$ composite plates. As can be seen in **Fig. 5.1.9**, present model are in good agreement with comparable results (3-D FEM solution and CR formulation based on conventional FSDT). The vertical and horizontal tip deflections against the end shear force for the anti-symmetric cross-ply $[90^o / 0^o / 90^o / 0^o]$ composite plates is presented in **Fig. 5.1.10**. From the result, like the symmetric cross-ply case, it can be observed that the result obtained by present model are fairly well matched with those of 3-D FEM solution. From **Fig. 5.1.9 and Fig. 5.1.10**, it can be also seen that the magnitude of the tip deflection can become severe in the case of anti-symmetric

cross-ply lay-up. In addition, the results obtained by CR formulation based on EFSDT and conventional FSDT are almost same because the effect of transverse shear deformation can be negligible in the case of thin plates.

5.1.4.3. Moderately thick sandwich plates

To further investigate geometric nonlinear behavior of the laminated structures, moderately thick sandwich plate ($L_1/h = L_2/h = 10$) is also considered. A sandwich plate is a very challenging problem because it experiences a significant shear deformation due to the flexible core material. For the sandwich plate, the material properties of a face sheet are the same as Eq. (5.1.37), and those of the core material are taken as:

$$\begin{aligned} &E_1 = E_2 = E_3 = E_L/1724, \\ &G_{12} = G_{23} = G_{13} = E_L/4310, \\ &v_{12} = v_{13} = v_{23} = 0.25. \end{aligned} \tag{5.1.38}$$

The sandwich plate is modeled with $100 \times 100 \times 2$ triangular element in the CR formulation based on EFSDT and $100 \times 100 \times 40$ quadratic solid element in the 3-D FEM analysis. The results obtained by present model are compared with those calculated by commercial software 3-D FEM solution as well as CR formulation based on conventional FSDT.

The rectangular sandwich plates with simply supported boundary condition is

considered. The geometry of the sandwich plates illustrated in **Fig. 5.1.11**. For the simply supported boundary condition, double sinusoidal mechanical pressure is prescribed on the top surface of the structure, which take the form of

$$P(x_\alpha, \tfrac{h}{2}; t) = P_o \sin(\tfrac{\pi}{L_1} \cdot x) \cdot \sin(\tfrac{\pi}{L_2} \cdot y). \tag{5.1.39}$$

The deflections for the center point of the structure against the magnitude of the sinusoidal pressure is depicted in **Fig. 5.1.12**. From **Fig. 5.1.12**, it can be observed that the deflections obtained by present model are fairly well matched with 3-D FEM solution in the case of linear elastic as well as geometrically nonlinear solution. The result of conventional FSDT, however, provides significantly underestimated value because conventional FSDT cannot accurately describe the severe transverse shear deformation of the sandwich plates. Additionally, geometric nonlinearity cannot be observed in the result of conventional FSDT due to their inflexible behavior. To further study on the geometrically nonlinear behavior, displacement and stresses are also investigated. The global distribution of the in-plane displacement is given in **Fig. 5.1.13**. For the in-plane displacement, the result of present model agree well with the 3-D FEM solution by capturing the zig-zag distribution, while conventional FSDT gives inaccurate distribution for the in-plane displacement. **Figs. 5.1.14 and 5.1.15** show the normalized distribution of in-plane stress. As can be seen in **Figs. 5.1.14 and 5.1.15**, present model fairly well capture the discontinuous distribution of the in-plane stresses, whereas conventional FSDT cannot. The normalized distribution of transverse shear stress based on constitutive (**Fig. 5.1.16**) as well as equilibrium approach (**Fig. 5.1.17**) are also

presented. In **Fig. 5.1.16**, transverse shear stress obtained by present model comparatively accurate by satisfying the shear free condition at the surfaces of the structure as well as shear continuity conditions at the layer interfaces. Conventional FSDT, however, cannot satisfy the transverse shear stress conditions and provide severe overestimated distribution at the face sheets of the sandwich plates. Transverse shear stress based on the equilibrium approach provides more accurate results as shown in **Fig. 5.1.17**. The kink shapes of transverse shear stress can be accurately captured by the present model, whereas conventional FSDT cannot represent the kink shape. Additionally, the result of present model is qualitatively and quantitavely close to the 3-D FEM solution as compared to the conventional FSDT. It is noteworthy that transverse shear forces obtained by present model and conventional FSDT are not exactly same because moment is dependent on the shear correction factors in 2-D plate problem. This is one of the merits of using the present model.

The rectangular sandwich plates with all clamped boundary condition is also investigated. In this case, uniform distributed pressure is applied on the top surface of the structure. The deflections for the center point of the structure against the magnitude of the uniform pressure is presented in **Fig. 5.1.18**. The present model provides reliable deflection as compared to the 3-D FEM solution in the case of linear elastic and geometrically nonlinear behavior. The result of the present model, however, is comparatively inaccurate as compared to those of **Fig. 5.1.12** because present model cannot accurately consider the edge effect caused by clamped boundary condition. **Fig. 5.1.19** shows the global distribution of the in-plane displacement, and results of the in-plane stress are depicted in

Figs. 5.1.20 and 5.1.21. As can be seen in **Figs. 5.1.19-21**, present model captures very well both the zig-zag shape of displacement as well as the discontinuous through-the-thickness variations of in-plane stress. However, conventional FSDT fail to provide reliable distributions of in-plane displacement and stresses. The results of transverse shear stress based on the constitutive and equilibrium approach are plotted in **Figs. 5.1.22 and 5.1.23**. From the **Figs. 5.1.22 and 5.1.23**, present model gives best compromised results as compared to the 3-D FEM solution. In prediction of transverse shear stress, conventional FSDT shows a terribly poor performance because conventional FSDT cannot describe the severe transverse shear deformation caused by flexible core material.

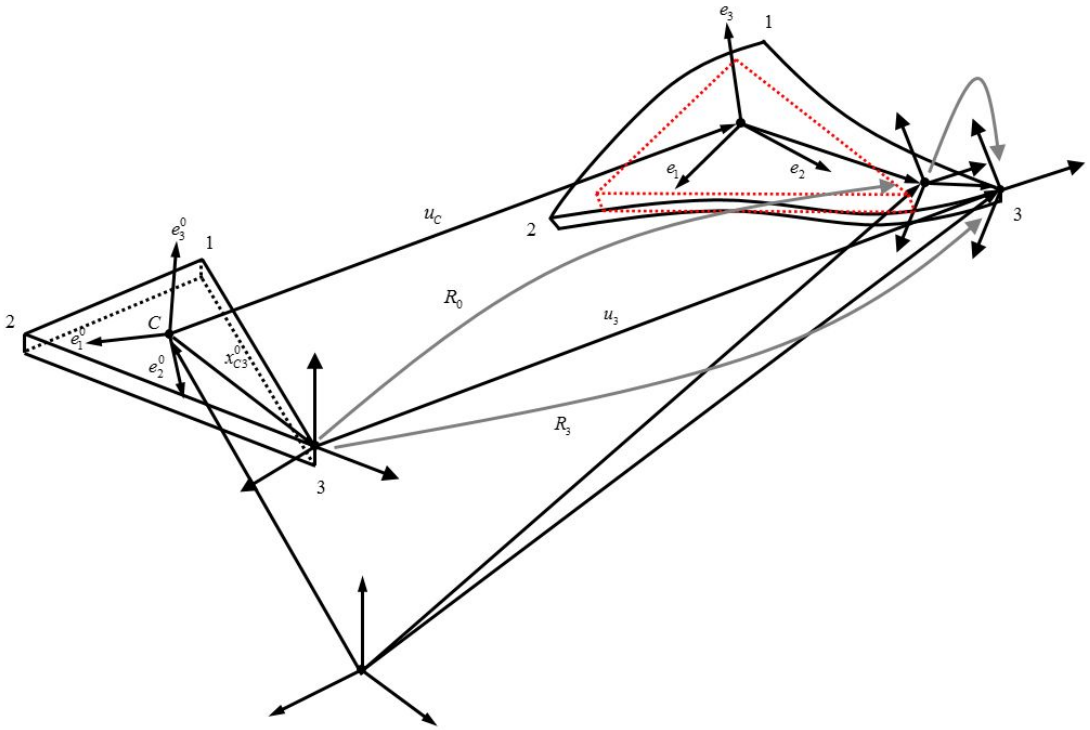

Fig. 5.1.1. Kinematics of EICR

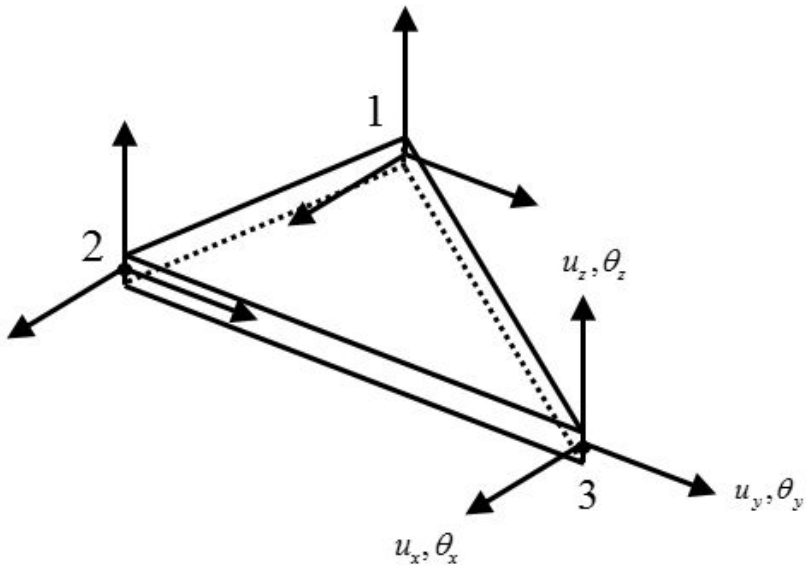

Fig. 5.1.2. Three-node plate element with 18 DOF

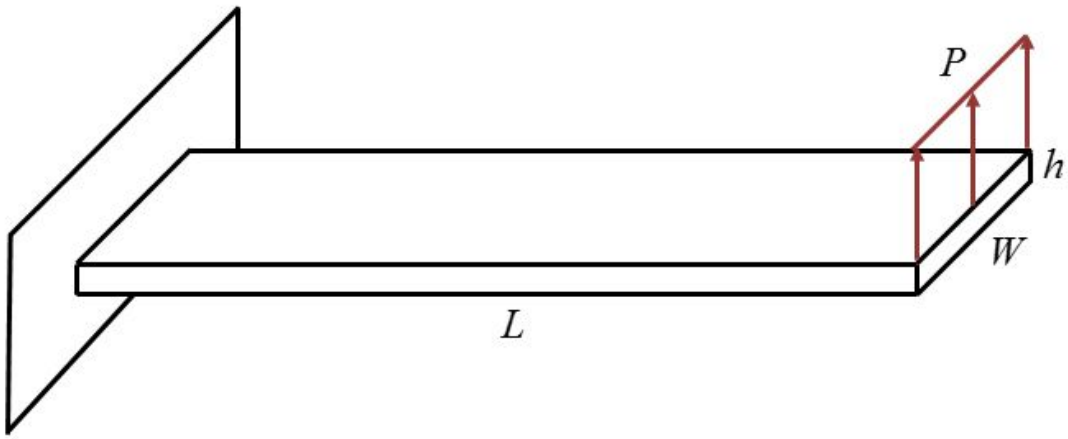

Fig. 5.1.3. Cantilever plate subjected to end shear force

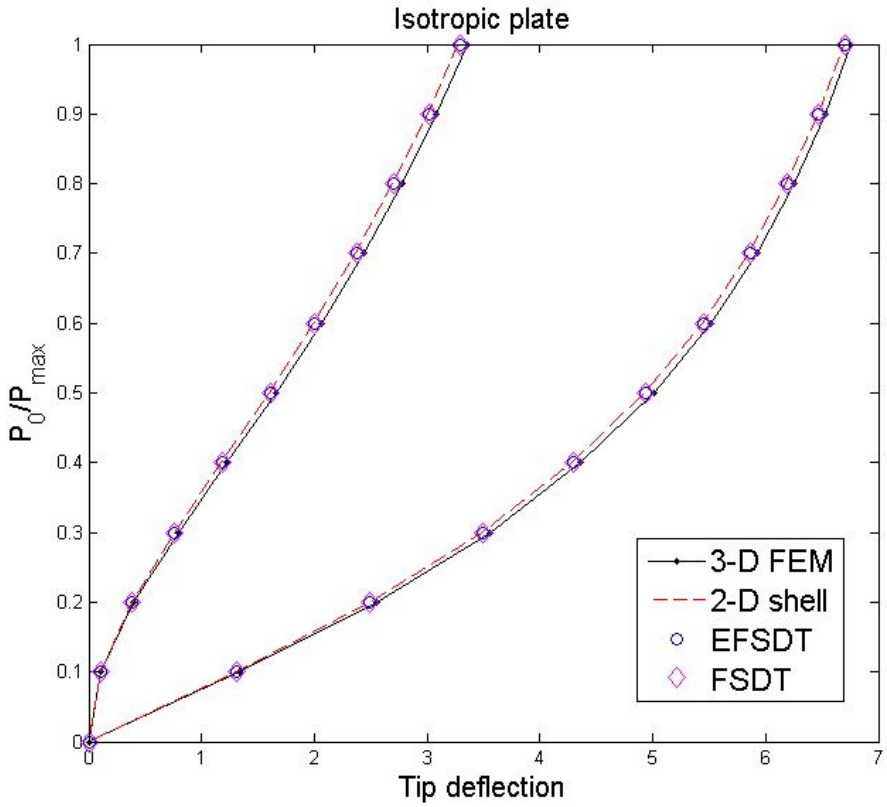

Fig. 5.1.4. Load-deflection curves for isotropic cantilever subjected to end shear force

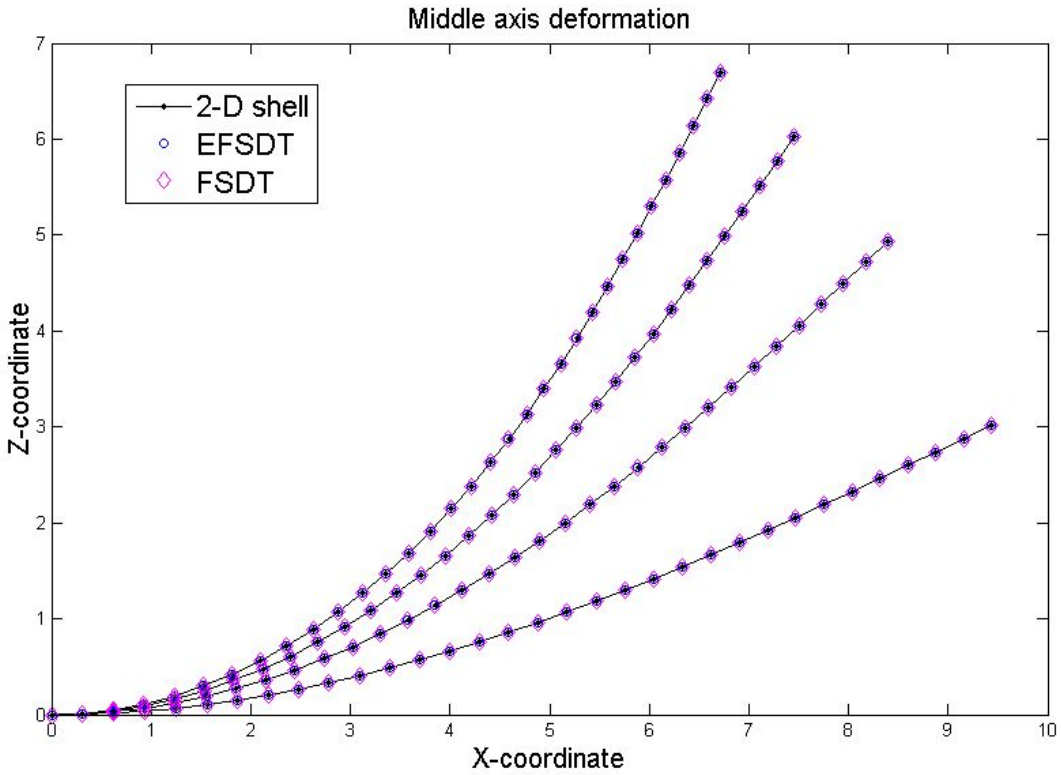

Fig. 5.1.5. Middle axis deformation for isotropic cantilever subjected to end shear force

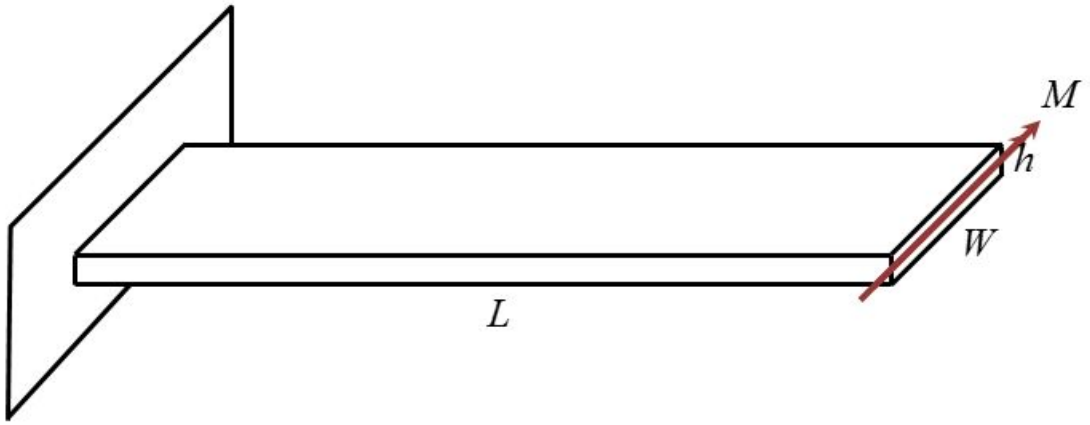

Fig. 5.1.6. Cantilever plate subjected to end bending moment

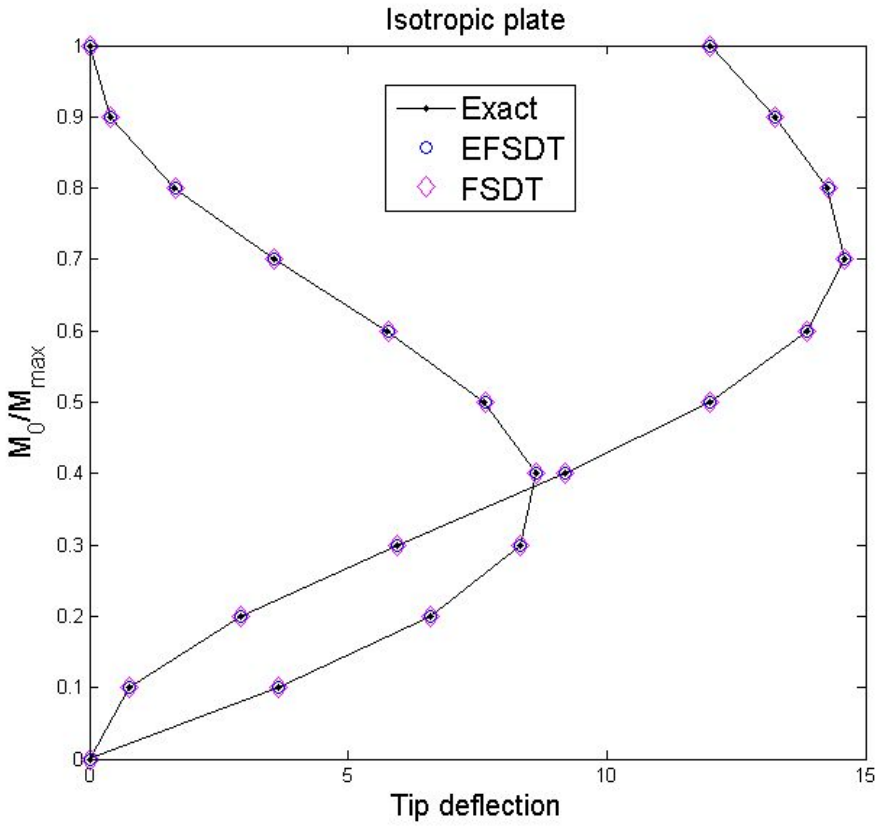

Fig. 5.1.7. Load-deflection curves for isotropic cantilever subjected to end bending moment

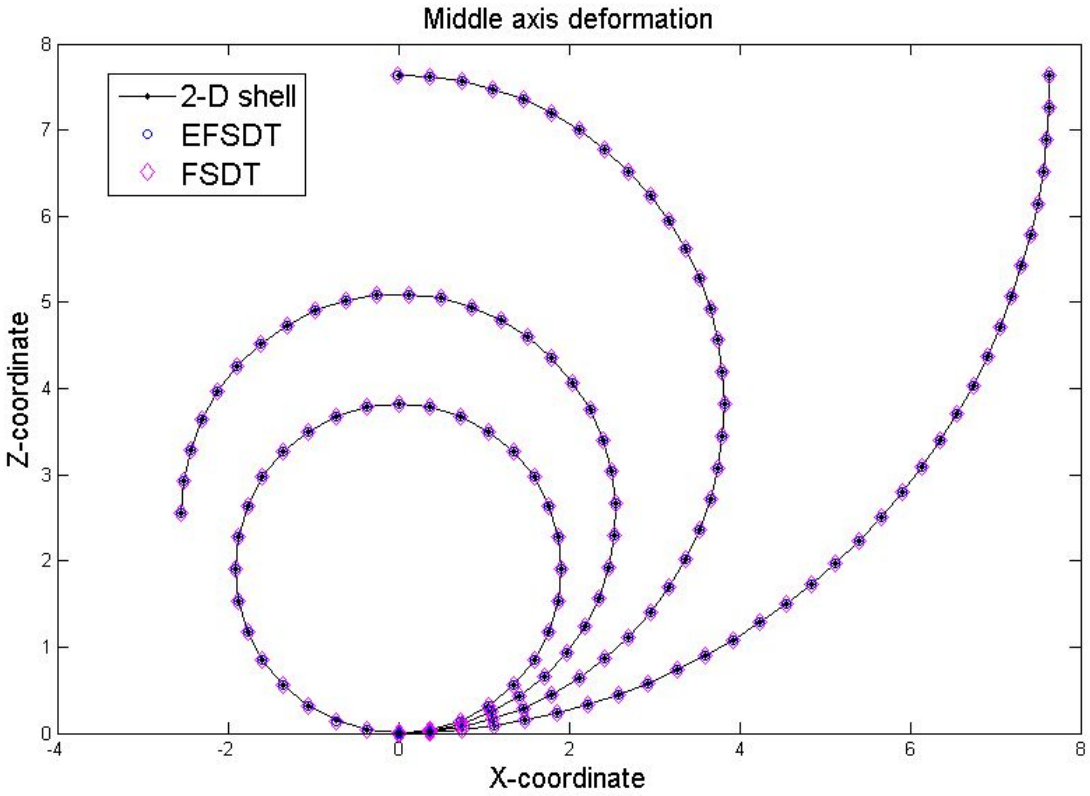

Fig. 5.1.8. Middle axis deformation for isotropic cantilever subjected to end bending moment

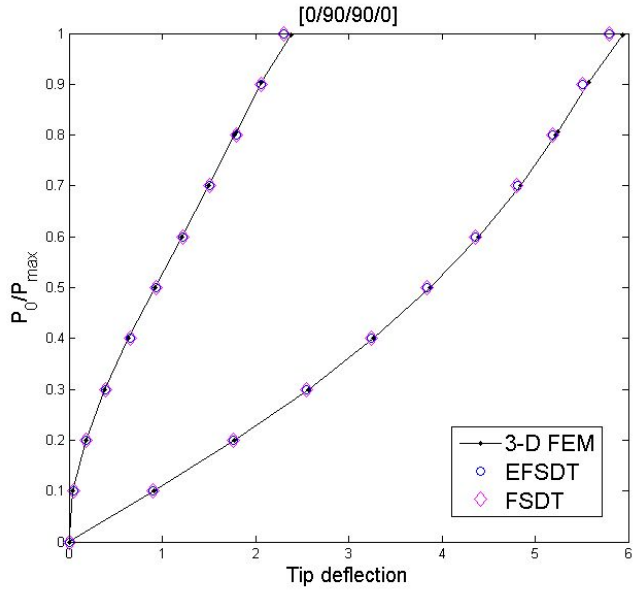

Fig. 5.1.9. Load-deflection curves for $[0^o/90^o/90^o/0^o]$ composite cantilever subjected to end shear force

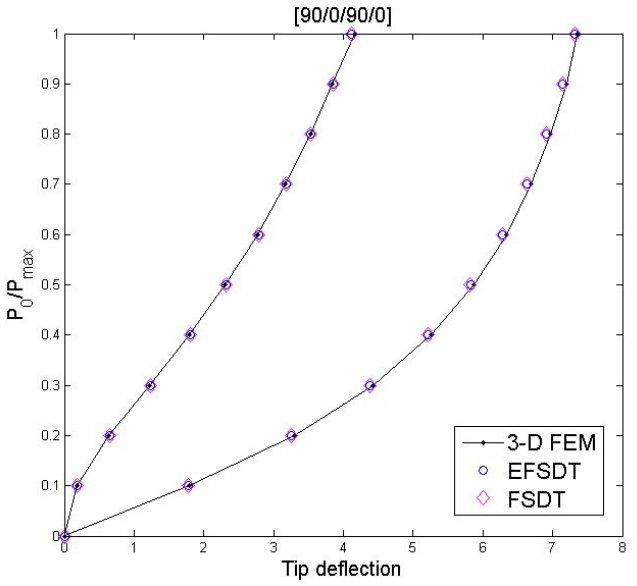

Fig. 5.1.10. Load-deflection curves for $[90^o/0^o/90^o/0^o]$ composite cantilever subjected to end shear force

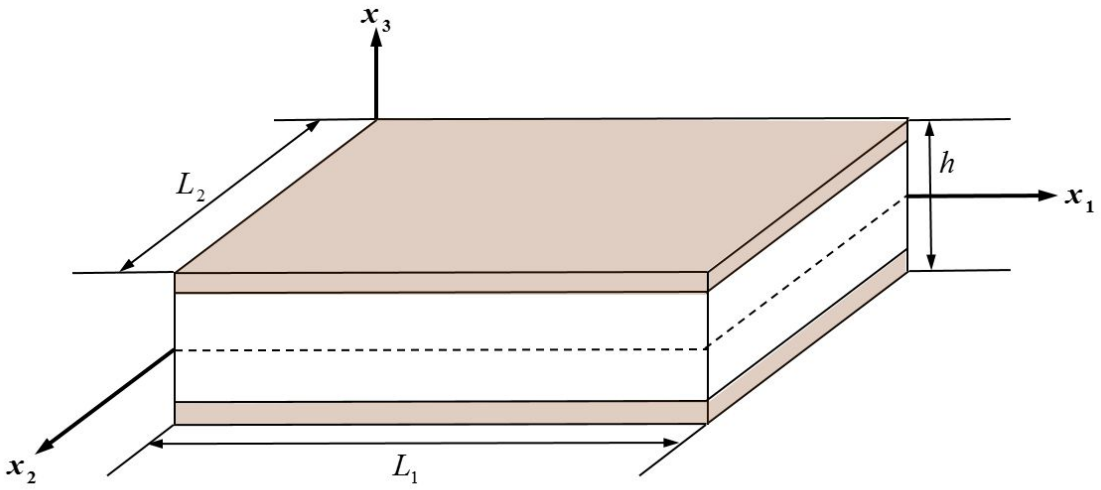

Fig. 5.1.11. Geometry of the sandwich plates

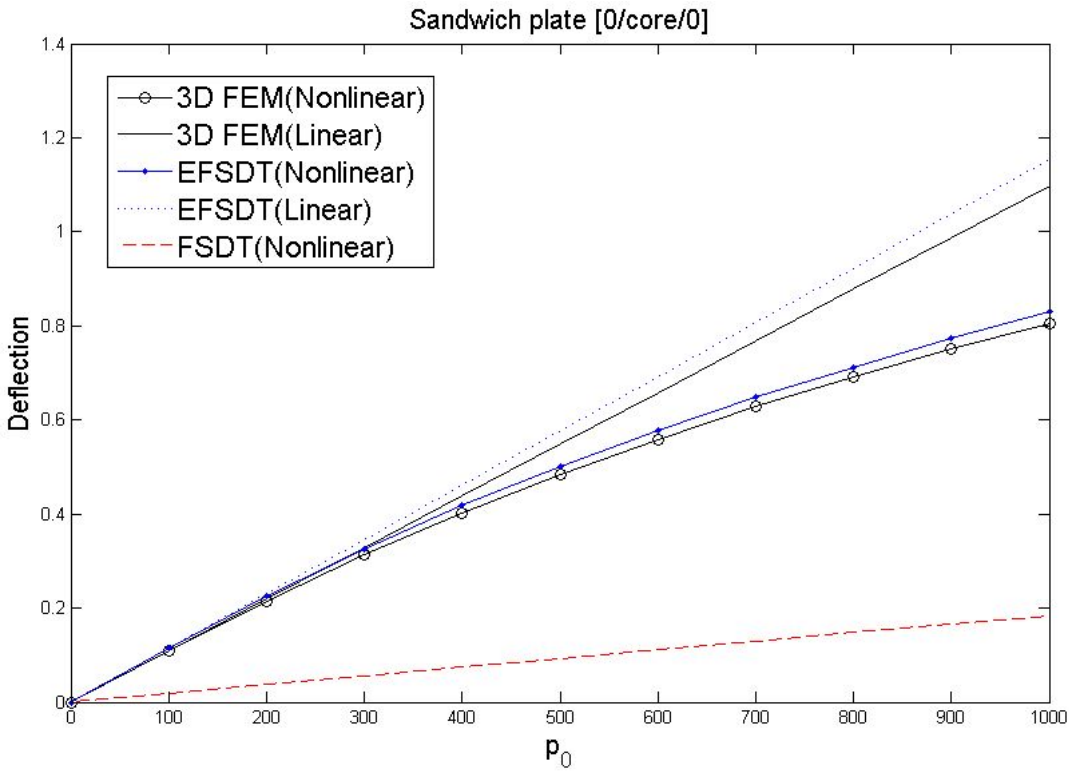

Fig. 5.1.12. Variation of deflection against the magnitude of pressure

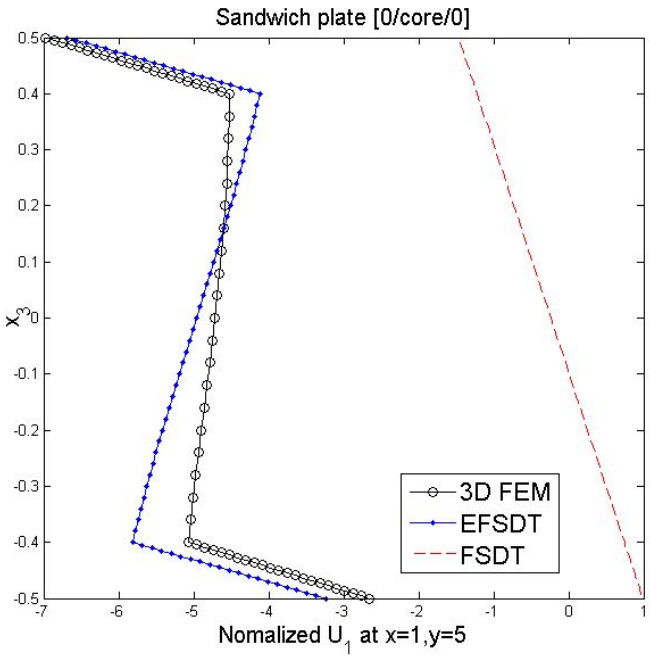

Fig. 5.1.13. In-plane displacement under sinusoidal pressure

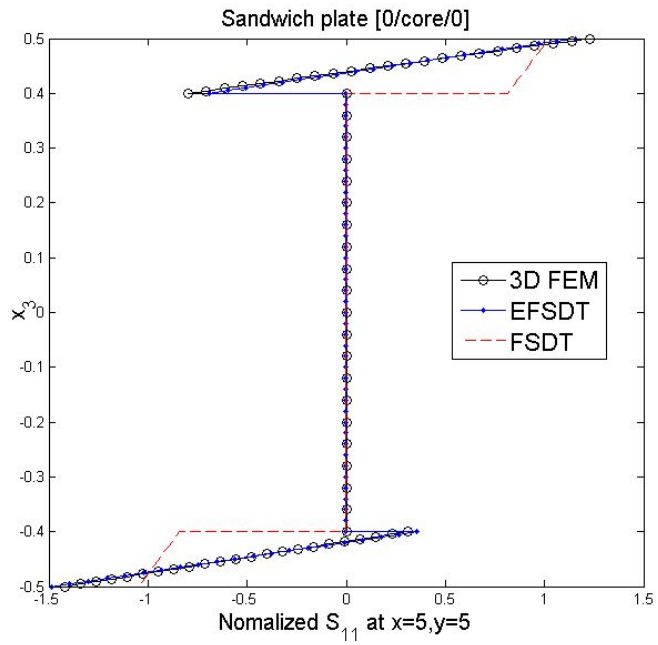

Fig. 5.1.14. In-plane stress under sinusoidal pressure

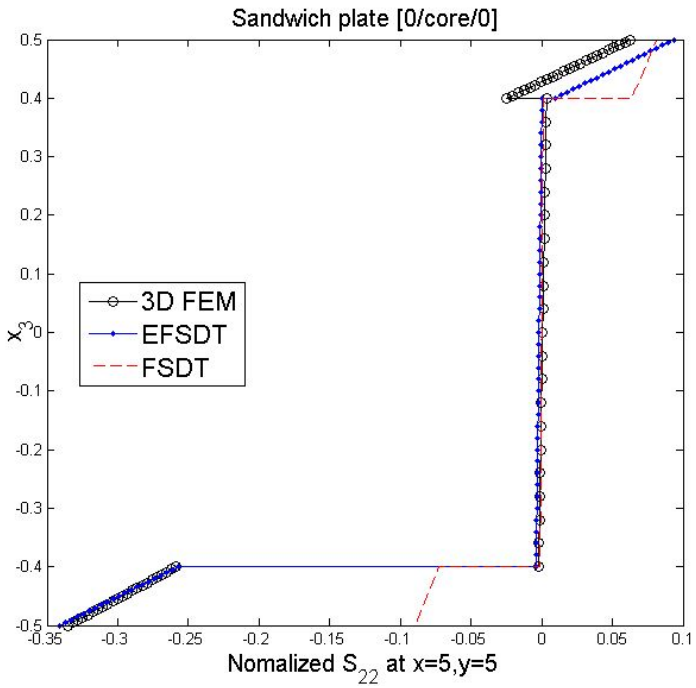

Fig. 5.1.15. In-plane stress under sinusoidal pressure

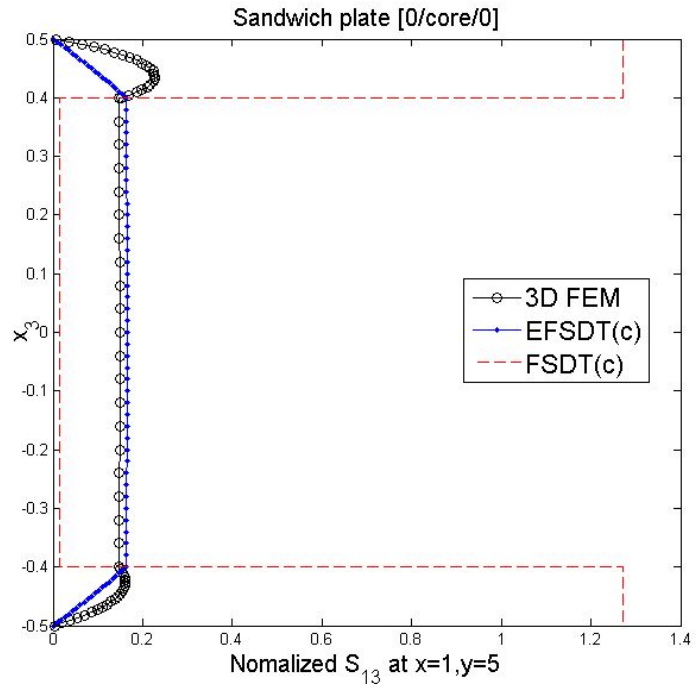

Fig. 5.1.16. Transverse shear stress (c) under sinusoidal pressure

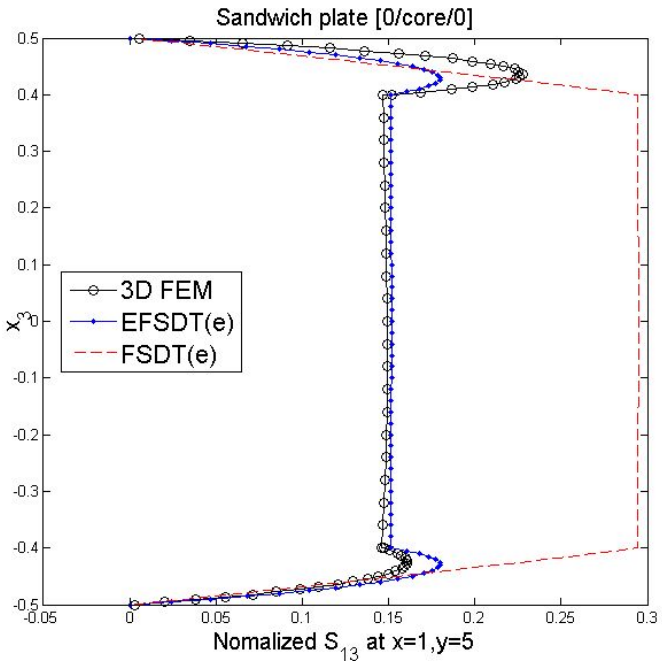

Fig. 5.1.17. Transverse shear stress (e) under sinusoidal pressure

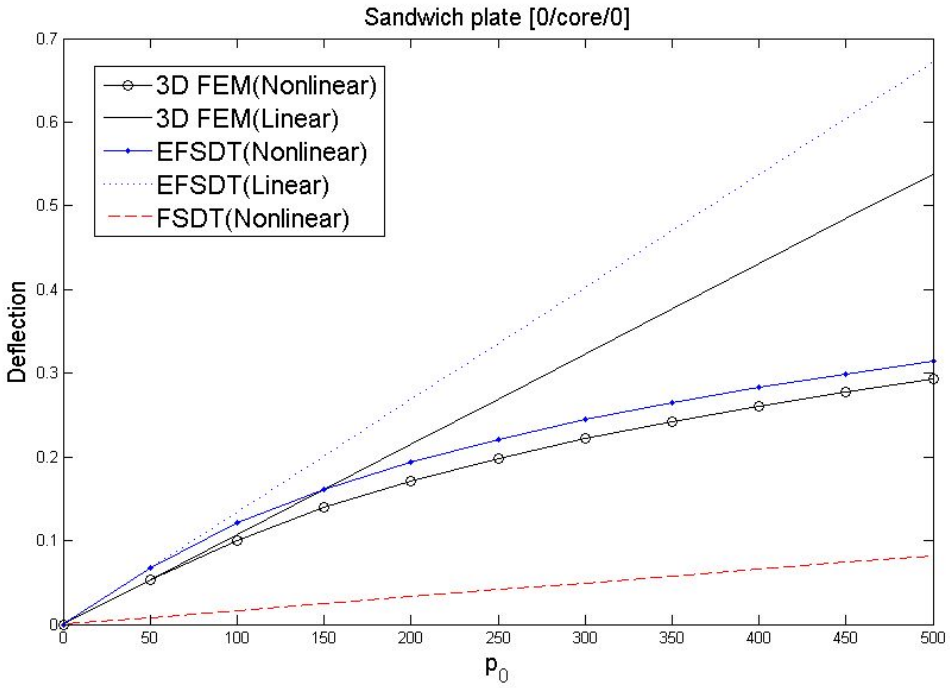

Fig. 5.1.18. Variation of deflection against the magnitude of pressure

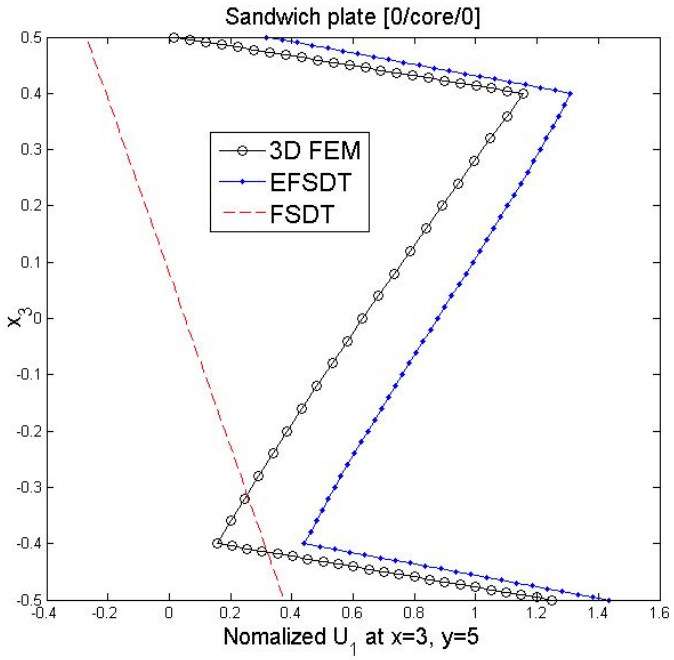

Fig. 5.1.19. In-plane displacement under uniform pressure

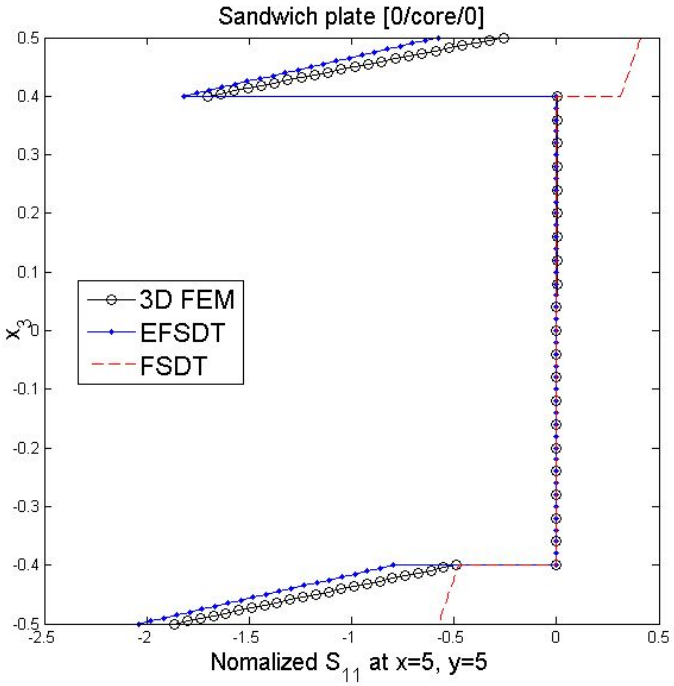

Fig. 5.1.20. In-plane stress under uniform pressure

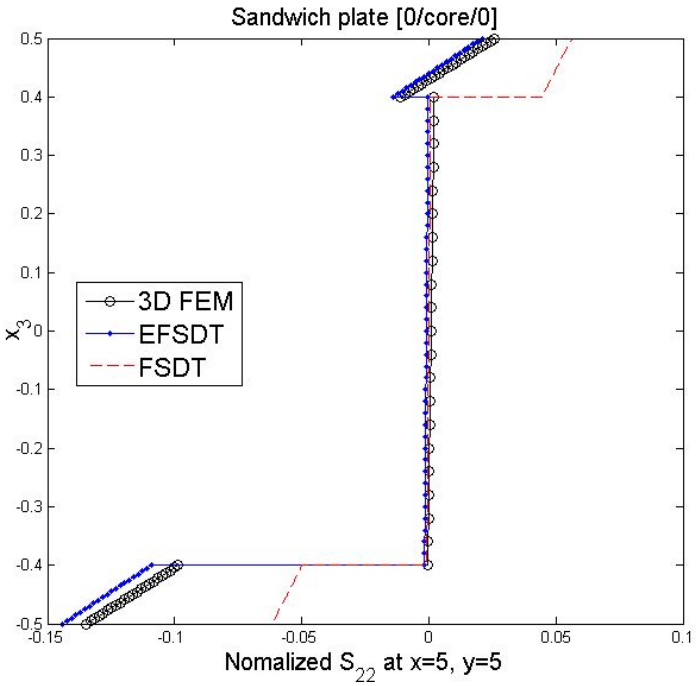

Fig. 5.1.21 In-plane stress under uniform pressure

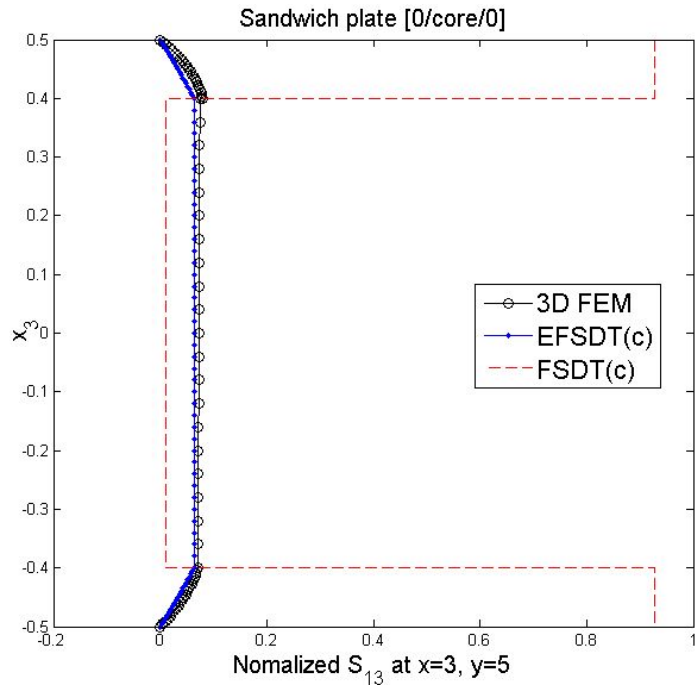

Fig. 5.1.22 Transverse shear stress (c) under uniform pressure

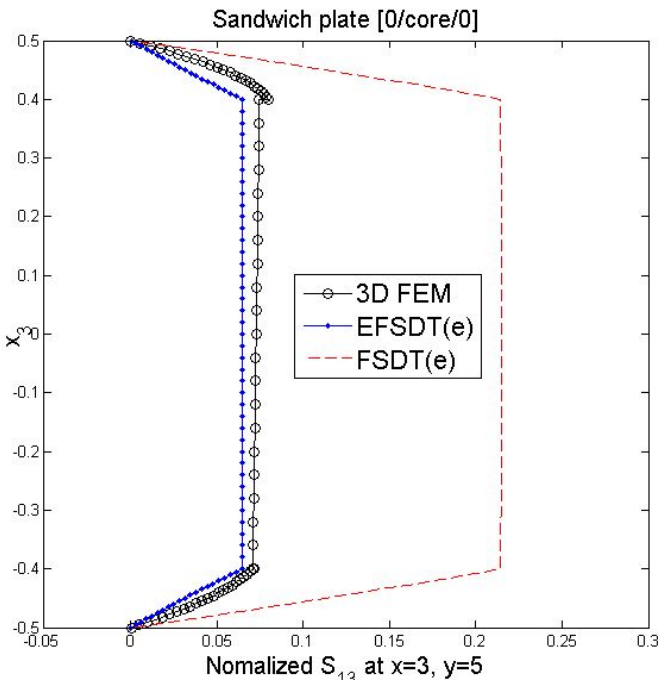

Fig. 5.1.23 Transverse shear stress (e) under uniform pressure

Chapter 6

Concluding Remarks

Efficient and accurate models based on enhanced theories are proposed in this dissertation for the thermo-mechanical analysis of laminated composite and sandwich plates. Enhanced theories can be categorized as follows: (1) enhanced first-order theories, (2) enhanced higher-order theories, (3) enhanced zig-zag theory. In addition, enhanced first-order theory is further extended to co-rotational formulation for the geometrically nonlinear analysis. The features of the enhanced theories developed in this dissertation can be summarized as follows:

- An enhanced first order shear deformation theory including transverse normal strain effect based on mixed variational theorem (i.e. EFSDTM_TN) has been developed in order to efficiently and accurately predict the thermo-elastic response of the laminated composite and sandwich plates. In EFSDTM_TN, an inventive approach is employed to effectively consider the contribution of the transverse normal strain effects without increasing unknown variables. Moreover, in-plane shear

correction factors are newly considered in EHOPT_TN to satisfy self-equilibrium state of the stress for the general configuration of the structures. Relationships between EHOPT_TN and FSDT_TN were systematically derived by the mixed variational theorem and least-square approximation. Through these relationships, the EHOPT_TN is recast by a FSDT_TN-like theory. Thus, the present method corresponding to the enhanced plate theory is similar to the FSDT_TN except for the transverse shear stiffness. Once the EFSDTM_TN is solved, the results of displacements and stresses are improved by using the recovery procedure. And then the transverse shear and normal stresses are reasonably improved by utilizing three dimensional stress equilibrium equations.

- EFSDT in the Laplace domain is proposed and tested numerically for the efficient and accurate viscoelastic analysis of laminated composite and sandwich plates. After applying Laplace transformation, the complexity of dealing with viscoelastic material behavior is equivalent to the linear elastic version in the Laplace domain. The relationships between conventional FSDT and EHOPT in the Laplace domain are systematically established by using strain energy transformation as well as least-square sense approximation. The accuracy of the results can be further improved via post-processing. Thus, the present theory preserves the computational advantage of conventional FSDT while improving the through-the-thickness local distributions of the displacements and

stresses.

- The enhanced higher-order shear deformation theory based on mixed formulation (EHSDTM) is fully developed to analyze the static behavior of laminated composite and sandwich plates. The mixed variational theorem (MVT) is employed to synthesize the quantic zig-zag model and the conventional HSDT. The MVT allows one to embrace the characteristics of the quantic zig-zag model as the conventional HSDT. This results in EHSDTM. The recovery process is then applied by introducing the in-plane correction factor that makes it possible to satisfy the stress condition at the top and bottom surfaces of plates. The EHSDTM is able to provide the accurate stress state including the boundary layer zone in practice.

- The enhanced Lo-Christensen-Wu theory is systematically derived by employing the mixed variational theorem (i.e. ELCWM). The independent transverse shear stresses fields based on the fifth-order zigzag theory assumed in this model, whereas the displacements, strains, and other stresses are based on the conventional LCW theory. The relationship between the two theories can be systematically established by solving the constraint equation for the independently assumed transverse shear strains. The recovery procedure is outlined, in which the least square concept is employed in order to correct the in-plane

stretching displacement. The ELCWM is efficient because it does not require the C^1 continuity shape function for the finite element implementation. At the same time, it could outperform the classical LCW, since it satisfies the transverse shear stress conditions without additional cost in terms of the number of unknown variables. Therefore, present ELCWM will be a viable means of analyzing the thermo-mechanical responses of the laminated composite and sandwich plates.

- The enhanced C^0-type efficient higher-order zig-zag theory via the mixed variational theorem (i.e. Enhanced C^0-type EHOZT) is systematically derived for the efficient and accurate thermo-mechanical analysis of laminated composite plates. The independent transverse shear stresses are obtained from the seventh order zig-zag model, whereas the displacements, strains, and other stresses are based on the C^0-type efficient higher-order zig-zag theory. The relationships between the two theories are derived by employing constraint equation of mixed variational theorem. The accuracy of the transverse shear stress can be reasonably improved by utilizing the recovery procedure. In addition, Enhanced C^0-type EHOZT possess the computational advantage because C^0-continuity shape function is only required in their finite element implementation by eliminating the first derivatives of the transverse displacement field.

- Co-rotational formulation based on the EFSDT is developed in order to

efficiently and accurately predict the geometrically nonlinear behavior of the laminated composite and sandwich plates. In EICR, the strain energy relationships between two theories (conventional FSDT and EHOPT) can be defined with similar manner as that of linear analysis model. Therefore, efficient and accurate analysis model based on the EFSDT can be further extended to the geometrically nonlinear problem.

To demonstrate the robustness, applicability, computational efficiency and accuracy of enhanced theories, a number of numerical problems were considered and compared with benchmark solution as well as those of available in the open literature. From the numerical results, one can conclude that the enhanced theories proposed in this dissertation can provide efficient and accurate tools for the thermo-mechanical, viscoelastic and geometrically nonlinear analysis of multilayered composite and sandwich plates.

Bibliography

[1] Mindlin RD. Influence of rotary inertia and shear on flexural motions of isotropic, elastic plates. J Appl Mech 1951; 18: 31-38.

[2] Reissner E. The effect of transverse shear deformation on the bending of elastic plates. J Appl Mech 1945; 12: 69-77.

[3] Reissner E. On a mixed variational theorem and on shear deformable plate theory. Int J Numer Methods Eng 1986; 23: 193-198.

[4] Whitney JM, Leissa AW. Analysis of heterogeneous anisotropic plates. J Appl Mech 1969; 36(2):261–6.

[5] Thai HT, Choi DH. A simple first-order shear deformation theory for laminated composite plates. Compos Struct 2013; 106: 754-763.

[6] Reddy JN. A Simple Higher-Order Theory for Laminated Composite Plates. J Appl Mech 1984; 51: 745-752.

[7] Kant T, Pandya BN. A simple finite element formulation of a higher-order theory for unsymmetrically laminated composite plates. Compos Struct 1988; 9(3):215–46.

[8] Reddy JN. Mechanics of Laminated Composite Plates and Shells. CRC Press,

2004.

[9] Lo KH, Christensen RM, Wu FM. A higher-order theory of plate deformation. Part 2: Laminated plates. J Appl Mech 1977; 44: 669-676.

[10] Carrera E. Evaluation of Layerwise Mixed Theories for Laminated Plates Analysis. AIAA J 1998; 36(5): 830-839.

[11] DiSciuva M. Bending, Vibration and buckling of simply supported thick multilayered orthotropic plates: an evaluation of a new displacement model. J Sound Vib 1986; 105: 425-442.

[12] Cho M, Parmerter RR. An efficient higher order plate theory for laminated composites. Compos Struct 1992; 20: 113-123.

[13] Cho M, Parmerter RR. Efficient Higher-Order Plate Theory for General Lamination Configuration. AIAA J, 1993; 31: 1299-1306.

[14] Wu Z, Chen WJ. Refined global–local higher-order theory and finite element for laminated plates. Int J Numer Methods Eng 2007; 69: 1627–70.

[15] Tessler A, DiSciuva M, Gherlone M. Refined Zigzag Theory for Homogeneous, Laminated Composite, and Sandwich Plates: A Homogeneous Limit Methodology for Zigzag Function Selection. NASA Technical Report 2010.

[16] Cho M, Kim JS. Four-noded finite element post-process method using a displacement field of higher order laminated composite plate theory. Comput Struct 1996; 61: 283-290.

[17] Cho M, Kim JS. Improved mindlin plate stress analysis for laminated composites in finite element method. AIAA J 1997; 35: 587-590.

[18] Kim JS, Cho M. Enhanced modeling of laminated and sandwich plates via strain energy transformation. Compos Sci Technol 2006; 66: 1575-1587.

[19] Kim JS, Cho M. Enhanced first-order theory based on mixed formulation and transverse normal effect. Int J Solids Struct 2007; 44: 1256-1276.

[20] Kim JS. Free vibration of laminated and sandwich plates using enhanced plate theories. J Sound Vib 2007; 308: 268-286.

[21] Carrera E. Theories and Finite Elements for Multilayered, Anisotropic, Composite Plates and Shells. Arch Comput Meth Engng 2002; 9(2): 87-140.

[22] Chen WJ, Wu Z. A selective review on recent development of displacement based laminated plate theories. Recent Patents Mech Eng 2008; 1: 29–44.

[23] Jonnalagadda KD, Tauchert TR, Blandford GE. Higher order thermoelastic composite plate theories, analytical comparison. J Therm Stresses 1993; 16: 265–284.

[24] Kant T, Khare RK. Finite element thermal stress analysis of composite laminates using a higher order theory. J Therm Stresses 1994; 17: 229–255.

[25] Rohwer K, Rolfs R, Sparr H. Higher-order theories for thermal stresses in layered plates. Int J Solids Struct 2001; 38: 3673–3687.

[26] Zenkour AM. Analytical solution for bending of cross-ply laminated plates under thermo-mechanical loading. Compos Struct 2004; 65: 367–379.

[27] Matsunaga H. A comparison between 2-D single-layer and 3-D layerwise theories for computing interlaminar stresses of laminated composite and sandwich plates subjected to thermal loadings. Compos Struct 2004; 64: 1611–77.

[28] Matsunaga H. Thermal buckling of cross-ply laminated composite and sandwich plates according to a global higher-order deformation theory. Compos Struct 2005; 68: 439–454.

[29] Matsunaga H. Thermal buckling of cross-ply laminated composite shallow shells according to a global higher-order deformation theory. Compos Struct 2007; 81: 210–221.

[30] Patel BP, Lele AV, Ganapathi M, Gupta SS, Sambandam CT. Thermo-flexural analysis of thick laminates of bimodulus composite materials. Compos Struct 2004; 63: 11–20.

[31] Khare RK, Kant T, Garg AK. Closed-form thermo-mechanical solutions of higher-order theories of cross-ply laminated shallow shells. Compos Struct 2003; 59: 313–340.

[32] Noor AK, Malik M. An assessment of five modeling approaches for thermo-mechanical stress analysis of laminated composite panels. Comput Mech 2000; 25: 43–58.

[33] Carrera E. An assessment of mixed and classical theories for the thermal stress analysis of orthotropic multilayered plates. J Therm Stresses 2000; 23: 797–831.

[34] Carrera E, Ciuffreda A. Closed-form solutions to assess multilayered-plate theories for various thermal stress problems. J Therm Stresses 2004; 27: 1001–1031.

[35] Cho M, Oh J. Higher-order zig–zag plate theory under thermo-electric–mechanical loads combined. Composites B 2003; 34: 67–82.

[36] Cho M, Oh JH. Higher Order Zig-Zag Theory for fully coupled thermos-electric-mechanical smart composite plates. Int J Solids Struct 2004; 41: 1331-1356.

[37] Oh, Cho. A finite element based on cubic zig–zag plate theory for the prediction of thermo-electric–mechanical behaviors. Int J Solids Struct 2004; 41: 1357–1375.

[38] Oh, Cho. Higher-order zig–zag theory for smart composite shells under mechanical–thermo-electric loading. Int J Solids Struct 2007; 44: 100–127.

[39] Kapuria S, Achary GGS. An efficient higher order zigzag theory for laminated plates subjected to thermal loading. Int J Solids Struct 2004; 41: 4661–4684.

[40] Zhen W, Wanji C. A quadrilateral element based on refined global–local higher-order theory for thermal/mechanical analysis of laminated plates. Int J Solids Struct 2007; 44: 3187–3217.

[41] Zhen W, Cheung YK, Lo SH, Wanji C. On the thermal expansion effects in the transverse direction of laminated composite plates by means of a global-local higher-order model. Int J Mech Sci 2010; 52: 970–981.

[42] Oh J, Cho M, Kim JS. Enhanced lower order shear deformation theory for fully coupled Electro-thermo-mechanical smart laminated plates. Smart Mater Struct 2007; 16(6): 2229–2241.

[43] Li J, Weng GJ. Effect of a Viscoelastic Interphase on the Creep and Stress/Strain Behavior of Fiber-Reinforced Polymer Matrix Composites. Compos Part B-Eng 1996; 27(6): 589–598.

[44] Crossman FW, Mauri RE, Warren WJ. Moisture altered viscoelastic response of Graphite/Epoxy composite. Adv Compos Mater-Environmental Effects 1978; 658: 205-220.

[45] Lin KY, Hwang IH. Thermo-Viscoelastic Analysis of Composite Materials. J Compos Mater 1989; 23: 554–569.

[46] Lin KY, Yi S. Analysis of Interlaminar Stress in Viscoelastic Composites. Int J Solid Struct 1991; 27: 929–945.

[47] Yi S, Hilton HH. Hygrothermal Effects on Viscoelastic Responses of Laminated Composites. Compos Eng 1995; 5: 183–193.

[48] Bradshaw RD, Brinson LC. Mechanical response of linear viscoelastic composite laminates incorporating non-isothermal physical aging effects. Compos Sci Technol 1999; 59: 1411–1427.

[49] Zak AR. Structural analysis of realistic solid-propellent materials. J Spacecraft Rockets 1967; 5: 270–275.

[50] Vallala V, Ruimi A, Reddy JN. Nonlinear Viscoelastic Analysis of Orthotropic Beams Using a General Third-Order Theory. Compos Struct 2012; 94: 3759–3768.

[51] Schapery RA. On the characterization of nonlinear viscoelastic materials. Polym Eng Sci 1969; 9(4): 295–310.

[52] Dillard DA, Straight MR, Brinson HF. The nonlinear viscoelastic characterization of graphite/epoxy composites. Polym Eng Sci 1987; 27(2): 116–123.

[53] Cederbaum G, Aboudi J. Dynamic Response of Viscoelastic Laminated Plates. J Sound Vib 1989; 133: 225–238.

[54] Chandiramani NK, Librescu L, Aboudi J. The Theory of Orthotropic Viscoelastic Shear Deformable Composite Flat Panels and their Dynamic Stability. Int J Solid Struct 1989; 25: 465–482.

[55] Chen TM. The Hybrid Laplace Transform/ Finite Element Method Applied to the Quasi-Static and Dynamic Analysis of Viscoelastic Timoshenko Beams. Int J Num Methods Eng 1995; 38: 509–522.

[56] Hilton HH, Yi S. Anisotropic Viscoelastic Finite Element Analysis of Mechanically and Hygrothermally Loaded Composites. Compos Eng 1993; 3: 123–135.

[57] Nguyen Sy N, Lee JH, Cho M. Application of the laplace transformation for the analysis of viscoelastic composite laminates based on equivalent single-layer theories. Int J Aeronaut. Space Sci 2012; 13: 458-467.

[58] Nguyen Sy N, Lee JH, Cho M. Efficient Higher-Order Zig-Zag Theory for Viscoelastic Laminated Composite Plates. Int J Solid Struct 2015; 62: 174-185.

[59] Cost TL, Becker EB. A Multidata Method of Approximate Laplace

Transform Inversion. Int J Num Methods Eng 1970; 2: 207–219.

[60] Davies B, Martin B. Numerical Inversion of the Laplace Transform: a Survey and Comparison of Methods. J Comput Phys 1979; 33: 1–32.

[61] Dubner H, Abate J. Numerical Inversion of Laplace Transforms by Relating Them to the Finite Fourier Cosine Transform. J Assoc Comput Mach 1968; 15: 115–123.

[62] Hassanzadeh H, Pooladi-Darvish M. Comparison of Different Numerical Laplace Inversion Methods for Engineering Applications. Appl Math Comput 2007; 189: 1966–1981.

[63] Narayanan GV, Beskos DE. Numerical Operational Methods for Time-Dependent Linear Problems. Int J Num Methods Eng 1982; 18: 1829–1854.

[64] Averill RC. Static and dynamic response of moderately thick laminated beams with damage. Compos Eng 1994; 4: 381–395.

[65] Tessler A, DiSciuva M, Gherlone M. A consistent refinement of first-order shear deformation theory for laminated composite and sandwich plates using improved zigzag kinematics. Int J Solid Struct 2010; 5: 341-367.

[66] Petrolo M, Cinefra M, Lamberti A, Carrera E. Evaluation of mixed theories for laminated plates through the axiomatic/asymptotic method. Compos Part B-Eng 2015; 76: 260–272.

[67] Carrera E, Petrolo M. Guidelines and recommendations to construct

theories for metallic and composite plates. AIAA J 2010; 48: 2852–2866.

[68] Carrera E. Theories and finite elements for multilayered plates and shells: a unified compact formulation with numerical assessment and benchmarking. Arch Comput Method E 2003; 10: 215–296.

[69] Kim JS. An asymptotic analysis of anisotropic heterogeneous plates with consideration of end effects. J Mech Mater Struct 2009; 4: 1535–1553.

[70] Xiaohui R, Wanji C, Zhen W. A C^0-type zig-zag theory and finite element for laminated composite and sandwich plates with general configurations. Arch Appl Mech 2012; 82: 391–406.

[71] Rankin CC, Brogan FA. An element independent corotational procedure for the treatment of large rotations. ASME J. Pressure Vessel Technology 1986; 108: 165–174.

[72] Rankin CC, Nour-Omid B. The use of projectors to improve finite element performance. Comput Struct 1988; 30: 257–267.

[73] Rankin CC, Nour-Omid B. Finite rotation analysis and consistent linearization using projectors. Comput Methods Appl Mech Eng 1991; 93: 353–384.

[74] Pacoste C. Co-rotational flat facet triangular elements for shell instability analysis. Comput Methods Appl Mech Eng 1998; 156: 75–110.

[75] Battini JM, Pacoste C. On the choice of local element frame for corotational triangular shell elements. Comput Methods Appl Mech Eng

2004; 20: 819–825.

[76] Battini JM, Pacoste C. On the choice of linear element frame for corotational triangular shells. Comput Methods Appl Mech Eng 2006; 195: 6362–6377.

[77] Felippa CA, Haugen B. A unified formulation of small-strain corotational finite elements: I. Theory. Comput Methods Appl Mech Eng 2005; 194: 2285–2335.

[78] Almeida FS, Awruch AM. Corotational nonlinear dynamic analysis of laminated composite shells. Finite Elem Anal Des 2011; 47: 1131–1145.

[79] Yang JS, Xia PQ. Finite element corotational formulation for geometric nonlinear analysis of thin shells with large rotation and small strain. Sci China 2012; 55: 3142–3152.

[80] Sze KY, Liu XH, Lo SH. Popular benchmark problems for geometric nonlinear analysis of shells. Finite Elem Anal Des 2004; 40: 1551–1569.

[81] Felippa CA. A study of optimal membrane triangles with drilling freedoms. Comput Methods Appl Mech Eng 2003; 192: 2125–2168.

[81] Felippa CA. A study of optimal membrane triangles with drilling freedoms. Comput Methods Appl Mech Eng 2003; 192: 2125–2168.

[82] Zhang YX, Kim KS. A simple displacement-based 3-node triangular element for linear and geometrically nonlinear analysis of laminated composite plates. Comput Methods Appl Mech Eng 2005; 194: 4607–4632.

[83] Kant T, Pendhari SS, Desai YM. An efficient semi-analytical model for composite and sandwich plates subjected to thermal load. J Therm Stresses 2008; 31: 77–103.

[84] Pagano NJ. Exact Solutions for Composite Laminates in Cylindrical Bending. J Compos Mater 1969; 3: 398-411.

[85] Pagano NJ, Hatfield SJ. Elastic Behavior of Multilayered Bidirectional Composites. AIAA J 1972; 10(7): 931-933.

Appendix

Appendix A. Derivation of the layer-wise constant to satisfy plane stress condition

Considering thermo-elastic problem, constitutive equation for the transverse normal stress in each layer can be given as:

$$\sigma_{33} = C_{3311}^{(i)}(\varepsilon_{11} - \alpha_{11}^{(i)}\Delta T) + C_{3322}^{(i)}(\varepsilon_{22} - \alpha_{22}^{(i)}\Delta T) + C_{3333}^{(i)}(\varepsilon_{33} - \alpha_{33}^{(i)}\Delta T) + C_{3312}^{(i)}(\gamma_{12}),$$

(A.1)

Under the plane stress condition $\sigma_{33} \approx 0$, following relationship can be derived as:

$$\varepsilon_{33}^{(i)} = -\frac{C_{3311}^{(i)}}{C_{3333}^{(i)}}\left(\varepsilon_{11} - \alpha_{11}^{(i)}\Delta T\right) - \frac{C_{3322}^{(i)}}{C_{3333}^{(i)}}\left(\varepsilon_{22} - \alpha_{22}^{(i)}\Delta T\right) - \frac{C_{3312}^{(i)}}{C_{3333}^{(i)}}\left(\gamma_{12}\right) + \alpha_{33}^{(i)}\Delta T,$$

(A.2)

where the transverse normal strain, $\varepsilon_{33}^{(i)}$, can be considered as pure mechanical

and thermal related terms:

$$\varepsilon_{33}^{(i)} = \varphi^{(i)}\Delta T = \varepsilon_{33}^{Mechanical} + \varepsilon_{33}^{Thermal}.$$

(A.3)

From Eqs. (A.2) and (A.3), following relationships of the transverse normal strain can be expressed as:

$$\varepsilon_{33}^{Mechanical} = -\frac{C_{3311}^{(i)}}{C_{3333}^{(i)}}\varepsilon_{11} - \frac{C_{3322}^{(i)}}{C_{3333}^{(i)}}\varepsilon_{22} - \frac{C_{3312}^{(i)}}{C_{3333}^{(i)}}\gamma_{12},$$
$$\varepsilon_{33}^{Thermal} = \left[\frac{C_{3311}^{(i)}}{C_{3333}^{(i)}}\alpha_{11}^{(i)} + \frac{C_{3322}^{(i)}}{C_{3333}^{(i)}}\alpha_{22}^{(i)} + \alpha_{33}^{(i)}\right]\Delta T = \varphi^{(i)}\Delta T.$$

(A.4)

where the relationship of the mechanical transverse normal strain, $\varepsilon_{33}^{Mechanical}$, is same with the general plane stress relationship. According to the thermal relationship in Eq. (A.4), layer-wise constant to satisfy plane stress condition can be derived as:

$$\varphi^{(i)} = \frac{C_{3311}^{(i)}}{C_{3333}^{(i)}}\alpha_{11}^{(i)} + \frac{C_{3322}^{(i)}}{C_{3333}^{(i)}}\alpha_{22}^{(i)} + \alpha_{33}^{(i)}.$$

(A.5)

Appendix B. Calculation process to determine $S_{\alpha}^{(k)}$ and $S_3^{(k)}$

The continuity conditions of transverse displacement field at the layer interfaces can be satisfied by applying the following relationship:

$$S_3^{(k)} = \left(\varphi^{(k)} - \varphi^{(k+1)}\right) T_o x_{3(k)} + \frac{1}{2}\left(\varphi^{(k)} - \varphi^{(k+1)}\right) T_1 x_{3(k)}^2. \tag{B.1}$$

From Eq. (B.1), the coefficients $b_{33}^{(k)}$ and $c_{33}^{(k)}$, which are the functions of layer-wise constant ($\varphi^{(k)}$), can be derived as:

$$b_{33}^{(k)} = \left(\varphi^{(k)} - \varphi^{(k+1)}\right) x_{3(k)}, \quad c_{33}^{(k)} = \left(\varphi^{(k)} - \varphi^{(k+1)}\right) x_{3(k)}^2. \tag{B.2}$$

In addition, the shear continuity conditions at layer interfaces can be expressed of the matrix form as:

$$\begin{aligned}[K\ ][S\ ] = {} & [A_1\ ]u_1^{(3)} + [A_2\ ]u_2^{(3)} + [B_1\ ]T_{0,1} + [B_2\ ]T_{0,2} \\ & + [C_1\ ]\frac{1}{2}T_{1,1} + [C_2\ ]\frac{1}{2}T_{1,2},\end{aligned} \tag{B.3}$$

where

$$\begin{aligned}[S\ ] &= \left[S_1^{(1)} \quad \cdots \quad S_1^{(N-1)} \quad S_2^{(1)} \quad \cdots \quad S_2^{(N-1)}\right]^T, \\ S_{\alpha}^{(k)} &= a_{\alpha\beta}^{(k)} u_{\beta}^{(3)} + b_{\alpha\beta}^{(k)} T_{o,\beta} + c_{\alpha\beta}^{(k)} \frac{1}{2} T_{1,\beta}.\end{aligned} \tag{B.4}$$

Matrix [K] is derived from this following algorithm:

$$
\begin{aligned}
&for\ i = 1:(N-1)\\
&\ for\ \ j = 1:(i-1)\\
&\qquad K(i,j) = (Q_{1313}^{(i+1)} - Q_{1313}^{(i)})(x_{3(i)}/h + 1/2 - 1)\\
&\qquad K(i,N-1+j) = (Q_{1323}^{(i+1)} - Q_{1323}^{(i)})(x_{3(i)}/h + 1/2 - 1)\\
&\qquad K(N-1+i,j) = (Q_{2313}^{(i+1)} - Q_{2313}^{(i)})(x_{3(i)}/h + 1/2 - 1)\\
&\qquad K(N-1+i,N-1+j) = (Q_{2323}^{(i+1)} - Q_{2323}^{(i)})(x_{3(i)}/h + 1/2 - 1)\\
&\ end\\
&\\
&for\ \ j = i+1:(N-1)\\
&\qquad K(i,j) = (Q_{1313}^{(i+1)} - Q_{1313}^{(i)})(x_{3(i)}/h + 1/2)\\
&\qquad K(i,N-1+j) = (Q_{1323}^{(i+1)} - Q_{1323}^{(i)})(x_{3(i)}/h + 1/2)\\
&\qquad K(N-1+i,j) = (Q_{2313}^{(i+1)} - Q_{2313}^{(i)})(x_{3(i)}/h + 1/2)\\
&\qquad K(N-1+i,N-1+j) = (Q_{2323}^{(i+1)} - Q_{2323}^{(i)})(x_{3(i)}/h + 1/2)\\
&\ end\\
&\\
&\qquad K(i,i) = Q_{1313}^{(i+1)}(x_{3(i)}/h + 1/2 - 1) - Q_{1313}^{(i)}(x_{3(i)}/h + 1/2)\\
&\qquad K(i,N-1+i) = Q_{1323}^{(i+1)}(x_{3(i)}/h + 1/2 - 1) - Q_{1323}^{(i)}(x_{3(i)}/h + 1/2)\\
&\qquad K(N-1+i,i) = Q_{2313}^{(i+1)}(x_{3(i)}/h + 1/2 - 1) - Q_{2313}^{(i)}(x_{3(i)}/h + 1/2)\\
&\qquad K(N-1+i,N-1+i) = Q_{2323}^{(i+1)}(x_{3(i)}/h + 1/2 - 1) - Q_{2323}^{(i)}(x_{3(i)}/h + 1/2)\\
&end
\end{aligned}
$$

(B.5)

Components of $[A_\alpha]$, $[B_\alpha]$ and $[C_\alpha]$ are computed as:

$$
\begin{aligned}
&\textit{for } i = 1:(N-1)\\
&\quad A_1(i) = 3(x_{3(i)}^2 - h^2/4)(Q_{1313}^{(i+1)} - Q_{1313}^{(i)})\\
&\quad A_1(N-1+i) = 3(x_{3(i)}^2 - h^2/4)(Q_{1323}^{(i+1)} - Q_{1323}^{(i)})\\
&\quad A_2(i) = 3(x_{3(i)}^2 - h^2/4)(Q_{2313}^{(i+1)} - Q_{2313}^{(i)})\\
&\quad A_2(N-1+i) = 3(x_{3(i)}^2 - h^2/4)(Q_{2323}^{(i+1)} - Q_{2323}^{(i)})\\
&\\
&\quad B_1(i) = \Lambda_B^{(i)}(Q_{1313}^{(i+1)} - Q_{1313}^{(i)}) + Q_{1313}^{(i+1)} b_{33}^{(i)} - \left(Q_{1313}^{(i)}\varphi^{(i)} - Q_{1313}^{(i+1)}\varphi^{(i+1)}\right) x_{3(i)}\\
&\quad B_1(N-1+i) = \Lambda_B^{(i)}(Q_{1323}^{(i+1)} - Q_{1323}^{(i)}) + Q_{1323}^{(i+1)} b_{33}^{(i)} - \left(Q_{1323}^{(i)}\varphi^{(i)} - Q_{1323}^{(i+1)}\varphi^{(i+1)}\right) x_{3(i)}\\
&\quad B_2(i) = \Lambda_B^{(i)}(Q_{2313}^{(i+1)} - Q_{2313}^{(i)}) + Q_{2313}^{(i+1)} b_{33}^{(i)} - \left(Q_{2313}^{(i)}\varphi^{(i)} - Q_{2313}^{(i+1)}\varphi^{(i+1)}\right) x_{3(i)}\\
&\quad B_2(N-1+i) = \Lambda_B^{(i)}(Q_{2323}^{(i+1)} - Q_{2323}^{(i)}) + Q_{2323}^{(i+1)} b_{33}^{(i)} - \left(Q_{2323}^{(i)}\varphi^{(i)} - Q_{2323}^{(i+1)}\varphi^{(i+1)}\right) x_{3(i)}\\
&\\
&\quad C_1(i) = \Lambda_C^{(i)}(Q_{1313}^{(i+1)} - Q_{1313}^{(i)}) + Q_{1313}^{(i+1)} c_{33}^{(i)} - \left(Q_{1313}^{(i)}\varphi^{(i)} - Q_{1313}^{(i+1)}\varphi^{(i+1)}\right) x_{3(i)}^2\\
&\quad C_1(N-1+i) = \Lambda_C^{(i)}(Q_{1323}^{(i+1)} - Q_{1323}^{(i)}) + Q_{1323}^{(i+1)} c_{33}^{(i)} - \left(Q_{1323}^{(i)}\varphi^{(i)} - Q_{1323}^{(i+1)}\varphi^{(i+1)}\right) x_{3(i)}^2\\
&\quad C_2(i) = \Lambda_C^{(i)}(Q_{2313}^{(i+1)} - Q_{2313}^{(i)}) + Q_{2313}^{(i+1)} c_{33}^{(i)} - \left(Q_{2313}^{(i)}\varphi^{(i)} - Q_{2313}^{(i+1)}\varphi^{(i+1)}\right) x_{3(i)}^2\\
&\quad C_2(N-1+i) = \Lambda_C^{(i)}(Q_{2323}^{(i+1)} - Q_{2323}^{(i)}) + Q_{2323}^{(i+1)} c_{33}^{(i)} - \left(Q_{2323}^{(i)}\varphi^{(i)} - Q_{2323}^{(i+1)}\varphi^{(i+1)}\right) x_{3(i)}^2\\
&\textit{end}
\end{aligned}
$$

(B.6)

where

$$
\begin{aligned}
\Lambda_B^{(i)} &= -\frac{h}{2}\left(\frac{\varphi^{(N)} - \varphi^{(1)}}{2} + \frac{\varphi^{(N)} + \varphi^{(1)}}{h} x_{3(i)}\right) - \left(\frac{1}{2} + \frac{x_{3(i)}}{h}\right)\sum_{k=1}^{N-1} b_{33}^{(k)} + \sum_{k=1}^{i-1} b_{33}^{(k)},\\
\Lambda_C^{(i)} &= -\frac{h^2}{4}\left(\frac{\varphi^{(N)} + \varphi^{(1)}}{2} + \frac{\varphi^{(N)} - \varphi^{(1)}}{h} x_{3(i)}\right) - \left(\frac{1}{2} + \frac{x_{3(i)}}{h}\right)\sum_{k=1}^{N-1} c_{33}^{(k)} + \sum_{k=1}^{i-1} c_{33}^{(k)}.
\end{aligned}
$$

(B.7)

$a_{11}^{(k)}$ represents k-th row of $[K]^{-1}[A_1]$, $a_{21}^{(k)}$ is $(N-1+k)$th row of $[K]^{-1}[A_1]$, $a_{12}^{(k)}$ is k-th row of $[K]^{-1}[A_2]$, and $a_{22}^{(k)}$ is $(N-1+k)$th row of $[K]^{-1}[A_2]$. $b_{\alpha\beta}^{(k)}$ and $c_{\alpha\beta}^{(k)}$ can be calculated with similar manner as that of $a_{\alpha\beta}^{(k)}$ (components of $[K]^{-1}[B_\alpha]$ and $[K]^{-1}[C_\alpha]$).

Appendix C. In-plane correction factors of EFSDTM_TN

The in-plane strains based on the FSDT_TN displacement fields (Eq. (2.1.14)) can be expressed as

$$\bar{E_e} = \bar{E_0} + x_3\bar{K_0} + x_3 I_e \bar{K_r} \,,$$

(C.1)

where

$$\bar{E} = \begin{bmatrix} \bar{E_{11}} & \bar{E_{22}} & 2\bar{E_{12}} \end{bmatrix}^T, \quad \bar{E_o} = \begin{bmatrix} \bar{u}_{1,1}^{(0)} & \bar{u}_{2,2}^{(0)} & \bar{u}_{1,2}^{(0)} + \bar{u}_{2,1}^{(0)} \end{bmatrix}^T,$$
$$\bar{K_o} = -\begin{bmatrix} \bar{u}_{3,11}^{(0)} & \bar{u}_{3,22}^{(0)} & 2\bar{u}_{3,12}^{(0)} \end{bmatrix}^T, \quad \bar{K_r} = \begin{bmatrix} \bar{\gamma}_{31,1}^{(0)} & \bar{\gamma}_{32,2}^{(0)} & \bar{\gamma}_{31,2}^{(0)} & \bar{\gamma}_{32,1}^{(0)} \end{bmatrix}^T,$$

(C.2)

and

$$I_e = \begin{bmatrix} 1 & 0 & 0 & 0 \\ 0 & 1 & 0 & 0 \\ 0 & 0 & 1 & 1 \end{bmatrix}.$$

(C.3)

From the Eq. (A.1), vectors of the resultant forces and moments are given by

$$\tilde{N}_{FSDT\_TN} = \begin{bmatrix} \bar{N}_{11} & \bar{N}_{22} & \bar{N}_{12} \end{bmatrix}^T = \left\langle \bar{\sigma}_{\alpha\beta}^{2D} \right\rangle = A\bar{E}_0 + B\bar{K}_0 + BI_e\bar{K}_r,$$
$$\tilde{M}_{FSDT\_TN} = \begin{bmatrix} \bar{M}_{11} & \bar{M}_{22} & \bar{M}_{12} \end{bmatrix}^T = \left\langle x_3\bar{\sigma}_{\alpha\beta}^{2D} \right\rangle = B\bar{E}_0 + D\bar{K}_0 + DI_e\bar{K}_r, \quad \text{(C.4)}$$

In which

$$A = \left\langle \tilde{Q} \right\rangle, \quad B = \left\langle x_3\tilde{Q} \right\rangle, \quad D = \left\langle x_3^2\tilde{Q} \right\rangle.$$

(C.5)

The in-plane strains derived from the EHOPT_TN displacement fields (Eq. (2.1.33)) are expressed by

$$E_e = \bar{E}_0 + x_3\bar{K}_0 + \tilde{\Phi}^{*(1)}K_r + \tilde{\Phi}^{*(2)}\bar{T}_o + \tilde{\Phi}^{*(3)}\left(\frac{1}{2}\bar{T}_1\right) - \bar{C}^N - x_3\bar{C}^M,$$

(C.6)

in which

$$E_e = \begin{bmatrix} E_{11} & E_{22} & 2E_{12} \end{bmatrix}^T, \quad \bar{C}^{(N,M)} = \begin{bmatrix} C_{1,1}^{(N,M)} & C_{2,2}^{(N,M)} & C_{1,2}^{(N,M)} + C_{2,1}^{(N,M)} \end{bmatrix}^T,$$
$$K_r = \begin{bmatrix} u_{1,1}^{(3)} & u_{2,2}^{(3)} & u_{1,2}^{(3)} & u_{2,1}^{(3)} \end{bmatrix}^T, \quad \bar{T}_\alpha = \begin{bmatrix} T_{\alpha,11} & T_{\alpha,22} & T_{\alpha,12} & T_{\alpha,21} \end{bmatrix}^T,$$
$$\tilde{\Phi}^{*(i)} = \begin{bmatrix} \tilde{\Phi}_{11}^{*(i)} & 0 & 0 & \tilde{\Phi}_{12}^{*(i)} \\ 0 & \tilde{\Phi}_{22}^{*(i)} & \tilde{\Phi}_{21}^{*(i)} & 0 \\ \tilde{\Phi}_{21}^{*(i)} & \tilde{\Phi}_{12}^{*(i)} & \tilde{\Phi}_{11}^{*(i)} & \tilde{\Phi}_{22}^{*(i)} \end{bmatrix}.$$

(C.7)

In order to derive in-plane correction factors ($\bar{C}^{(N,M)}$), it is needed to express the resultant forces and moments based on EHOPT_TN in the vector form as follows:

$$\tilde{N}_{EHOPT\_TN} = A\bar{E}_0 + B\bar{K}_0 + E^{(1)}K_r + E^{(2)}\bar{T}_o + E^{(3)}\left(\frac{1}{2}\bar{T}_1\right) - A\bar{C}^N - B\bar{C}^M,$$
$$\tilde{M}_{EHOPT\_TN} = B\bar{E}_0 + D\bar{K}_0 + F^{(1)}K_r + F^{(2)}\bar{T}_o + F^{(3)}\left(\frac{1}{2}\bar{T}\right)_1 - B\bar{C}^N - D\bar{C}^M.$$

(C.8)

where

$$E^{(i)} = <\tilde{Q}\cdot\tilde{\Phi}^{*(i)}>, \quad F^{(i)} = <x_3\tilde{Q}\cdot\tilde{\Phi}^{*(i)}>.$$

(C.9)

According to the relationships of Eq. (2.1.24), stress resultants of FSDT_TN can be rewritten as:

$$\tilde{N}_{FSDT\_TN} = A\bar{E}_0 + B\bar{K}_0 + B\cdot\tilde{\Gamma}^{*(1)}K_r - B\cdot\tilde{\Gamma}^{*(2)}\bar{T}_o - B\cdot\tilde{\Gamma}^{*(3)}\left(\frac{1}{2}\bar{T}_1\right),$$
$$\tilde{M}_{FSDT\_TN} = B\bar{E}_0 + D\bar{K}_0 + D\cdot\tilde{\Gamma}^{*(1)}K_r - D\cdot\tilde{\Gamma}^{*(2)}\bar{T}_o - D\cdot\tilde{\Gamma}^{*(3)}\left(\frac{1}{2}\bar{T}_1\right).$$

(C.10)

where

$$\tilde{\Gamma}^{*(i)} = \begin{bmatrix} \Gamma_{11}^{*(i)} & 0 & 0 & \Gamma_{12}^{*(i)} \\ 0 & \Gamma_{22}^{*(i)} & \Gamma_{21}^{*(i)} & 0 \\ \Gamma_{21}^{*(i)} & \Gamma_{12}^{*(i)} & \Gamma_{11}^{*(i)} & \Gamma_{22}^{*(i)} \end{bmatrix},$$
$$\Gamma_{\alpha\beta}^{*(1)} = \left[\Gamma_{\alpha\beta}^{(1)}\right]^{-1}, \quad \Gamma_{\alpha\beta}^{*(2)} = \left[\Gamma_{\alpha\gamma}^{(1)}\right]^{-1}\left[\Gamma_{\gamma\beta}^{(2)}\right],$$
$$\Gamma_{\alpha\beta}^{*(3)} = \left[\Gamma_{\alpha\gamma}^{(1)}\right]^{-1}\left[\Gamma_{\gamma\beta}^{(3)}\right].$$

(C.11)

Based on the Saint-Venant's principle, the differences between resultant forces

and moments presented in Eqs. (C.8) and (C.10) can be expressed as

$$\begin{aligned}\tilde{N}_{EHOPT\_TN}-\tilde{N}_{FSDT\_TN}&=\left[E^{(1)}-B\cdot\tilde{\Gamma}^{*(1)}\right]K_r+\left[E^{(2)}+B\cdot\tilde{\Gamma}^{*(2)}\right]\overline{T}_o\\&\quad+\left[E^{(3)}+B\cdot\tilde{\Gamma}^{*(3)}\right]\left(\frac{1}{2}\overline{T}_1\right)-A\overline{C}^N-B\overline{C}^M\approx 0,\\\tilde{M}_{EHOPT\_TN}-\tilde{M}_{FSDT\_TN}&=\left[F^{(1)}-D\cdot\tilde{\Gamma}^{*(1)}\right]K_r+\left[F^{(2)}+D\cdot\tilde{\Gamma}^{*(2)}\right]\overline{T}_o\\&\quad+\left[F^{(3)}+D\cdot\tilde{\Gamma}^{*(3)}\right]\left(\frac{1}{2}\overline{T}_1\right)-B\overline{C}^N-D\overline{C}^M\approx 0.\end{aligned}$$

(C.12)

From the Eq. (C.12), the in-plane correction factors can be obtained by:

$$\begin{aligned}\begin{bmatrix}c_{\alpha\beta}^{N(\phi)}\\c_{\alpha\beta}^{M(\phi)}\end{bmatrix}&=\begin{bmatrix}A&B\\B&D\end{bmatrix}^{-1}\begin{bmatrix}E^{(1)}-B\cdot\tilde{\Gamma}^{*(1)}\\F^{(1)}-D\cdot\tilde{\Gamma}^{*(1)}\end{bmatrix},\\\begin{bmatrix}c_{\alpha\beta}^{N(T_o)}\\c_{\alpha\beta}^{M(T_o)}\end{bmatrix}&=\begin{bmatrix}A&B\\B&D\end{bmatrix}^{-1}\begin{bmatrix}E^{(2)}+B\cdot\tilde{\Gamma}^{*(2)}\\F^{(2)}+D\cdot\tilde{\Gamma}^{*(2)}\end{bmatrix},\\\begin{bmatrix}c_{\alpha\beta}^{N(T_1)}\\c_{\alpha\beta}^{M(T_1)}\end{bmatrix}&=\begin{bmatrix}A&B\\B&D\end{bmatrix}^{-1}\begin{bmatrix}E^{(3)}+B\cdot\tilde{\Gamma}^{*(3)}\\F^{(3)}+D\cdot\tilde{\Gamma}^{*(3)}\end{bmatrix},\end{aligned}$$

(C.13)

where

$$c_{\alpha\beta}^{N,M(\phi,T_o,T_1)}=\begin{bmatrix}\underline{c_{11}^{N,M(\phi,T_o,T_1)}}&0&0&\underline{c_{12}^{N,M(\phi,T_o,T_1)}}\\0&\underline{c_{22}^{N,M(\phi,T_o,T_1)}}&\underline{c_{21}^{N,M(\phi,T_o,T_1)}}&0\\c_{21}^{N,M(\phi,T_o,T_1)}&c_{12}^{N,M(\phi,T_o,T_1)}&c_{11}^{N,M(\phi,T_o,T_1)}&c_{22}^{N,M(\phi,T_o,T_1)}\end{bmatrix}.$$

(C.14)

In this study, the underline terms given Eq. (C.14) are selected as coefficients

of the in-plane correction factors.

Appendix D. Calculation process to determine $a_{\alpha\gamma}^{*(k)}$

The shear continuity conditions at layer interfaces can be expressed of the matrix form as:

$$[K^*][S^*] = [A_1^*]\phi_1^* + [A_2^*]\phi_2^*,$$

(D.1)

$$[S^*] = [S_1^{*(1)} \cdots S_1^{*(N-1)} \; S_2^{*(1)} \cdots S_2^{*(N-1)}]^T, \qquad S_\alpha^{*(k)} = a_{\alpha\beta}^{*(k)}\phi_\beta^*$$

(D.2)

Matrix [K*] is derived from this following algorithm:

$$\begin{aligned}
&for\ i = 1:(N-1)\\
&\ for\ \ j = 1:(i-1)\\
&\quad K^*(i,j) = (Q_{2313}^{*(i+1)} - Q_{2313}^{*(i)})(x_{3(i)}^*/h + 1/2 - 1)\\
&\quad K^*(i,N-1+j) = (Q_{2323}^{*(i+1)} - Q_{2323}^{*(i)})(x_{3(i)}^*/h + 1/2 - 1)\\
&\quad K^*(N-1+i,j) = (Q_{1313}^{*(i+1)} - Q_{1313}^{*(i)})(x_{3(i)}^*/h + 1/2 - 1)\\
&\quad K^*(N-1+i,N-1+j) = (Q_{1323}^{*(i+1)} - Q_{1323}^{*(i)})(x_{3(i)}^*/h + 1/2 - 1)\\
&\ end\\
&end
\end{aligned}$$

(D.3)

And the components of $[A_\alpha^*]$ are computed as:

$$\begin{aligned}
&for\ i = 1:(N-1)\\
&\ A_1^*(i) = 3(x_{3(i)}^2 - h^2/4)(Q_{1323}^{*(i+1)} - Q_{1323}^{*(i)})\\
&\ A_1^*(N-1+i) = 3(x_{3(i)}^2 - h^2/4)(Q_{1313}^{*(i+1)} - Q_{1313}^{*(i)})\\
&\ A_2^*(i) = 3(x_{3(i)}^2 - h^2/4)(Q_{2323}^{*(i+1)} - Q_{2323}^{*(i)})\\
&\ A_2^*(N-1+i) = 3(x_{3(i)}^2 - h^2/4)(Q_{2313}^{*(i+1)} - Q_{2313}^{*(i)})\\
&end
\end{aligned}$$

(D.4)

$a_{11}^{*(k)}$ represents (k) th row of $[K^*]^{-1}[A_1^*]$, $a_{21}^{*(k)}$ is $(N-1+k)$ th row of $[K^*]^{-1}[A_1^*]$, $a_{12}^{*(k)}$ is (k)th row of $[K^*]^{-1}[A_2^*]$, and $a_{22}^{*(k)}$ is $(N-1+k)$th row of $[K^*]^{-1}[A_2^*]$.

Appendix E. Definitions of the resultants and stiffness

Stress resultants and stiffness given in Eqs. (2.2.18) and (2.2.21) are defined by:

$$\begin{aligned}
&\bar{E}_o^* = \left[\bar{\varepsilon}_{11}^{o*} \quad \bar{\varepsilon}_{22}^{o*} \quad 2\bar{\varepsilon}_{12}^{o*}\right]^T, \qquad E_o^* = \left[\varepsilon_{11}^{o*} \quad \varepsilon_{22}^{o*} \quad 2\varepsilon_{12}^{o*}\right]^T,\\
&\bar{K}_o^* = \left[\bar{\varepsilon}_{11}^{(1)*} \quad \bar{\varepsilon}_{22}^{(1)*} \quad 2\bar{\varepsilon}_{12}^{(1)*}\right]^T, \quad K_o^* = \left[\varepsilon_{11}^{(1)*} \quad \varepsilon_{22}^{(1)*} \quad 2\varepsilon_{12}^{(1)*}\right]^T,\\
&K_h^* = \left[\phi_{1,1}^* \quad \phi_{2,2}^* \quad \phi_{1,2}^* \quad \phi_{2,1}^*\right]^T,\\
&\tilde{C}^* = \begin{bmatrix} C_{11}^* & 0 & 0 & C_{12}^* \\ 0 & C_{22}^* & C_{21}^* & 0 \\ C_{21}^* & C_{12}^* & C_{11}^* & C_{22}^* \end{bmatrix}, \quad \tilde{\Gamma}^* = \begin{bmatrix} \Gamma_{11}^* & 0 & 0 & \Gamma_{12}^* \\ 0 & \Gamma_{22}^* & \Gamma_{21}^* & 0 \\ \Gamma_{21}^* & \Gamma_{12}^* & \Gamma_{11}^* & \Gamma_{22}^* \end{bmatrix}.
\end{aligned}$$

(E.1)

And

$$\begin{aligned}
&A^* = \left\langle Q_e^* \right\rangle, \quad B^* = \left\langle x_3 \cdot Q_e^* \right\rangle, \quad D^* = \left\langle x_3^2 \cdot Q_e^* \right\rangle, \quad G^* = \left\langle \tilde{\Phi}_s^{*T} \cdot Q_s^* \cdot \tilde{\Phi}_s^* \right\rangle,\\
&E^* = \left\langle Q_e^* \cdot \tilde{\Phi}_e^* \right\rangle, \quad F^* = \left\langle x_3 \cdot Q_e^* \cdot \tilde{\Phi}_e^* \right\rangle, \quad H^* = \left\langle \tilde{\Phi}_e^{*T} \cdot Q_e^* \cdot \tilde{\Phi}_e^* \right\rangle.
\end{aligned}$$

(E.2)

where

$$\tilde{\Phi}_e^* = \begin{bmatrix} \tilde{\Phi}_{11}^* & 0 & 0 & \tilde{\Phi}_{12}^* \\ 0 & \tilde{\Phi}_{22}^* & \tilde{\Phi}_{21}^* & 0 \\ \tilde{\Phi}_{21}^* & \tilde{\Phi}_{12}^* & \tilde{\Phi}_{11}^* & \tilde{\Phi}_{22}^* \end{bmatrix}, \quad \tilde{\Phi}_s^* = \begin{bmatrix} \tilde{\Phi}_{11,3}^* & \tilde{\Phi}_{12,3}^* \\ \tilde{\Phi}_{21,3}^* & \tilde{\Phi}_{22,3}^* \end{bmatrix}.$$

(E.3)

Appendix F. Strain energy expression for the viscoelastic materials

The strain energy expressions for the linear-elastic and viscoelastic materials are given as:

$$U = \min_{\varepsilon_{33}} U^{3D} = \int_0^t \left\langle \sigma_{\alpha\beta}(w)\dot{\varepsilon}_{\alpha\beta}(w) + \sigma_{3\alpha}(w)\dot{\gamma}_{3\alpha}(w) \right\rangle dw.$$

(F.1)

By applying the Laplace transformation to Eq. (F.1), strain energy expression in Laplace domain can be derived as follows:

$$\begin{aligned} U^* &= L\left[\int_0^t \left\langle \sigma_{\alpha\beta}(w)\dot{\varepsilon}_{\alpha\beta}(w) + \sigma_{3\alpha}(w)\dot{\gamma}_{3\alpha}(w) \right\rangle dw \right] \\ &= \frac{1}{s}\left\langle L\left[\sigma_{\alpha\beta}(w)\dot{\varepsilon}_{\alpha\beta}(w) \right] + L\left[\sigma_{3\alpha}(w)\dot{\gamma}_{3\alpha}(w) \right] \right\rangle. \end{aligned}$$

(F.2)

Eq. (F.2) can be rearranged with considering multiplication and convolution theorem of the Laplace transformation as:

$$U^* = \left(\frac{1}{s}\right)\frac{1}{2\pi i}\lim_{T\to\infty}\int_{c-iT}^{c+iT}\left[\eta(s-\eta)\left\langle \begin{matrix} Q^*_{\alpha\beta\gamma\mu}(\eta)\varepsilon^*_{\gamma\mu}(\eta)\varepsilon^*_{\alpha\beta}(s-\eta) \\ +Q^*_{3\alpha 3\beta}(\eta)\gamma^*_{3\beta}(\eta)\gamma^*_{3\alpha}(s-\eta) \end{matrix} \right\rangle \right] d\eta,$$

(F.3)

where

$$\begin{aligned} &L\left[F(t)\cdot G(t) \right] \Rightarrow \frac{1}{2\pi i}\lim_{T\to\infty}\int_{c-iT}^{c+iT} F^*(\sigma)\cdot G^*(s-\sigma)d\sigma, \\ &L\left[(F*G)(t) \right] = L\left[\int_0^t F(\tau)\cdot G(t-\tau)d\tau \right] \Rightarrow F^*(s)\cdot G^*(s). \end{aligned}$$

(F.4)

The compact form of the strain energy expression in Laplace domain can be written as:

$$U^* = \mathop{\mathrm{I}}_{\eta}\left[\left\langle Q^*_{\alpha\beta\gamma\mu}(\eta)\varepsilon^*_{\gamma\mu}(\eta)\varepsilon^*_{\alpha\beta}(s-\eta) + Q^*_{3\alpha 3\beta}(\eta)\gamma^*_{3\beta}(\eta)\gamma^*_{3\alpha}(s-\eta)\right\rangle\right].$$

(F.5)

Appendix G. In-plane correction factor of EHSDTM

The in-plane strains based on the conventional HSDT displacement field given in Eq. (3.1.6) can be expressed by:

$$\bar{E_e} = \bar{E_0} + x_3\bar{K_0} + \sum_{i=1}^{3} x_3^i I_e \bar{K}_g^{(i)},$$

(G.1)

where

$$\begin{aligned}
\bar{E_e} &= \left[\bar{u}^{(0)}_{1,1} \quad \bar{u}^{(0)}_{2,2} \quad \left(\bar{u}^{(0)}_{1,2} + \bar{u}^{(0)}_{2,1}\right)\right]^T, \\
\bar{K_0} &= -\left[\bar{u}^{(0)}_{3,11} \quad \bar{u}^{(0)}_{3,22} \quad 2\bar{u}^{(0)}_{3,12}\right]^T, \\
\bar{K}_g^{(i)} &= \left[g^{(i)}_{31,1} \quad g^{(i)}_{32,2} \quad g^{(i)}_{31,2} \quad g^{(i)}_{32,1}\right]^T,
\end{aligned} \tag{G.2}$$

and

$$I_e = \begin{bmatrix} 1 & 0 & 0 & 0 \\ 0 & 1 & 0 & 0 \\ 0 & 0 & 1 & 1 \end{bmatrix}.$$

(G.3)

The stress resultants vector using Eq. (G.1) is given by

$$\tilde{\bar{N}} = \left\langle \bar{\sigma}_{\alpha\beta}^{2D} \right\rangle = A\bar{E}_0 + B\bar{K}_0 + \sum_{i=1}^{3} F^{(i)} I_e \bar{K}_g^{(i)}, \tag{G.4}$$

in which

$$\tilde{\bar{N}} = \begin{bmatrix} \bar{N}_{11} & \bar{N}_{22} & \bar{N}_{12} \end{bmatrix}^T, \quad A = \left\langle \tilde{Q} \right\rangle, \quad B = \left\langle x_3 \tilde{Q} \right\rangle, \tag{G.5}$$

where $\tilde{Q}$ is 3×3 matrix corresponding to $Q_{\alpha\beta\gamma\omega}$ given in Eq. (1.2.6), A and B are 3×3 matrices that are well-known transformed reduced stiffness matrices in the conventional FSDT. The higher-order stiffness matrix $F^{(i)}$ is defined as $F^{(i)} = \left\langle x_3^{(i)} \tilde{Q} \right\rangle$.

The in-plane strains based on the recovered displacement field given in Eq. (3.1.24) are written by

$$E_e = \bar{E}_0 + x_3 \bar{K}_0 + \frac{h^2}{24} I_e \bar{K}_g^{(2)} + \sum_{i=1}^{3} \tilde{\Phi}^{*(i)}(x_3) \cdot K_\psi^{(i)} - \tilde{\mathrm{c}}, \tag{G.6}$$

where

$$\begin{aligned} K_\psi^{(i)} &= \begin{bmatrix} \psi_{1,1}^{(i+2)} & \psi_{2,2}^{(i+2)} & \psi_{1,2}^{(i+2)} & \psi_{2,1}^{(i+2)} \end{bmatrix}^T, \\ \tilde{c} &= \begin{bmatrix} c_{1,1} & c_{2,2} & \left(c_{1,2} + c_{2,1}\right) \end{bmatrix}^T, \\ \tilde{\Phi}^{*(i)}(x_3) &= \begin{bmatrix} \tilde{\Phi}_{11}^{*(i)}(x_3) & 0 & 0 & \tilde{\Phi}_{12}^{*(i)}(x_3) \\ 0 & \tilde{\Phi}_{22}^{*(i)}(x_3) & \tilde{\Phi}_{21}^{*(i)}(x_3) & 0 \\ \tilde{\Phi}_{21}^{*(i)}(x_3) & \tilde{\Phi}_{12}^{*(i)}(x_3) & \tilde{\Phi}_{11}^{*(i)}(x_3) & \tilde{\Phi}_{12}^{*(i)}(x_3) \end{bmatrix}, \end{aligned} \tag{G.7}$$

in which

$$\tilde{\Phi}^{*(i)}(x_3) = \tilde{\Phi}^{(i)}(x_3) - \frac{1}{h}\left\langle \tilde{\Phi}^{(i)}(x_3) \right\rangle. \tag{G.8}$$

In order to calculate the three-dimensional in-plane stresses, it is needed to express the transverse normal stress in the vector form. Furthermore, it should be expressed in terms of the two-dimensional in-plane strains to obtain arbitrary functions c_α. From equations (3.1.2), (3.1.5) and (3.1.26), the recovered transverse normal stress can be rewritten by

$$\hat{\sigma}_{33} = -\sum_{i=1}^{3} \tilde{\Phi}^{t(i)}(x_3) \cdot K_\psi^{(i)}, \tag{G.9}$$

in which

$$\tilde{\Phi}^{t(i)}(x_3) = \left[\tilde{\Phi}_{11}^{t(i)}(x_3) \quad \tilde{\Phi}_{22}^{t(i)}(x_3) \quad \tilde{\Phi}_{21}^{t(i)}(x_3) \quad \tilde{\Phi}_{12}^{t(i)}(x_3) \right], \tag{G.10}$$

where

$$\tilde{\Phi}_{\alpha\beta}^{t(i)}(x_3) = \int_{-\frac{h}{2}}^{x_3} C_{\alpha 3 \mu 3} \varepsilon_{\mu\beta}^{(i)}(x_3). \tag{G.11}$$

Form Eqs. (G.6) and (G.9), the stress resultants vector is expressed by

$$\begin{aligned} \tilde{N} = \left\langle \sigma_{\alpha\beta}^{2D} + \overline{C}_{\alpha\beta 33}\hat{\sigma}_{33} \right\rangle = A\overline{E}_0 + B\overline{K}_0 + \frac{h^2}{24} A I_e \overline{K}_g^{(2)} \\ + \sum_{i=1}^{3} \left(E^{(i)} - E^{t(i)} \right) \cdot K_\psi^{(i)} - A\tilde{\mathfrak{c}}, \end{aligned} \tag{G.12}$$

in which

$$\tilde{N} = \begin{bmatrix} N_{11} & N_{22} & N_{12} \end{bmatrix}^T, \quad \bar{C}_{\alpha\beta 33} = C_{\alpha\beta 33} / C_{3333},$$
$$E^{(i)} = \left\langle \tilde{Q} \cdot \tilde{\Phi}^{*(i)} \right\rangle, \quad E^{\mathrm{t}(i)} = \left\langle \tilde{C}_{et} \cdot \tilde{\Phi}^{\mathrm{t}(i)} \right\rangle, \tag{G.13}$$
$$\tilde{C}_{et} = \begin{bmatrix} \bar{C}_{1133} & \bar{C}_{2233} & \bar{C}_{1233} \end{bmatrix}^T.$$

Now one needs to express the higher-order strain vector $K_{\psi}^{(i)}$ of the recovered displacement field in terms of the strain vector $\bar{K}_g^{(i)}$ of the conventional HSDT. To this end, using equation (3.1.10) yields

$$K_{\psi}^{(i)} = \Gamma_R^{(i)} \bar{K}_g^{(i)}, \tag{G.14}$$

where the 4 × 4 matrix $\Gamma_R^{(i)}$ can be calculated by using (3.1.10). This procedure is cumbersome but straightforward, and therefore omitted for a brevity.

The difference between in-plane stress resultants presented in (G.4) and (G.12), after applying (G.14), can be expressed as:

$$\sum_{i=1}^{3} \left[\left(E^{(i)} - E^{t(i)} \right) \cdot \Gamma_R^{(i)} - F^{(i)} I_e \right] \bar{K}_g^{(i)} + \frac{h^2}{24} A I_e \bar{K}_g^{(2)} - A\tilde{\mathrm{c}} = 0, \tag{G.15}$$

The difference should be vanished so that the recovered strain vector satisfies the equilibrium. From equation (G.15), the correction strain vector can be calculated, since the matrix *A* is always invertible, as follows:

$$\tilde{c} = \sum_{i=1}^{3} \tilde{c}^{(i)} \bar{K}_g^{(i)}, \tag{G.16}$$

in which $\tilde{c}^{(i)}$ are 3 × 4 matrices.

Appendix H. In-plane correction factors of ELCWM

The in-plane strains based on conventional LCW which given in Eq. (3.2.9) can be expressed as

$$E_e = E_o + \sum_{k=1}^{3}\left[\frac{1}{k}\left(x_3^{(k)}K_o^{(k-1)} + x_3^{(k)}I_eK_r^{(k-1)}\right)\right], \tag{A.40}$$

Where

$$\begin{aligned} E_e &= \begin{bmatrix} E_{11} & E_{22} & 2E_{12} \end{bmatrix}^T, \\ E_o &= \begin{bmatrix} u_{1,1}^o & u_{2,2}^o & u_{1,2}^o + u_{2,1}^o \end{bmatrix}^T, \\ K_o^{(i)} &= -\begin{bmatrix} u_{3,11}^{(i)} & u_{3,22}^{(i)} & 2u_{3,12}^{(i)} \end{bmatrix}^T, \\ K_r^{(i)} &= \begin{bmatrix} \gamma_{31,1}^{(i)} & \gamma_{32,2}^{(i)} & \gamma_{31,2}^{(i)} & \gamma_{32,1}^{(i)} \end{bmatrix}^T, \end{aligned} \tag{A.41}$$

and

$$I_e = \begin{bmatrix} 1 & 0 & 0 & 0 \\ 0 & 1 & 0 & 0 \\ 0 & 0 & 1 & 1 \end{bmatrix}. \tag{A.42}$$

Using the Eq. (H.1), vector of the stress resultants forces is given as follows:

$$\begin{aligned} \tilde{N}_{\alpha\beta} &= \left\langle \sigma_{\alpha\beta} \right\rangle = \begin{bmatrix} N_{11} & N_{22} & N_{12} \end{bmatrix}^T \\ &= A^{(0)}E_o + \sum_{m=1}^{3}\left[\frac{1}{k}A^{(m)}K_o^{(m-1)} + \frac{1}{k}A^{(m)}I_eK_r^{(m-1)}\right] \\ &\quad + \overline{A}^{(0)}u_3^{(1)} + 2\overline{A}^{(1)}u_3^{(2)} - \tilde{N}_{\alpha\beta}^{\theta}, \end{aligned} \tag{A.43}$$

in which

$$\left[A^{(k)} \ , \ \overline{A}^{(k)} \right] = \left[< x_3^{(k)} \tilde{C} > , < x_3^{(k)} \overline{C} > \right], \tag{A.44}$$

where $\tilde{C}$ is 3 x 3 matrix corresponding to $C_{\alpha\beta\gamma\omega}$ and $\overline{C}$ is 3 x 1 vectors corresponding to $C_{\alpha\beta 33}$ given in Eq. (3.2.24). And $\tilde{N}_{\alpha\beta}^{\theta}$ is vector of the thermal stress resultants forces as follows:

$$\tilde{N}_{\alpha\beta}^{\theta} = \left[N_{11}^{\theta} \quad N_{22}^{\theta} \quad N_{12}^{\theta} \right]^T = \left\langle \sigma_{\alpha\beta}^{\theta} \right\rangle = \left[A_{\theta}^{(0)} + \overline{A}_{\theta}^{(0)} \right] \theta, \tag{A.45}$$

in which

$$\begin{aligned} &\left[A_{\theta}^{(0)} \ , \ \overline{A}_{\theta}^{(0)} \right] = \left[< \tilde{C}\tilde{\alpha} > , < \overline{C}\alpha_{33} > \right], \\ &\tilde{\alpha} = [\alpha_{11} \quad \alpha_{22} \quad \alpha_{12}]^T. \end{aligned} \tag{A.46}$$

And the in-plane strains derived from the recovered displacements given in Eq. (3.2.30) are expressed as

$$E_e^* = E_o + \frac{h^2}{24} K_r^{(1)} + \sum_{k=1}^{3} \left[\frac{1}{k} x_3^{(k)} K_o^{(k-1)} + \Phi_{\alpha\beta}^{(k)} K_h^{(k)} \right] - \tilde{c}, \tag{A.47}$$

in which

$$\begin{aligned} E_e^* &= \left[E_{11}^* \quad E_{22}^* \quad 2E_{12}^* \right]^T, \\ K_h &= \left[\phi_{1,1}^{(i)} \quad \phi_{2,2}^{(i)} \quad \phi_{1,2}^{(i)} \quad \phi_{2,1}^{(i)} \right]^T, \\ \tilde{c} &= \left[c_{1,1} \quad c_{2,2} \quad (c_{1,2} + c_{2,1}) \right]^T, \end{aligned} \tag{A.48}$$

In the Eq. (H.8),superscript $(\bullet)^*$ makes distinctly difference between vector of in-plane strain fields based on recovered displacements and those of obtained by

conventional LCW which given in Eq. (H.1).

Through the relationships between the two theories given in Eq. (3.2.16), transverse shear strain based on the recovered fifth-order zig-zag model can be expressed in terms of the conventional LCW as following different manner:

$$\begin{bmatrix} \phi_\beta^{(1)} \\ \phi_\beta^{(2)} \\ \phi_\beta^{(3)} \end{bmatrix} = \begin{bmatrix} \tilde{\Gamma}_{11} & \tilde{\Gamma}_{12} & \tilde{\Gamma}_{13} \\ \tilde{\Gamma}_{21} & \tilde{\Gamma}_{22} & \tilde{\Gamma}_{23} \\ \tilde{\Gamma}_{31} & \tilde{\Gamma}_{32} & \tilde{\Gamma}_{33} \end{bmatrix} \begin{bmatrix} \gamma_{3\alpha}^{(0)} \\ \gamma_{3\alpha}^{(1)} \\ \gamma_{3\alpha}^{(2)} \end{bmatrix}. \tag{A.49}$$

In order to calculate these in-plane correction factors, it is needed to express the stress resultant forces based on ELCW in the vector form. From Eq. (H.8), vectors of the stress resultants forces are given by

$$\begin{aligned} \tilde{N}_{\alpha\beta}^* &= \left\langle \sigma_{\alpha\beta}^* \right\rangle = \begin{bmatrix} N_{11}^* & N_{22}^* & N_{12}^* \end{bmatrix}^T \\ &= A^{(0)} E_o + \frac{h^2}{24} A^{(0)} K_r^{(1)} - A^{(0)} \tilde{c} \\ &+ \sum_{m=1}^{3} \left[\frac{1}{k} A^{(m)} K_o^{(m-1)} + \left(\sum_n^3 \tilde{E}^{(n)} \hat{\Gamma}_{nm} \right) K_r^{(m-1)} \right] \\ &+ \overline{A}^{(0)} u_3^{(1)} + 2\overline{A}^{(1)} u_3^{(2)} - \tilde{N}_{\alpha\beta}^{\theta}, \end{aligned} \tag{A.50}$$

where,

$$\begin{aligned} \tilde{E}^{(i)} &= < \tilde{C} \tilde{\Phi}^{(i)} >, \; \tilde{\Phi}^{(i)} = \begin{bmatrix} \Phi_{11}^{(i)} & 0 & 0 & \Phi_{12}^{(i)} \\ 0 & \Phi_{22}^{(i)} & \Phi_{21}^{(i)} & 0 \\ \Phi_{21}^{(i)} & \Phi_{12}^{(i)} & \Phi_{11}^{(i)} & \Phi_{22}^{(i)} \end{bmatrix}, \\ \hat{\Gamma}_{ij} &= \begin{bmatrix} \tilde{\Gamma}_{ij}(1,1) & 0 & 0 & \tilde{\Gamma}_{ij}(1,2) \\ 0 & \tilde{\Gamma}_{ij}(2,2) & \tilde{\Gamma}_{ij}(2,1) & 0 \\ 0 & \tilde{\Gamma}_{ij}(1,2) & \tilde{\Gamma}_{ij}(1,1) & 0 \\ \tilde{\Gamma}_{ij}(2,1) & 0 & 0 & \tilde{\Gamma}_{ij}(2,2) \end{bmatrix}. \end{aligned} \tag{A.51}$$

By means of considering Saint-Venant's principle the differences between in-plane stress resultant forces given as Eqs. (H.4) and (H.11) can be expressed as

$$\begin{aligned}\tilde{N}^{*}-\tilde{N}=&\frac{h^{2}}{24}A^{(0)}K_{r}^{(1)}\\&+\sum_{m=1}^{3}\left[\left\{\left(\sum_{n}^{3}\tilde{E}^{(n)}\hat{\Gamma}_{nm}\right)-\frac{1}{k}A^{(m)}I_{e}\right\}K_{r}^{(m-1)}\right]-A^{(0)}\tilde{c}=0.\end{aligned}\tag{A.52}$$

Using Eq. (H.9), vector of in-plane correction factors, $\tilde{c}$, can be obtained as follows:

- In-plane correction factors:

$$\tilde{c}=\left[A^{(0)}\right]^{-1}\left[\frac{h^{2}}{24}A^{(0)}K_{r}^{(1)}+\sum_{m=1}^{3}\left[\left\{\left(\sum_{n}^{3}\tilde{E}^{(n)}\hat{\Gamma}_{nm}\right)-\frac{1}{k}A^{(m)}I_{e}\right\}K_{r}^{(m-1)}\right]\right].\tag{A.53}$$

Appendix I. Expression of the symmetric operator and loading vector

Algebraic equation of ELCW given in Eq. (3.2.35) as follows:

$$L_{ij}X_j = F_i, \quad (i,j = 1,2,\cdots,11) \tag{I.1}$$

where L_{ij} is a symmetric operator to solve algebraic equation, and it can be expressed as

$$\begin{aligned}
&L_{(1,1)} = -A_{11}^{(0)}p^2 - A_{66}^{(0)}q^2,\ L_{(1,2)} = -\left(A_{12}^{(0)} + A_{66}^{(0)}\right)pq,\\
&L_{(1,3)} = -A_{11}^{(1)}p^2 - A_{66}^{(1)}q^2,\ L_{(1,4)} = -\left(A_{12}^{(1)} + A_{66}^{(1)}\right)pq,\\
&L_{(1,5)} = -A_{11}^{(2)}p^2 - A_{66}^{(2)}q^2,\ L_{(1,6)} = -\left(A_{12}^{(2)} + A_{66}^{(2)}\right)pq,\\
&L_{(1,7)} = -A_{11}^{(3)}p^2 - A_{66}^{(3)}q^2,\ L_{(1,8)} = -\left(A_{12}^{(3)} + A_{66}^{(3)}\right)pq,\\
&L_{(1,9)} = 0,\ L_{(1,10)} = A_{13}^{(0)}p,\ L_{(1,11)} = 2A_{13}^{(1)}p,\\
&L_{(2,2)} = -A_{66}^{(0)}p^2 - A_{22}^{(0)}q^2,\ L_{(2,3)} = -\left(A_{12}^{(1)} + A_{66}^{(1)}\right)pq,\\
&L_{(2,4)} = -A_{66}^{(1)}p^2 - A_{22}^{(1)}q^2,\ L_{(2,5)} = -\left(A_{12}^{(2)} + A_{66}^{(2)}\right)pq,\\
&L_{(2,6)} = -A_{66}^{(2)}p^2 - A_{22}^{(2)}q^2,\ L_{(2,8)} = -\left(A_{12}^{(3)} + A_{66}^{(3)}\right)pq,\\
&L_{(2,9)} = 0,\ L_{(2,10)} = A_{23}^{(0)}p,\ L_{(2,11)} = 2A_{23}^{(1)}p,\\
&L_{(3,3)} = -A_{55}^{(0)} - A_{11}^{(2)}p^2 - A_{66}^{(2)}q^2,\\
&L_{(3,4)} = -\left(A_{12}^{(2)} + A_{66}^{(2)}\right)pq,\\
&L_{(3,5)} = -2A_{55}^{(1)} - A_{11}^{(3)}p^2 - A_{66}^{(3)}q^2,\\
&L_{(3,6)} = -\left(A_{12}^{(3)} + A_{66}^{(3)}\right)pq,\\
&L_{(3,7)} = -3A_{55}^{(2)} - A_{11}^{(4)}p^2 - A_{66}^{(4)}q^2,\\
&L_{(3,8)} = -\left(A_{12}^{(4)} + A_{66}^{(4)}\right)pq,\\
&L_{(3,9)} = -A_{55}^{(0)}p,\ L_{(3,10)} = \left(A_{13}^{(1)} - A_{55}^{(1)}\right)p,\\
&L_{(3,11)} = \left(2A_{13}^{(2)} - A_{55}^{(2)}\right)p,
\end{aligned} \tag{I.2}$$

$$
\begin{aligned}
&L_{(4,4)} = -A_{44}^{(0)} - A_{66}^{(2)} p^2 - A_{22}^{(2)} q^2, \\
&L_{(4,5)} = -\left(A_{12}^{(3)} + A_{66}^{(3)} \right) pq, \\
&L_{(4,6)} = -2A_{44}^{(1)} - A_{66}^{(3)} p^2 - A_{22}^{(3)} q^2, \\
&L_{(4,7)} = -\left(A_{12}^{(4)} + A_{66}^{(4)} \right) pq, \\
&L_{(4,8)} = -3A_{44}^{(2)} - A_{66}^{(4)} p^2 - A_{22}^{(4)} q^2, \\
&L_{(4,9)} = -A_{55}^{(0)} q, \\
&L_{(4,10)} = \left(A_{23}^{(1)} - A_{44}^{(1)} \right) q,\ L_{(4,11)} = \left(2A_{23}^{(2)} - A_{44}^{(2)} \right) q, \\
&L_{(5,5)} = -2A_{55}^{(2)} - A_{11}^{(4)} p^2 - A_{66}^{(4)} q^2,\ L_{(5,6)} = -\left(A_{12}^{(3)} + A_{66}^{(4)} \right) pq, \\
&L_{(5,7)} = -6A_{55}^{(3)} - A_{11}^{(5)} p^2 - A_{66}^{(5)} q^2,\ L_{(5,8)} = -\left(A_{12}^{(5)} + A_{66}^{(5)} \right) pq, \\
&L_{(5,9)} = -2A_{55}^{(1)} p,\ L_{(5,10)} = \left(A_{13}^{(2)} - 2A_{55}^{(2)} \right) p, \\
&L_{(5,11)} = 2\left(A_{13}^{(3)} - A_{55}^{(3)} \right) p, \\
&L_{(6,6)} = -4A_{44}^{(2)} - A_{66}^{(4)} p^2 - A_{22}^{(4)} q^2, \\
&L_{(6,7)} = -\left(A_{12}^{(5)} + A_{66}^{(5)} \right) pq, \\
&L_{(6,8)} = -6A_{44}^{(3)} - A_{66}^{(5)} p^2 - A_{22}^{(5)} q^2,\ L_{(6,9)} = -2A_{44}^{(1)} q, \\
&L_{(6,10)} = \left(A_{23}^{(2)} - 2A_{44}^{(2)} \right) q,\ L_{(6,11)} = 2\left(A_{23}^{(3)} - A_{44}^{(3)} \right) q, \\
&L_{(7,7)} = -9A_{55}^{(4)} - A_{11}^{(6)} p^2 - A_{66}^{(6)} q^2, \\
&L_{(7,8)} = -\left(A_{12}^{(6)} + A_{66}^{(6)} \right) pq, \\
&L_{(7,9)} = -3A_{55}^{(2)} p, L_{(7,10)} = \left(A_{13}^{(3)} - 3A_{55}^{(3)} \right) p, \\
&L_{(7,11)} = \left(2A_{13}^{(4)} - 3A_{55}^{(4)} \right) p, \\
&L_{(8,8)} = -9A_{44}^{(4)} - A_{66}^{(6)} p^2 - A_{22}^{(6)} q^2,\ L_{(8,9)} = -3A_{44}^{(2)} q, \\
&L_{(8,10)} = \left(A_{23}^{(3)} - 3A_{44}^{(3)} \right) q,\ L_{(8,11)} = \left(2A_{23}^{(4)} - 3A_{44}^{(4)} \right) q, \\
&L_{(9,9)} = -A_{55}^{(0)} p^2 - A_{44}^{(0)} q^2,\ L_{(9,10)} = -A_{55}^{(1)} p^2 - A_{44}^{(1)} q^2, \\
&L_{(9,11)} = -A_{55}^{(2)} p^2 - A_{44}^{(2)} q^2, \\
&L_{(10,10)} = -A_{33}^{(0)} - A_{55}^{(2)} p^2 - A_{44}^{(2)} q^2, \\
&L_{(10,11)} = -A_{33}^{(1)} - A_{55}^{(3)} p^2 - A_{44}^{(3)} q^2, \\
&L_{(11,11)} = -4A_{33}^{(2)} - A_{55}^{(4)} p^2 - A_{44}^{(4)} q^2,
\end{aligned}
\tag{I.3}
$$

And the loading vector F_i can be obtained by following the same procedure described above in Eqs. (3.2.22) and (3.2.25).

Detail expression of loading vector F_i can be expressed as:

$$
\begin{aligned}
&F_{i(1,1)} = N^{\theta}_{11,1} + N^{\theta}_{12,2}, \quad F_{i(2,1)} = N^{\theta}_{21,1} + N^{\theta}_{22,2}, \\
&F_{i(3,1)} = M^{\theta}_{11,1} + M^{\theta}_{12,2}, \quad F_{i(4,1)} = M^{\theta}_{21,1} + M^{\theta}_{22,2}, \\
&F_{i(5,1)} = R^{(2)\theta}_{11,1} + R^{(2)\theta}_{12,2}, \quad F_{i(6,1)} = R^{(2)\theta}_{21,1} + R^{(2)\theta}_{22,2}, \\
&F_{i(7,1)} = R^{(3)\theta}_{11,1} + R^{(3)\theta}_{12,2}, \quad F_{i(8,1)} = R^{(3)\theta}_{21,1} + R^{(3)\theta}_{22,2}, \\
&F_{i(9,1)} = -\tilde{t}_3, \qquad\qquad F_{i(10,1)} = -\frac{h}{2}\tilde{t}_3 + N^{\theta}_{33}, \\
&F_{i(11,1)} = -\frac{h^2}{4}\tilde{t}_3 + 2M^{\theta}_{33}.
\end{aligned}
\tag{I.4}
$$

In the symmetric operator L_{ij}, it should be noted that the coefficients, such as $A^{(k)}_{ij}$, etc., are the same as those obtained by LCW except for the transverse shear stiffness, i.e., $A^{(k)}_{44}$ and $A^{(k)}_{55}$ terms.

국문 요약

본 논문에서는 복합재료 구조물의 보다 향상된 열-기계적 거동 및 점탄성 거동에 대한 해석을 위한 개선된 해석 모델들이 제안되었다. 또한, 선형 해석에 국한되어 있던 개선된 해석 모델에 비선형 특징을 추가적으로 고려해줌으로써 복합재료 구조물의 기하 비선형 거동을 보다 정확하게 해석하고자 하였다. 개선된 해석 모델에서는 계산 과정의 효율성과 변위 및 응력 분포 결과의 정확도를 동시에 만족시키기 위한 방안으로써 서로 독립적인 두 개의 변위장이 각각 가정되며, 본 연구의 주된 목적으로써 변형 에너지 변환 과정 또는 혼합 변분 이론의 구속 방정식에 근거하여 각각 독립적으로 가정되는 두 변위장 사이의 관계를 정의해주고자 하였다. 정의되는 관계식에 따라, 개선된 이론들은 복합재료 구조물의 거동을 해석함에 있어서 비교적 간단한 계산 과정만이 요구되는 동시에 후처리 과정을 통해 고차 성분들을 복원하여 줌으로써 변위 및 응력 분포 결과의 정확도를 비약적으로 향상시키고자 하였다.

본 논문을 통해 제안된 개선된 해석 모델들은 다음과 같은 장점을 갖는다.

- 적층 구조물의 각 층별 경계에서의 횡방향 전단응력 연속 조건이 만족된다.
- 적층 구조물의 표면 전단 무응력 조건이 만족된다.
- 주 변수는 적층 수에 독립적이기 때문에, 계산의 효율성이 증대된다.

- 유한요소 해석 과정에서 C^0 함수만이 요구된다.

개선된 해석 모델들의 정확성 및 효율성은 여러 수치예제 결과들로부터 엄밀하게 검증하였다.

주요어 : 개선된 해석 모델, 변형 에너지 변환 과정, 열-기계적 거동 해석, 점탄성 거동 해석, 기하 비선형 거동 해석

학 번 : 2009-20740